

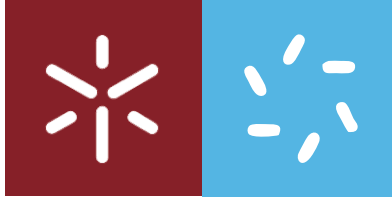


Ana Rita Oliveira Rodrigues

**Magnetoliposomes based on nickel/silica
and ferrite nanoparticles as nanocarriers
for potential antitumor drugs**

Universidade do Minho
Escola de Ciências





Universidade do Minho

Escola de Ciências

Ana Rita Oliveira Rodrigues

**Magnetoliposomes based on nickel/silica
and ferrite nanoparticles as nanocarriers
for potential antitumor drugs**

Tese de Doutoramento
Programa Doutoral em Física (MAP-fis)

Trabalho efetuado sob a orientação da
**Professora Doutora Elisabete M. S. Castanheira
Coutinho**

e do
Professor Doutor Paulo J. G. Coutinho

Agosto 2017

DECLARAÇÃO

Nome: Ana Rita Oliveira Rodrigues

Endereço electrónico: ritarodrigues@fisica.uminho.pt

Título tese:

Magnetoliposomes based on nickel/silica and ferrite nanoparticles as nanocarriers for potential antitumor drugs

Orientadores:

Professora Doutora Elisabete Maria dos Santos Castanheira Coutinho

Professor Doutor Paulo José Gomes Coutinho

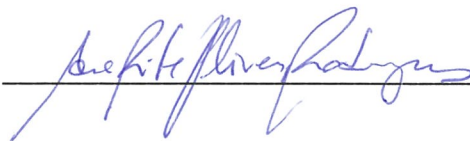
Ano de conclusão: 2017

Designação do Ramo de Conhecimento do Doutoramento: Física, Programa Doutoral MAP-fis

É AUTORIZADA A REPRODUÇÃO INTEGRAL DESTA TESE/TRABALHO APENAS PARA EFEITOS DE INVESTIGAÇÃO, MEDIANTE DECLARAÇÃO ESCRITA DO INTERESSADO, QUE A TAL SE COMPROMETE;

Universidade do Minho, 31 / 08 / 2017

Assinatura: _____




STATEMENT OF INTEGRITY

I hereby declare having conducted my thesis with integrity. I confirm that I have not used plagiarism or any form of falsification of results in the process of the thesis elaboration.

I further declare that I have fully acknowledged the Code of Ethical Conduct of the University of Minho.

University of Minho, 31 / 08 / 2017

Full name: Ana Rita Oliveira Rodrigues

Signature:  _____

ACKNOWLEDGEMENTS

In the end of this long and very important journey of my life, I would like to thank, individually, to all who in many and different ways contributed for the success of this project.

First of all, I would like to express my deepest sincere gratitude to my supervisors Professor Dr. Elisabete Castanheira Coutinho and Professor Dr. Paulo Coutinho, who since early, have given me so many opportunities to work in this world which I am so passionate about. I am grateful for the unconditional support and for all the scientific knowledge learned that made me grow as a research scientist. Thank you for the commitment and dedication to this work, your advice has been priceless.

To Professor Dr. Maria João Queiroz, from the Chemistry Center of the University of Minho, for the potentially antitumor compounds.

Professor Dr. Bernardo Almeida and Professor Dr. João Pedro Araújo, for the evaluation of magnetic properties at the Institute of Physics of Materials of the University of Porto (IFIMUP).

Professor Dr. Isabel Ferreira and Dr. Ricardo Calhella for cell line studies at the Mountain Research Center (CIMO) of the Polytechnic Institute of Bragança.

To the Foundation for a Science and Technology for the PhD grant (SFRH / BD / 90949/2012) and to the Doctoral Program MAP-fis for the opportunities. Also to the Department and Physics Center, for the equipment and materials that make the execution of this work possible.

A special thanks to my mom and dad, brother and grandparents for my education, inspirations and intellectual motivation that have always been present in my life. To my lover Nuno for the patience, encouragement and endless spoiling that helped me so much in the moments of greater work and stress.

To all my friends and colleagues, for the constant support and for all theories and discussions that have made this project even more pleasurable.

To all, Thank you very much!

The author, Ana Rita Oliveira Rodrigues, was supported by the Portuguese Foundation for Science and Technology (in portuguese FCT – Fundação para a Ciência e a Tecnologia) with the PhD grant SFRH/BD/90949/2012.

This work was also funded by the Strategic Funding of the Centre of Physics of University of Minho (CFUM) - PEst-C/FIS/UI0607/2013, and by the Centre of Physics of Minho and Porto Universities (CF-UM-UP) - UID/FIS/04650/2013.



Governo da República Portuguesa



UNIÃO EUROPEIA
Fundo Social Europeu

FCT Fundação para a Ciência e a Tecnologia

MINISTÉRIO DA CIÊNCIA, TECNOLOGIA E ENSINO SUPERIOR

ABSTRACT

Magnetoliposomes based on nickel/silica and ferrite nanoparticles as nanocarriers for potential antitumor drugs

Cancer is one of the diseases with higher incidence among the world population nowadays, with a huge mortality rate. Most of antitumor drugs used in chemotherapy are toxic and cause systemic side effects. In biomedicine, the potential of magnetic nanoparticles has been increasingly recognized, due to their unique size and physicochemical properties. Nanoparticles with superparamagnetic behavior are preferred for these purposes, as they exhibit a strong magnetization only when an external magnetic field is applied.

The development of liposomes entrapping magnetic nanoparticles, the so-called magnetoliposomes, allows a safer use of powerful anticancer drugs in chemotherapy as they can overcome many pharmacokinetics problems and systemic toxicity. Furthermore, magnetoliposomes can be guided and localized to the therapeutic site of interest by external magnetic field gradients and used in cancer treatment by hyperthermia.

In this work, nickel/silica core/shell and several ferrite nanoparticles were synthesized. Magnetic nanoparticles with nickel core and silica shell were prepared by soft chemical methods, using tetraethyl orthosilicate (TEOS) and different surfactants as templating media. Nickel nanoparticles without silica shell showed sizes of 66 ± 24 nm, while the ones with silica shell are larger and more polydisperse. Magnetic nickel nanoparticles and several ferrite nanoparticles, namely of nickel ferrite (NiFe_2O_4), manganese ferrite (MnFe_2O_4) and magnetite (Fe_3O_4) were obtained by coprecipitation method. All these nanoparticles show a crystalline structure and generally small diameters, exhibiting size distributions of 11 ± 5 nm for nickel ferrite, 26 ± 7 nm for manganese ferrite and 11.6 ± 1.6 nm for magnetite nanoparticles. The magnetic properties indicate a superparamagnetic behavior at room temperature for all types of ferrite particles, with magnetic squareness values (M_r/M_s) below 0.1. However, nickel nanoparticles showed a ferromagnetic behavior. Magnetite nanoparticles revealed to be the ones with higher saturation magnetization of 62 emu/g, while manganese ferrite and nickel ferrite nanoparticles exhibited values of 36 emu/g and 23.54 emu/g, respectively.

All the prepared nanoparticles were incorporated in liposomes by different procedures, thereby producing distinct magnetoliposomes. Either the magnetic nanoparticles were entrapped in liposomes, originating aqueous magnetoliposomes (AMLs), or covered with a lipid bilayer, forming solid magnetic liposomes (SMLs). A new and promising route for the synthesis of SMLs was developed and the coverage of the nanoparticles with a lipid bilayer was proven by FRET (Förster Resonance Energy Transfer) measurements, using fluorescent-labelled lipids (with the fluorophores NBD and Rhodamine). Both AMLs and SMLs revealed to be suitable for biomedical applications, possessing sizes below 150 nm and a narrow size distribution. Both AMLs and SMLs based on manganese ferrite nanoparticles showed superparamagnetic behavior at room temperature, the SMLs exhibiting a high saturation magnetization of 34.16 emu/g, similar to the observed for net manganese ferrite nanoparticles.

Membrane fusion between both types of magnetoliposomes (AMLs and SMLs) and GUVs (Giant Unilamellar Vesicles, used as models of cell membranes) was confirmed by FRET assays, showing the potential of these bionanosystems to release drugs by fusion with cell membranes. New potential antitumor drugs, thienopyridine derivatives with proven antitumor activity, were successfully incorporated into both aqueous and solid magnetoliposomes, with high encapsulation efficiencies (> 75%). Moreover, *in vitro* assays in several human tumor cell lines, namely HeLa (cervical carcinoma), MCF-7 (breast adenocarcinoma), T3M4 (pancreatic cancer), HCT15 (colon adenocarcinoma) and NCI-H460 (non-small cell lung carcinoma) revealed that AMLs based on MnFe_2O_4 nanoparticles are able to release the encapsulated compounds and to inhibit the growth of human tumor cells. Overall, these results point to a promising application of these systems in oncological therapy, simultaneously as nanocarriers for antitumor drugs and hyperthermia agents.

RESUMO

Magnetolipossomas baseados em nanopartículas de níquel/sílica e ferrites como nanotransportadores de potenciais fármacos antitumorais

O cancro é uma das doenças com maior incidência na população mundial na atualidade, com uma taxa de mortalidade enorme. Uma grande parte dos fármacos usados em quimioterapia são tóxicos e causam efeitos secundários. Na área da Biomedicina, o potencial das nanopartículas magnéticas tem sido cada vez mais reconhecido, devido ao seu tamanho reduzido e às suas propriedades físico-químicas únicas. Para aplicações biomédicas, estas nanopartículas devem apresentar um comportamento superparamagnético à temperatura ambiente, uma vez que exibem elevada magnetização apenas na presença de um campo magnético externo.

O desenvolvimento de lipossomas contendo nanopartículas magnéticas (magnetolipossomas) permite uma utilização mais segura de fármacos antitumorais potentes na quimioterapia, uma vez que estes nanossistemas podem superar muitos dos problemas de farmacocinética e de toxicidade sistémica. Além disso, os magnetolipossomas podem ser guiados e localizados no local terapêutico de interesse através de gradientes de campo magnético externo e ainda ser utilizados no tratamento do cancro por hipertermia magnética.

Neste trabalho, foram sintetizadas nanopartículas núcleo/coroa de níquel/sílica e várias ferrites. Assim, foram preparadas nanopartículas magnéticas com núcleo de níquel e coroa de sílica por métodos químicos suaves, usando tetraetilortossilicato (TEOS) e diferentes agentes surfactantes como moldes. As nanopartículas de níquel sem coroa de sílica mostraram tamanhos de 66 ± 24 nm, enquanto as que possuem cobertura de sílica são maiores e mais polidispersas.

Nanopartículas magnéticas de níquel e vários tipos de ferrites, nomeadamente ferrite de níquel (NiFe_2O_4), ferrite de manganês (MnFe_2O_4) e magnetite (Fe_3O_4), foram obtidas pelo método de coprecipitação. Todas estas nanopartículas possuem uma estrutura cristalina e diâmetros geralmente pequenos, exibindo uma distribuição de tamanhos de 11 ± 5 nm para a ferrite de níquel, 26 ± 7 nm para a ferrite de manganês e $11,6 \pm 1,6$ nm para a magnetite. As propriedades magnéticas revelaram um comportamento superparamagnético à temperatura ambiente para todas as nanopartículas de ferrite, com valores de razão magnética (M_r/M_s) inferiores a 0,1. No entanto, as nanopartículas de níquel apresentaram um comportamento ferromagnético. As nanopartículas de magnetite foram as

que apresentaram uma maior magnetização de saturação, com um valor de 62 emu/g, enquanto as ferrites de manganês e de níquel apresentaram valores de 36 emu/g e 23,54 emu/g, respetivamente.

Todas as nanopartículas preparadas foram encapsuladas em lipossomas usando diferentes procedimentos, produzindo assim magnetolipossomas distintos. As nanopartículas foram, quer encapsuladas em lipossomas, originando magnetolipossomas aquosos (AMLs) ou cobertas com uma bicamada lipídica, formando magnetolipossomas sólidos (SMLs). Foi desenvolvido um novo método promissor para a síntese de SMLs, tendo sido provada a cobertura das nanopartículas com uma bicamada lipídica usando medidas de FRET (Transferência de Energia de Ressonância de Förster), usando lípidos marcados com sondas fluorescentes (com os fluoróforos NBD e Rodamina). Tanto os AMLs como os SMLs, revelaram ser apropriados para aplicações biomédicas, exibindo tamanhos inferiores a 150 nm e uma estreita distribuição de tamanhos. Ambos os magnetolipossomas sólidos e aquosos baseados em ferrites de manganês apresentaram um comportamento superparamagnético à temperatura ambiente, tendo os SMLs apresentado uma elevada magnetização de saturação de 34,16 emu/g, semelhante ao valor obtido para as nanopartículas isoladas de ferrite de manganês.

A fusão membranar entre os magnetolipossomas e modelos de membranas celulares (vesículas unilamelares gigantes, GUVs) foi confirmada por ensaios de transferência de energia (FRET), mostrando o potencial destes bionanossistemas para a libertação de fármacos através de fusão membranar. Novos potenciais fármacos antitumorais, derivados de tienopiridinas, com atividade antitumoral previamente comprovada, foram incorporados nos magnetolipossomas sólidos e aquosos, com elevadas eficiências de encapsulação (> 75%). Além disso, ensaios *in vitro* em várias linhas celulares tumorais humanas, nomeadamente HeLa (carcinoma cervical), MCF-7 (adenocarcinoma da mama), T3M4 (cancro pancreático), HCT15 (adenocarcinoma do cólon) e NCI-H460 (células não-pequenas de cancro do pulmão) revelaram que os magnetolipossomas aquosos baseados em nanopartículas de ferrite de manganês são capazes de libertar os compostos encapsulados e inibir o crescimento das células tumorais. apontando para uma aplicação promissora destes sistemas na terapia oncológica, simultaneamente como agentes de hipertermia e nanoencapsulamento de fármacos antitumorais. Em suma, estes resultados apontam para uma aplicação promissora destes sistemas em terapia oncológica, atuando simultaneamente como nanotransportadores de fármacos antitumorais e como agentes para hipertermia magnética.

General Index

Acknowledgements	V
Abstract	VII
Resumo	IX
General Index	XI
Figures Index	XIII
Tables Index	XXI
Compounds list	XXV
Symbols and Abbreviations List	XXVII
Thesis Outline	XXXI

Chapter 1 – Introduction.....1

1. Goal and motivation.....	3
2. Nanotechnology as a tool for biomedicine.....	3
3. Studied molecules and organized molecular aggregates.....	5
3.1 Thienopyridine derivatives.....	5
3.2 Liposomes.....	7
3.2.1 <i>Structural Unit</i>	8
3.2.2 <i>Self-assembling</i>	9
3.2.3 <i>Synthesis and characterization</i>	10
3.2.3.1 <i>Fluorescence anisotropy measurements</i>	12
3.2.3.2 <i>Resonance energy transfer measurements</i>	12
3.2.4 <i>The ideal system for drug delivery</i>	14
3.2.4.1 <i>Steric stability</i>	15
3.2.4.2 <i>PEGylation</i>	16
3.2.4.3 <i>Specific functionalization for cancer</i>	17
3.3 Magnetic nanoparticles.....	17
3.3.1 <i>Magnetic nanoparticles for biomedical applications</i>	18
3.3.2 <i>Magnetic nanoparticles studied in this thesis</i>	19
3.3.2.1 <i>Core-shell nanoparticles</i>	19

3.3.2.1.1	<i>Nickel/silica core-shell (Ni/SiO₂) nanoparticles</i>	20
3.3.2.2	<i>Iron oxide-based nanoparticles</i>	20
3.3.2.3	<i>Transition metal ferrite nanoparticles</i>	22
3.3.3	<i>The origin of superparamagnetic behavior</i>	23
3.3.4	<i>Magnetic nanoparticles synthesis and characterization</i>	26
3.3.4.1	<i>Hysteresis loop</i>	27
3.3.4.1.1	<i>Langevin function</i>	29
3.3.4.2	<i>Zero-field cooled and field cooled curves</i>	29
3.4	<i>Magnetoliposomes for cancer therapy</i>	30
3.4.1	<i>Aqueous and solid magnetoliposomes synthesis</i>	31
3.4.1.1	<i>Structural and magnetic characterization</i>	33
3.4.2	<i>Magnetic controlled chemotherapy</i>	35
3.4.3	<i>Hyperthermia</i>	38
3.4.3.1	<i>Magnetic hyperthermia</i>	39
3.4.4	<i>Synergetic thermo/chemotherapy</i>	42
4.	<i>References</i>	45
Chapter 2 – Results and discussion as a compilation of articles		59
2.1	<i>Magnetoliposomes based on nickel/silica core/shell nanoparticles: Synthesis and characterization</i>	61
2.2	<i>Magnetic liposomes based on nickel ferrite nanoparticles for biomedical applications</i>	89
2.3	<i>Magnetoliposomes based on manganese ferrite nanoparticles as nanocarriers for antitumor drugs</i>	129
2.4	<i>Magnetic liposomes as nanocarriers for promising antitumor thieno[3,2-<i>b</i>]pyridin-7-arylamines: photophysical and biological studies</i>	161
2.5	<i>Solid and aqueous magnetoliposomes as nanocarriers for a new potential drug active against breast cancer</i>	193
Chapter 3 – Overview of results		225
3.1	<i>References</i>	232
Chapter 4 – Conclusions and future perspectives		233

FIGURES INDEX

Chapter 1

- Figure 1.1.** Illustrative figure of the different structures of nanocarriers and their approximate sizes. For comparison, the sizes of biological nanostructures are shown at the top of the figure [adapted from The British Society for Nanomedicine Copyright 2012].....4
- Figure 1.2.** Structures of the thienopyridine derivatives - compounds A, B, C and D.....5
- Figure 1.3.** Representation of a liposome (left); structure of the lipid bilayer of liposomes (right) [adapted from Bozzuto *et al.* 2015].....7
- Figure 1.4.** Representation of a phospholipid molecule and its organization in a lipid bilayer, or membrane [adapted from Alberts *et al.* 2004].....8
- Figure 1.5.** Possible colloidal phases resulting from self-aggregation of phospholipids in water, in different conditions. Different types of liposomes are shown in the center of the figure [adapted from Lasic 1998].....10
- Figure 1.6.** Energy level scheme of donor and acceptor molecules showing the coupled transitions in the case where vibrational relaxation is faster than energy transfer (very weak coupling) and illustration of the integral overlap between the emission spectrum of the donor and the absorption of the acceptor [adapted from Valeur 2001].....13
- Figure 1.7.** Nanoencapsulation systems for drug delivery applications [adapted from Namdeo *et al.* 2008].....14
- Figure 1.8.** (a) Face-centered cubic spinel structure of magnetite. (b) Magnification of one tetrahedron and one adjacent octahedron sharing an oxygen atom. Large spheres labelled by Fe^{tet} and Fe^{oct} represent iron atoms on tetrahedrally and octahedrally coordinated sublattices, respectively. Oxygen atoms are shown as small spheres. The lattice parameters a in the (001) plane and c in the direction perpendicular to it are identical under equilibrium conditions but differ for tetragonal systems. The lower symmetry in this case also leads to the distinction between axial O^{ax} and equatorial O^{eq} atoms. Arrows indicate the shift directions of the oxygen atoms from their ideal positions for an internal parameter $u > 0$ (internal vibrational energy) [adapted from Friák *et al.* 2007].....21

Figure 1.9. Magnetic domain and domain wall representation (left). Domain wall (B) with gradual reorientation of the magnetic moment between two domains (A) and (C) (right).....	23
Figure 1.10. Nanoscale transition of magnetic nanoparticles from ferromagnetism to superparamagnetism; energy diagram of magnetic nanoparticles.....	25
Figure 1.11. Typical hysteresis curve of a ferromagnetic sample.....	28
Figure 1.12. Schematic representation of aqueous magnetoliposomes (AMLs) and solid magnetoliposomes (SMLs).....	31
Figure 1.13. CLSM images of Alexa-loaded magnetic GUVs over time [adapted from Nappini <i>et al.</i> 2011]. First line: Alexa is colored in green, and magnetic nanoparticles in red (a) in the absence of AMF at time zero, (b) exposed for 15 min to 200 Hz AMF, and (c) 15 min after the field application. Magnetic GUVs again exposed to 200 Hz AMF for (d) 15 min and (e) 15 min after the last field application. Second line: CLSM pictures obtained by removing the nanoparticle fluorescent contribution from the first line pictures.....	33
Figure 1.14. Schematic comparison between conventional chemotherapy and magnetic controlled chemotherapy.....	35
Figure 1.15. Cellular changes induced by hyperthermia that lead to tumor cell death (apoptosis and/or necrosis) [adapted from Bettaieb <i>et al.</i> 2013].....	39
Figure 1.16. Comparative study of plain chemotherapy with its combination with RF induced hyperthermia [adapted from Li <i>et al.</i> 2013]. A: Tumor volume evolution in time. Tumor image and size and histopathologic evaluation - B: PBS control group. C: Combined hyperthermia and chemotherapy.....	44

Chapter 2

Chapter 2.1

Figure 1. Structures of the fluorescent labeled lipids and the dye Nile Red.....	69
---	----

Figure 2. Absorption spectra of Ni@SiO₂ nanoparticles dispersed in ethanol. The Ni cores were synthesized in aqueous CTAB solution. **A:** without silica shell; **B:** with silica

shell added to Ni NPs dispersed in AOT/cyclohexane using different [TEOS]/[Ni] ratios.....72

Figure 3. S_{11} scattering matrix element for Ni NPs, Ni@SiO₂ NPs and vesicles.....74

Figure 4. SEM images of nickel nanoparticles synthesized in CTAB aqueous solution with citric acid (1:0.75), at different amplifications. Inset: Particles size histogram of image **B** and fitting to a Gaussian distribution.....75

Figure 5. SEM images of nickel nanoparticles coated with silica shell. **A:** [TEOS]/[Ni] = 5:1 (TEOS added in AOT/cyclohexane solution); **B:** [TEOS]/[Ni] = 42:1 (TEOS added in ethanol solution with MDA).....76

Figure 6. A: Magnetization hysteresis cycle of the nickel nanoparticles at room temperature. **B:** Enlargement of the hysteresis loop of Figure 6A, in the low field region.....76

Figure 7. Fluorescence spectra ($\lambda_{exc} = 465$ nm, no Rhodamine excitation) of DMLs covered with AOT labeled with only NBD-C₆-HPC (1×10^{-2} μ M); DMLs labeled with only Rhodamine B-DHPE (1×10^{-2} μ M) and DMLs labeled with both NBD-C₆-HPC (1×10^{-2} μ M) and Rhodamine B-DHPE (1×10^{-2} μ M). Inset: Spectral overlap (spectra are normalized) between the fluorescence emission of the donor (NBD-C₆-HPC) and the absorption of the acceptor (Rhodamine B-DHPE).....78

Figure 8. SEM images of dry magnetoliposomes of nickel nanoparticles (without silica shell) covered by an AOT surfactant double layer. Inset: Particles size histogram of image **A** and fitting to a Gaussian distribution.....80

Figure 9. SEM images of dry magnetoliposomes of nickel nanoparticles covered by a DOPG lipid bilayer. Inset: Particles size histogram of image **A** and fitting to a Gaussian distribution.....80

Figure 10. Fluorescence spectra ($\lambda_{exc} = 400$ nm) of AMLs of Egg-PC and Ni/silica core/shell NPs containing both NBD-C₆-HPC (10^{-6} M) and Nile Red (2×10^{-6} M), before and after interaction with GUVs. Inset: Spectral overlap (spectra are normalized) between the fluorescence emission of the donor (NBD-C₆-HPC) and the absorption of the acceptor (Nile Red)..... 81

Figure 11. Schematic illustration of the fusion between the GUVs and magnetoliposomes labeled with both NBD-C₆-HPC and Nile Red.....82

Chapter 2.2

Figure 1 Structures of the fluorescent labeled lipids and the dye Nile Red.....98

Figure 2. UV-Visible absorption spectra of NiFe₂O₄ particles synthesized by the coprecipitation method, before and after calcination at 800°C for 2 hours.....100

Figure 3. XRD pattern of the NiFe₂O₄ NPs, before and after calcination at 800°C. (▼) β-FeNaO₂ phase; (▽) NiO phase. Inset: XRD pattern before calcination.....101

Figure 4. TEM images (**A** and **C**) of the synthesized NiFe₂O₄ NPs, calcinated at 800°C, at different amplifications. **B:** Particles size histogram of image **A** and fitting to a Gaussian distribution. **D:** Corresponding electron diffraction pattern.....103

Figure 5. EDAX elemental analysis of area corresponding to Figure **4C**.....103

Figure 6. Magnetic moment per gram of NiFe₂O₄ NPs (synthesized in the presence of citric acid, calcinated at 800°C) *versus* applied magnetic field. Inset: Hysteresis loop at room temperature.....105

Figure 7. ZFC and FC magnetization curves of NiFe₂O₄ NPs synthesized in the presence of citric acid calcinated at 800°C.....106

Figure 8. A, B. SEM images of the synthesized DMLs based on NiFe₂O₄ NPs. In image **B**, a negative staining was applied.....108

Figure 9. A. Fluorescence spectra ($\lambda_{exc} = 400$ nm) of AMLs of egg lecithin and NiFe₂O₄ NPs containing both NBD-C₁₂-HPC and Nile Red, before and after interaction with GUVs. Inset: Spectral overlap (spectra are normalized) between the fluorescence emission of the donor (NBD-C₁₂-HPC) and the absorption of the acceptor (Nile Red). **B.** Schematic representation of membrane fusion between AMLs and GUVs.....109

Figure 10. Fluorescence spectra ($\lambda_{exc} = 470$ nm, no Rhodamine excitation) of DMLs covered with DOPG labeled with only NBD-C₁₂-HPC; DMLs labeled with only Rhodamine B-DOPE and DMLs labeled with both NBD-C₁₂-HPC and Rhodamine B-DOPE.....110

Figure 11. A. Fluorescence spectra ($\lambda_{exc} = 470$ nm) of DMLs labeled with NBD-C₁₂-HPC and Rhodamine B-DOPE, before and after interaction with GUVs. **B:** Illustration of the

fusion between the GUVs and DMLs labeled with both NBD-C₁₂-HPC and Rhodamine B-DOPE.....111

Figure S1. TEM images of the synthesized NiFe₂O₄ NPs, containing NiO-rich particles (the larger ones).....119

Figure S2. EDAX elemental analysis of area corresponding to Figure S1A.....119

Chapter 2.3

Figure 1. Structure of the methyl 3-amino-6-(benzo[*d*]thiazol-2-ylamino)thieno[3,2-*b*]pyridine-2-carboxylate (1).....134

Figure 2. XRD pattern of the MnFe₂O₄ NPs. Left: Without thermal treatment. Right: Calcinated at 800°C. **A** and **B**: Synthesis time of 6 hours. **C** and **D**: Synthesis time of 2 hours and results of Rietveld analysis (MnFe₂O₄: space group Fd-3m:2 (227); CIF 1528316; Fe₂O₃: space group R-3 2/c (167); CIF 9000139).....140

Figure 3. UV-Visible absorption spectra of MnFe₂O₄ nanoparticles synthesized by the coprecipitation method. Inset: Tauc plot.....142

Figure 4. A, B: TEM images of the synthesized MnFe₂O₄ NPs at different amplifications. **C:** Particles size histogram of image **A** and fitting to a Gaussian distribution. **D:** EDAX elemental analysis of area corresponding to image **A**..... 143

Figure 5. Magnetization hysteresis loop of MnFe₂O₄ NPs measured at room temperature. Inset: Enlargement of the loop, in the low field region.....144

Figure 6. ZFC and FC magnetization curves of manganese ferrite nanoparticles.....145

Figure 7. TEM image of the solid magnetoliposomes (SMLs) containing MnFe₂O₄ NPs.....147

Figure 8. A. Fluorescence spectra ($\lambda_{exc} = 400$ nm) of AMLs of egg lecithin and MnFe₂O₄ NPs containing both NBD-C₁₂-HPC and Nile Red, before and after interaction with GUVs. Inset: Spectral overlap (spectra are normalized) between the fluorescence emission of the donor (NBD-C₁₂-HPC) and the absorption of the acceptor (Nile Red). **B.** Schematic representation of membrane fusion between AMLs and GUVs.....148

Figure 9. Fluorescence spectra ($\lambda_{exc} = 470$ nm, no rhodamine excitation) of SMLs covered with DOPG labeled with only NBD-C₆-HPC and SMLs labeled with both NBD-C₆-HPC and rhodamine B-DOPE.....149

Figure 10. A. Fluorescence spectra ($\lambda_{exc} = 560$ nm) of SMLs based on MnFe₂O₄ NPs covered with DOPG labeled with Rhodamine B-DOPE before and after interaction with GUVs. **B.** Schematic representation of the fusion between the GUVs and labeled SMLs.....150

Figure 11. Fluorescence spectra ($\lambda_{exc} = 360$ nm) of compound **1** (3×10^{-6} M) in liposomes and magnetoliposomes of Mn ferrite nanoparticles. **A.** Liposomes and AMLs of the phospholipid Egg-PC; **B.** Liposomes and SMLs of the phospholipid DOPG.....151

Figure 12. A. Fluorescence spectra ($\lambda_{exc} = 360$ nm) of AMLs of Egg-PC and MnFe₂O₄ NPs containing both NBD-PE (4×10^{-6} M) and compound **1** (4×10^{-6} M), before and after interaction with GUVs. **B.** Fluorescence spectra ($\lambda_{exc} = 360$ nm) of compound **1** (4×10^{-6} M) in SMLs of DOPG and MnFe₂O₄ NPs before and after interaction with GUVs.....152

Figure S1. Size distribution of Egg-PC aqueous magnetoliposomes (AMLs) containing MnFe₂O₄ nanoparticles.....159

Figure S2. Size distribution of DOPG solid magnetoliposomes (SMLs) containing MnFe₂O₄ nanoparticles.....159

Chapter 2.4

Figure 1. Structure of compound **1**, *N*-(3-methoxyphenyl)-thieno[3,2-*b*]pyridin-7-amine), and compound **2**, *N*-(2-methoxy-phenyl)thieno[3,2-*b*]pyridin-7-amine).....166

Figure 2. Structure of the labeled lipids NBD-C₆-HPC and Rhodamine B-DOPE.....169

Figure 3. A: Absorption spectra of 2×10^{-5} M solutions of compound **1** in dichloromethane and ethanol, as examples. **B:** Normalized fluorescence spectra ($\lambda_{exc} = 310$ nm) of 3×10^{-6} M solutions of compound **1** in several solvents.....172

Figure 4. A: Absorption spectra of 2×10^{-5} M solutions of compound **2** in dichloromethane and ethanol, as examples. **B:** Normalized fluorescence spectra ($\lambda_{exc} = 310$ nm) of 3×10^{-6} M solutions of compound **2** in several solvents.....172

Figure 5. Fluorescence spectra ($\lambda_{exc} = 470$ nm, no rhodamine excitation) of SMLs with DPPC bilayer labeled with only NBD-C₆-HPC and SMLs labeled with both NBD-C₆-HPC and rhodamine B-DOPE.....174

Figure 6. Magnetization hysteresis cycles, measured at 316 K, of neat MnFe₂O₄ nanoparticles, DPPC SMLs and Egg-PC AMLs containing MnFe₂O₄ NPs.....176

Figure 7. Normalized fluorescence spectra of compounds **1** and **2** (3×10^{-6} M) in liposomes and magnetoliposomes (Egg-PC AMLs and DPPC SMLs), at room temperature ($\lambda_{exc} = 310$ nm). **A:** Compound **1**; **B:** Compound **2**.....177

Figure S1. Size distribution (by intensity) obtained from DLS for solid magnetoliposomes of DPPC containing manganese ferrite nanoparticles, at 25°C.....190

Figure S2. SEM image (with application of a negative staining) for solid magnetoliposomes of the lipid DPPC containing manganese ferrite nanoparticles, showing an aggregate of two magnetoliposomes.....190

Chapter 2.5

Figure 1. Structure of the diarylurea derivative of thienopyridine.....198

Figure 2. SEM image of magnetite nanoparticles prepared by coprecipitation method in aqueous solution. Inset: Particles size histogram and fitting to a Gaussian distribution.....205

Figure 3. SEM images of magnetite nanoparticles prepared by reverse coprecipitation method in aqueous solution. **A:** Addition of all Fe²⁺ at once; **B:** Addition of Fe²⁺ in five portions, with 10 minutes intervals. Insets: Particles size histograms and fitting to Gaussian distributions.....205

Figure 4. Rietveld analysis of XRD patterns of the sample, with (A) and without (B) preferred orientation correction at (1 1 0) plane.....206

Figure 5. A: Magnetization hysteresis cycle of magnetite nanoparticles at T = 300 K. **B:** Enlargement of the hysteresis loop of Figure **5A**, in the low field region.....207

Figure 6. SEM image of solid magnetoliposomes of the lipid DPPC containing magnetite nanoparticles.....211

Figure 7. Fluorescence spectra ($\lambda_{\text{exc}} = 290 \text{ nm}$) of compound 1 ($3 \times 10^{-6} \text{ M}$) in liposomes and magnetoliposomes (AMLs and SMLs) of DPPC containing magnetite nanoparticles, and in SMLs after interaction with GUVs.....212

Figure S1. Structures of the fluorescent labeled lipids and the dye Nile Red.....222

Figure S2. ZFC and FC magnetization curves of Fe_3O_4 nanoparticles.....223

Figure S3. Size distribution obtained by DLS for aqueous magnetoliposomes of Egg phosphatidylcholine containing magnetite NPs (at 25°C).....223

Figure S4. Fluorescence spectra ($\lambda_{\text{exc}} = 410 \text{ nm}$) of AMLs containing magnetite NPs, labelled with both NBD- C_6 -HPC ($2 \times 10^{-6} \text{ M}$) and Nile Red ($2 \times 10^{-6} \text{ M}$), before and after interaction with GUVs. **A:** AMLs of Egg-PC; **B:** AMLs of DPPC.....224

Figure S5. Size distribution obtained by DLS for solid magnetoliposomes of DOPG containing magnetite NPs (at 25°C).....224

Figure S6. Size distribution obtained by DLS for solid magnetoliposomes of DPPC containing magnetite NPs (at 25°C).....224

Chapter 3

Figure 3.1. Blocking temperature distributions obtained from derivative $d(\text{ZFC-FC})/dT$228

Figure 3.2. Images of an aqueous solution of SMLs based on MnFe_2O_4 NPs under a magnetic field gradient.....231

TABLES INDEX

Chapter 1

Table 1.1. Cell inhibition activity of the thienopyridine derivatives on several human tumor cell lines and in non-tumor porcine liver primary cells (PLP2). Results for ellipticine are also shown for comparison.....6

Table 1.2. Structure and physicochemical characteristics of the phospholipids used for magnetoliposomes synthesis.....9

Chapter 2

Chapter 2.1

Table 1. Hydrodynamic diameter (obtained by DLS) of Ni nanoparticles with and without silica shell, prepared by several synthesis methods.....73

Table 2. Hydrodynamic diameter (obtained by DLS) of aqueous magnetoliposomes incorporating Ni NPs with and without silica shell.....79

Chapter 2.2

Table 1. Selected Rietveld analysis parameters.....102

Table 2. EDAX atomic percentages considering only Ni, Fe and O contributions and comparison with the values predicted for NiFe₂O₄ NPs.....104

Table 3. Magnetization saturation (M_s), mass (m) and size (d) of the synthesized NPs.....107

Table S1. EDAX atomic percentages considering only Ni, Fe and O contributions and comparison with the values predicted for NiO NPs.....119

Chapter 2.3

Table 1. Selected Rietveld analysis parameters.....141

Table 2. Atomic percentages of individual elements in MnFe₂O₄ nanoparticles.....142

Table 3. Magnetization saturation (M_s), mass (m) and size (d) of the synthesized manganese ferrite nanoparticles.....146

Table 4. Steady-state fluorescence anisotropy (r) values for antitumor compound 1 in liposomes (without NPs), aqueous magnetoliposomes (AMLs) and solid magnetoliposomes (SMLs).....152

Chapter 2.4

Table 1. Maximum absorption (λ_{abs}) and emission (λ_{em}) wavelengths, molar absorption coefficients (ϵ) and fluorescence quantum yields (Φ_F) for the thieno[3,2-*b*]pyridine derivatives 1 and 2 in several solvents.....173

Table 2. Coercive field (H_c), saturation magnetization (M_s), remnant magnetization (M_r) and ratio M_r/M_s for manganese ferrite NPs and magnetoliposomes.....176

Table 3. Steady-state fluorescence anisotropy (r) values and maximum emission wavelengths (λ_{em}) for diarylamines 1 and 2 in several liposome and magnetoliposome formulations, at 25°C and 55°C.....178

Table 4. Encapsulation efficiencies ($EE\%$) of compounds 1 and 2 in magnetoliposomes.....179

Table 5. Growth inhibitory activity of drug-loaded aqueous magnetoliposomes on various human tumor cell lines and non-tumor porcine liver primary cells (PLP2).....180

Table S1. Growth inhibitory activity of drug-loaded solid magnetoliposomes on various human tumor cell lines and non-tumor porcine liver primary cells (PLP2).....191

Chapter 2.5

Table 1. Steady-state fluorescence anisotropy (r) values for antitumor compound 1 in liposomes, aqueous magnetoliposomes (AMLs) and solid magnetoliposomes (SMLs).....213

Table S1. Selected Rietveld analysis parameters.....222

Chapter 3

Table 3.1. Crystalline structure and size of the prepared nanoparticles, obtained by DLS, XRD, SEM, TEM and Langevin fit to $M(H)$227

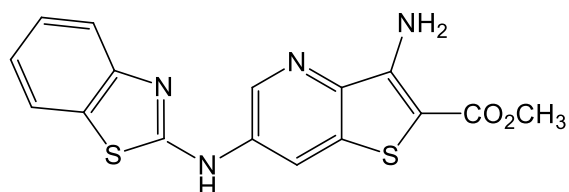
Table 3.2. Blocking temperature (T_B), saturation magnetization (M_s), remnant magnetization (M_r), magnetic squareness value (M_r/M_s) and coercive field (H_c) of the synthesized NPs, at room temperature.....228

Table 3.3. Hydrodynamic diameter of magnetoliposomes obtained by DLS and diameters of synthesized magnetoliposomes obtain by SEM and TEM. Liposomes (without magnetic nanoparticles) sizes are also shown for comparison.....230

Table 3.4. Saturation magnetization (M_s), remnant magnetization (M_r), magnetic squareness value (M_r/M_s) and coercive field (H_c) of aqueous and solid magnetoliposomes based on $MnFe_2O_4$, at room temperature.....230

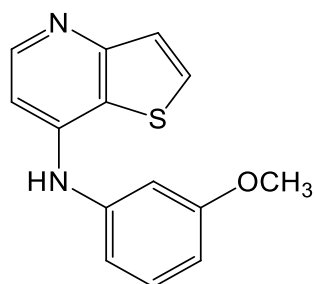
COMPOUNDS LIST

Chapter 2.3 “Magnetoliposomes based on manganese ferrite nanoparticles as nanocarriers for antitumor drugs”, *RSC Advances* **6** (2016) 17302-17313.

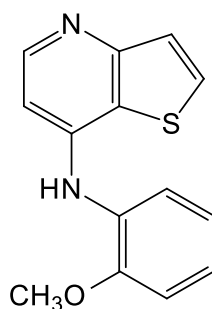


Compound **A** (correspondent to compound **1** in article **2.3**)
(methyl 3-amino-6-(benzo[*d*]thiazol-2-ylamino)thieno[3,2-*b*]pyridine-2-carboxylate)

Chapter 2.4 “Magnetic liposomes as nanocarriers for promising antitumor thieno[3,2-*b*]pyridin-7-arylamines: photophysical and biological studies”, *RSC Advances* **7** (2017) 15352-15361.

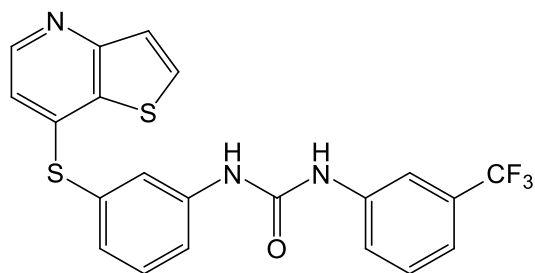


Compound **B** (correspondent to compound **1** in article **2.4**)
(N-(3-methoxyphenyl)- thieno[3,2-*b*]pyridin-7-amine)



Compound **C** (correspondent to compound **2** in article **2.4**)
(N-(2-methoxy-phenyl)thieno[3,2-*b*]pyridin-7-amine)

Chapter 2.5 “Solid and aqueous magnetoliposomes as nanocarriers for a new potential drug active against breast cancer”, *Colloids and Surfaces B: Biointerfaces*, **158** (2017) 460-468.



Compound **D** (correspondent to compound **1** in article **2.5**)
1-[3-(Trifluoromethyl)phenyl]-3-[3-(thieno[3,2-b]pyridin-7-ylthio)phenyl]urea

SYMBOLS AND ABBREVIATION LIST

- A375-C5** – melanoma cell line
- AC** – Alternating Current
- AFM** – Atomic Force Microscopy
- AMLs** – Aqueous Magnetoliposomes
- AOT** – bis(2-ethylhexyl)sulfosuccinate sodium salt
- BBB** – Blood Brain Barrier
- Ch** – cholesterol
- CHEMS** – cholesteryl hemisuccinate
- CLSM** – Confocal Laser Scanning Microscopy
- CQ/UM** – Center of Chemistry of the University of Minho
- Cryo-TEM** – Cryogenic Transmission Electron Microscopy
- CTAB** – cetyltrimethylammonium bromide
- DC** – Direct Current
- DLS** – Dynamic Light Scattering
- DMLs** – Dry Magnetoliposomes (stands for the same type of structure as SMLs)
- DNA** – deoxyribonucleic acid
- DOPG** – 1,2-Dioleoyl-*sn*-glycero-3-phospho-*rac*-(1-glycerol) (sodium salt)
- DPPC** – 1,2-Dipalmitoyl-*sn*-glycero-3-phosphocholine
- EE** – Encapsulation Efficiency
- Egg-PC** – egg yolk phosphatidylcholine
- EPR** – Enhanced Permeability and Retention
- FDA** – Food and Drug Administration
- FFF** – Field-Flow Fractionation
- FRET** – Förster Resonance Energy Transfer
- FC** – Field Cooled
- GI₅₀** – growth inhibition concentration of 50% of cells
- GRAS** – Generally Regarded as Safe
- GUVs** – Giant Unilamellar Vesicles
- HCT15** – colon adenocarcinoma cell line
- HeLa** – cervical carcinoma cell line
- HepG2** – hepatocellular carcinoma cell line

λ – wavelength
 λ_{abs} – absorption wavelength
 λ_{exc} – excitation wavelength
 λ_{em} – emission wavelength
LUVs – Large Unilamellar Vesicles
M²⁺ – metal ion double-charged
MCF-7 – breast adenocarcinoma cell line
MDA – mercaptododecanoic acid
MDA-MB-231 – breast adenocarcinoma cell line (metastatic)
MDR1 – multidrug resistance protein
MGLs – Magnetoliposomes
MLVs – Multilamellar Vesicles
MNPs – Magnetic Nanoparticles
MPS – Mononuclear Phagocyte System
M_r – remnant magnetization
MRI – Magnetic Resonance Imaging
M_s – saturation magnetization
MW – Molecular Weight
NBD-C₆-HPC – 2-(6-(7-nitrobenz-2-oxa-1,3-diazol-4-yl)amino)hexanoyl-1-hexadecanoyl-*sn*-glycero-3-phosphocholine
NBD-C₁₂-HPC – 2-(12-(7-nitrobenz-2-oxa-1,3-diazol-4-yl)amino)dodecanoyl-1-hexadecanoyl-*sn*-glycero-3-phosphocholine
NBD-PE – N-(7-nitrobenz-2-oxa-1,3-diazol-4-yl)-1,2-dihexadecanoyl-*sn*-glycero-3-phosphoethanolamine (triethylammonium salt)
NCI-H460 – non-small cell lung carcinoma cell line
NPs – nanoparticles
PBS – phosphate-buffered saline
PC – phosphatidylcholine
PEG – polyethylene glycol
PET – Positron Emission Tomography
PLP2 – non-tumor porcine liver primary cells
RES – Reticuloendothelial System
RF – Radio Frequency
Rh – rhodamine

Rhodamine B-DOPE – N-(lissamine Rhodamine B sulfonyl)-1,2-dioleoyl-*sn*-3-phosphatidylethanolamine (ammonium salt)

Rhodamine B-DHPE – N-(lissamine Rhodamine B sulfonyl)-1,2-dipalmitoyl-*sn*-3-phosphoethanolamine (ammonium salt)

ROS – Reactive Oxygen Species

SAR – Specific Absorption Rate

SANs – Small Angle Neutron Scattering

SAXs – Small Angle X-ray Scattering

SEM – Scanning Electron Microscopy

SMLs – Solid Magnetoliposomes (stands for the same type of structure as DMLs)

SQUID – Superconducting Quantum Interference Device

SUVs – Small Unilamellar Vesicles

T_B – Blocking Temperature

T3M4 – pancreatic cancer cell line

TEM – Transmission Electron Microscopy

TEOS – tetraethyl orthosilicate

UV – Ultraviolet

ULVs – Unilamellar Vesicles

VSM – Vibrating Sample Magnetometer

XRD – X-Ray Diffraction

ZFC – Zero-Field Cooled

THESIS OUTLINE

The present dissertation is separated into four chapters. A brief description of each chapter is described below.

Chapter 1 contains a comprehensive introduction, with the basic theoretical principles of magnetoliposomes and their components (magnetic nanoparticles and liposomes). An overall literature review is contemplated, in the context of the state of art, both on the synthesis and applications of magnetic nanoparticles based bionanosystems. This chapter intends to improve the comprehension of this thesis, making clear the wide context of the research, and serving as a complement to the articles introduction, in Chapter 2.

Chapter 2 comprises a compilation of the published articles, in international scientific journals with ISI index, within the scope of this doctoral thesis. Each article is here presented as a sub-chapter and the format has been uniformized, so it does not correspond to the journal formatting. Yet, references format has been maintained according with the publishing journal. The alignment of this second chapter is as follows:

2.1 “Magnetoliposomes based on nickel/silica core/shell nanoparticles: Synthesis and characterization”, *Materials Chemistry and Physics*, **148** (2014) 978-987.

2.2 “Magnetic liposomes based on nickel ferrite nanoparticles for biomedical applications”, *Physical Chemistry Chemical Physics*, **17** (2015) 18011-18021.

2.3 “Magnetoliposomes based on manganese ferrite nanoparticles as nanocarriers for antitumor drugs”, *RSC Advances*, **6** (2016) 17302-17313.

2.4 “Magnetic liposomes as nanocarriers for promising antitumor thieno[3,2-*b*]pyridin-7-arylamines: photophysical and biological studies”, *RSC Advances*, **7** (2017) 15352-15361.

2.5 “Solid and aqueous magnetoliposomes as nanocarriers for a new potential drug active against breast cancer”, *Colloids and Surfaces B: Biointerfaces*, **158** (2017) 460-468.

Chapter 3 contains a general overview of the results by comparison of the experimental results reported in the articles on chapter 2. Unpublished results of some additional experiments, also carried out in the context of this thesis, are included in the discussion of this chapter, for comparison.

Chapter 4 reports the conclusions of all the experimental work developed within this thesis, as well as the perspectives for future work.

Chapter 1

Introduction

1. Goal and motivation

Since Hippocrates, the physicist known as the father of Modern Medicine, the practice of medicine has been revolutionized by major scientific advances and new approaches. Nowadays, one of the main tendencies in modern medicine research is the development of intelligent nanosystems, the so-called “smart pills”, to improve both treatment and diagnosis, not only in cancer but also in other diseases. In terms of economic interests, this trend represents a big slice of the scientific investment. According to Markets and Markets, by 2020, the global investment is expected to reach 3830 million U.S. dollars, with annual growth rate of 16.16% (2014 - 2020).¹

Concerning cancer statistics, the International Agency for Research on Cancer predicts that, in 2030, the global burden is expected to reach 21.7 million new cases, and 13 million deaths.² Furthermore, these numbers can even be larger, due to the adoption of unhealthy lifestyles, such as poor diet, smoking habits, physical inactivity, and others. So, knowing that cancer is currently the second leading cause of death globally and considering cancer statistics, the motivation behind this work is to make a scientific contribution to achieve more efficient therapies and to reduce cancer mortality. Thus, the goal is to develop a promising bionanosystems, the magnetoliposomes, to improve the treatment of cancer. Magnetoliposomes are highly differentiated from conventional solutions in chemotherapy. This novel bionanosystem can be magnetically guided to therapeutic sites in human body, avoiding cytotoxicity and systemic side effects. It can be applied in the treatment of cancer by dual therapy, combining synergistic magnetic hyperthermia and targeted drug delivery capabilities in a single system, improving treatment from the start. So, this scientific contribution is focused on the development of these amazing nanosystems, thus aiming to replace the current traditional high spectrum chemotherapy approaches which lead to severe problems to patients.

2. Nanotechnology as a tool for biomedicine

Nowadays, nanomedicine is used in the whole world to improve patients' lives suffering from a range of disorders, including cancer. In the field of nanomedicine, nanotechnology has produced significant advances, namely in diagnosis, therapy, and bioengineering.³ The integration of advanced nanotechnological tools, both in diagnosis and therapy, has shown high potential to revolutionize healthcare.

The main obstacles in the fight against cancer are due to difficulties in early diagnosis, cytotoxicity associated with antitumor drugs used in conventional chemotherapy, and the lack of more efficient therapies. Due to their toxicity, most of the active molecules cause severe systemic side effects.^{4,5} As result, the dosage of active molecules used in conventional chemotherapy is often selected by how much a patient can physically withstand, rather than by how much is needed to treatment. Typically, in this type of therapy, less than 0.1% of the drugs are taken up by tumor cells and the remaining 99.9% attack healthy tissues, making the efficiency of the treatment being compromised from the start.⁶⁻⁸

The application of nanomaterials in the treatment of cancer has already shown to improve drugs behavior. In fact, the first success in nanomedicine research was the approval of liposomal doxorubicin for clinical use.⁹ Since then, an entire research field was launched and different nanoencapsulation systems have been investigated (figure 1.1). Liposomes,¹⁰ polymers¹¹ and hydrogels¹² are some examples of these nanocarriers that aim to overcome the difficulties of drugs biodistribution.

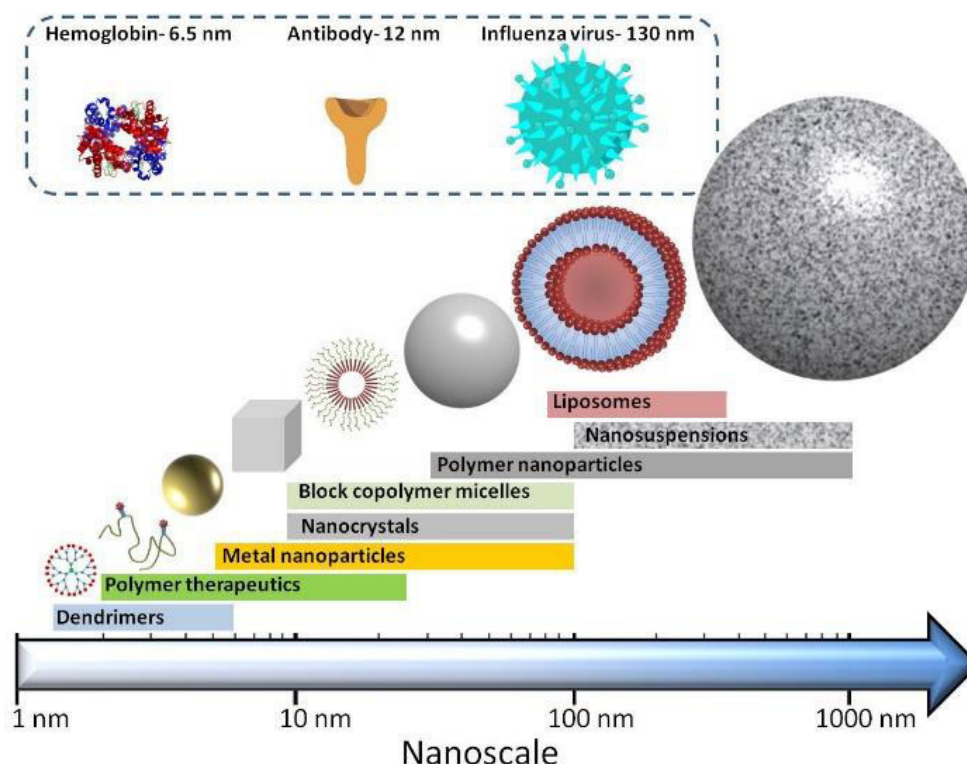
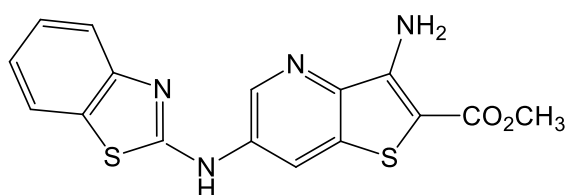


Figure 1.1. Illustrative figure of the different structures of nanocarriers and their approximate sizes. For comparison, the sizes of biological nanostructures are shown at the top of the figure [adapted from The British Society for Nanomedicine Copyright 2012].¹³

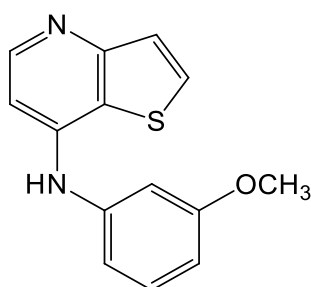
3. Studied molecules and organized molecular aggregates

3.1 Thienopyridine derivatives

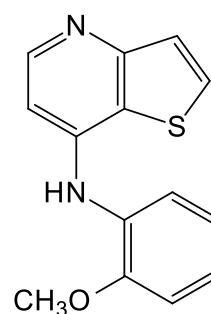
New promising compounds are systematically emerging in the pharmacological industry for the treatment of different diseases. These biologically active molecules promise new treatments for patients and advances in healthcare. The promising antitumor compounds used in this work were all synthesized at the Centre of Chemistry of University of Minho (CQ-UM). In the framework of this PhD thesis, four new thienopyridine derivatives were studied (figure 1.2).



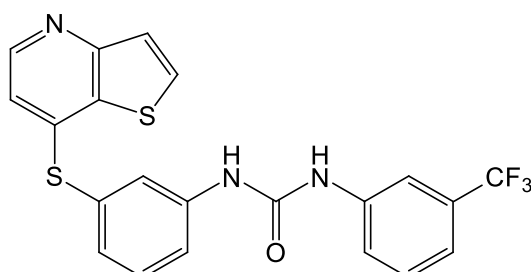
Compound A (compound **1** in article 2.3)
(methyl 3-amino-6-(benzo[*d*]thiazol-2-ylamino)thieno[3,2-*b*]pyridine-2-carboxylate)



Compound B (compound **1** in article 2.4)
(*N*-(3-methoxyphenyl)-thieno[3,2-*b*]pyridin-7-amine)



Compound C (compound **2** in article 2.4)
(*N*-(2-methoxyphenyl)thieno[3,2-*b*]pyridin-7-amine)



Compound D (compound **1** in article 2.5)
1-[3-(Trifluoromethyl)phenyl]-3-[3-(thieno[3,2-*b*]pyridin-7-ylthio)phenyl]urea

Figure 1.2. Structures of the thienopyridine derivatives - compounds **A**, **B**, **C** and **D**.

Thienopyridine derivatives are of great interest in organic chemistry because of their wide range of biological activities. The thienopyridine skeleton has been reported as possessing promising biological activities, namely antitumor, antiangiogenic, or even both activities.¹⁴ Dual antitumor and antiangiogenic activity is of large importance to the development of novel cancer therapeutic strategies.¹⁵

The thienopyridine derivatives used in this study are biologically active molecules that can potentially be used as anticancer agents. When tested *in vitro*, compounds **A**, **B** and **C** exhibited very low growth inhibitory concentrations (GI_{50}) in several human tumor cell lines,^{14,16} and compound **D** revealed to be especially active against breast cancer cells¹⁵ (table 1.1).

Table 1.1. Cell inhibition activity of the thienopyridine derivatives on several human tumor cell lines and in non-tumor porcine liver primary cells (PLP2). Results for ellipticine are also shown for comparison.

Human cell lines ^a	GI_{50} values ^b (μ M)				
	Compound A ¹⁶	Compound B ¹⁴	Compound C ¹⁴	Compound D ¹⁵	Ellipticine ¹⁴
PLP2	---	1.94 \pm 0.16	6.56 \pm 0.2	---	2.06 \pm 0.03
HepG2	---	5.02 \pm 0.06	18.00 \pm 1.29	---	5.38 \pm 1.11
HeLa	---	0.09 \pm 0.00	1.40 \pm 0.06	---	3.28 \pm 0.67
MCF-7	6.0 \pm 0.1	0.25 \pm 0.03	5.88 \pm 0.86	1.2	4.32 \pm 1.03
MDA-MB-231	---	---	---	5.0	---
HCT15	---	0.28 \pm 0.03	5.40 \pm 0.89	---	1.91 \pm 0.06
A375-C5	3.5 \pm 0.00	---	---	---	---
NCI-H460	6.4 \pm 0.5	0.31 \pm 0.04	5.91 \pm 0.21	---	5.77 \pm 0.95

^aHuman tumor cell lines: HepG2 (hepatocellular carcinoma), HeLa (cervical carcinoma), hormone-dependent MCF-7 and hormone independent MDA-MB-231 (breast adenocarcinoma), HCT15 (colon carcinoma), A375-C5 (melanoma), and NCI-H460 (non-small cell lung cancer).

^b GI_{50} values correspond to the compound concentration which inhibited 50% of cell growth.

Moreover, compound **A** has shown a very low affinity for the multidrug resistance protein (MDR1), a protein that promotes drug resistance in cells.¹⁷ Compound **B** revealed to be more active than the well-known anticancer agent ellipticine against some of the human cell lines studied, namely MCF-7 (breast adenocarcinoma), NCI-H460 (non-small cell lung cancer), HepG2 (hepatocellular carcinoma), HCT15 (colon adenocarcinoma), and HeLa (cervical carcinoma), while compound **C** showed the same behavior just against

HeLa cell line.¹⁴ Concerning compound **D**, this active molecule exhibits a strong antitumor activity against MCF-7 and MDA-MB-231 (two breast adenocarcinoma cell lines), the latter being the most aggressive, with high metastatic activity, and difficult to treat.¹⁵

3.2 Liposomes

Liposomes are nanosized vesicles of spherical shape made of natural nontoxic molecules, biologically inert and weakly immunogenic. First discovered by Alec Douglas Bangham in the sixties at the Babraham Institute, University of Cambridge, their structure consists of single or multiple concentric lipid bilayers encapsulating an aqueous compartment (figure 1.3).

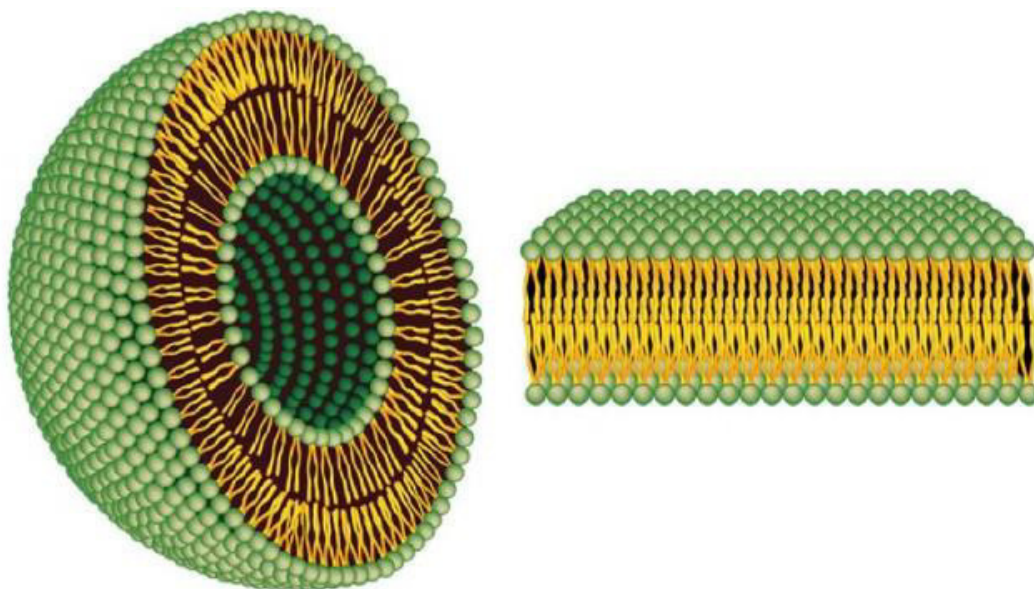


Figure 1.3. Representation of a liposome (left) and structure of the lipid bilayer of liposomes (right) [adapted from Bozzuto *et al.* 2015].¹⁸

Liposomes morphology is similar to that of cellular membranes. Because of all the advantageous properties, liposomes have been widely used to decrease drug toxicity and target specific cancer cells.¹⁹ Liposomes have been described as ideal drug delivery systems that can overcome many of the problems associated with other nanosystems, such as those involving solubility, pharmacokinetics, *in vivo* stability and toxicity.^{20,21} Also, due to their amphipathic composition, incorporated substances can be either hydrophilic or hydrophobic, the first ones being incorporated in the aqueous cavity and the second inserted or adsorbed on the membrane.²²⁻²⁴

3.2.1 Structural unit

Liposomes are molecular aggregates mostly formed by phospholipids, the structural unit that is the main constituent of biological membranes. The phospholipids are amphipathic molecules with a polar and hydrophilic head, consisting of a phosphate group and a base (choline, ethanolamine, glycerol, etc.), and a non-polar and hydrophobic tail consisting of fatty acid chains (figure 1.4). The variation in head groups and hydrophobic chains leads to the existence of a wide variety of phospholipids. As for electric charge, phospholipids can be divided into ionic (cationic or anionic), nonionic (neutral) or zwitterionic (neutral, with opposite charges on different atoms).

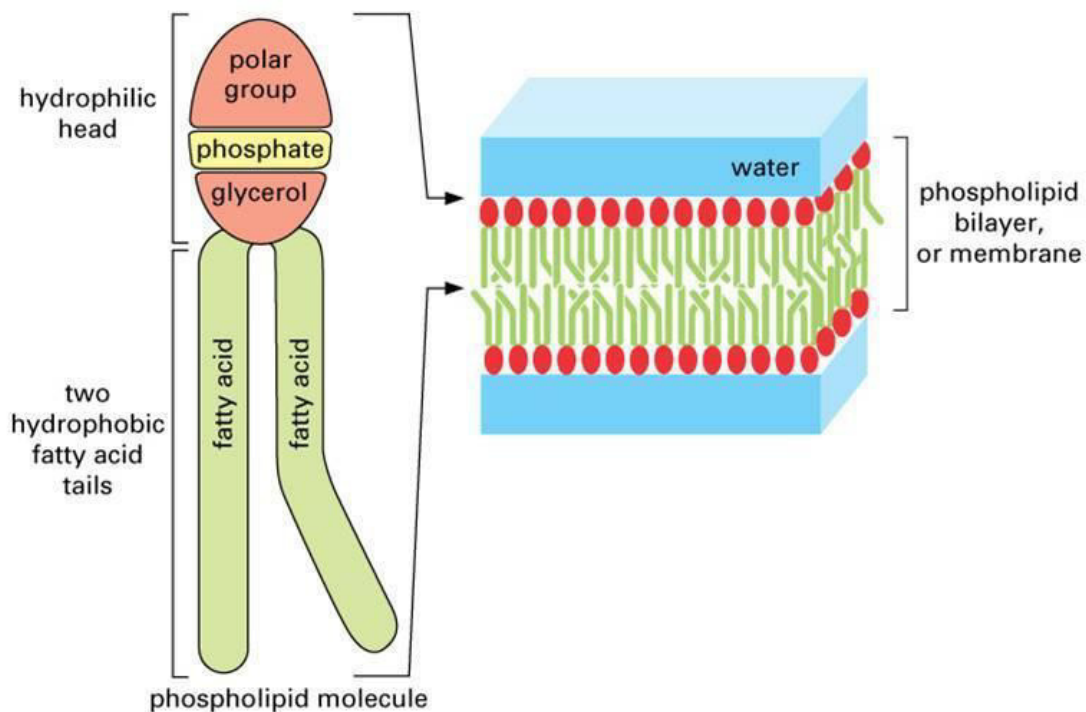
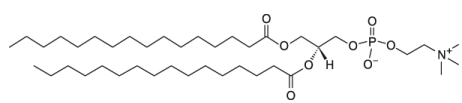
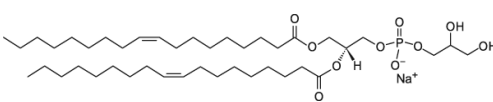
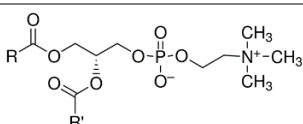


Figure 1.4. Representation of a phospholipid molecule and its organization in a lipid bilayer, or membrane [adapted from Alberts *et al.* 2004].²⁵

Phospholipids rigidity is regulated by a transition temperature, that is the temperature from which a lipid membrane goes from a gel phase to a liquid crystalline phase. In the gel phase, the hydrocarbon phase of the lipids is ordered and so the membrane is rigid. On the other hand, in the liquid crystalline phase, the tails are left with freer movements and the hydrophilic heads become fully hydrated, the membrane becoming more fluid. Transition temperature depends on phospholipid structure, increasing with tail length and decreasing with unsaturation degree.²⁶ So, phospholipids

have different physical and chemical properties and their aggregates size, charge, structure and rigidity or fluidity can be manipulated depending on the chosen structural unit. For example, unsaturated phosphatidylcholine species from natural sources, such as egg or soybean phosphatidylcholine, form more permeable bilayer vesicles. Otherwise, saturated phospholipids with long acyl chains, such as dipalmitoyl-phosphatidylcholine, form the same bilayer structures, but more rigid and rather impermeable when in the gel phase.²⁷⁻²⁹ In this work, three different types of phospholipids were used for magnetoliposomes synthesis. The structures and the physicochemical characteristics of each one are shown in the table below (table 1.2).^{30,31} Also, the double-chain surfactant AOT (bis(2-ethylhexyl)sulfosuccinate) sodium salt, was used for size confinement in the synthesis of nickel nanoparticles, as well as for the preparation of solid magnetoliposomes.

Table 1.2. Structure and physicochemical characteristics of the phospholipids used for magnetoliposomes synthesis.

	Structure	Electric charge	Transition temperature
DPPC	 1,2-dipalmitoyl- <i>sn</i> -glycero-3-phosphocholine	Zwitterionic	41° C ³²
DOPG	 1,2-dioleoyl- <i>sn</i> -glycero-3-phospho-(1'- <i>rac</i> -glycerol)	Anionic	-18° C ³²
Egg-PC	 R, R' = fatty acid residues L- α -phosphatidylcholine (from egg yolk)	Zwitterionic	very low

3.2.2 Self-assembling

Phospholipids spontaneously form closed structures, such as liposomes, when hydrated in aqueous solutions. This self-assembling process occurs because, in aqueous media, the phospholipids are obliged to organize due to hydrophilic/hydrophobic interactions, electrostatic interactions, and van der Waals interactions. In this process, the

disordered system forms organized structures to avoid contact between non-polar parts and water molecules, energetically unfavorable, while keeping water molecules in contact with the polar part of the phospholipids.³³ The way phospholipid molecules self-organize in aqueous media depends on the conditions in the lipid–water mixture (concentration and ionic strength) and polar to non-polar area ratio of the phospholipids.^{34, 35} This way, molecular aggregates with specific structures can be prepared (figure 1.5). For instance, molecules with a large polar area form micelles, while molecules with smaller polar area form inverted micelles. Liposomes are obtained from phospholipids with similar polar and non-polar area.³⁵ Regarding the size and number of layers, liposomes can be classified as multilamellar vesicles (MLVs, size > 100 nm), large unilamellar vesicles (LUVs, > 100 nm) or small unilamellar vesicles (SUVs, < 100 nm) (figure 1.5).

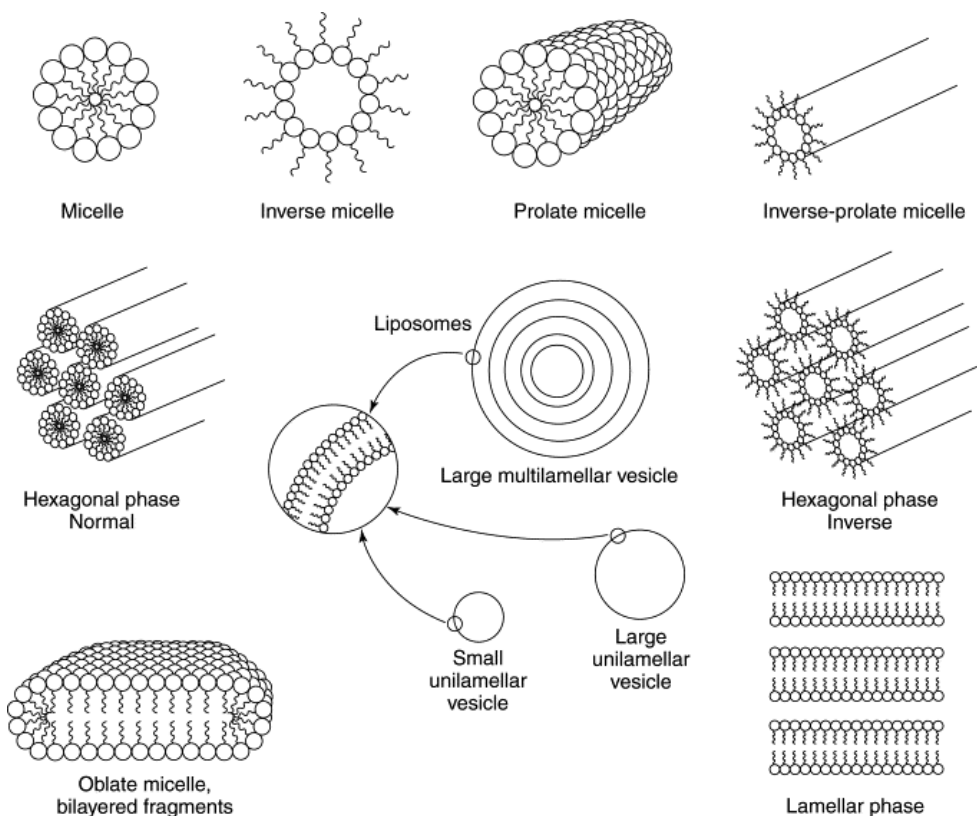


Figure 1.5. Possible colloidal phases resulting from self-aggregation of phospholipids in water, in different conditions. Different types of liposomes are shown in the center of the figure [adapted from Lasic 1998].³⁵

3.2.3 Synthesis and characterization

As it was stated, liposome properties vary considerably with lipid composition, surface charge and size. Nevertheless, also important is the preparation method that plays

an important role on the liposome final properties. For example, the formation of unilamellar vesicles or multilamellar vesicles (MLVs) depends on the synthesis method.¹⁸

The range of liposomes preparation techniques has increased over the past decade. Some examples of the most conventional techniques are thin-film hydration or the Bangham method, reversed phase evaporation and several modified ethanol-injection techniques that are really attractive.^{18,36} Another promising technique is the microfluidic-based method that allows strict control of the lipid-hydration process.³⁷ Nowadays, new techniques have been developed for the improvement of liposomes size, polydispersity and drug encapsulation efficiency, such as supercritical fluid technology, dual asymmetric centrifugation, membrane contactor technology, cross-flow filtration technology and freeze-drying technology.³⁶ Additionally to the synthesis method, some procedures can help reducing liposomes size, such as sonication,³⁸ high pressure extrusion³⁹ and microfluidization⁴⁰.

In this work, the chosen technique to prepare liposomes was the conventional method of ethanolic injection. The advantages of this method are its potential for scale up, the simplicity of the procedure, low cost and low expenditure of time. It consists in the injection of a lipid solution in ethanol, under vigorous vortexing, to an aqueous solution, above the melting transition temperature of the lipids. Liposomes with a reasonably homogeneous population, although rather dilute, with small sizes in the range of 30-110 nm¹⁹ are generally obtained.

Liposomes behavior in biological environment is directly related with their shape, size, surface features and lamellarity. Thus, the characterization of liposomes in that context is of extreme importance to ensure their good *in vitro* and *in vivo* performance.¹⁸ For the determination of size and polydispersity, there are several options available and the techniques most frequently used are dynamic light scattering (DLS),⁴¹ size-exclusion chromatography⁴² and field-flow fractionation (FFF)⁴³. DLS is a simple and rapid technique that measures the intensity fluctuation of the scattered light in time, that occur because of the Brownian motion of liposomes. Thus, the analysis of these intensity fluctuations allows determination of the distribution of diffusion coefficients of the liposomes, which are converted into size distribution.

Also, electron microscopy techniques, such as cryo-TEM and TEM, using freeze-fracturing, has been employed for the characterization of liposomes.^{18,44,45} Moreover, atomic force microscopy (AFM) can measure the three-dimensional profile of the

liposomes.⁴⁶ Unfortunately, despite microscopy provides a precise determination of liposome size, it is a very expensive technique and requires specific equipment.

3.2.3.1 Fluorescence anisotropy measurements

Fluorescence anisotropy is a very sensitive and reproducible technique that provides a spectroscopic parameter that can be interpreted in terms of liposomes local fluidity. When the fluorophores are located in the liposomes, this type of measurements offers the possibility of detecting alterations in membrane physical properties at different depths of the lipid bilayer and can be used to detect whether the encapsulated drugs are preferentially located inside the lipid bilayer or in the aqueous phase of the liposomes.

Steady-state anisotropy (r) measures the rotational diffusion of a molecule from the difference in the correlation of polarization in fluorescence, that is, between the excited and emitted photons. The way that fluorescent molecules behave in the absorption and emission of polarized light depends on the excited state lifetime (τ), rotational correlation time (τ_c) and intrinsic anisotropy (r_0) (equation 1.1).

$$\frac{1}{r} = \frac{1}{r_0} \left(1 + \frac{\tau}{\tau_c}\right) \quad (1.1)$$

Unlike the excited state lifetime, which is characteristic of the fluorophore (however dependent on solvent polarity or quenching processes, for instance), the rotational correlation time depends on the microenvironment viscosity. Thus, when the rotational correlation time is slower than the excited state lifetime, the light emitted by a fluorophore excited with polarized light, is also polarized. This occurs when the fluorescent molecules are in rigid and high viscosity microenvironments, for example conjugated to large biomolecules, in low temperature organic solvents, or in lipid membranes (or polymers) at room temperature. On the other hand, when the rotational correlation time is faster than the excited state lifetime, the molecule rotates before emitting the photon and, in this case, the emitted light is depolarized. This happens when the fluorescent molecules are in solvents with low viscosity, such as water.⁴⁷

3.2.3.2 Resonance energy transfer measurements

FRET (Förster Resonance Energy Transfer) is a fluorescence technique that allows the study of molecular interactions. In the context of this work, this was an important assay, because it allowed the investigation of nonspecific interactions between

magnetoliposomes and models of cell membranes, keeping in mind future drug delivery applications. Moreover, FRET also permitted to confirm the synthesis of solid magnetoliposomes by a new route that was developed in the framework of this thesis.

This technique depends on the non-radiative transfer of excitation energy transfer between two fluorescent molecules. Non-radiative transfer of excitation energy requires an interaction between a donor molecule and an acceptor molecule, and it can only occur if the emission spectrum of the donor overlaps the absorption spectrum of the acceptor (figure 1.6), so that several vibronic transitions in the donor have practically the same energy as the corresponding transitions in the acceptor. Such transitions are coupled (figure 1.6), that is, in resonance.⁴⁸

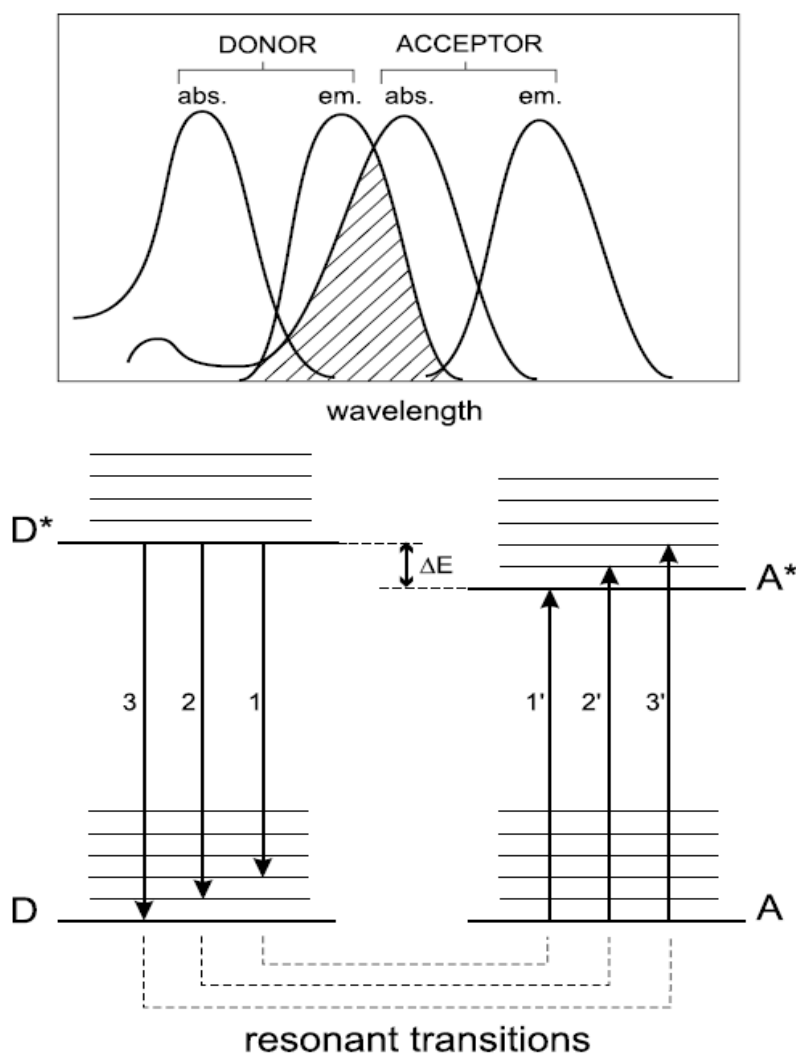
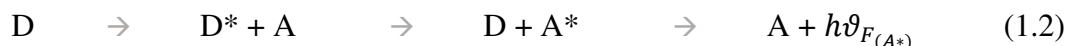


Figure 1.6. Energy level scheme of donor and acceptor molecules showing the coupled transitions in the case where vibrational relaxation is faster than energy transfer (very weak coupling) and illustration of the integral overlap between the emission spectrum of the donor and the absorption of the acceptor [adapted from Valeur 2001].⁴⁸

Energy transfer occurs when a donor excited molecule (D^*) transfers its energy to an acceptor molecule (A), through a dipole interaction (equation 1.2, where h is Planck's constant and ϑ the frequency of the emitted photon). Then, an inhibition of donor fluorescence molecule is observed, as well as a decrease of the lifetime. On the other hand, an increase in the fluorescence emission of the acceptor molecule is observed.



The FRET efficiency depends on the lifetime of the donor, that must be long enough for the energy transfer to occur; the distance between the donor and acceptor that must be between 1 and 10 nm and dipolar orientation that must be approximately parallel.⁴⁹

3.2.4 The ideal system for drug delivery

The need for development of an ideal drug delivery system relies in the requirement to safely protect and transport the promising, however toxic, drugs to the therapeutic sites of interest. Nowadays, the potential of liposomes is widely recognized. Among all the nanoencapsulation systems that are being investigated for biomedical applications (figure 1.7), such as dendrimers, polymers and so on, liposomes are the most promising ones.

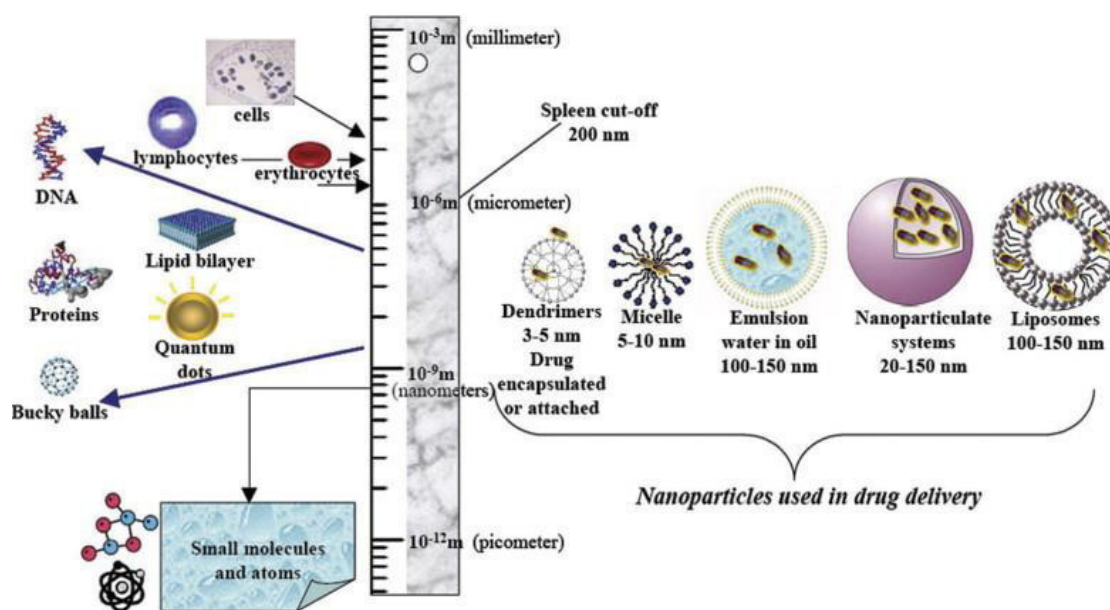


Figure 1.7. Nanoencapsulation systems for drug delivery applications [adapted from Namdeo *et al.* 2008].⁵⁰

3.2.4.1 Steric stability

The stability of liposomes plays an important role for *in vivo* application, and it can be affected by chemical, physical or biological processes. Chemical stability is related with liposome composition, while physical stability is associated with aggregation and fusion of the vesicles. On the other hand, biological stability depends on biological entities that interact with these systems and is therefore directly related to the route of administration.⁵¹ To overcome liposomes instability, physicochemical parameters of the nanosystem must be controlled. Here, the properties of this system, such as size, structure, chemical composition, charge density and permeability, can be manipulated by the preparation method.

The physical instability can be avoided by the inclusion of electrical charge in the liposomes, that will reduce vesicles fusion and aggregation. Moreover, surface charge density can also influence the interaction of liposomes with cells, however this influence remains not completely understood. It has been reported that cationic liposomes preferably target tumor vasculature,⁵² while anionic ones are captured by monocytes/blood neutrophils.²² The latter behavior has been used to target the brain through the blood brain barrier (BBB),⁵³ a highly selective semipermeable membrane that obstructs influx of most compounds from blood to brain, thus blocking the delivery of therapeutic agents to brain. Otherwise, the non-specific interaction of cationic liposomes with anionic species in the blood results in rapid clearance from circulation by the reticuloendothelial system (RES),⁵⁴ while neutral and negative surface charges reduce the adsorption of serum proteins,⁵⁵ resulting in longer circulation half-lives. Furthermore, cationic liposomes have been endorsed for gene therapy. The presence of positively charged amines facilitates binding with anions such as those found in DNA to form lipoplexes (cationic liposome-nucleic acid complexes). The resultant lipoplexes have positive charge which facilitates the adsorption of the nanosystem onto the negatively charged cell membranes, by electrostatic interaction. Unfortunately, cationic liposomes can cause cytotoxicity, limiting their safety for clinical use.⁵⁶ Thus, anionic liposomes have been proposed for delivery of other therapeutic molecules.

The biodistribution of the encapsulated drugs is directly related with the chemical stability of the liposomes. In order to accomplish higher drug accumulation in the sites of interest, it is essential to take into account several issues on the design and preparation of liposomes, such as lipid composition, cholesterol and PEG-lipid content, size and shape.⁵⁷ For enhanced permeability and retention (EPR) effect of loaded drugs, the size of the

liposomes should be small. Vesicles with approximately 400 nm in size have been reported to perform extravasation into tumors.⁵⁸ Yet, a more successful extravasation has been shown to occur for liposomes with sizes below 200 nm.⁵⁹ Concerning membrane permeability, cholesterol has been shown to play a strategic role, as it prevents early drug release. In fact, the incorporation of cholesterol has been proven to cause increased phospholipid packing in the lipid bilayer.⁶⁰ Furthermore, egg phosphatidylcholine liposomes with cholesterol, in (7:3) proportion, are commonly used as models of cell membranes.^{61,62} Moreover, Senior *et al.* reported that liposomes obtained from phosphatidylcholine (PC) with saturated fatty acyl chains are more stable in blood than liposomes prepared from PC with unsaturated fatty acyl chains.⁶³ Membrane permeability can also be regulated by the transition temperature of the phospholipids. Liposomes based on phospholipids with a high transition temperature ($> 37^{\circ}\text{C}$) are rigid at physiological temperature and so less permeable. Otherwise, liposomes with a low transition temperature ($< 37^{\circ}\text{C}$) are more permeable and so more susceptible to early release of encapsulated drugs at physiological temperature.⁶⁴

3.2.4.2 PEGylation

Conventional liposomal formulations reduce the toxicity of compounds *in vivo*; however, the rapid elimination from the bloodstream restricts its therapeutic effectiveness.^{65,66} Polyethylene glycol (PEG) is the biocompatible polymer most commonly used in drug delivery, due to its long history of safety in humans and classification as «Generally Regarded as Safe» (GRAS) by the U.S. Food and Drug Administration (FDA). PEGylation is the process of both covalent and non-covalent attachment of PEG polymer chains to other structures such as liposomes. Two main methods of PEGylation have been developed. The first consists in the physicochemical binding of PEG (or functionalized PEG) to the bare or previously modified surface of nanoparticles. The other consists in chemical coupling, either *in situ* during particle preparation, or by chemisorption of functionalized PEG on nanoparticles surface.⁶⁷⁻⁷⁰

The PEGylation process increases the size and molecular weight of conjugated biomolecules, while improving their pharmacokinetics and pharmacodynamics by increasing water solubility, protecting from enzymatic degradation, reducing renal clearance and limiting immunogenic and antigenic reactions.⁷¹ That is, PEGylation is able to reduce clearance through glomerular filtration and RES or proteolytic degradation. In fact, in the nineties, Klibanov *et al.* reported that PEGylation increased the blood

circulation half-life of systemically administered liposomes from < 30 min to up to 5 h.⁷² Also, it was demonstrated that liposomes coated with PEG of 750 Da up to 5 kDa, have a prolonged blood circulation time and reduced uptake by the mononuclear phagocyte system (MPS) when compared with non-PEGylated ones.⁷³ However, the differences in circulation time between formulations with increasing PEG size (range: 350 Da – 2 kDa) were negligible.⁷⁴

3.2.4.3 Specific functionalization for cancer

Concerning the application of liposomes as a drug delivery system in cancer therapy, and in order to specifically target cancer cells, recent studies revealed that the functionalization of liposomes surface improves efficacy. Some strategies regarding liposomes surface functionalization focus on active targeting to sites of interest and triggered release of the therapeutic agents. The resulting liposomal system can be used to increase drug accumulation and improves drug delivery in cancer therapy.^{75,76} These strategies are based on pathological differences of tumors microenvironment, such as the overexpression of folate or transferrin receptors on the surface of many tumor cell types and the acidic pH within cancer cells.⁷⁷ Regarding the latter property, the anionic lipid cholesteryl hemisuccinate (CHEMS) has been added to the surface of liposomes, as it allows them to be pH-sensitive. In fact, Hafez *et al.* have shown that liposomes functionalized with CHEMS fuse after the pH is lowered below a critical value between 4.0 and 6.7.⁷⁸ Also, folate receptor-targeted liposomes have been reported for the delivery of therapeutic agents to tumor cells, with significantly higher cellular uptake and cytotoxicity compared to non-targeting liposomes.^{79,80} Actually, Low *et al.* showed that folate receptor-targeted PEGylated liposomes loaded with doxorubicin demonstrated a 45-fold higher uptake and 85-times more cytotoxicity when compared with unmodified ones.⁸¹ Moreover, other strategies have been explored to specifically target cancer cells, for instance, the attachment of antibodies⁸² and the incorporation of small peptides⁵³ that target specific membrane proteins.

3.3 Magnetic Nanoparticles

Magnetic nanoparticles are small particles that can be manipulated using magnetic fields, possessing at least one dimension less than 100 nm and one magnetic component on its composition. Due to their size, they have a large surface/volume ratio and thus unique physicochemical and magnetic properties, such as mass and heat transfer that are

different from macrometric scale materials.⁵¹ There are two main classes of magnetic nanoparticles:⁸³

- Metallic nanoparticles: those composed of metals, such as cobalt (Co), iron (Fe), manganese (Mn) and nickel (Ni) or metal alloys, such as iron-platinum (FePt) or iron-cobalt (FeCo) nanoparticles.
- Metal oxide nanoparticles: the ones composed of iron oxides doped with diamagnetic metals as Co^{2+} , Fe^{2+} , Mn^{2+} and Ni^{2+} .

3.3.1 *Magnetic nanoparticles for biomedical applications*

Freeman *et al.* were the first to introduce the use of magnetism in medicine in the 1960s.⁸⁴ Since then, it is accepted that magnetic fields are not specially contraindicated for humans and the potential of magnetic nanoparticles has been recognized in many biological applications.⁸⁵ Furthermore, concerning the ability to target specific sites of interest and to produce heat, magnetic nanoparticles have been widely investigated for drug delivery, hyperthermia and biological imaging, as magnetic resonance imaging (MRI) contrast agents. At nanometric scale and depending on materials, ferromagnetic and ferrimagnetic nanoparticles exhibit a magnetic behavior that is important for biomedical applications, the superparamagnetic behavior. This type of magnetism is characterized by a very large magnetic moment, but only in the presence of an external magnetic field. When the external magnetic field is removed, no remnant magnetization is observed and the net moment of the particles is randomized to zero.^{52,86-88}

Despite the large potential of magnetic nanoparticles for biomedical applications, they exhibit, in some cases, prolonged tissue retention (more than the need for treatment) and contain heavy metals which seriously raise concerns to their toxicity. Renal filtration is the ideal route for nanoparticles removal from the body and it can be increased by adjusting some parameters such as surface characteristics, shape, and size of the nanoparticles.⁸⁹ Alternative mechanisms for nanoparticles clearance are being studied, such as intracellular degradation that may lead to the utilization of currently unexploited pathways for particle clearance.⁹⁰

3.3.2 *Magnetic nanoparticles studied in this thesis*

3.3.2.1 *Core-shell nanoparticles*

Core-shell nanoparticles consist in particles possessing a core or inner material surrounded by an outer shell of a coating material. In the case of magnetic core-shell nanoparticles, the inner material is magnetic and it can be a metallic or metal oxide nanoparticle. Core-shell nanoparticles have been a focus of attention over the past two decades, because of their several advantages over simple nanoparticles.⁹¹ The major benefits associated with this type of structure rely on properties improvement, with simultaneous avoidance of undesirable effects. For biomedical applications, the use of core-shell structures offers huge advantages, such as improved thermal and chemical stability and solubility, less cytotoxicity, higher biocompatibility, easier conjugation with other bioactive molecules and so on.⁹¹⁻⁹³

Shell structure and composition are key parameters for keeping physical properties of the core unaltered. For instance, the shell of magnetic nanoparticles must be small, as the saturation magnetization can be deteriorated with increasing shell thickness.⁹⁴ Concerning shell composition, different materials can be used from organic to inorganic ones. In biomedical applications, the most usual are dextran,⁹¹ polyethylene glycol^{95,96} (as discussed previously) or chitosan⁹⁷ for the organic, and gold,^{98,99} silica (SiO₂)^{100,101} or carbon¹⁰² for the inorganic ones. A lot of studies have been carried out to evidence the better results of core-shell nanoparticles in biomedical applications. For instance, iron oxide nanoparticles coated with dextran were the first used as MRI contrast agents in the late 1970s with success.⁹¹ More recently, a basic MRI system based on superparamagnetic iron oxide core with SiO₂ shell, functionalized for radiolabeling with ⁶⁴Cu and ¹¹¹In, was found to be more efficient in imaging when compared to the commercially used agent Feridex.¹⁰³ Also, iron/carbon core-shell nanoparticles have shown potentialities as contrast agents for MRI, with very low toxicity.¹⁰² Moreover, Kayal and his team have shown the potentiality of the gold shell for iron nanoparticles in drug delivery.⁹⁸ The data revealed great affinity for amine groups in anticancer drugs such as doxorubicin, providing a structural stabilization and a platform for better surface chemistry between drugs and carriers.⁹⁸ Furthermore, Morris *et al.* showed, in a folate responsive tumor cell targeted gene transfection experiment, that histidine-modified chitosan (of molecular weight 15 kDa) increases nuclear uptake of the nanoparticles, indicating that chitosan can act as an adequate organic shell layer.¹⁰⁴

3.3.2.1.1 Nickel/silica core-shell (Ni/SiO₂) nanoparticles

Nickel has been known to be an important magnetic material. It is considered a metal of biological interest, as it presents magnetic properties at room temperature.¹⁰⁵ However, nickel nanoparticles have some issues related to their toxicity, high reactivity and the fact that they are easily degraded due to high surface/volume ratio.

During the past decade, it has been demonstrated that coating of metal or oxide nanoparticles with a SiO₂ shell gives rise to many new and unusual physical chemical properties, such as improved stability and precise control of surface chemistry that allows to modulate drug loading and site-specific targeting.¹⁰⁶⁻¹⁰⁸ The use of a core-shell structure allows a safe utilization of metals like nickel, thus taking advantage of the magnetic core. SiO₂ is a widely employed shell material, being a particularly beneficial coating for biomedical applications, since it can be easily functionalized and is resistant to degradation within a cellular environment, whilst still being biocompatible. Concerning the magnetic properties, silica coating has been recognized as promising to suppress magnetic dipolar interaction between nanoparticles and so promoting superparamagnetic behavior.¹⁰⁹

Previous studies have shown that internalized SiO₂-coated magnetic nanoparticles are biocompatible with stem cells.^{110,111} The properties of Ni/SiO₂ nanoparticles strongly depend on the method used for preparation. The work of Fu and coworkers¹¹² revealed that the magnetic properties of Ni/SiO₂ core/shell nanoparticles get worse with increasing SiO₂ shell, due to the presence of the nonmagnetic silica coating. In fact, the saturation magnetization decreases from 46 emu/g to 37 emu/g, with increasing shell from 2 nm to 13 nm. Despite this, the thermal stability of core-shell nanoparticles increases, as the oxidation temperature of the nickel core of Ni/SiO₂ nanoparticles is 100° C higher than that for pure nickel nanoparticles.¹¹²

3.3.2.2 Iron oxide-based nanoparticles

Iron-oxide based nanoparticles are of great interest in biomedical research because of their superparamagnetic properties, good biocompatibility and non-toxicity.¹¹³ This type of nanoparticles is made of iron, oxygen and/or OH groups, with some differences in the valence of iron and on the crystalline structure. The main forms with biological interest of these nanoparticles are magnetite (Fe₃O₄) and its oxidized form maghemite (γ -Fe₂O₃).¹¹⁴

The crystalline structure of the magnetite nanoparticles is face centered cubic inverse spinel, consisting of a cubic close-packed array of oxide ions where all of the Fe^{2+} ions occupy half of the octahedral sites and the Fe^{3+} ions split evenly across the remaining octahedral and tetrahedral sites (figure 1.8). Coupling between magnetic moments of the iron moieties located at tetrahedral and octahedral sites results in a ferromagnetic ordering in bulk. Maghemite structure is a cubic defect spinel, similar to that of magnetite but with vacancies in the cation sub-lattice. Oxygen anions give rise to a cubic close-packed array, while iron cations are distributed over tetrahedral sites and octahedral sites. The resulting magnetic behavior is ferromagnetic.

At the nanoscale, magnetite and maghemite present different magnetic behaviors when compared to those of the bulk materials. Below a critical diameter, an assembly of non-interacting magnetite nanoparticles exhibits superparamagnetism at high temperatures and a ferromagnetic (ferrimagnetic for maghemite) behavior below the blocking temperature (T_B).

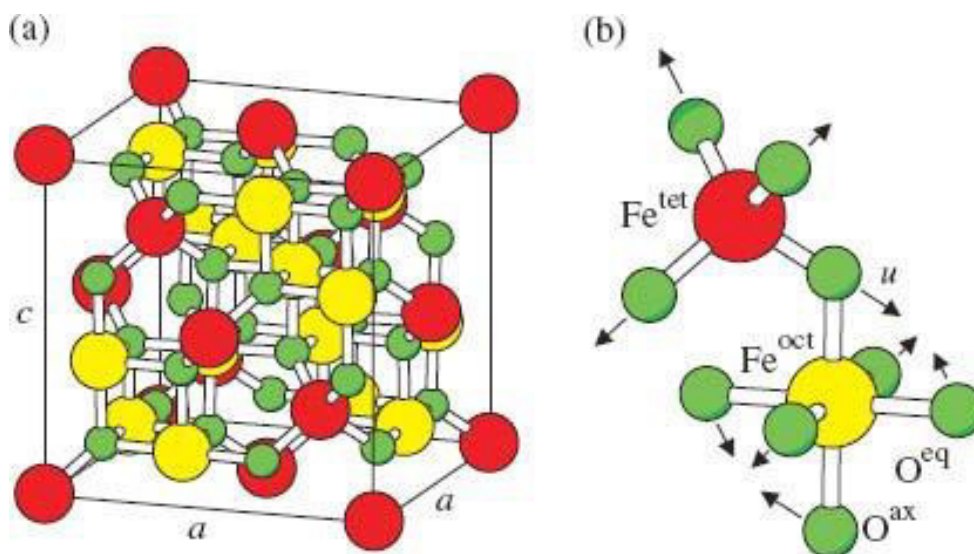


Figure 1.8. (a) Face-centered cubic spinel structure of magnetite. (b) Magnification of one tetrahedron and one adjacent octahedron sharing an oxygen atom. Large spheres labelled by Fe^{tet} and Fe^{oct} represent iron atoms on tetrahedrally and octahedrally coordinated sublattices, respectively. Oxygen atoms are shown as small spheres. The lattice parameters a in the (001) plane and c in the direction perpendicular to it are identical under equilibrium conditions but differ for tetragonal systems. The lower symmetry in this case also leads to the distinction between axial O^{ax} and equatorial O^{eq} atoms. Arrows indicate the shift directions of the oxygen atoms from their ideal positions for an internal parameter $u > 0$ (internal vibrational energy) [adapted from Friák *et al.* 2007].¹¹⁵

3.3.2.3 Transition metal ferrite nanoparticles

Even with all the very good physicochemical, magnetic and biocompatibility properties, the iron oxide-based nanoparticles present some less desirable interactions in physiological environment due to the high content of iron atoms being weakly distinguished from those of hemoglobin.¹¹⁶ Moreover, the presence of Fe^{2+} , which can be oxidized to Fe^{3+} , may compromise the magnetic properties of magnetite nanoparticles. Alternatively, much attention has been dedicated to the development of transition metal ferrites (MFe_2O_4 , $\text{M} = \text{Mn, Ni, Co, Zn}$), with enhanced magnetic properties and strong interest for biomedical applications. Transition metal ferrite nanoparticles are remarkably soft-magnetic with superparamagnetic behavior at the nanoscale, high saturation magnetization, good chemical stability and high biocompatibility.¹¹⁷

This type of ferrites presents a spinel structure, with a cubic close-packed arrangement of oxygen atoms, with M^{2+} and Fe^{3+} in two different crystallographic sites. The spinel structure contains two cation sites for metal cation occupancy. Metal cations are either tetrahedrally coordinated with oxygen in the 8 tetrahedral sites or occupy 16 octahedral sites which possess octahedral coordination. Magnetically, spinel ferrites display ferrimagnetic behavior and their electrical and magnetic properties depend upon the choice of M cation and its distribution between tetrahedral and octahedral sites. Also, the properties of the nanoparticles are highly sensitive to preparation methods, annealing temperature, chemical composition and nature of dopants.^{118,119}

In this work, focus was made on nickel ferrite (NiFe_2O_4) and manganese ferrite (MnFe_2O_4) nanoparticles because of their outstanding properties for therapy and diagnosis. NiFe_2O_4 nanoparticles have been proposed as less cytotoxic for HeLa cells than cobalt (CoFe_2O_4) or zinc ferrite (ZnFe_2O_4), being more promising for biomedical applications.^{120,121} Also, MnFe_2O_4 nanoparticles have shown a good biocompatibility and slight toxicity against HeLa cells.¹²⁰ Moreover, MnFe_2O_4 nanoparticles have received an increased attention because of their higher magnetic susceptibility, comparing with other ferrite nanoparticles.¹²² Due to their small sizes, these nanoparticles have been proposed as positive contrast agents for magnetic resonance imaging. It is known that the surface atom ratio and the particle degradation rate are inversely proportional to the particle size. Larger particles exhibit a lower surface Mn^{2+} ratio and slower release of Mn^{2+} than small ones, leading to a small longitudinal relaxivity. Therefore, reducing their size is considered an important strategy to improve the longitudinal relaxivity, as observed for MnO colloids with 2-3 nm size.^{123,124} Also, MnFe_2O_4 nanoparticles are promising

hyperthermia agents. M. Mozaffari *et al.* reported that 10 g/l of MnFe_2O_4 nanoparticles in the presence of an AC magnetic field ($f = 400$ kHz) increase temperature by 5°C after 20 minutes.¹²⁵ Likewise, NiFe_2O_4 nanoparticles are also suitable for magnetic hyperthermia. Small NiFe_2O_4 nanoparticles with a saturation magnetization of 49.5 emu/g showed high enough self-heating temperature for killing cancer cells.¹²⁶

3.3.3 The origin of superparamagnetic behavior

In bulk, the magnetic behavior of ferromagnetic materials, like iron, nickel and cobalt, arises from magnetic domain structures. Magnetic domains are regions of uniform magnetization where individual magnetic moments spontaneously align in the same direction, as a result of several interactions that occur in magnetic materials, such as exchange, anisotropy and dipolar interactions.¹²⁷ With the creation of magnetic domains and because they can point in different directions, the magnetostatic energy is minimized, thus reducing the intensity of the field. The interface that separates magnetic domains is called domain wall and its thickness is limited by the anisotropy of the material. Here, the magnetization rotates coherently from the moment in one domain to the one in the neighbor domain, as we can see in figure 1.9 (b).

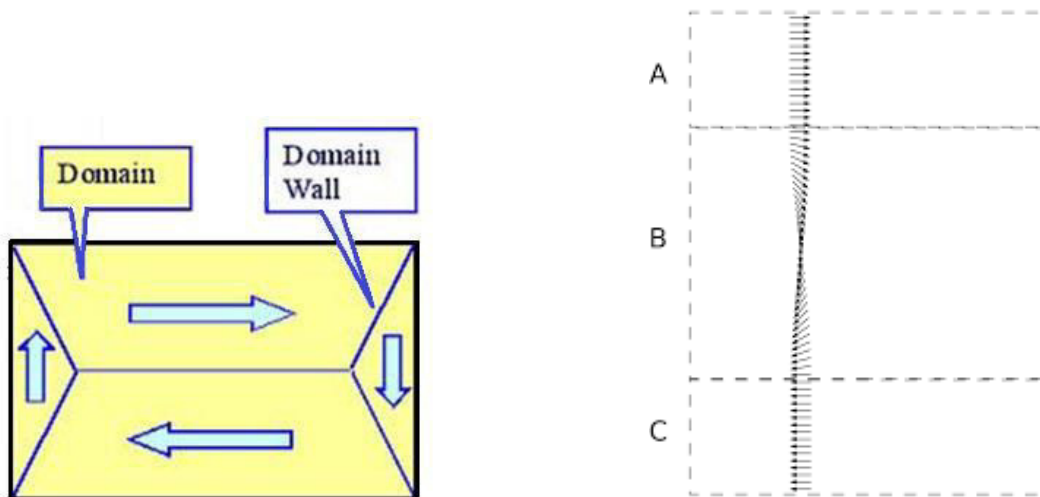


Figure 1.9. Magnetic domain and domain wall representation (left). Domain wall (B) with gradual reorientation of the magnetic moment between two domains (A) and (C) (right).

When the size of a ferromagnetic material decreases, the energy required for domain formation increases and, below a critical diameter, the formation of domains becomes energetically unfavorable. Below this critical diameter, it is energetically more expensive to form a domain wall than to withstand the magnetostatic energy of a single

domain system and the nanoparticles become superparamagnetic. That is, the state of uniform magnetization becomes the state of lower energy. In this state, the magnetization of the nanoparticles is approximated as one giant moment, by summing the individual magnetic moments (μ) of each constituent atom. This approximation is called the “macro-spin approximation” and is responsible for the strong magnetic moment in superparamagnetic nanoparticles.

The critical size for single domain, D_{cr} , is the largest size that a ferromagnetic particle may have above which it will be energetically more favorable to divide itself into two or more domains, and is given by equation 1.3.¹²⁸

$$D_{cr} = \frac{72\sqrt{AK_{\mu}}}{\mu_0 M_s^2} \quad (1.3)$$

where A is the exchange stiffness constant, K_{μ} the uniaxial anisotropy constant (assumed > 0), M_s the saturation magnetization and μ_0 is the vacuum magnetic permeability ($4\pi \times 10^{-7}$ H/m). Critical diameter varies from material to material and, according to literature, it occurs at sizes below 30 nm.¹²⁸

For single-domain nanoparticles, the fraction of nanoparticles that can change from a stable magnetic configuration to another is proportional to $e^{(K_{\mu}V/k_B T)}$, where V the particle volume, k_B the Boltzmann’s constant, and T the absolute temperature. Decreasing the particles size, the anisotropic energy ($K_{\mu}V$), that is the energy which separates the two energetically equivalent magnetization directions, decreases until the thermal energy ($k_B T$) causes fluctuations of the whole magnetic moments. In this situation, thermal fluctuations can affect the orientation of magnetization if they are large enough to overcome the magnetic anisotropy barrier. So, the magnetic anisotropy works as an energy barrier that blocks the magnetic moments. But, if temperature is above the so-called blocking temperature (T_B), that is the temperature above which the thermal fluctuations are activated, the energy is high enough to overcome the anisotropy energy barrier, the magnetic moments get unblocked and the magnetization is lost. T_B depends on particle size and other factors.¹²⁹ For ferromagnetic materials, the magnetic anisotropic energy is much larger than thermal energy ($k_B T$) (figure 1.10 (blue line)). However, when nanoparticles are small enough for thermal energy to overcome the anisotropy energy ($K_{\mu}V$), the magnetization is no longer stable and the particle becomes superparamagnetic (figure 1.10 (red line)).

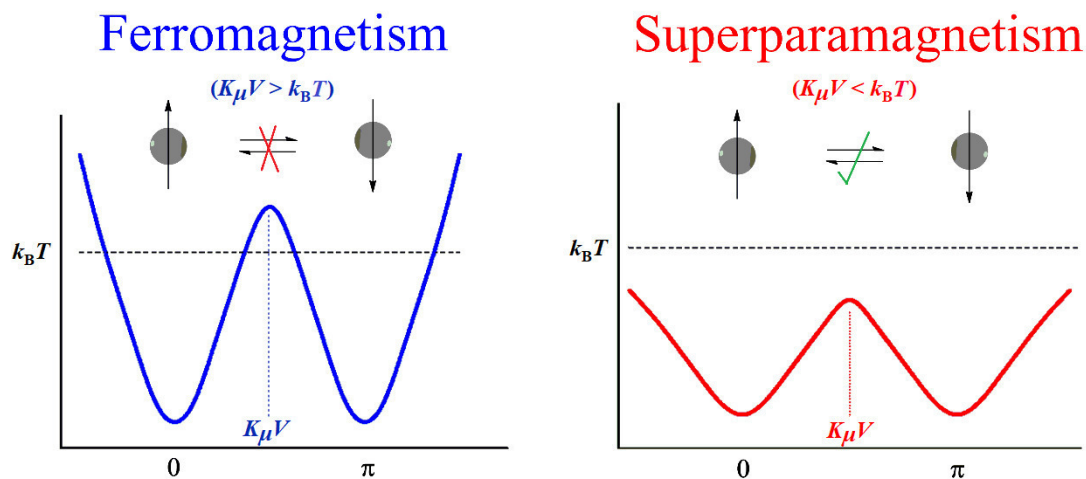


Figure 1.10. Nanoscale transition of magnetic nanoparticles from ferromagnetism to superparamagnetism; energy diagram of magnetic nanoparticles.

The relaxation time of the moment of a superparamagnetic nanoparticle (τ_N), is given by the Néel expression, equation 1.4.¹²⁹

$$\tau_N = \tau_0 e^{\frac{K_\mu V}{k_B T}} \quad (1.4)$$

where τ_0 is the characteristic time of the material (10^{-9} - 10^{-12} s). A given experiment will have its own window of measurement time (τ_m) and depending on this time, two situations can be observed:

- $\tau_m \gg \tau_N$ - the time window of the measurement is longer than the time needed for the particles magnetic moment to flip; the particle is said to be in a superparamagnetic state.
- $\tau_m \ll \tau_N$ - the experimental time scale is shorter than the moment flipping time; the particle is said to be in the blocked state.

Thus, the blocking temperature, defined as the mid-point between ferromagnetic and superparamagnetic state, can be defined as the temperature at which the system goes from blocked to unblocked, and $T = T_B$ for $\tau_m = \tau_N$. Thus, as the blocking temperature depends on the experimental time scale, the blocking temperature can be easily obtained by equation 1.6.¹²⁹

$$\tau_m = \tau_0 e^{\frac{K_\mu V}{k_B T}} \Leftrightarrow \ln\left(\frac{\tau_m}{\tau_0}\right) = \frac{K_\mu V}{k_B T_B} \quad (1.5)$$

$$T_B = \frac{K_{\mu}V}{k_B \ln\left(\frac{\tau_m}{\tau_0}\right)} \quad (1.6)$$

So, magnetic nanoparticles above T_B and with size below D_{cr} , are superparamagnetic and can easily reach the saturation magnetization in the presence of an applied field, but upon field removal, magnetization returns to zero due to the thermal fluctuations.¹³⁰ Thus, this type of magnetic nanoparticles is characterized by the absence of hysteresis, coercivity and remnant magnetization at room temperature (for $T_B < \text{room temperature}$).

3.3.4 *Magnetic nanoparticles synthesis and characterization*

As it was already mentioned and justified, in biomedical applications magnetic nanoparticles with superparamagnetic behavior are preferred.^{52,87,88} High magnetization and low coercivity values are ideal properties of superparamagnetic nanoparticles for biomedical applications. With high magnetization values, magnetic nanoparticles can be easily controlled by the presence of an external magnetic field, while low coercivity values lead to reduced force required to randomized sample magnetization to zero.

The magnetic behavior and physicochemical properties of magnetic nanoparticles, such as size distribution, shape and surface chemistry, strongly depend on the synthesis method. The preparation method determines the degree of structural defects or impurities in the particles, as well as the distribution of such defects and, consequently, their magnetic properties.^{19,131-133} Due to this strong dependence, many protocols for the synthesis of magnetic nanoparticles have been established. These protocols aim to yield monodisperse colloids uniform in size and shape and to accomplish a proper control of crystallinity and magnetic properties,¹³⁴ in which the entire uniform physicochemical properties of the ensemble directly reflect the properties of single particles.¹³⁵ Up to now, many synthesis methods have been reported in literature, including coprecipitation, microemulsion, thermal decomposition, solvothermal technique, chemical vapor deposition, combustion synthesis and many others.¹²⁷ Among all, coprecipitation seems to be the most appropriate for good size distributions and magnetic properties.¹³⁶ This method has been widely used for biomedical applications, as it is a simple and efficient chemical pathway,¹⁰⁹ that does not require harmful materials and procedures, being cost-effective.¹³⁷

The characterization of magnetic nanoparticles is important to confirm the proper physical, chemical and magnetic properties of the synthesized particles. As the superparamagnetic behavior is dependent on the crystallite size, and it only occurs below critical diameters, it is essential to measure particles size and polydispersity. On the other hand, the magnetic properties of nanoparticles also depend on the distributions of ions on the crystallographic lattice sites and so the crystalline structure of the nanoparticles must be assessed. Concerning magnetic properties, the magnetic materials are best described in terms of their magnetization dependence on applied magnetic field, the so-called hysteresis loop, and by the magnetization dependence on temperature, the zero-field cooled (ZFC) and the field cooled (FC) curves.¹³⁸ This type of measurements is made in magnetometers and the most common equipments used are the Superconducting Quantum Interference Device (SQUID) and the Vibrating Sample Magnetometer (VSM). In this work, the magnetic properties were evaluated in a SQUID apparatus, that is the most sensitive equipment to measure magnetic fields, with a resolution of 10^{-4} nT. It can measure very weak magnetic fields, such as those generated by the human body, being useful for many biomedical applications.¹³⁹ The high sensitivity of this equipment makes it one essential instrument in the area of nanomagnetism.¹⁴⁰ Typically, the working parameters of a SQUID are:¹⁴¹

- static field up to 14 T, with an accuracy of 10^{-5} T;
- temperature range: 1.8 - 400 K, with an accuracy of 0.01 K.

3.3.4.1 Hysteresis loop

The hysteresis loop gives relevant information about the magnetization of magnetic nanoparticles. Important magnetic parameters can be obtained from this type of measurements, specifically the degree at which the sample remains magnetized when the applied field is removed, the so-called remnant magnetization (M_r), and how easily the residual sample magnetization can be removed, the coercive field (H_c). This measurement is performed by fixing the temperature and measuring the magnetization at a range of applied magnetic fields (figure 1.11).

Before start measuring, the sample is completely demagnetized with an external magnetic field. Then, the application of an increasing magnetic field causes the alignment of the magnetic moments of the material, until a maximum value of magnetization. This state is called the saturation magnetization (M_s) and corresponds to the situation where

all the magnetic moments in the nanoparticles are aligned with the applied field (point “a”, figure 1.11). By reducing the applied field to zero, the curve moves from point “a” to point “b”, which represents the remnant magnetization. As the magnetic field is reversed, the curve reaches point “c”, where the magnetic moment has been reduced to zero. This is called the coercivity, or coercive force, and represents the required force to remove residual magnetism of the sample. Then, the applied field is increased in the negative direction till the material becomes magnetically saturated, but in the opposite direction, at point “d”. Point “e” is reached reducing the field to zero, that represents the residual magnetism, but in the other direction. Now, increasing again the applied magnetic field in the positive direction, the magnetic moment returns again to zero. At this point “f”, the curve did not return to the original graph because some force is required to remove the residual magnetism. This way, the curve will take a different path from point “f” back to the saturation point, where the loop is complete.

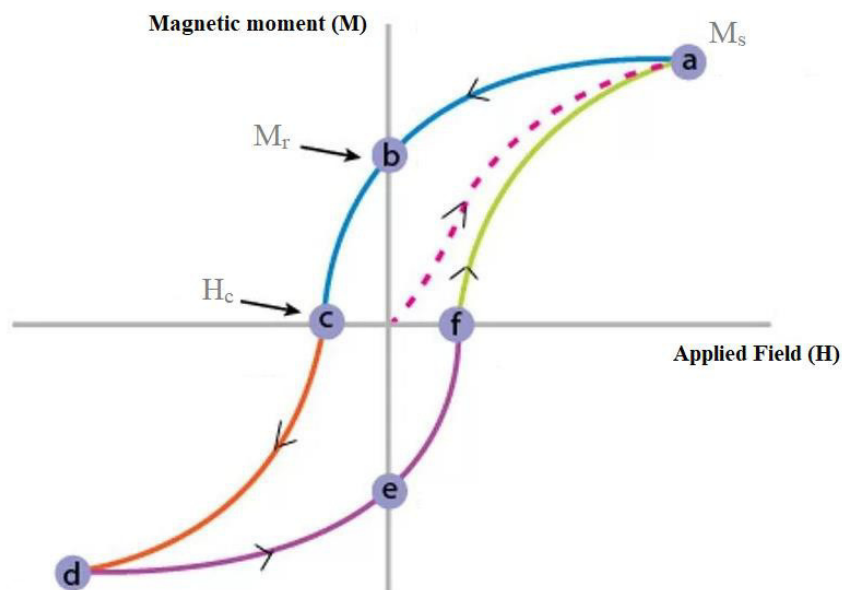


Figure 1.11. Typical hysteresis curve of a ferromagnetic sample.

For ferromagnetic materials, the remnant magnetic moment and coercivity are observed at zero field, while, for superparamagnetic ones, these values tend to zero and the material is said to have no hysteresis. The ratio between the remnant magnetization and the saturation magnetization, M_r/M_s , is called the magnetic squareness value and varies from 0 to 1.¹¹⁸ The presence of a superparamagnetic behavior can be related to the value of this ratio. If its value is below 0.1, it means that more than 90% of the magnetism

is lost upon removal of the applied magnetic field and the material is considered superparamagnetic.^{118,121,142}

3.3.4.1.1 Langevin function

For an ensemble of superparamagnetic particles above the blocking temperature, the magnetization under an external magnetic field can be described by the Langevin function (equation 1.7),

$$M(H, T) = N\mu L\left(\frac{\mu H}{k_B T}\right) = N\mu\left(\coth\left(\frac{\mu H}{k_B T}\right) - \frac{k_B T}{\mu H}\right) \quad (1.7)$$

where μ is the magnetic moment and N the number of moments per volume. The magnetic moment of the nanoparticles is given by $\mu = M_s V$, where M_s is the saturation magnetization and V the volume of the nanoparticle.¹⁴³ Thus, this equation reveals that the shape of the magnetization curve depends on the volume of magnetic nanoparticles, and nanoparticles size can be estimated. With known volume, V , and using spherical nanoparticles volume equation, $V = \frac{1}{6}\pi D^3$, the diameter of the nanoparticle, D , is easily estimated.¹⁴⁴

3.3.4.2 Zero-field cooled and field cooled curves

The magnetic response of a magnetic material to an external magnetic field at a given temperature is not always the same, and depends on whether the sample has been cooled with or without an applied field. Zero-field cooled and field cooled measurements are made by fixing the applied magnetic field and measuring the magnetization at different temperatures. First, the sample is cooled under an applied field of $H \sim 100$ Oe and then the magnetization is measured with increasing temperature (applied field of $H \sim 50$ Oe) – FC curve. Then, the sample is again cooled down, but now without any applied field, and the magnetization is measured with increasing temperature, under the same field of $H \sim 50$ Oe – ZFC curve. Here, as the temperature increases, the blocked magnetic moments start to align with the applied field and the magnetization of the sample increases. However, as soon as thermal energy overcome the anisotropic energy, thermal fluctuations cause the misalignment of the magnetic moments and a decrease of the magnetization is observed, with increasing temperature. Thus, ZFC curve peak corresponds to the blocking temperature (T_B), above which the sample becomes superparamagnetic. Because of thermal equilibrium, above T_B , ZFC and FC curves

coincide and the system is in a superparamagnetic state. However, below T_B , the magnetization in FC curve does not tend to zero, because of the moments that remain partially aligned with the applied field ($H \sim 100$ Oe) and the nanoparticles display a ferromagnetic behavior.¹⁴⁵

3.4 Magnetoliposomes for cancer therapy

In previous chapters 3.2 and 3.3, the outstanding properties of liposomes and magnetic nanoparticles for biological applications, especially for cancer therapy, were described. It was stated that liposomes are, to date, the most used encapsulation systems for drug delivery and that the magnetic nanoparticles are suitable for therapeutic applications, taking advantage of magnetic guidance and inductive heating properties. However, each system has its own limitations. For instance, liposomes present some *in vivo* issues, namely their recognition and capture by the immune system¹⁴⁶ and the localization in therapeutic sites for drug release. On the other hand, magnetic nanoparticles have the tendency to agglomerate and form sediments which could be a safety concern.¹⁴⁷ In order to overcome these problems, magneto-sensitive liposomes have been proposed.¹⁴⁸

Magnetoliposomes result from the encapsulation of magnetic nanoparticles into liposomes and were first described by De Cuyper and Joniau in 1988.¹⁴⁹ The combination of liposomes and magnetic nanoparticles allows the concentration of the nanosystem in the treatment area of patient by magnetic forces, often augmented by magnetic agglomeration, and avoids *in vivo* nanoparticles accumulation, thus assuring biocompatibility. Therefore, singular limitations of both liposomes and magnetic nanoparticles are overwhelmed, and the resulting magnetoliposomes join the optimal properties of both in a single nanosystem.

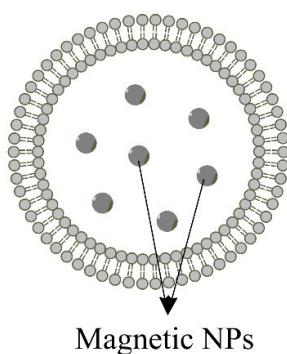
The scientific community has been addressing magnetoliposomes as a new encouraging system for cancer therapy with the potential to cause an important impact in the dramatic cancer statistics.¹⁴⁸ This versatile nanosystem is promising, not only in cancer therapy, but also in diagnosis. It can provide combined synergistic drug delivery and hyperthermia treatment^{150,151} at specific target sites and co-instantaneous MRI.¹⁵² This new approach to cancer therapy aims to replace the current traditional chemotherapy which leads to severe problems to patients, such as the high drug dosage, large side effects and low efficacy.

Considering their potentialities, significant attention has been recently dedicated to the development of these hybrid nanosystems. Furthermore, several studies ranging from general biophysical research to triggered release demonstrations have been done to enhance the application of magnetoliposomes in cancer therapy. In order to specifically target cancer cells, magnetoliposomes functionalization can be performed in a similar way as described in the previous chapter 3.2.4. In fact, work from Bothun and coworkers showed that magnetoliposomes with average diameter of 174 ± 53 nm and 0.1 mol% of folate present a higher uptake when compared with non-targeted magnetoliposomes after 180 min.¹⁵³ It was also reported that PEGylated magnetoliposomes of PC/Cholesterol 2:1 + 4 mol % of a PEGylated lipid showed good stability in terms of mean diameter and polydispersity index (PI) for 35 days.¹⁵⁴ Moreover, the latter magnetoliposomes also exhibited a retention capability of their magnetic content for at least 20 days.¹⁵⁴

3.4.1 Aqueous and solid magnetoliposomes synthesis

Over the past decade, different approaches to associate magnetic nanoparticles with liposomes, resulting in distinct magnetoliposomes, have been proposed.¹⁴⁸ The magnetic nanoparticles can be encapsulated directly into the aqueous lumen of liposomes^{155,156} or covered by a lipid bilayer^{157,158}. More recently, a new approach describes the conjugation of iron oxide nanoparticles to the liposome surface.¹⁵⁹ Concerning particles encapsulation into the lumen of liposomes, the magnetic nanoparticles can be dispersed in the inner aqueous phase, forming aqueous magnetoliposomes (AMLs), or the inner aqueous phase can be replaced by a nanoparticles cluster, originating solid magnetoliposomes (SMLs), as shown in figure 1.12.

Aqueous Magnetoliposomes



Solid Magnetoliposomes

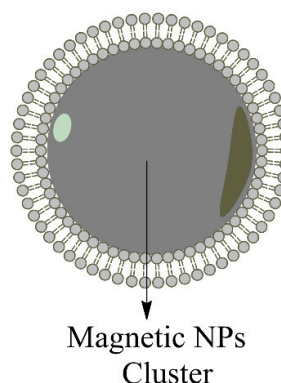


Figure 1.12. Schematic representation of aqueous magnetoliposomes (AMLs) and solid magnetoliposomes (SMLs).

Different structures make the magnetoliposomes more suitable for different applications and so spatial location of the magnetic nanoparticles inside the liposomes is a key factor. For instance, for imaging, magnetoliposomes with magnetic nanoparticles in the inner lumen of liposomes are preferred and this has been the most studied structure.¹⁴⁸ As nanoencapsulation systems, AMLs are more advantageous, as they can carry both hydrophilic and hydrophobic drugs, while SMLs can only carry hydrophobic ones. On the other hand, SMLs are more promising for magnetic guided transport of hydrophobic drugs and hyperthermia applications.^{160,161}

In literature, several techniques for the synthesis of AMLs have been established. Pradhan and coworkers have successfully synthesized AMLs containing lauric acid-coated MnFe_2O_4 nanoparticles. In their work, they used two different methods, thin film hydration and double emulsion, and the obtained magnetoliposomes showed sizes around 300 nm diameter.¹⁶² Later on, the same team, reported smaller AMLs composed of DPPC:Chol:DSPE-PEG 80:20:5 molar ratio, prepared by thin film hydration, with hydrodynamic diameters of 156 ± 11 nm that were promising for hyperthermia.¹⁰ Also, reverse-phase method followed by sequential extrusion was used for the synthesis of magnetoliposomes with a size range from 130 to 180 nm.¹⁶¹ Likewise, the already mentioned method of ethanol injection can also be adapted for the synthesis of small AMLs in a simple way, as it will be described in chapter 2.

Concerning the synthesis of SMLs, conventionally it consists on the growth of a second lipid layer around magnetic nanoparticles covered by a monolayer (previously synthesized in the presence of lipids or surfactants).^{163,164} As it will be described on chapter 2 (articles 2.2 and 2.3), in this work, a new method for the synthesis of SMLs with improved magnetic properties was developed. This was an important achievement because most of the magnetic nanoparticles with appropriate magnetic properties require a calcination step. Regarding this fact, the new method stands out because the coating of nanoparticles cluster with the lipid bilayer occurs only after nanoparticle synthesis, with no risk of “burning” the lipid bilayer. Other procedures for SMLs, in which nanoparticles synthesis and lipid bilayer coating are done separately, have been proposed. For instance, Andresen and coworkers synthesized SMLs by mixing small liposomes (obtained by strong sonication with tip) with magnetic nanoparticles, followed by dialysis.²⁰ These SMLs are structurally similar to the ones obtained by our method. Yet, our preparation method is much simpler and expedite, without the need for dialysis procedure, that can take up to two days.

3.4.1.1 Structural and magnetic characterization

To be suitable for biomedical applications, magnetoliposomes must be small and should present superparamagnetic properties at room temperature. Thus, structural and magnetic characterization is essential. However, this is a challenging study, due to all the components and contributions that this hybrid magnetic nanosystem presents.

Giant magnetoliposomes can be easily observed and characterized by light and fluorescence microscopy. Also, these microscopy methodologies can be used to investigate the elastic properties of giant magnetoliposomes by studying the deformation of the lipid bilayers under an applied magnetic field.¹⁵⁵ Moreover, Nappini and coworkers have been investigating the release of Alexa dye under AC magnetic field, by confocal laser scanning microscopy (CLSM).^{165,166} Alexa-loaded GUVs (without magnetic nanoparticles) showed no release of the dye over time.¹⁶⁶ On the other hand, Alexa-loaded magnetic GUVs (incorporating core/shell cobalt ferrite/silica nanoparticles) and under AC magnetic field showed a progressive reduction of the fluorescent intensity of Alexa inside the vesicles (figure 1.13).¹⁶⁶

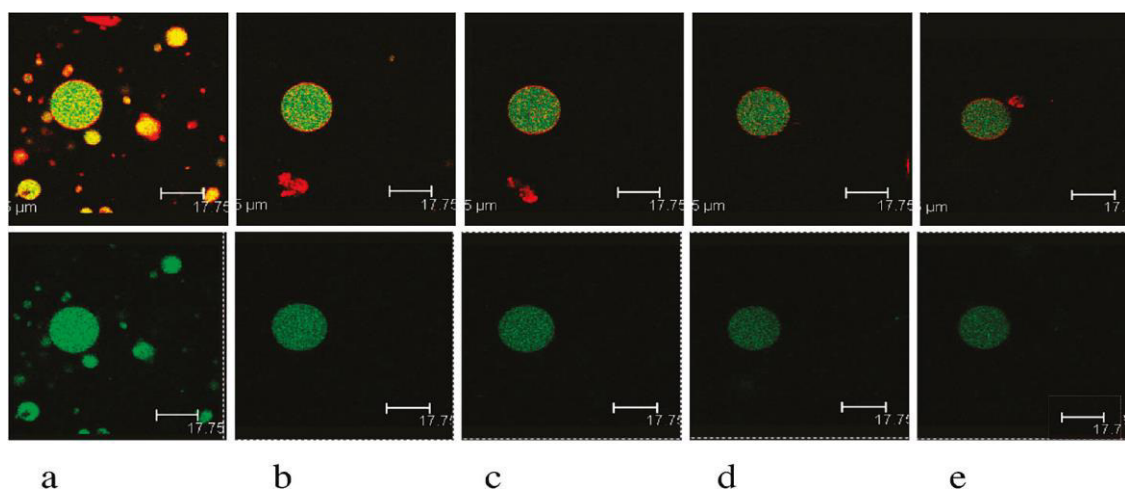


Figure 1.13. CLSM images of Alexa-loaded magnetic GUVs over time [adapted from Nappini *et al.* 2011].¹⁶⁶ **First line:** Alexa is colored in green, and magnetic nanoparticles in red (a) in the absence of AMF at time zero, (b) exposed for 15 min to 200 Hz AMF, and (c) 15 min after the field application. Magnetic GUVs again exposed to 200 Hz AMF for (d) 15 min and (e) 15 min after the last field application. **Second line:** CLSM pictures obtained by removing the nanoparticle fluorescent contribution from the first line pictures.

Thus, for drug delivery applications, magnetic GUVs are more promising than the nonmagnetic ones, as they can improve the release of encapsulated compounds. However, to be suitable for biomedical applications, magnetoliposomes should be small (100-200

nm) and, at this range, the characterization of magnetoliposomes become more difficult because of the physical constraints of light (the *diffraction limited* in optical microscopy). Thus, other techniques have been used to characterize small magnetoliposomes.¹⁴⁸ For instance, for structural investigation at the nanoscale, the most used are DLS,^{167,168} small angle X-ray scattering (SAXS)¹⁵⁷ and neutron scattering (SANS)¹⁵⁹. Nonetheless, and at this range, electron microscopy has been widely used in the context of the visualization of small magnetoliposomes. Conventional TEM technique requires a high vacuum environment which is highly destructive for any water based system. Thus, it is only suitable for SMLs which do not present an inner aqueous phase.^{169,170} Yet, it is possible to use this technique for AMLs if they are preserved, for instance, by chemical fixation or sample drying. However, many structural changes occur during these processes and the result images could not correspond to the AMLs original structure. A more suitable microscopy technique for the visualization of small aqueous magnetoliposomes in their original state is cryogenic TEM. With this technique, the magnetoliposomes structure is preserved in a layer of vitreous ice, keeping them safe from drying effects or the vacuum during visualization.¹⁴⁸ So, concerning the structural characterization of magnetoliposomes, all the above-mentioned methodologies have their own pros and cons. Therefore, a well-balanced combination of different techniques is required to obtain information about magnetoliposomes structure.

Regarding magnetoliposomes magnetism, it is important to assess the magnetic properties to confirm the superparamagnetic state of the system, as well as to understand which structures possess the larger magnetization. Recent studies have shown that SMLs¹⁶⁰ present better magnetic properties, as they keep almost the same magnetic properties as the neat nanoparticles, while AMLs¹⁶¹ display poor magnetic characteristics, similar to those of the aqueous ferrofluid. In fact, for AMLs, even if magnetic nanoparticles are superparamagnetic, the other components should induce a strong decrease of the maximum saturation magnetization, as both water and lipids are diamagnetic and the ratio between NPs and lipid + water is small. On the other hand, for SMLs, the contribution of the diamagnetic lipids is almost negligible (because the ratio between NPs and lipid is much larger than in AMLs), and as the cluster of magnetic nanoparticles favors interparticle magnetic interaction, the magnetic moments alignment is favored.

3.4.2 Magnetic controlled chemotherapy

Most of the anticancer drugs used in chemotherapy are severely toxic and cause systemic side effects. In drug delivery, magnetoliposomes are very promising because they can protect and transport drugs to the therapeutic sites of interest, by means of external magnetic field gradients. A comparison of drug biodistribution between conventional chemotherapy and magnetic controlled chemotherapy is represented in figure 1.14. With this therapeutic approach, a safer use of powerful, however toxic, anticancer drugs is accomplished.

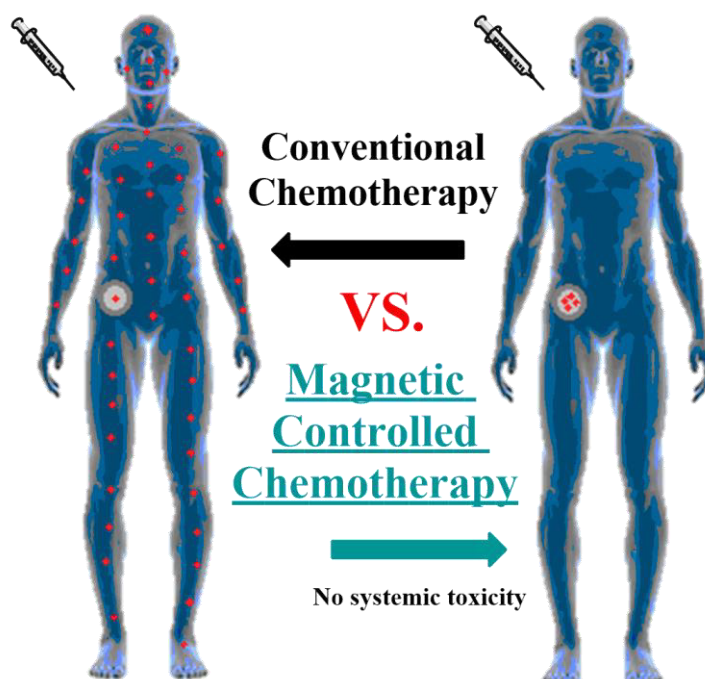


Figure 1.14. Schematic comparison between conventional chemotherapy and magnetic controlled chemotherapy.

The use of drug-loaded magnetoliposomes is an alternative approach to conventional chemotherapy that originates an improved treatment. Magnetic guided drug delivery involves four important steps:¹⁷¹

1. Drug loading into magnetoliposomes;
2. Injection of the magnetoliposomes; either intravenous or intra-arterial;
3. Magnetoliposomes guidance and accumulation in the treatment area using high-gradient external magnetic fields. Such fields are generated by rare-

earth permanent magnets, generally NdFeB magnets with a very high surface flux density;

4. Triggered drug release, induced by environmental changes.

With this approach, the uptake of the drug by tumor cells at the target sites is increased¹⁷² and systemic drug concentration is avoided¹⁷³. Thus, a more efficient treatment is accomplished and lower drug dosages can be used.

Magnetoliposomes flow in blood is regulated by the magnetic forces that act on magnetic nanoparticles in circulation, as a result from the applied external magnetic field. The magnetic fluid is localized in the site of interest when magnetic forces are exerted on the linear blood flow of the arteries or capillaries.¹⁶⁴ As it was already mentioned, the saturation magnetization of nanoparticles is very important for their application. In fact, the magnetic force of attraction that can be exerted on magnetoliposomes by the external field is proportional to the saturation magnetization of superparamagnetic nanoparticles, and is given by equation 1.8,¹⁷¹

$$\vec{F}_m = V(\vec{M}_s \cdot \nabla)\vec{B} \quad (1.8)$$

where F_m is the magnetic force of the nanoparticle, V the particle volume and B the magnetic field intensity.

After accumulation of magnetoliposomes in the area of interest, drug release can be triggered by physicochemical variations of the microenvironment, such as temperature or pH, depending on the functionalization of magnetoliposomes. So, besides physical and magnetic properties, surface functionalization is also important and compromises the efficacy of the magnetically-guided drug delivery. Furthermore, treatment efficacy can also be influenced by the external magnetic field geometry, strength and duration, as well as the injection route. Such parameters depend on the patient physiology, as body weight, blood volume, cardiac output, peripheral resistance of the circulatory system and organ function.¹⁷⁴ Recently, many efforts have been done to demonstrate the potentialities of magnetic controlled chemotherapy.

A comparative study between liposomes and magnetoliposomes loaded with paclitaxel (FDA approved cancer chemotherapeutic agent) were carried out by Zhang and coworkers.¹⁷⁵ In this study, the pharmacokinetics, *in vivo* distribution and cytotoxicity of the anticancer drug were investigated. An evident higher antitumor efficiency was observed for the formulation of paclitaxel loaded in magnetoliposomes, with a higher

drug distribution localized in the tumor tissues than in plasma, heart liver, spleen, lung, and kidney tissues. Additionally, they showed that, under the influence of an external magnetic field, the magnetoliposomes reached the peak concentration very quickly, attaining 19.85 μg of drug per g of mice weight at $\frac{1}{4}$ h.¹⁷⁵

One of the most challenging tumors to treat is the brain tumor, because of the difficulty to cross the blood brain barrier (BBB). In this context, magnetoliposomes seem also to be a promising therapeutic approach. The transmigrability of magnetoliposomes over a BBB model (composed of human brain sourced primary cells) was evaluated by Ding and collaborators. For that purpose, a BBB specific transporter that allows transferrin to attach and cross the BBB membrane,¹⁷⁶ was embedded onto the magnetoliposome surface and transmigration was evaluated for nanocarriers with and without transferrin receptor in the presence of magnetic forces (guided delivery). The results evidenced that, by means of magnetic forces and transferrin receptor-mediated transportation, 50 to 100% higher transmigration was obtained.¹⁷⁷ Still regarding the treatment of brain tumors, very good *in vivo* results were obtained in a study using cationic magnetoliposomes loaded with paclitaxel, that showed 5-15 fold higher concentration in rats brain, when magnetic controlled drug delivery was used.¹⁷⁸

Although *in vitro* and *in vivo* investigations have already shown encouraging results for the use of magnetoliposomes in magnetic controlled drug delivery, the effectiveness of the therapy is limited from the physical point of view. Most of the promising results were obtained on small animals. Moreover, the problem of magnetic targeting currently on investigation is related with the guidance of magnetic particles to deeper tissues, as needed in humans, where the sites of interest are farther away from the magnet source. As it is known, the magnetic field forces decay rapidly with distance, by a factor of $1/r^a$ (with, $2 \leq a \leq 5$, depending on external field geometry).¹⁷⁹ Thus, the application of magnetoliposomes in magnetic controlled chemotherapy is limited to relatively shallow targets in the human body. Although rare-earth NdFeB magnets achieves a 10-15 cm penetration depth,¹⁸¹ this is not enough for human deep tissues applications. Recent studies have been carried out in order to find a perfect geometry for a deeper tissue penetration of the field.¹⁸² For instance, a clinical MRI scanner that steers and tracks magnetic carriers in real time was upgraded by inserting steering coils, and the high magnetic field of the equipment (1.5 T) enables the magnetic material to be fully magnetized throughout the body, even in deep tissues.¹⁸³

3.4.3 *Hyperthermia*

Hyperthermia is a type of therapy in which body tissues are exposed to toxic amounts of thermal energy.¹⁸⁴ This is a very old idea with more than 5000 years old and first known in a written medical report from the ancient Egypt.¹⁸⁵ This is not surprising, as our natural body response to pathogens is fever. However, past technologies could not deliver effective and homogeneous heating to all sites, particularly to deep tissues. So, just recently, with improved technologies, more attention has been paid to hyperthermia. In 2013, in USA and Europe, there were more than 350 ongoing clinical trials that incorporate hyperthermia as part of the treatment.¹⁸⁶

The success of this type of therapy in cancer treatment is related to a characteristic physiological difference between normal and tumor cells. Tumor cells are more sensitive to high temperatures than healthy ones, as the poor vasculature leads to a differential heating, with higher temperatures being achieved in tumors compared to normal tissues, where heat may be dissipated by the circulating blood. Another important feature of hyperthermia in cancer therapy is that it kills cells most efficiently at low pH and hypoxic environment, as occurs in the tumor core. This is a tumor region relatively resistant to chemotherapy because it is exposed to lower concentrations of drug.¹⁸⁷

Hyperthermia induces cell death by apoptosis and/or necrosis.^{188,189} However, in dual therapy (chemotherapy/hyperthermia), the heat-induced drug cytotoxicity mechanism remains not well known. Yet, several studies suggest that it can be related to cell membrane permeability, inhibition of DNA-repair and acceleration of the cytotoxic chemical reactions at high temperatures.¹⁹⁰ Different lethal cellular changes can be induced by thermal treatment (figure 1.15). For instance, cells can suffer from mitotic catastrophe, permanent G1 (phase one of cell cycle division) arrest, and loss of clonogenic or reproductive cell capacity.¹⁹¹ Moreover, it has been demonstrated that heat may increase the production of reactive oxygen species (ROS) as a consequence of the enhancement of biochemical reactions and cell metabolism.^{192,193}

Hyperthermia efficacy is strongly dependent on the temperature generated at the target site, exposure time and tumor characteristics.¹⁹⁴ Depending on the type of heating, hyperthermia can be categorized into local, regional and whole body. For local hyperthermia, heat is induced only in the tumor, while for regional hyperthermia heat is induced in a larger area, such as whole tissue or organ. On the other hand, whole body hyperthermia is applied throughout the body and is used to treat metastatic cancer cells. Moreover, depending on the range of heat, hyperthermia can be classified as:¹⁹⁵

- ✓ Ablation hyperthermia – for high temperatures $> 46^{\circ}\text{C}$ (up to 56°C). Induce cells necrosis, coagulation or carbonization.
- ✓ Moderate hyperthermia – for moderate temperature ($41^{\circ}\text{C} < T < 46^{\circ}\text{C}$). Induce lethal effects both at cellular and tissue levels.
- ✓ Diathermia - for lower temperature ($T < 41^{\circ}\text{C}$). Used for rheumatic treatment in physiotherapy.

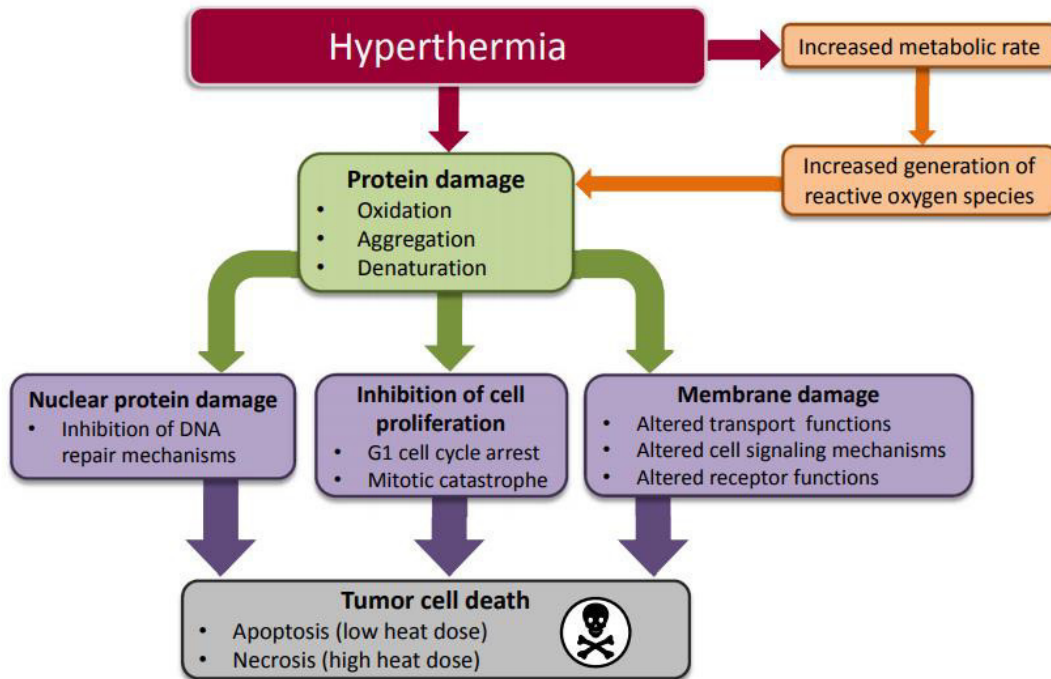


Figure 1.15. Cellular changes induced by hyperthermia that lead to tumor cell death (apoptosis and/or necrosis) [adapted from Bettaieb *et al.* 2013].¹⁸⁷

3.4.3.1 Magnetic Hyperthermia

Many approaches involving laser, ionizing radiation and microwaves have been used to apply hyperthermia in cancer treatment. However, these techniques can cause side effects, like ionization of genetic material or lack of selectiveness in radiation and microwaves therapies.¹⁹⁶ In this context, hyperthermia based on magnetic nanoparticles provides a novel solution to this problem. It allows to remotely induce a local temperature increase through the magnetic energy loss of magnetic nanoparticles, under an AC external magnetic field. Here, the inductive heating property of nanoparticles, under an AC magnetic field, can be controlled by the magnetic properties, as heating is inversely related to the coercive field and directly proportional to the saturation magnetization.¹⁹⁷ Moreover, activation of the nanoheaters (magnetic nanoparticles) can be controlled by

the external field and the temperature increase occurs mainly in well-defined tumor regions, without damaging healthy tissues. The electromagnetic radiation used in this type of hyperthermia is in the radio-frequency range (between several kHz and 1 MHz), that is nontoxic and allows high penetration in deeper tissues.¹⁹⁸ Nevertheless, a study of a whole-body exposure to a higher radio frequency of 220 MHz showed that human body can tolerate the heat by sweating.¹⁹⁹

Under an AC magnetic field, the moments of superparamagnetic nanoparticles randomly flip the magnetization direction between the parallel and antiparallel spin orientation. This random orientation converts magnetic energy loss into thermal energy. Hyperthermia heating effect of magnetic nanoparticles under an AC magnetic field results from several mechanisms of energy loss that occur during magnetization relaxation, such as hysteresis loss and Néel and Brown relaxations. The relative contribution of each process depends on particle size. Superparamagnetic nanoparticles (size < 30 nm) generate heat by physical rotation of the nanoparticles in fluid (Brownian relaxation) and by rotation of the atomic magnetic moment within the particles themselves (Néel relaxation).²⁰⁰

The efficiency of a given material to generate heat under an AC magnetic field is measured in terms of specific absorption rate (SAR). This is a key parameter that determines heating generation in the tissue and describes the amount of magnetic energy converted into heat per time and mass. The SAR is proportional to the rate of temperature increase, for the adiabatic case, and is expressed in Watt per kilogram (equation 1.9)

$$SAR = 4.1868 \frac{P}{m_e} = C_e \frac{dT}{dt} \quad (1.9)$$

where P is the electromagnetic wave power absorbed by the sample, m_e is the mass of the sample, and C_e is the specific heat capacity of the sample.²⁰¹ High specific absorption rate is preferred for hyperthermia, as it implies a lower exposure time and also lower dosages to be administered to the patient.

For a given superparamagnetic material, the SAR is very precisely determined by the volume ratio of magnetic nanoparticles in the tissue. Rosensweig showed that SAR in a uniform magnetic field only depends upon the nature and the volume fraction of the superparamagnetic particles according to equation 1.10,²⁰²

$$SAR = 4.1868 \pi \mu_0^2 \frac{\phi M_s^2 V}{10000 K_\mu T} H_0^2 v \frac{2\pi v \tau}{1+(2\pi v \tau)^2} \quad (1.10)$$

where V is the crystal volume, K_{μ} the anisotropy constant, T the temperature, φ the volume fraction of superparamagnetic material, M_s the saturation magnetization, ν the frequency of the AC magnetic field, H_0 is the magnetic field intensity and τ is the relaxation time.²⁰² If the AC magnetic field interacts with intracellular ions, Eddy currents can be formed, leading to a significant heating in normal tissues. This way, normal cells can be damaged, so a limit must be imposed. As SAR is directly proportional to the frequency and magnitude of the applied field, in order to avoid any damaging of healthy tissues, $H_0\nu$ factor should not exceed a value that was estimated as $5 \times 10^9 \text{ Am}^{-1}\text{s}^{-1}$.^{203,204}

The use of magnetic materials as hyperthermia agents date back to 1957, when Gilchrist and his group heated various tissue samples with maghemite materials exposed to a 1.2 MHz magnetic field.²⁰⁵ Since then, several research groups have reported encouraging results using magnetic nanoparticles as hyperthermia agents and numerous publications describing a variety of different types of magnetic materials have been published.

The use of magnetoliposomes for hyperthermia is very promising as the encapsulation of the nanoheaters into liposomes improves their efficacy *in vivo*. The inclusion of targeting ligands for specifically target cancer cells, as in drug delivery, can also provide a better local heating.²⁰⁶ Cancer cells membrane contains more anionic lipids than the one of normal cells, leading to a higher overall negatively-charged cell surface.²⁰⁷ Thus, cationic magnetoliposomes have shown to be a favorable approach for hyperthermia, because the electrostatic interactions favor the accumulation of magnetic nanoparticles in tumor cells. This fact was demonstrated by Kobayashi and co-workers in animals with several types of tumors.²⁰⁸ For that purpose, cationic magnetoliposomes containing 3 mg/tumor of Fe_2O_3 were directly injected into solid tumors and the animals were irradiated several times for 30 minutes, with an AC magnetic field of 118 kHz. The results showed an evident decrease in the volume of tumors with tumor regression in 96% of the animals.²⁰⁸

Interestingly, antitumor immune activity has been observed in magnetic hyperthermia treatment. Yanase *et al.* have shown effective regression of tumor volume, not only in the tumor under an AC magnetic field, but also in non-exposed tumors in experiments with models of T-9 rat glioma. This behavior resulted from the migration of natural killer cells and CD8^+ and CD4^+ T-cells (CD4^+ T cells are essential in the formation of protective memory CD8^+ T cells, that are very important for immune defense against intracellular pathogens and for tumor surveillance), not only into the

heated tumor, but also into the tumors without thermal treatment.²⁰⁹ Also, tumor-specific immune response can be induced by heat shock proteins that are highly expressed within and around tumors.²¹⁰ Thus, magnetic hyperthermia is indeed a promising tool for cancer treatment, as it can also induce biological responses, being able to kill tumors located far from hyperthermia incidence, such as metastatic cancer cells.

3.4.4 Synergistic thermo/chemotherapy

The joint use of magnetic hyperthermia and drug delivery has a large potential in the treatment of cancer, mainly because the local temperature increase could enhance cytotoxicity of chemotherapeutic drugs. In fact, several studies have shown an increased cytotoxic behavior of many anticancer drugs when a combination of hyperthermia and chemotherapy is used.^{190,211-213} In this type of combined therapy, the best capacities of individual therapies are utilized, as well as their synergistic effects, improving treatment efficacy. Moreover, another advantage in the use of combined therapy relies on the fact that tumors core is less vascularized and, therefore, drugs are not equally distributed, with a lack of drug delivery being observed in the tumor core. With combined hyperthermia, this undesirable effect is offset because high temperatures are more efficiently achieved in the tumor core, due to the less efficient cooling by blood circulation. Furthermore, in tumor regions with better vascular permeability (tumor shell), mild hyperthermia between 40 – 43° C results in a better blood supply and, so, drug uptake is also improved in these regions.²¹⁴

In drug delivery, high magnetic field gradients are required to a proper control of the magnetic nanoparticles position and AC magnetic fields are responsible for the hyperthermia effect. Heat production under AC magnetic field is proportional to the frequency of the field, and so high frequencies give rise to a larger heating effect. However, this can be a safety problem because Eddy currents can be generated, leading to non-specific heating that can damage both healthy and cancer tissues. With combined therapy, drug cytotoxicity enhancement occurs at mild hyperthermia temperatures and, so, combined therapy does not require temperatures as high as those for hyperthermia alone (~ 43° C or higher).²¹⁴ Therefore, the SAR for combined therapy does not need to be that high and lower frequencies and amplitudes of the external fields could be used. Mild hyperthermia is easy, safe and cost-effective, and can be practically performed at any medical facility.

In this context, magnetoliposomes are versatile nanosystems suitable for combined therapy, as the local temperature increase originated by the hyperthermic effect can trigger the fast and improved release of encapsulated anticancer drugs in target sites. Thus, the therapeutic efficiency is improved due to simultaneous application of hyperthermia and drug delivery. Several research groups have already performed some studies with encouraging results for combined therapy with magnetoliposomes.

The efficacy of hyperthermia and chemotherapy alone or combined was evaluated by Itoh and his team.²¹⁵ In this study, the enhancement of cisplatin and adriamycin cytotoxicity in human bladder cancer cell line was evaluated. Alone, mild hyperthermia (~ 41° C) and chemotherapy with low drug concentration (20 µg/mL of cisplatin or 4 µg/mL of adriamycin) revealed an unsuccessful treatment. But, when combined therapy was used, the efficacy of treatment was significantly higher, so efficient as the use of 10 times the concentration of cisplatin (200 µg/mL).²¹⁵ Moreover, it was also demonstrated that drug dosage can be reduced, therefore decreasing side effects of therapy.²¹⁵ Another study has shown that magnetoliposomes based on magnetite nanoparticles loaded with paclitaxel are promising for combined chemotherapy and hyperthermia. Here, *in vitro* cytotoxicity studies were performed in HeLa cell lines, under an AC magnetic field of 10 kA/m intensity and 432 kHz frequency. When combined therapy was applied to magnetoliposomes with 100 nM paclitaxel, 89% of the tumor cells were killed.²¹⁶ More recently, Hardiansyah and coworkers reported that doxorubicin loaded aqueous magnetoliposomes containing citric-acid coated magnetite nanoparticles for integrated application of chemotherapy and magnetic hyperthermia (drug concentration of 1 µM and high-frequency AC magnetic field) are effective against colorectal cancer cells.²¹⁷ Concerning the applied magnetic field characteristics, better results were obtained for magnetoliposomes based on cobalt ferrite nanoparticles that showed a better release of the encapsulated dye carboxyfluorescein under low-frequency AC magnetic field.²¹⁸

The regression of bladder cancer *in vivo* obtained from synchronizing hyperthermia and chemotherapy was evaluated in a comparative study by Li and coworkers. For that purpose, they used a magnetite-based system loaded with 500 mg/mL of the drug 5-fluorouracil (5-FU) functionalized with anti-human epidermal growth factor receptor 2 (anti-HER2) antibody for cancer cell-specific targeting.²¹⁹ The nanosystem was injected in tail vein (1 dose per day for 4 days) and phosphate-buffered saline (PBS) was used as a control. For combined therapy, the rats were exposed to 1.3 MHz radio frequency (RF) for 15 minutes, 24 hours after injection. Compared with PBS control

group, use of drug only and no RF-induced hyperthermia treatment, a significant tumor regression was observed for combined therapy (figure 1.16). Moreover, the histopathologic evaluation showed no detectable pathological findings in major organs.²¹⁹ In this study, very good results were reported using RF as source of the alternating magnetic field. Yet, advanced studies must be performed using lower frequencies as sources for AC magnetic field, to make a safe use of magnetic nanoparticles in mild hyperthermia.

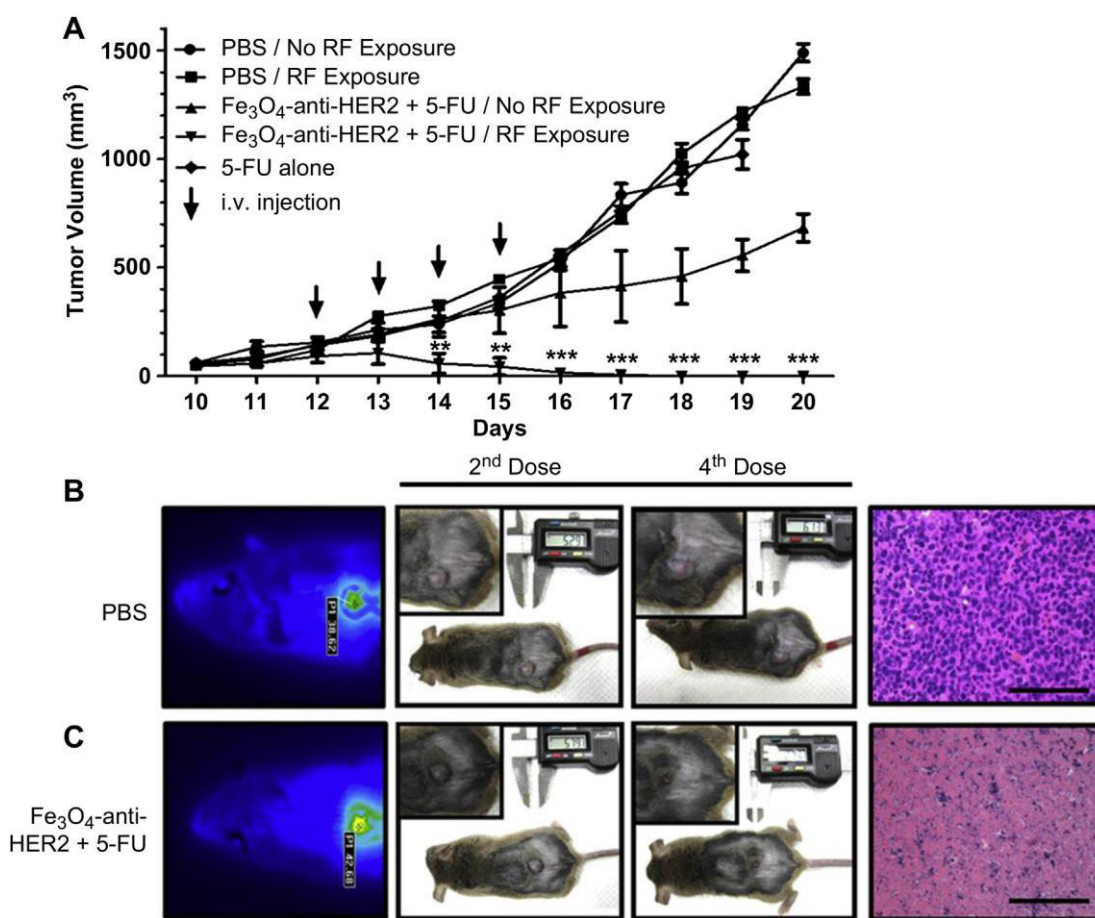


Figure 1.16. Comparative study of plain chemotherapy with its combination with RF induced hyperthermia [adapted from Li *et al.* 2013].²¹⁹ **A:** Tumor volume evolution in time. Tumor image and size and histopathologic evaluation - **B:** PBS control group. **C:** Combined hyperthermia and chemotherapy.

4. References

1. <http://www.marketsandmarkets.com/search.asp?Search=smart+pills&x=0&y=0>; accessed: May 2017.
2. Ferlay, J., Soerjomataram, I., Ervik, M., Dikshit, R., Eser, S., Mathers, C. *Cancer Incidence and Mortality Worldwide: GLOBOCAN 2012 v1.0*, IARC CancerBase No. 11 Lyon, France: International Agency for Research on Cancer, 2013.
3. Timko, B. P., Whitehead, K., Gao, W., Kohane, D. S., Farokhzad, O., Anderson, D. Langer, R., *Annu. Rev. Mater. Res.* **41** (2011) 1-20.
4. Kuznetsov, A. A., Harutyunyan, A. R., Dobrinsky, E. K., *Scientific and Clinical Applications of Magnetic Carriers*, Plenum Press, New York, 1997.
5. Kuznetsov, A. A., Filippov, V. I., Kuznetsov, O. A., Gerlivanov, V. G., Dobrinsky, E. K., Malashin, S. I., *J. Magn. Magn. Mater.* **194** (1999) 22-30.
6. Reszka, R., Beck, P., Fichtner, I., Hentschel, M., Richter, J., Kreuter, J., *J. Pharmacol. Exp. Ther.* **280** (1997) 232-237.
7. Van der Veldt, A. A. M., Hendrikse, N. H., Smit, E. F., Mooijer, M. P. J., Rijnders, A. Y., Gerritsen, W. R., Van der Hoeven, J. J. M., Windhorst, A. D., Lammertsma, A. A., Lubberink, M., *Eur. J. Nucl. Med. Mol. Imaging* **37** (2010) 1950-1958.
8. Perry, M., *The chemotherapy Source Book*, 2nd edition, Williams & Wilkins, Baltimore, 1996.
9. Lasic, D.D., Papahadjopoulos, D., *Science* **267** (1995) 1275–1276.
10. Pradhan, P., Giri, J., Rieken, F., Koch, C., Mykhaylyk, O., Döblinger, M., Banerjee, R., Bahadur, D., Plank, C., *J. Control. Release* **142** (2010) 108-121.
11. Li, F., Sun, J., Zhu, H., Wen, X., Lin, C., Shi, D., *Colloids Surf. B: Biointerfaces* **88** (2011) 58-62.
12. Mitsumata, T., Honda, A., Kanazawa, H., Kawai, M., *J. Phys. Chem. B* **116** (2012) 12341-12348.
13. <http://www.britishsocietynanomedicine.org/what-is-nanomedicine.html>; accessed: May 2017.

14. Queiroz, M.-J. R. P., Peixoto, D., Calhelha, R. C., Soares, P., Santos, T., Lima, R. T., Campos, J. F., Abreu, R. M. V., Ferreira, I. C. F. R., Vasconcelos, M. H., *Eur. J. Med. Chem.* **69** (2013) 855-862.
15. Machado, V. A., Peixoto, D., Queiroz, M.-J., Soares, R., *J. Cell. Biochem.* **117** (2016) 2791–2799.
16. Queiroz, M.-J. R. P., Calhelha, R. C., Vale-Silva, L. A., Pinto, Nascimento, E. M. S.-
J. Eur. J. Med. Chem. **45** (2010) 5732.5738.
17. Costa, C. N. C., Hortelão, A. C. L., Ramos, J. M. F., Oliveira, A. D. S., Calhelha, R. C., Queiroz, M.-J. R. P., Coutinho, P. J. G., Castanheira, E. M. S., *Photochem. Photobiol. Sci.* **13** (2014) 1730-1740.
18. Bozzuto, G., Molinari, A., *Int. J. Nanomedicine* **10** (2015)10 975–999.
19. Akbarzadeh, A., Rezaei-Sadabady, R., Davaran, S., Joo, S. W., Zarghami, N., Hanifehpour, Y., Samiei, M., Kouhi, M., Nejati-Koshki, K., *Nanoscale Res. Lett.* **8** (2013) 102-111.
20. Andresen, T. L., Jensen, S. S., Jorgensen, K., *Prog. Lipid Res.* **44** (2005) 68-97.
21. Ochekepe, N. A., Olorunfemi, P. O., Ngwuluka, N. C., *Trop. J. Pharm. Res.* **8** (2009) 265-274.
22. Poste, G., Cucana, C., Raz, A., Bugelski, P., Kirsh, R., Fidler, I. J., *Cancer Res.* **24** (1982) 1412-1422.
23. Mezei, M., Gulasekharam, V., *J. Pharm. Pharmacol.* **34** (1982) 473-474.
24. Juliano, R. L., *Trends Pharmacol. Sci.* **2** (1981) 39-42.
25. Alberts, B., Bray, D., Hopkin, K., Johnson, A., Lewis, J., Raff, M., Roberts, K., Walter, P., *Essential Cell Biology*, 2nd edition, Garland Science, 2004.
26. Tien, H T., Leitmannova, O., *Membrane Biophysics: As Viewed from Experimental Bilayer Lipid Membranes*, 1st Edition, Elsevier Science, Michigan, 2000.
27. Sahoo, S. K., Labhasetwar, V. *DDT* **8** (2003) 1112-1120.
28. Gabizon, A., Goren, D., Cohen, R., Barenholz, Y., *J. Control Release* **53** (1998) 275–279.
29. Allen, T. M., *Drugs* **54** (1997) 8–14.

30. Feitosa, E., Barreleiro, P. C. A., Olofson, G., *Chem. Phys. Lipids* **105** (2000) 201-213.
31. Lentz, B. R., *Chem. Phys. Lipids* **50** (1989) 171-190.
32. <https://avantilipids.com/tech-support/liposome-preparation/lipids-for-liposome-formation/>; accessed: May 2017.
33. Olsson, U., Wurz, U., Strey, R., *J. Phys. Chem.* **97** (1993) 4535-4539.
34. Lasic, D. D., *Biophys. J* **67** (1995) 1358-1362.
35. Lasic, D. D. *TIBTECH* **16** (1998) 220-227.
36. Huang, Z., *Asian Journal of Pharmaceutical Sciences* **9** (2014) 176-182.
37. Yu, B., Lee, R. J., Lee, L. J., *Methods Enzymol.* **465** (2009) 129–141.
38. Saunders, L., Perrin, J., Gammack, D., *J. Pharm. Pharmacol.* **14** (1962) 567-572.
39. Hope, M., Bally, M., Webb, G., Cullis, P. R., *BBA-Biomembranes* **812** (1985) 55-65.
Horsman, M. R., J. Overgaard., *Clin. Oncol. (R. Coll. Radiol.)* **19** (2007) 418-426.
40. Pradhan, P., Guan, J., Lu, D., Wang, P. G., Lee, L. J., Lee, R. J., *Anticancer Res.* **28** (2008) 943-947.
41. Palmer, A. F., Wingert, P., Nickels, J., *Biophys. J.* **85** (2003) 1233–1247.
42. Grabielle-Madelmont, C., Lesieur, S., Ollivon, M., *J. Biochem. Bioph. Meth.* **56** (2003) 189–217.
43. Moon, M. H., Giddings, J. C., Pharm, J., *J. Pharm. Biomed. Anal.* **11** (1993) 911–920.
44. Frederik, P. M., Hubert, D. H., *C Methods Enzymol.* **391** (2005) 431–448.
45. Ruozi, B., Belletti, D., Tombesi, A., *Int. J. Nanomedicine* **6** (2011) 557–563.
46. Jass, J., Tjärnhage, T., Puu, G., *Methods Enzymol.* **367** (1993) 199–213.
47. Sauer, M., Hofkens, J., Enderlein, J., *Handbook of Fluorescence Spectroscopy and Imaging*. Weinheim Wiley-VCH, 2011.
48. Valeur, B., *Molecular Fluorescence – Principles and Applications*, Wiley-VCH, Weinheim, 2001.

49. Wells, C. H., *Introduction to Molecular Photochemistry*, Chapman and Hall Ltd., London, 1972.
50. Namdeo, M., Saxena, S., Tankhiwale, R., Bajpai, M., Mohan, Y. M., Baijai, S. K., *J. Nanosci. Nanotechnol.* **8** (2008) 3247-71.
51. Batista, C. M., Carvalho, C. M. B., Magalhães, N. S. S., *Braz. J. Pharm. Sci.* **43** (2007) 167-178.
52. Dandamudi, S., Campbell, R. B., *Biochem. Biophys. Res. Commun.* **3** (2007) 427-438.
53. Jain, S., Mishra, V., Singh, P., Dubey, P. K., Saraf, D. K., Vyas, S. P., *Int. J. Pharm.* **261** (2003) 43-55.
54. Zhao, W., Zhuang, S., Qi, X. R., *Int. J. Nanomed.* **6** (2011) 3087-3098.
55. Alexis, F., Pridgen, E., Molnar, L. K., Farokhzad, O. C., *Mol. Pharm.* **5** (2008) 505-515.
56. Lv, H., Zhang, S., Wang, B., Cui, S., Yan, J., *J. Control. Release* **114** (2006) 100-109.
57. Dai, Z., *Advances in Nanotheranostic I: Design and Fabrication of theranostic nanoparticles*, Springer, Beijing, 2016.
58. Danhier, F., Feron, O., Pr at, V., *J. Control Release.* **148** (2010)135-46.
59. Sawant, R. R., Torchilin, V. P., *AAPS J.* **14** (2012) 303-15.
60. Damen, J., *Biochim. Biophys. Acta* **665** (2005) 538-545.
61. Toniolo, C., Crisma, M., Formaggio, F., Peggion, C., Monaco, V., Goulard, C., Rebuffat, S., Bodo, B., *J. Am. Chem. Soc.* **118** (1996) 4952-4958.
62. Crisma, M., Barazza, A., Formaggio, F., Kaptein, B., Broxterman, B. Q., Kamphuis, J., Toniolo, C., *Tetrahedron* **57** (2001) 2813-2825.
63. Senior, J., *FEBS Lett.* **145** (1982) 109-114.
64. Sharma, A., *International Journal of Pharmaceutics*, **154** (1997) 123-140.
65. Gabizon, A., Catane, R., Uziely, B., Kaufman, B., Safra, T., Cohen, R., *Cancer Res.* **54** (1994) 987-992.

66. Gabizon, A., Chisin, R., Amselem, S., Druckmann, S., Cohen, R., Goren, D., *Br. J. Cancer* **64** (1991) 1125–1132.
67. Illés, E., Szekeres, M., Kupcsik, E., Tóth, I. Y., Farkas, K., Jedlovszky-Hajdú, A., Tombácz, E., *Colloids Surf. A Physicochem Eng. Asp.* **460** (2014) 429–440.
68. Veisoh, O., Gunn, J. W., Zhang, M., *Adv. Drug Deliv. Rev.* **62** (2010) 284–304.
69. Mishra, B., Patel, B. B., Tiwari, S., *Nanomed. Nanotechnol.* **6** (2010) 9–24.
70. Thong-On, B., Rutnakornpituk, B., Wichai, U., Rutnakornpituk, M., *J. Nanopart. Res.* **14** (2012) 953–965.
71. Milla, P., Dosio, F., Cattell, L., *Curr. Drug Metab.* **1** (2012) 105–119.
72. Klibanov, A. L., Maruyama, K., Torchilin, V. P., Huang, L., *FEBS letters* **268** (1990) 235–237.
73. Mori, A., Klibanov, A. L., Torchilin, V. P., Huang, L., *FEBS Lett.* **284** (1991) 263–266.
74. Santos, N., Allen, C., Doppen, A.-M., Anantha, M., Cox, K. A. K., Gallagher, R. C., Karlsson, G., Edwards, K., Kenner, G., Samuels, L., Webb, M. S., Bally, M. B., *Biochim. Biophys. Acta* **1768** (2007) 1367–1377.
75. Torchilin, V. P., *Nat. Rev. Drug. Discov.* **4** (2005) 145–160.
76. Elbayoumi, T. A., Torchilin, V. P., *Methods Mol. Biol.* **605** (2010) 1–27.
77. Zwicke, G. L., Mansoori, G. A., Jeffery, C. J., *Nano Rev.* **3** (2012) 4302–3412.
78. Hafez, I. M., Ansell, S., Cullis, P. R., *Biophys. J.* **79** (2000) 1438–1446.
79. Muthu, M. S., Kulkarni, S. A., Raju, A., Feng, S. S., *Biomaterials* **33** (2012) 3494–3501.
80. Malhi, S. S., Budhiraja, A., Arora, S., *Int. J. Pharm.* **432** (2012) 63–74.
81. Low, P. S., Henne, W. A., Doorneweerd, D. D., *Acc. Chem. Res.* **41** (2007) 120–129.
82. Elmi, M. M., Sarbolouki, M. N., *Int. J. Pharm.* **215** (2001) 45–50.

83. Chen, X., *Nanoplatfrom-Based Molecular Imaging*, 2nd edition, John Wiley & Sons Inc, New Jersey, 2011.
84. Freeman, M. W., Arrott, A., Watson, J. H. L., *J. Appl. Phys.* **31** (1960) 404-405.
85. Mornet, S., Vasseur, S., Gras, F., Duguet, E., *J. Mater. Chem.* **14** (2004) 2161-2175.
86. Cullity, B. D., *Introduction to Magnetic Materials*, Addison-Wesley, Philippines, 1972.
87. Gregoriadis, G., *Trends Biotechnol.* **13** (1995) 527-537.
88. Markides, H., Rotherham, M., El Haj, A. J., *J. Nanomater.* **2012** (2012) 1-11.
89. Chouly, C., Pouliquen, D., Lucet, I., Jeune, J. J., Jallet, P., *J. Microencapsul.* **13** (1996) 245–255.
90. Longmire, M., Choyke, P. L., Kobayashi, H., *Nanomedicine (Lond)* **3** (2008) 703–717.
91. Chatterjee, K., Sarkar, S., Rao, K. J., Paria, S., *Adv. Colloid. Interface. Sci.* **209** (2014) 8–39.
92. Law, W.-C., Yong, K.-T., Roy, I., Xu, G., Ding, H., Bergey, E. J., *J. Phys. Chem. C.* **112** (2008) 7972–7.
93. Sounderya, N., Zhang, Y., *Recent. Pat. Biomed. Eng.* **1** (2008) 34-42.
94. Thanh, N. T. K., Green, L. A.W., *Nano Today* **5** (2010) 213—230.
95. Choi, Y., Kim, K., Hong, S., Kim, H., Kwon, Y.-J., Song, R., *Bioconjug. Chem.* **22** (2011) 1576-1586.
96. Higuchi, Y., Oka, M., Kawakami, S., Hashida, M., *J. Control Release* **125** (2008) 131-136.
97. Lin, Y., Zhang, L., Yao, W., Qian, H., Ding, D., Wu, W., *ACS Appl. Mater. Interfaces* **3** (2011) 995-1002.
98. Kayal, S., Ramanujan, R. V., *J. Nanosci. Nanotechnol.* **10** (2010) 5527-5539.
99. Jafari, T., Simchi, A., Khakpash, N., *J. Colloid Interface Sci.* **345** (2010) 64-71.
100. Selvan, S. T., Tan, T. T. Y., Yi, D. K., Jana, N. R., *Langmuir* **26** (2009) 11631-11641.

101. Vibin, M., Vinayakan, R., John, A., Raji, V., Rejiya, C. S., Vinesh, N. S., *J. Nanoparticle Res.* **13** (2011) 2587-2596.
102. Mu, Q., Yang, L., Davis, J. C., Vankayala, R., Hwang, K. C., Zhao, J., *Biomaterials* **31** (2010) 5083-5090.
103. Patel, D., Kell, A., Simard, B., Deng, J., Xiang, B., Lin, H.-Y., *Biomaterials* **31** (2010) 2866-2873.
104. Morris, V. B., Sharma, C. P., *Int. J. Pharm.* **389** (2010) 176-185.
105. Bangs, L. B., *Pure Appl. Chem.* **68** (1996) 1873-1879.
106. Dong-Sik, B., Kyong-Sop, H., Adair, J. H., *J. Mater. Chem.* **12** (2002) 3117-3120.
107. Hardikar, V. V., Matijević, E., *J. Colloid Interface Sci.* **221** (2000) 133-136.
108. Josephson, L., Tsung, C. H., Moore, A., Weissleder, R., *Bioconjugate* **10** (1999) 186-191.
109. Laurent, S., Forge, D., Port, M., Roch, A., Robic, C., Vander, E., Muller, R. N., *Chem. Rev.* **108** (2008) 2064–2110.
110. Huang, D. M., Chung, T. H., Hung, Y., Lu, F., Wu, S.-H., Mou, C. Y., Yao, M., Chen, Y. C., *Toxicol. Appl. Pharmacol.* **231** (2008) 208-215.
111. Kim, T., Momin, E., Choi, J., Kim, T., Momin, E., Choi, J., Yuan, K., Zaidi, H., Kim, J., Park, M., Lee, N., McMahon, M. T., Quinones-Hinojosa, A., Bulte, J. W. M., Hyeon, T., Gilad, A. A., *J. Am. Chem. Soc.* **133** (2011) 2955-2961.
112. Fu, W., Yang, H., Chang, L., Li, M., Bala, H., Yu, Q., Zou, G., *Colloids and Surfaces A: Physicochem. Eng. Aspects* **262** (2005) 71–75
113. Mahmoudi, M., Sant, S., Wang, B., Laurent, S., Sen, T., *Adv. Drug Deliv. Rev.* **63** (2011) 24–46.
114. Fernández-Remolar, D. C., *Iron Oxides, Hydroxides and Oxy-hydroxides*, Encyclopedia of Astrobiology, 1268-1270, 2014.
115. Friák, M., Schindlmayr, A., Scheffler, M., *New J. Phys.* **9** (2007) 1-15.
116. Sharifi, I., Shokrollahi, H., Amiri, S., *J. Magn. Magn. Mater.* **324** (2012) 903-915.

117. Pereira, C., Pereira, A. M., Fernandes, C., Rocha, M., Mendes, R., Garcia, M. P. F., Guedes, A., Tavares, P. B., Grenèche, J.-M., Araújo, J. P., Freire, C., *Chem. Mater.* **24** (2012) 1496-1504.
118. Mathew, D. S., Juang, R.-S., *Chem. Eng. J.* **129** (2007) 51-65.
119. Vestal, C. R., Zhang, J. Z., *Int. J. Nanotechnol.* **1** (2004) 240–263.
120. Tomitaka, A., Hirukawa, A., Yamada, T., Morishit, S., Takemura, Y., *J. Magn. Magn. Mater.* **321** (2009) 1482–1484.
121. Khanna, L., Verma, N.K., *J. Magn. Magn. Mater* **336** (2013) 1-7.
122. Cabrera, L. I., Somoza, A., Marco, J. F., Serna, C. J., Morales, M. P., *J. Nanoparticle Res.* **14** (2012) 1-14.
123. Li, Z., Wang, S. X., Sun, Q., Zhao, H. L., Lei, H., Lan, M. B., Cheng, Z. X., Wang, X. L., Dou, S. X., Lu, G. Q. M., *Adv. Healthcare Mater.* **2** (2013) 958–964.
124. Baek, M. J., Park, J. Y., Xu, W., Kattel, K., Kim, H. G., Lee, E. J., Patel, A. K., Lee, J. J., Chang, Y., Kim, T. J., Bae, J. E., Chae, Lee, G. H., *ACS Appl. Mater. Interfaces* **2** (2010) 2949–2955.
125. Mozaffari, M., Behdadfar, B., Amighian, J., *IJPS.* **4** (2008) 115-118.
126. Lee, S. W., Bae, S., Takemura, Y., Yamashita, E., Kunisaki, J., Zurn, S., Kim, C. S., *IEEE Trans. Magn.* **42** (2006) 2833-2835.
127. Akbarzadeh, A., Samiei, M., Davaran, S., *Nanoscale Res. Lett.* **7** (2012) 144-157.
128. Baumgartner, J., Bertinetti, L., Widdrat, M., Hirt, A. M., Faivre, D., *Plos. one* **8** (2013) 57070-57076.
129. Issa, B., Obaidat, I. M., Albiss, B. A., Haik, Y., *Int. J. Mol. Sci.* **14** (2013) 21266-21305.
130. Altavilla, C., Ciliberto, E., *Inorganic Nanoparticles: Synthesis, Applications, and Perspectives*, CRC Press Taylor & Francis Group, New York, 2011.
131. Perez, J. A. L., Quintela, M. A. L., Mira, J., Rivas, J., Charles, S. W., *J. Phys. Chem. B* **101** (1997) 8045–8047.
132. Lee, Y., Lee, J., Bae, C. J., Park, J. G., Noh, H. J., *Adv. Func. Mater.* **2005** (2005) 15, 503–509.

133. Sjogren, C. E., Johansson, C., Naevestad, A., Sontum, P. C., Saebo, K. B., *Magn. Reson. Imaging*. **15** (1997) 55–67.
134. Teja, A. S., Koh, P-Y., *Prog. Cryst. Growth Ch.* **55** (2009) 22-45.
135. Bao, Y., Pakhomov, A. B., Krishnan, K. M., *J. Appl. Phys.* **99** (2006) 107-114.
136. Kumar, S., *J. Nanomed. Nanotechol.* **4** (2013) 130-132.
137. Indira, T. K., Lakshmi, P. K., *Int. J. Pharm. Sci. Nanotechnol.* **3** (2010) 1035-1042.
138. Ludbrook, B. M., *The magnetic properties of selected rare earth nitrides grown by pulsed laser deposition*, Master Thesis, Victoria University of Wellington, 2009.
139. Cohen, D, *IEEE Trans. Magnetics* **6** (1975) 694–700.
140. Kazakova, O., Webster, C., Tzalenchuk, A., Metrological challenges of nanomagnetism, Crown copyright, Hampton Road, 2005.
141. Sawicki, M., Stefanowicz, W., Ney, A., *Semicond. Sci. Technol.* **26** (2011) 64006-64022.
142. Schulz, D.L., Sailer, R.A., Caruso, A.N., Superparamagnetic Transition Metal Iron Oxygen Nanoparticles, US Patent No. 0194733, 2009.
143. Ludwig, F., Heim, E., Schilling, M., *J. Appl. Phys.* **101** (2007) 113909-112919
144. Du, Y., Lai, P T., Leung, C. H., Pong, P. W. T., *Int. J. Mol. Sci.* **14** (2013) 18682–18710.
145. Sattler, K.D., *Handbook of Nanophysics: Principles and Methods*, CCR Press, Boca Raton, 2010.
146. Seow, Y., Wood, M., *J. Mol. Ther.* **17** (2009) 767-777.
147. Medeiros, S. F., Santos, A.M., Fessi, H., Elaissari, A., *Int. J. Pharm.* **403** (2011) 139-161.
148. Monnier, C. A., Burnand, D., Rothen-Rutishauser, B., Lattuada, M., Petri-Fink, A., *Eur. J. Nanomed.* **6** (2014) 201–215.
149. Cuyper, M., Joniau, M., *Eur. Biophys. J.* **15** (1988) 311–319.

150. Nuytten, N., Hakimhashemi, M., Ysenbaert, T., Defour, L., Trekker, J., Soenen, S. J. H., Meeren, P. V., Cuyper, M., *Colloids Surf. B* **80** (2010) 227-231.
151. Tromsdorf, U. I., Bigall, N. C., Kaul, M. G., Bruns, O. T., Nikolic, M. S., Mollwitz, B., Sperling, R. A., Reimer, R., Hohenberg, H., Parak, W. J., Forster, S., Beisiegel, U., Adam, G., Weller, H., *Nano Lett.* **7** (2007) 2422-2427.
152. Weinmann, H.-J., Ebert, W., Misselwitz, B., Schmitt-Willich, H., *Eur. J. Radiol.* **46** (2003) 33-44.
153. Bothun, G. D., Lelis, A., Chen, Y., Scully, K., Anderson, L. E., Stoner, M. A., *Nanomedicine: NBM* **7** (2011) 797-805.
154. Skouras, A., Mourtas, S., Markoutsas, E., Goltstein, M.-C., Wallon, C., Catoen, S., Antimisariaris, S. G., *Nanomed Nanotech. Biol. Med.* **7** (2011) 572-579.
155. Beaune, G., Ménager, C., Cabuil, V., *J. Phys. Chem. B* **112** (2008) 7424-7433.
156. Bothun, G. D., Preiss, M. R., *J. Colloid Interface Sci.* **357** (2011) 70-74.
157. Bonnaud, C., Monnier, C. A., Demurtas, D., Jud, C., Vanhecke, D., Montet, X., *ACS Nano* **8** (2014) 3451-3460.
158. Amstad, E., Kohlbrecher, J., Müller, E., Schweizer, T., Textor, M., Reimhult, E., *Nano Lett.* **11** (2011) 1664-1670.
159. Floris, A., Ardu, A., Musinu, A., Piccaluga, G., Fadda, A. M., Sinico, C., *Soft Matter.* **7** (2011) 6239-6247.
160. Zhang, S., Niu, H., Zhang, Y., Liu, J., Shia, Y., Zhang, X., Cai, Y., *J. Chromatogr. A* **1238** (2012) 38-45.
161. García-Jimeno, S., Escribano, E., Queralt, J., Estelrich, J., *Int. J. Pharm.* **405** (2011) 181-187.
162. Pradhan, P., Giri, J., Banerjee, R., Bellare, J., Bahadur, D., *J. Magn. Magn. Mater.* **311** (2007) 208-215.
163. Lubbe, A. S., Bergemann, C., Brock, J., McClure, D. G., *J. Magn. Magn. Mater.* **194** (1999) 149-155.
164. Meledandri, C. J., Ninjbadgar, T., Brougham, D. F., *J. Mater. Chem.* **21** (2011) 214-222.

165. Nappini, S., Bonini, M., Ridi, F., Baglioni, P., *Soft Matter* **7** (2011) 4801-4811.
166. Nappini, S., Kayal, A. T., Berti, D., Nordèn, B., Baglioni, P., *J. Phys. Chem. Lett.* **2** (2011) 713–718.
167. Faria, M. R., Cruz, M. M., Gonçalves, M. C., Carvalho, A., Feio, G., Martins, M. B., *Int. J. Pharm.* **446** (2013) 183–190.
168. Garnier, B., Tan, S., Miraux, S., Bled, E., Brisson, A. R., *Contrast Media Mol. Imaging* **7** (2012) 231–239.
169. Qiu, D., An, X., Chen, Z., Ma, X., *Chem. Phys. Lipids* **165** (2012) 563–570.
170. Conde, A. J., Batalla, M., Cerda, B., Mykhaylyk, O., Plank, C., Podhajcer, O., *Lab. Chip.* **14** (2014) 4506–4512.
171. Estelrich, J., Escribano, E., Queralt, J., Busquets, M. A., *Int. J. Mol. Sci.* **16** (2015) 8070-8101.
172. Dobson, I., *Drug Dev. Res.* **67** (2006) 55–60.
173. Saiyed, Z., Telang, S., Ramchand, C., *Biomagn. Res. Technol.* **1** (2003) 2-9.
174. Widder, K. J., Senyei, A.E., Scarpelli, D.G., *Proc. Soc. Exp. Biol. Med.* **158** (1978) 141–146.
175. Zhang, J. Q., Zhang, Z. R., Yang, H., Tan, Q. Y., Qin, Q. Y., Qiu, X. L., *Pharm. Res.* **22** (2005) 573-583.
176. Hu, K., Li, J., Shen, Y., Lu, W., Gao, X., Zhang, Q., Jiang, X., *J. Control. Release* **134** (2009) 55-61.
177. Ding, H., Sagar, V., Agudelo, M., Pilakka-Kanthikeel, S., Atluri, V. S. R., Raymond, A., Nair, M. P., *Nanotech.* **25** (2014) 55-101.
178. Zhao, M., Chang, J., Fu, X., Liang, C., Liang, S., Yan, R., Li, A., *J. Drug. Deliv.* **20** (2012) 416-421.
179. Polyak, B., Fishbein, I., Chorny, M., Alferiev, I., Williams, D., Yellen, B., Friedman, G., Levy, R. J., *PNAS* **105** (2008) 698–703.
181. Goodwin, S., Peterson, C., Hoh, C., Bittner, C., *J. Magn. Magn. Mater.* **194** (1999) 132–139.

182. Mathieu, J. B., Martel, S., *Magn. Reson. Med.* **63** (2010) 1336–1345.
183. Pouponneau, P., Savadogo, O., Napporn, T., Yahia, L., Martel, S., *J. Biomater. Mater. Res. B Appl. Biomater.* **93** (2010) 203–211.
184. Nielsen, O. S., Horsman, M., Overgaard, J., *Eur. J. Can.* **37** (2001) 1587-1596.
185. Bryan, C. P., *Ancient Egyptian medicine: the Papyrus Ebers*, Ares Publishers, Chicago 1974.
186. Torres-Lugo, M., Rinaldi, C., *Nanomedicine (Lond)* **8** (2013) 1689–1707.
187. Bettaieb, A., Wrzal, P. K., Averill-Bates, D. A., *Hyperthermia: Cancer Treatment and Beyond, Cancer Treatment - Conventional and Innovative Approaches*, Letícia Rangel (Ed.), 2013.
188. Bettaieb, A., Averill-Bates, D. A., *Biochem. Cell Biol.* **86** (2008) 521-38.
189. Samali, A., Holmberg, C. I., Sistonen, L., Orrenius, S., *FEBS Lett.* **461** (1999) 306-310.
190. Issels, R. D., *Eur. J. Cancer.* **44** (2008) 2546-2554.
191. Sugahara, T., Van der Zee, J., Kampinga, H. H., Vujaskovic, Z., Kondo, M., Ohnishi, T., Li, G., Park, H. J., Leeper, D. B., Ostapenko, V., Repasky, E. A., Watanabe, M., Song, C. W., *Int. J. Hyperthermia* **24** (2008) 123-140.
192. Moriyama-Gonda, N., Shiina, H., Urakami, S., Wada, Y., Terashima, M., *Eur. Urol.* **38** (2000) 235-240.
193. Pallepati, P., Averill-Bates, D. A., *Free Radic. Biol. Med.* **50** (2011) 667-679.
194. Raaphorst, G. P., Freeman, M. L., Dewey, W. C., *Radiat. Res.* **79** (1979)390–402.
195. Kumar, C. S. S. R., Mohammad, F., *Adv. Drug Deliv. Rev.* **63** (2011) 789–808.
196. Chicheł, A., Skowronek, J., Kubaszewska, M., Kanikowski, M., *Rep. Pract. Oncol. Radiother.* **12** (2007) 267-275.
197. Li-Ying, Z., Yong-Hua, D., Ling, Z., Hong-Chen, G., *Chin. Phys. Lett.* **24** (2010) 483-486.

198. Bañobre-López, M., Teijeiro, A., Rivas, J., *Rep. Pract. Oncol. Radiother.* **18** (2013) 397–400.
199. Adair, E. R., Blick, D. W., Allen, S. J., Mylacraine, K. S., Ziriach, J. M., Scholl, D. M., *Bioelectromagnetics* **26** (2005) 448-461.
200. Shliomis, M. I. P. A. F., Morozov, K. I., Yu, S. I. J., *Magn. Magn. Mater.* **85** (1990) 85, 40-46.
201. Laurent, S., Dutz, S., Häfeli, U. O., Mahhmoudi, M., *Adv. Colloid Interface Sci.* **166** (2011) 8–23.
202. Rosensweig, R. E. J., *Magn. Magn. Mater.* **252** (2002) 370-374.
203. Hergt, R., Dutz, S., *J. Magn. Magn. Mater.* **311** (2007) 187–192.
204. Shubitidze, F., Kekalo, K., Stigliano, R., Baker, I., *J. Appl. Phys.* **117** (2015) 94302-94314.
205. Gilchrist, R. K., Medal, R., Shorey, W. D., Hanselman, R. C., Parrott, J. C., Taylor, C. B., *Ann. Surg.* **146** (1957) 596-606.
206. Escalona, M. M., Sáez-Fernández, E., Prados, J. C., Melguizo, C., Arias, J.L., *Int. J. Pharm.* **504** (2016) 11–19.
207. Chen, B., Le, W., Wang, Y., Li, Z., Wang, D., Ren, L., Lin, L., Cui, S., Hu, J. J., Hu, Y., Yang, P., Ewing, R. C., Shi, D., Cui, Z. *Theranostics* **6** (2016) 1887-1898.
208. Kobayashi, T., *Biotechnol. J.* **6** (2011) 1342–1347.
209. Yanase, M., Shinkai, M., Honda, H., Wakabayashi T., *Jpn. J. Cancer Res.* **89** (1998) 775–782.
210. Kobayashi, T., Ito, A., Honda, H., *Magnetic Nanoparticle-Mediated Hyperthermia and Induction of Anti-Tumor Immune Responses*, Hyperthermic Oncology from Bench to Bedside pp 137-150, 2016
211. Hildebrandt, B., Wust, P., Ahlers, O., Dieing, A., Sreenivasa, G., Kerner, T., Felix, R., Riess, H., *Crit. Rev. Oncol. Hematol.* **43** (2002) 33-56.
212. Dahl, O., *Recent Results Cancer Res.* **107** (1988) 157-169.
213. Bates, D. A., Mackillop, W. J., *Int. J. Radiat. Oncol. Biol. Phys.* **16** (1989) 187-91.

214. Rao, W., Deng, Z.-S., Liu, J., *Crit. Rev. Biomed. Eng.* **38** (2010) 101–116.
215. Itoh, Y., Yamada, Y., Kazaoka, Y., Ishiguchi, T., Honda, N., *Exp. Ther. Med.* **1** (2010) 319-323.
216. Kulshrestha, P., Gogoi, M., Bahadur, D., Banerjee, R., *Colloids Surf., B.* **96** (2012) 1-7.
217. Hardiansyah, A., Huang, L.-Y., Yang, M.-C., Liu, T.-Y., Tsai, S.C., Yang, C.-Y., Kuo, C.-Y., Chan, T.-Y., Zou, H.-M., Lian, W.-N., Lin, C.-H., *Nanoscale Res. Lett.* **9** (2014) article 497.
218. Nappini, S., Bombelli, F.B., Bonini, M., Norden, B., Baglioni, P. *Soft Matter.* **6** (2010) 154–162.
219. Li, T.-J., Huang, C.-C., Ruan, P.-W., Chuang, K.-Y., Huang, K.-J., Dhieh, D.-B., Yeh, C.-S., *Biomaterials* **34** (2013) 7873-7883.

Chapter 2

Results and discussion as a compilation of articles

2.1

Magnetoliposomes based on nickel/silica core/shell nanoparticles: Synthesis and characterization

Ana Rita O. Rodrigues, I. T. Gomes, Bernardo G. Almeida, J. P. Araújo, Elisabete M. S. Castanheira, Paulo J. G. Coutinho

Materials Chemistry and Physics **148** (2014) 978-987

INDEX

1. Abstract
2. Introduction
3. Experimental
4. Results and discussion
5. Conclusions
6. Acknowledgments
7. References

1. Abstract

In the present work, nickel magnetic nanoparticles with diameters lower than 100 nm, with and without silica shell, were synthesized by microheterogeneous templating. The magnetic properties of the nanoparticles show a typical ferromagnetic behavior with a coercive field of 80 Oe. Dry magnetoliposomes (DMLs) with diameter between 58 nm and 76 nm were obtained from the synthesis of nanoparticles in the presence of a lipid or surfactant layer, and aqueous magnetoliposomes (AMLs) were obtained by encapsulation of the nanoparticles in liposomes. FRET (Förster resonance energy transfer) experiments were performed to study the non-specific interactions between aqueous magnetoliposomes and giant unilamellar vesicles (GUVs), as models of cell membranes. It was possible to detect membrane fusion between GUVs and AMLs containing both NBD-C₆-HPC (donor) and the dye Nile Red (acceptor).

2. Introduction

Nanotechnology has produced significant advances in biomedicine, namely in diagnosis, therapy and bioengineering [1]. The potential of magnetic nanoparticles for biomedical applications has been recognized, as they offer major advantages due to their unique size and physicochemical properties [2].

Liposomes (nanosized vesicles made of amphiphilic phospholipid molecules in water) are biologically inert and weakly immunogenic, and have been described as ideal drug delivery systems [3-5]. This nanoencapsulation system can overcome many of the problems associated with other systems used for therapy, such as those involving solubility, pharmacokinetics, *in vivo* stability and toxicity [6,7]. Liposomes entrapping magnetic nanoparticles (magnetoliposomes) are of large importance in drug delivery, as they can be guided and localized to the therapeutic site of interest by external magnetic field gradients and used in cancer treatment by hyperthermia [8,9]. In diagnosis, magnetoliposomes have been proposed as T2 contrast agents (negative contrast enhancement) in MRI [10], while in therapy they have been used as a chemotherapy alternative through magnetic-controlled drug delivery and thermotherapy [11-13].

In biomedicine, nanoparticles with superparamagnetic behavior are preferred, as they exhibit a strong magnetization only when an external magnetic field is applied [5,14,15]. Iron and nickel nanoparticles are superparamagnetic when their size is smaller

than a critical value, 20 nm for iron [16] and 30 nm for nickel [17]. Due to the wide applications of magnetoliposomes, much attention has been paid to the synthesis of different kinds of magnetic nanoparticles [18-20] and liposomes [14,21-23], as each potential application requires specific properties.

Nickel exhibits magnetic properties at room temperature and, therefore, is considered a metal of biological interest. However, particles of nickel have some issues such as potential toxicity, high reactivity and easy degradation due to the high surface/volume ratio. In order to overcome these problems and make them compatible for biological applications, nickel magnetic nanoparticles are typically protected by coatings, such as gold or silica, forming a core-shell structure [18,24,25]. Silica is a particular beneficial coating for nanoparticles, since it can easily be functionalized and it is resistant to degradation within a cellular environment, whilst still being biocompatible [26,27]. In fact, previous studies have shown that internalized silica-coated magnetic nanoparticles are biocompatible with stem cells [26,27].

The synthesis methods of magnetoliposomes and their constituents will determine their final shape, size distribution, surface chemistry and magnetic properties [15,28]. Techniques for magnetic nanoparticle synthesis have been developed to yield nearly monodisperse colloids, consisting of uniform nanoparticles both in size and shape. In these systems, the entire uniform physicochemical properties directly reflect the properties of single particles [29,30].

In this work, both aqueous and dry magnetoliposomes, based on nickel nanoparticles or nickel/silica core/shell nanoparticles were prepared by several soft templating methods and characterized. The interaction between the prepared magnetoliposomes and models of cell membranes (giant unilamellar vesicles, GUVs) was also evaluated using FRET (Förster Resonance Energy Transfer). These studies are important for future drug delivery applications using magnetoliposomes as drug carriers.

3. Experimental

All the solutions were prepared using spectroscopic grade solvents and ultrapure water (Milli-Q grade).

3.1 Nickel nanoparticles preparation

Ni nanoparticles (NPs) were prepared using a Nickel chloride (Merck) stock solution (~0.2 M). For Ni²⁺ reduction, hydrazine monohydrate (N₂H₄.H₂O) 64-65% and

sodium hydroxide solution (NaOH, 50% in water), from Sigma-Aldrich, were used as received.

Citric acid (Merck) was added in some assays in a molar ratio 1:0.75, as it prevents nanoparticles aggregation and favours monodispersity [28].

3.1.1 Ni NPs in aqueous CTAB solution

CTAB (cetyltrimethylammonium bromide) was obtained from Sigma-Aldrich. Ni NPs were synthesized in an aqueous solution of this cationic surfactant, according to a procedure adapted from [31]. An aqueous solution of CTAB (0.025 M), nickel chloride (0.02 M) and trace acetone (10 μ L/ml) was first prepared. Then, 1 M of N_2H_4 and 10M NaOH solution were added in sequence. After 30 minutes at 60°C, Ni NPs were formed.

3.1.2 Ni NPs coated with lipid or double-chain surfactant

AOT (bis(2-ethylhexyl)sulfosuccinate) sodium salt from Sigma-Aldrich and DOPG (1,2-Dioleoyl-*sn*-glycero-3-[phospho-*rac*-(1-glycerol)]), from Avanti Polar Lipids, were used to control NPs size growth [32]. Ni NPs coated with a layer of AOT or DOPG molecules were synthesized by carrying out the reduction of nickel chloride in the presence of lipid/surfactant molecules. An experimental procedure previously described by Meledandri *et al.* [33] was followed. One fifth of the total DOPG amount (0.2 mM DOPG) was slowly added to a 1 mM nickel chloride aqueous solution under magnetic stirring, followed by the addition of 0.9 M N_2H_4 and 13 M NaOH to precipitate the nickel. After 5 minutes, the remaining DOPG (0.8 mM) was slowly added to the mixture. After about 20 minutes at 60°C, Ni NPs covered by a DOPG layer were obtained [33].

Ni NPs covered with an AOT layer were synthesized by a similar procedure using a 56 mM solution of AOT in methanol. After about 20 minutes, under vigorous magnetic stirring at 60°C, NPs were formed. After cooling, Ni NPs were washed by magnetic decantation with methanol/acetone (50/50 v/v) solution and dispersed in water.

3.1.3 NPs with silica shell

The synthesized NPs were covered with a silica shell obtained by TEOS (tetraethyl orthosilicate, from Sigma Aldrich) hydrolysis. Different shell sizes were achieved by the addition of different amounts of TEOS into a solution of nanoparticles dispersed either in AOT/cyclohexane (0.1 M) or in ethanol [34]. In the latter method,

MDA (mercaptododecanoic acid) was added to the particles in a 1:1 ratio to promote TEOS binding to the nanoparticles.

3.2 Preparation of magnetoliposomes

Aqueous magnetoliposomes (AMLs) are formed when the magnetic nanoparticles are encapsulated in liposomes. Both dipalmitoyl phosphatidylcholine (DPPC) and egg yolk phosphatidylcholine (Egg-PC), from Sigma-Aldrich, were used for lipid vesicle formation. A 10 mM DPPC or Egg-PC solution in ethanol was injected, under vigorous vortexing, to an aqueous solution of nanoparticles, above the melting transition temperature of the lipids (ethanolic injection method [33,36]). After encapsulation, the ferrofluid was washed with water and purified by magnetic decantation and centrifugation to remove all the non-encapsulated NPs.

Dry magnetoliposomes (DMLs) were synthesized by slowly adding a volume of DOPG or AOT solution, equivalent to that used in the synthesis of the NPs coated with lipid or surfactant, so that a second lipid/surfactant layer is formed above the previous layer. Excess of lipid/surfactant was removed by repeated cycles of magnetic decantation followed by washing with methanol/acetone (50/50 v/v) solution.

3.3 Preparation of Giant Unilamellar Vesicles (GUVs)

Soybean lecithin (*L*- α -Phosphatidylcholine), from Sigma-Aldrich, was used for GUVs preparation, using a procedure previously described [37,38]. A film of soybean lecithin was obtained by evaporation under an argon stream of a 1 mM lipid solution. This film was incubated with 20 μ L of water at 45°C for 45 minutes. Then, 3 mL of 0.1 M glucose solution was added, and the resulting mixture was again incubated at 37°C.

3.4 Spectroscopic measurements

3.4.1 General methods

Absorption spectra were recorded in a Shimadzu UV-3101PC UV-vis-NIR spectrophotometer. Fluorescence measurements were performed using a Fluorolog 3 spectrofluorimeter, equipped with double monochromators in both excitation and emission and a temperature controlled cuvette holder. Fluorescence spectra were corrected for the instrumental response of the system.

3.4.2 FRET measurements

The interaction of magnetoliposomes with models of biological membranes (GUVs) was evaluated by Förster Resonance Energy Transfer (FRET). FRET efficiency, Φ_{RET} , defined as the proportion of donor molecules that have transferred their excess energy to acceptor molecules, was calculated through donor emission quenching, by taking the ratio of the donor integrated fluorescence intensities in the presence of acceptor and in the absence of acceptor [39]. The distance between donor and acceptor molecules was determined through the FRET efficiency (equation (1)),

$$r_{\text{AD}} = R_0 \cdot \left[\frac{1 - \Phi_{\text{RET}}}{\Phi_{\text{RET}}} \right]^{1/6} \quad (1)$$

where R_0 is the Förster radius (critical distance), that can be obtained by the spectral overlap between the donor emission and the acceptor absorption [39].

FRET assays were employed to confirm the formation of the second lipid bilayer in the dry magnetoliposomes (DMLs). For that purpose, the rhodamine B labeled lipid Rhodamine-DHPE (1,2-dipalmitoyl-*sn*-glycero-3-phosphoethanolamine-*N*-(lissamine rhodamine B sulfonyl) (ammonium salt) (from Avanti Polar Lipids, structure shown below – Fig. 1) was included the first lipid layer, while the nitrobenzoxazole labeled lipid NBD-C₆-HPC (1-palmitoyl-2-{6-[(7-nitro-2-1,3-benzoxadiazol-4-yl)amino]hexanoyl}-*sn*-glycero-3-phosphocholine) (from Avanti Polar Lipids, Fig. 1) was included in the second lipid layer.

For the study of the interaction of magnetoliposomes with GUVs, the former were labeled with both NBD-C₆-HPC and the hydrophobic probe Nile Red (from Fluka, structure in Fig. 1).

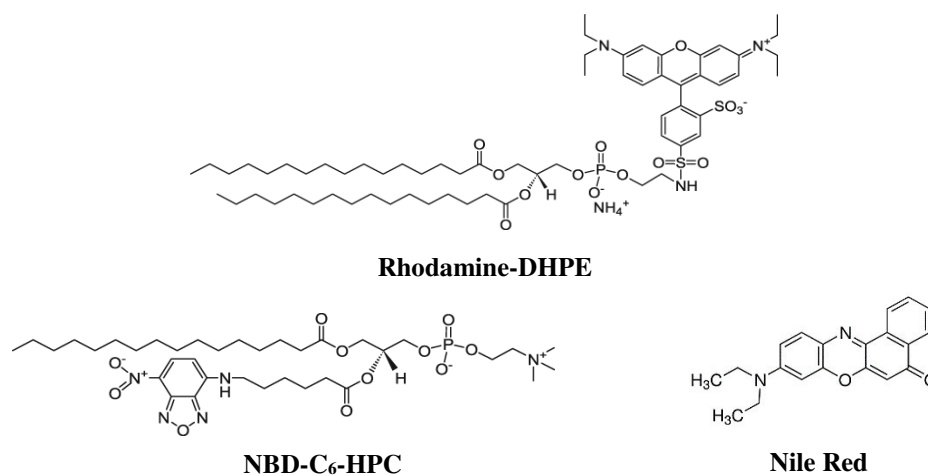


Fig. 1. Structures of the fluorescent labeled lipids and the dye Nile Red.

The fluorescence quantum yield, Φ_s , of the energy donor (in both cases, the dye NBD) in magnetoliposomes was determined by the standard method, equation (2) [40,41],

$$\Phi_s = \left[\frac{(A_r F_s n_s^2)}{(A_s F_r n_r^2)} \right] \Phi_r \quad (2)$$

where A is the absorbance at the excitation wavelength, F the integrated emission area and n the refraction index of the solvents used. Subscripts refer to the reference (r) or sample (s). The absorbance at the excitation wavelength was always lower than 0.1 to avoid the inner filter effects. The NBD-C₆-HPC molecule intercalated in lipid membranes was used as reference, $\Phi_r = 0.32$ at 25°C, as reported by Invitrogen [42].

3.5 Structural and magnetic characterization

Scanning electron microscopy (SEM) images of nickel nanoparticles and dry magnetoliposomes were recorded using a Scanning Electron Microscope *FEI - Nova 200 NanoSEM*. The processing of SEM images was performed using ImageJ software. It consisted in enhancing local contrast followed by automatic local thresholding and particle analysis. The area of each particle allowed an estimation of the particle diameter. The resulting histograms were fitted to Gaussian distributions.

Magnetic hysteresis cycles of nickel NPs were measured at room temperature in a Superconducting Quantum Interference Device (SQUID) magnetometer (Quantum Design MPMS5XL), with applied magnetic fields up to 5.5 T.

NPs mean diameter and size distribution (polydispersity index) were measured using a Dynamic Light Scattering (DLS) equipment (NANO ZS Malvern Zetasizer) at 25°C, using a He-Ne laser of $\lambda = 632.8$ nm and a detector angle of 173°. Five independent measurements were performed for each sample.

The experimentally obtained intensity autocorrelation function, $G^{(2)}(\tau)$, has the form [43,44]

$$G^{(2)}(\tau) = A \left[1 + B |g^{(1)}(\tau)|^2 \right] \quad (3)$$

where A is the baseline, B is a spatial coherence factor, τ is the delay time, and $g^{(1)}(\tau)$ is the first-order normalized electric field time correlation function.

For a polydisperse system, $g^{(1)}(\tau)$ decays as a weighted sum of single exponentials. These weights are modeled by Gaussian distributions, such that

$$g^{(1)}(\tau) = \int_0^\infty \sum_i \frac{a_i}{\sigma_i \sqrt{2\pi}} \exp\left(-\left[\frac{(s-s_i)}{\sqrt{2}\sigma_i}\right]^2\right) \exp(-\tau/s) ds \quad (4)$$

where a_i is the weight of each Gaussian population.

The decay lifetime, s , depends on the translational diffusion coefficient, D_z , which can be related to the particle hydrodynamic diameter through the Stokes-Einstein equation. A “size distribution” can thus be obtained, which is represented by $G_I(d)$, as each particle population is weighted by the intensity of scattered light it originates. In order to obtain the real size distribution of the sample, in which each particle population is weighted by its number fraction, $G_n(d)$, the variation of light scattering intensity with particle size (and shape) must be introduced [45],

$$G_I(d) = G_n(d)I_s(d) \quad (5)$$

where $I_s(d)$ is the scattered intensity per particle.

For spherical particles, and in the case of Rayleigh regime (valid for $x = \pi d/\lambda \ll 1$), this factor scales with d^6 . For situations where the refractive index of the particles and the medium are similar, the Rayleigh-Gans-Debye (RGD) theory is valid and the scattering light intensity is proportional to the square of the particle volume and to a form factor, $P(R) = f(R)^2$ [46]. For other situations, the value of $I_s(d)$ must be calculated using appropriate theories, such as Mie theory (spherical particles) or Aden-Kerker theory (spherical coated particles).

4. Results and discussion

4.1 Characterization of Ni nanoparticles

4.1.1 Absorption spectra

Fig. 2 shows the absorption spectrum of nickel nanoparticles obtained from the synthesis in CTAB microemulsions, without (A) and with silica shell (B). Considering the reported cytotoxicity of Ni NPs for several human cell lines [47,48], the presence of the silica shell could be important for biomedical applications of these magnetic nickel nanoparticles. As referred, the biocompatibility of silica nanoparticles and magnetic nanoparticles with a silica-shell was previously demonstrated [26,27].

The formation of Ni metal nanoparticles is confirmed by the absorption in the whole spectral range and plasmon absorption band at 288 nm (Fig. 2). This plasmon absorption band is very sensitive to the local dielectric environment and results from a resonant coherent oscillation of the free electrons at the surface of a spherical NP (LSPR - localized surface plasmon resonance) that is induced by the electromagnetic field of incident light [49].

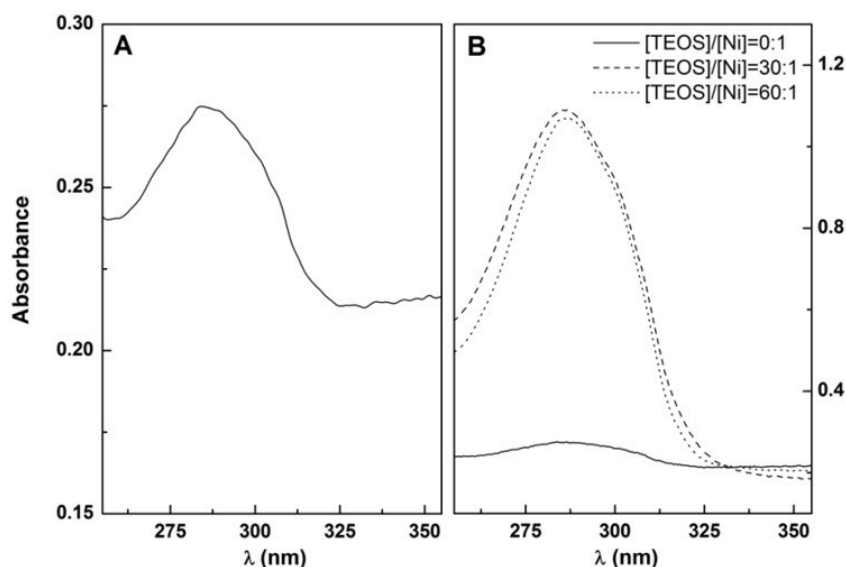


Fig. 2. Absorption spectra of Ni@SiO₂ nanoparticles dispersed in ethanol. The Ni cores were synthesized in aqueous CTAB solution. **A:** without silica shell; **B:** with silica shell added to Ni NPs dispersed in AOT/cyclohexane using different [TEOS]/[Ni] ratios.

Core-shell nickel nanoparticles with different silica shell sizes were formed by the addition of TEOS at several concentrations. A strong SPR enhancement is observed after coating (Fig. 2B), indicating a change in the dielectric constant of the medium surrounding the NPs, confirming formation of the silica shell (Fig. 2B). However, no further increase in absorption intensity was observed for [TEOS]/[Ni] molar ratio above 30:1. This can be attributed to the method used for the formation of the silica shell. As TEOS is added to the Ni NPs dispersed in a AOT/cyclohexane solution, the sol-gel process occur within AOT reverse micelles. This can limit the shell growth. For gold nanoparticles, very small changes are observed in the plasmon band [50]. On the other hand, a band near 270 nm was reported for SiO₂ nanoparticles obtained from sol-gel processing [51]. Thus, the huge absorbance increase upon coating of Ni NPs with SiO₂ should originate from absorption and/or scattering of the silica layer.

4.1.2 DLS measurements

DLS measurements revealed that particles size and size distribution are influenced by the synthesis method. Hydrodynamic diameters of Ni NPs with different [silica]/[Ni] ratios and without silica shell are shown in Table 1.

Table 1 - Hydrodynamic diameter (obtained by DLS) of Ni nanoparticles with and without silica shell, prepared by several synthesis methods.

Ni NPs synthesis method	[TEOS]:[Ni]	Hydrodynamic diameter (nm)		
		Intensity Distribution	Number Distribution	
			Core	Shell thickness
Aqueous CTAB solution TEOS added in AOT/cyclohexane	0:1	88 ± 7	84 ± 7	---
	10:1	157 ± 16	84 ± 7	34 ± 7
	30:1	175 ± 24	84 ± 7	42 ± 12
	60:1	185 ± 21	84 ± 7	48 ± 10
Covered with one AOT layer	0:1	100 ± 9	95 ± 13	---
Covered with one DOPG layer	0:1	79 ± 6	76 ± 6	---

The scattered light per particle, $I_s(d)$, needed to obtain the real size distributions from DLS data, was calculated using the equations proposed by Aden-Kerker [52] with a Fortran implementation developed by Quirantes *et al.* [53]. Fig. 3 plots s_{11} , an element of the scattering matrix (proportional to I_s/I_0 [46]), as function of particle diameter for unpolarized light of 632.8 nm at 173° scattering angle and a bulk refractive index of 1.36042 (ethanol at 25°C). For Ni NPs, a refractive index of $m(\text{Ni}) = 1.97006 + 3.72121i$ [54] was used. In the case of Ni@SiO₂ core/shell NPs, a value of 1.45702 [55] was used for the refractive index of silica, either considering a constant Ni core with a diameter of 100 nm, or a constant SiO₂ shell of 50 nm thickness. For vesicles, a bilayer with 5 nm thickness was used with a refractive index of 1.435 [56].

It is observed that Rayleigh regime is only valid for Ni NPs up to 20 nm diameter. The RGD approximation is better, but the oscillations do not occur at the same particle sizes and the minima are much more pronounced. In the case of vesicles, the RGD approximation is quite good.

The number weighted size distributions could then be obtained by fitting a Gaussian distribution to the calculated $G_n(d)$ from equation (5). In the case of Ni@SiO₂, a Gaussian shell size distribution was considered superimposed on the distribution

obtained for bare Ni NPs and a sum was calculated for different particles having the same total diameter. The results of this procedure are shown in Table 1 and the recovered mean size are approximately 4 nm less than those obtained from intensity weighted size distributions, $G_i(d)$. The eventual effect of the ~2nm AOT or DOPG overcoat was not considered.

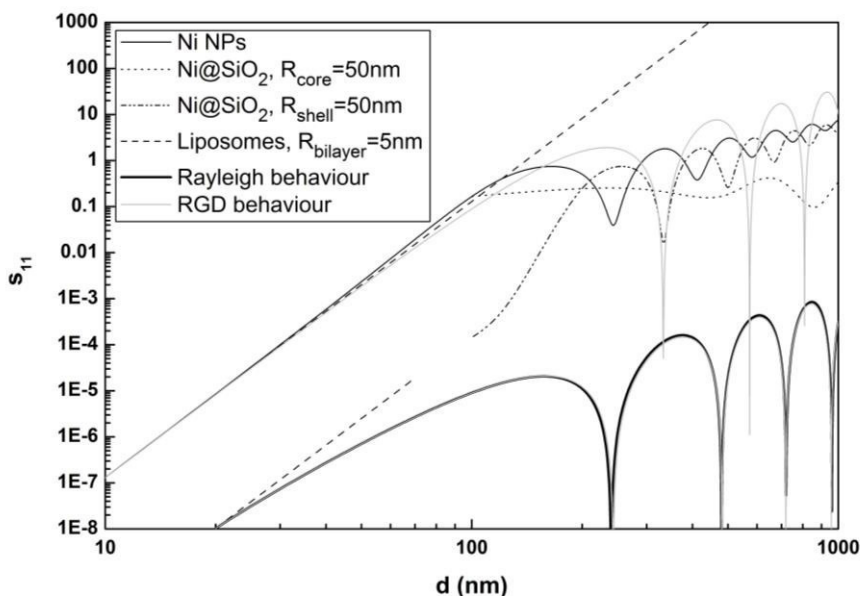


Figure 3. S_{11} scattering matrix element for Ni NPs, Ni@SiO₂ NPs and vesicles.

Comparing the hydrodynamic diameter of Ni NPs with and without silica shell, it is possible to confirm the formation of the shell based on size increase with the [TEOS]/[Ni] ratio. Above [TEOS]:[Ni] = 30:1, the increase of the shell size is smaller, which can be caused by the limited space of the water pools inside AOT reverse micelles (as already referred), that in fact control the particles size. Core/shell nanoparticles are generally more polydisperse, as inferred from a larger size distribution.

The smallest particles, with hydrodynamic diameters in the order of 80 nm and narrow size distribution, were obtained from the synthesis of NPs (without silica shell) covered with a layer of the phospholipid DOPG. This shows that the lipid layer contributes to avoid particle aggregation and to reduce size and polydispersity. However, some degree of aggregation is expected in these systems, as the lipid/surfactant layer is supposed to have the hydrophobic chains turned to the outer phase.

4.1.3 SEM microscopy

Scanning Electron Microscopy (SEM) allow the direct observation of 2D projections of NPs structure, surface morphology and size. SEM images generally

revealed nanoparticles with radius lower than 100 nm for almost all the synthesis methods employed. The NPs synthesized in CTAB aqueous solution revealed diameters between 63.4 and 104 nm (Fig. 4), with a size distribution of 66 ± 24 nm obtained from the histogram of image B. This result is slightly lower than the size distribution obtained from DLS measurements, indicating particle dimerization in aqueous media. Phase contrast SEM images (Fig. 4C *versus* Fig. 4D) confirmed that the particles obtained are metal nanoparticles.

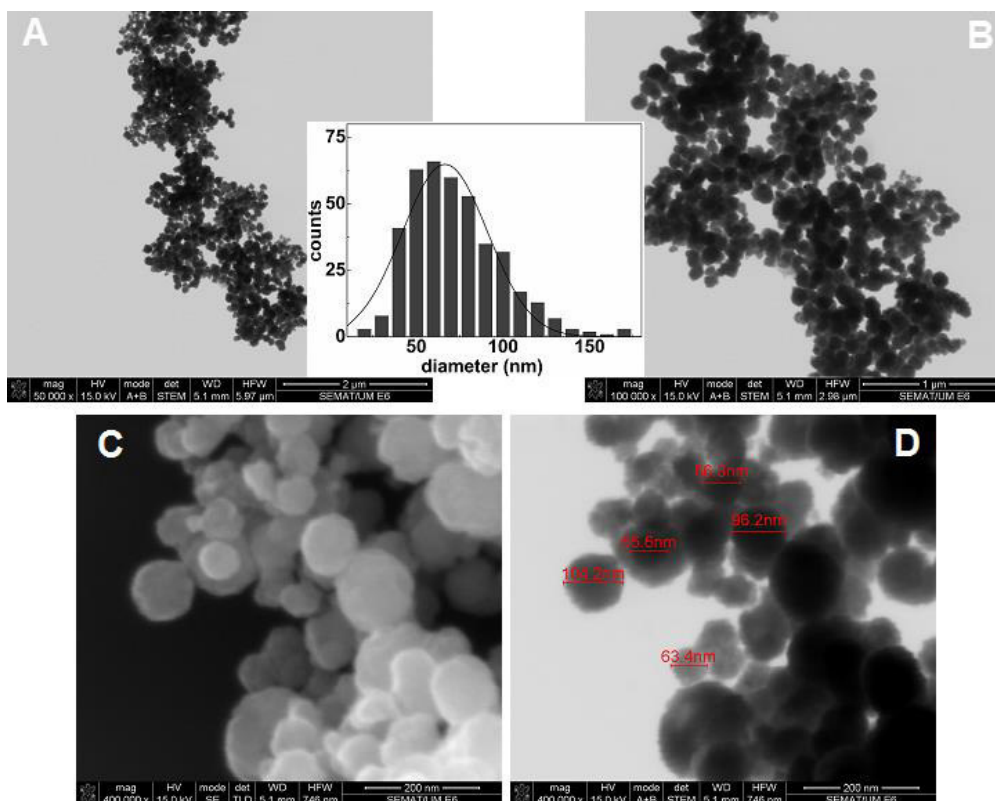


Fig. 4. SEM images of nickel nanoparticles synthesized in CTAB aqueous solution with citric acid (1:0.75), at different amplifications. Inset: Particles size histogram of image B and fitting to a Gaussian distribution.

The increase in size of the shell is proportional to TEOS concentration and is dependent on the synthesis process (Fig. 5). As referred, two processes were used for the coating with silica shell. In the first, TEOS was added in an AOT solution in cyclohexane, and the shell growth is controlled by the size of water pools of AOT reverse micelles. In the second, shell growth is not limited, as TEOS is added in ethanol together with a binding agent (MDA). A disadvantage of the first method is the low NPs concentration obtained (Fig. 5A). As expected, the second method yields particles with a much larger silica shell, attaining more than 400 nm diameter for high [TEOS]/[Ni] ratio (Fig. 5B).

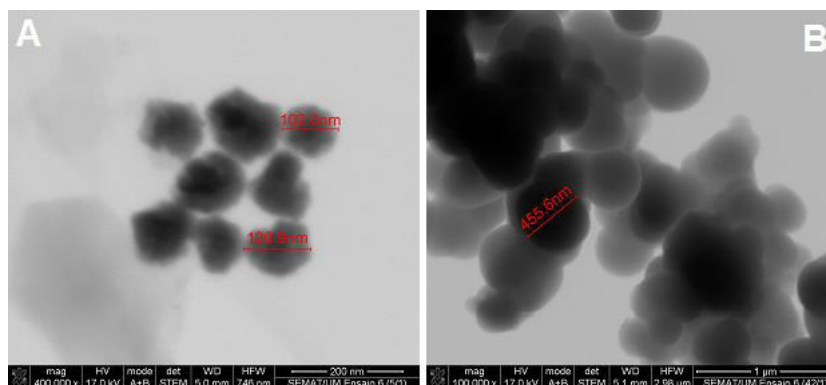


Fig. 5. SEM images of nickel nanoparticles coated with silica shell. **A:** [TEOS]/[Ni] = 5:1 (TEOS added in AOT/cyclohexane solution); **B:** [TEOS]/[Ni] = 42:1 (TEOS added in ethanol solution with MDA).

4.1.4 Magnetic Properties

The magnetic properties of the nanoparticles synthesized in CTAB aqueous solution were characterized by measuring their corresponding magnetic hysteresis loop, which shows the relationship between the induced magnetic moment and the applied magnetic field (H). Fig. 6 shows the hysteresis cycle measured on the prepared nickel nanoparticles. Typical ferromagnetic properties were observed, reaching the saturation at about 1 kOe (0.1 T). The nickel nanoparticles exhibit some slight hysteresis (Fig. 6B), indicating an oxidation of the particles, with the formation of a NiO (antiferromagnetic) surface layer around the metallic particles. In fact, the obtained hysteresis loop (Fig. 6A) is identical to the one previously reported for Ni NPs with a NiO layer [57]. The coercive field of the Ni NPs is 80 Oe (Fig. 6B – point c) and is lower than the value reported, at room temperature, for NPs with NiO layer prepared by similar methods, which indicates a smaller amount of nickel oxidation on our prepared particles.

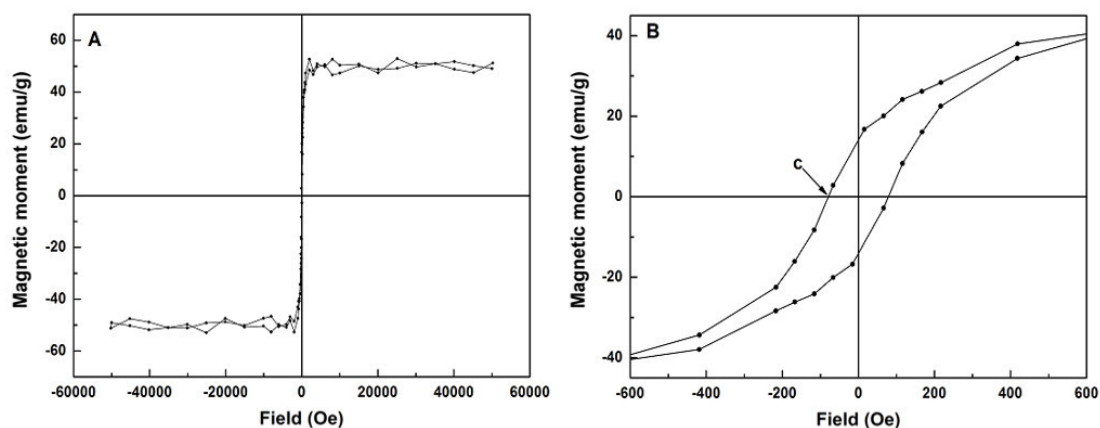


Fig. 6. A: Magnetization hysteresis cycle of the nickel nanoparticles at room temperature. **B:** Enlargement of the hysteresis loop of Figure 6A, in the low field region.

In order to estimate the thickness of the NiO layer from the magnetic hysteresis cycles, the particles were considered to have a well ordered Ni core covered by a non-magnetic NiO shell (with thickness δ) that acted as a magnetic “dead layer” [58]. In this respect, the measured saturation magnetization (M_s) of the particles is proportional to the volume fraction of the core, which carries the spontaneous magnetization. If the shell thickness δ is small, then the saturation magnetization can be determined, to first order, by [58]

$$M_s = M_{s0} \left(1 - \frac{6\delta}{D}\right) \quad (6)$$

where D is the particle diameter and M_{s0} is the saturation magnetization for a bulk Ni sample ($M_{s0} = 55$ emu/g). Here, for particles with diameter of 84 nm and with $M_s = 51.2$ emu/g, the obtained NiO layer thickness is $\delta = 1.1$ nm, which corresponds to about 3 unit cells. This shows that the synthesis of Ni particles using the cationic surfactant CTAB allows attaining an improvement of the NPs magnetic properties, relative to previous methods employing Triton X-100 as surfactant [57].

4.2 Characterization of magnetoliposomes

4.2.1 FRET assays in DMLs

As described in the Experimental Section, two types of magnetoliposomes were synthesized, aqueous magnetoliposomes (AMLs) and dry magnetoliposomes (DMLs). In DMLs, clusters of magnetic nanoparticles were covered by the double chain surfactant AOT or the anionic phospholipid DOPG. The coating by a double lipid (or surfactant) layer was confirmed by FRET assays. The NBD labeled lipid NBD-C₆-HPC, included in the second lipid layer of the DMLs, acts as energy donor, while the labeled lipid Rhodamine B-DHPE was included in the first lipid/surfactant layer, acting as energy acceptor.

Fig. 7 presents evidence for FRET occurrence between NBD and Rhodamine (Rh). Inset illustrates the spectral overlap between the emission of the donor (NBD) and the absorption of the acceptor (Rhodamine B), indispensable condition for FRET to occur. Fluorescence spectra of DMLs containing only donor or acceptor and DMLs containing both labeled lipids were measured, exciting only the donor NBD ($\lambda_{exc} = 465$ nm), at the same dilution factor. As expected, characteristic NBD emission ($\lambda_{em} = 520$ nm) is detected for DMLs labeled only with NBD-C₆-HPC, while negligible fluorescence is observed for

the DMLs containing only Rhodamine-DHPE. It is possible to verify that for DMLs with both donor and acceptor molecules, the emission in the NBD-C₆-HPC region notably decreases, with a strong rise in the Rhodamine B region, proving the formation of the second lipid layer in DMLs.

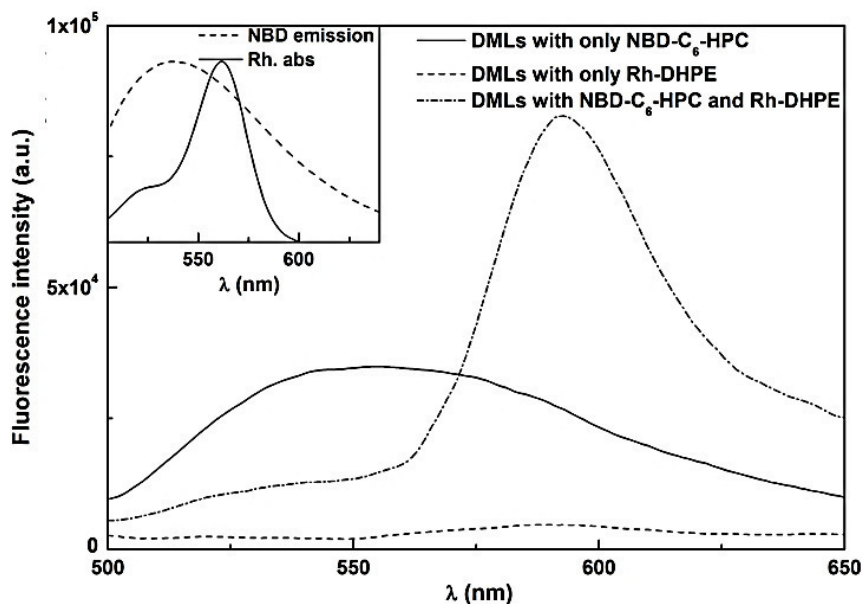


Fig. 7. Fluorescence spectra ($\lambda_{exc} = 465$ nm, no Rhodamine excitation) of DMLs covered with AOT labeled with only NBD-C₆-HPC (1×10^{-2} μ M); DMLs labeled with only Rhodamine B-DHPE (1×10^{-2} μ M) and DMLs labeled with both NBD-C₆-HPC (1×10^{-2} μ M) and Rhodamine B-DHPE (1×10^{-2} μ M). Inset: Spectral overlap (spectra are normalized) between the fluorescence emission of the donor (NBD-C₆-HPC) and the absorption of the acceptor (Rhodamine B-DHPE).

Using the standard method, the fluorescence quantum yield of the donor in magnetoliposomes (in the absence of acceptor) was determined as $\Phi_D = 0.185$. FRET measurements revealed an energy transfer efficiency of 31%, with a corresponding donor-acceptor distance of 7.6 nm. Cell membrane has a typical thickness of 7 to 9 nm [59]. Therefore, these results clearly indicate that the labeled lipids Rhodamine B-DHPE and NBD-C₆-HPC are placed in the first and second lipid layer, respectively, in the structures formed. This confirms the structure of lipid bilayer around nickel nanoparticles and the synthesis of DMLs.

4.2.2 SEM microscopy and DLS measurements

Dry magnetoliposomes (DMLs) can be observed by SEM microscopy, as their structure does not present an inner water pool. On the contrary, the structure of aqueous magnetoliposomes (AMLs) is destroyed by the vacuum system used in SEM.

The sizes of AMLs, prepared by using either DPPC or Egg-PC phospholipids, were determined by DLS (Table 2). The size of liposomes (without Ni NPs) is also shown, for comparison.

As previously reported, the size of Egg-PC liposomes is usually smaller than the one for DPPC liposomes prepared by the same technique (ethanolic injection) [60]. The results on Table 2 show that the presence of Ni nanoparticles contributes to a diameter increase relative to liposomes without NPs, this effect being more significant in DPPC magnetoliposomes.

The entrapment of core/shell Ni/silica nanoparticles in liposomes contribute definitely to avoid particle aggregation, as the measured mean diameters are significantly lower for AMLs than for the corresponding nanoparticles (Table 1). Comparing both lipid systems, the Egg-PC AMLs are more promising for applications in drug transport and delivery, considering their size and size distribution.

SEM micrographs of DMLs of Ni nanoparticles covered by a double layer of the anionic surfactant AOT or of the phospholipid DOPG are presented in Figures 8 and 9, respectively. Fig. 8B shows AOT DMLs with size varying between 58 and 76 nm, with a relatively low polydispersity. From the fit to a Gaussian distribution of the particles size histogram obtained from the image processing of Figure 8A (Fig. 8 - inset), a particle diameter of 67 ± 26 nm was calculated. DLS measurements allowed to determine a hydrodynamic diameter of 115 ± 26 nm, pointing to extended aggregation in aqueous media.

Table 2 - Hydrodynamic diameter (obtained by DLS) of aqueous magnetoliposomes incorporating Ni NPs with and without silica shell.

Phospholipid	[TEOS]:[Ni]	Hydrodynamic diameter (nm)	
		Intensity distribution	Number distribution (fixed shell of 5 nm thickness)
Egg-PC	without NPs	92 ± 10	90 ± 7
	0:1	103 ± 20	---
	10:1	126 ± 33	---
	20:1	135 ± 34	---
DPPC	without NPs	115 ± 12	113 ± 9
	0:1	146 ± 34	---
	20:1	175 ± 23	---

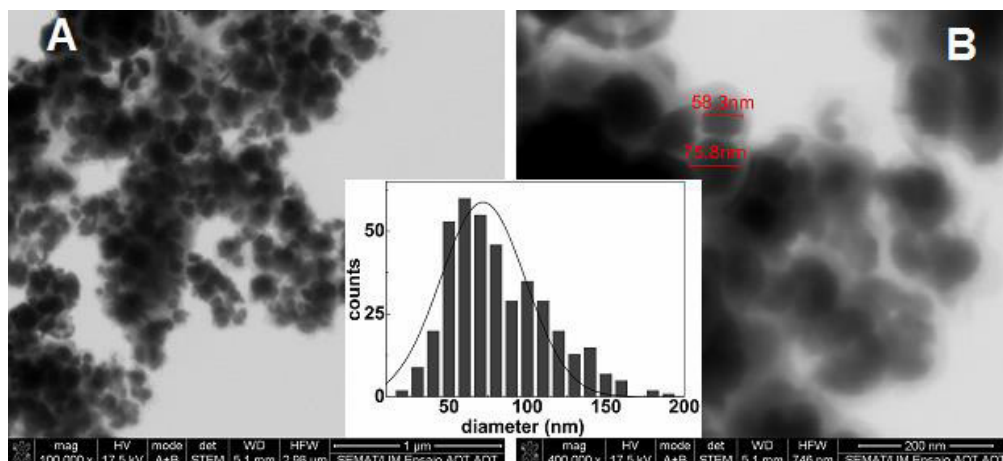


Fig. 8. SEM images of dry magnetoliposomes of nickel nanoparticles (without silica shell) covered by an AOT surfactant double layer. Inset: Particles size histogram of image A and fitting to a Gaussian distribution.

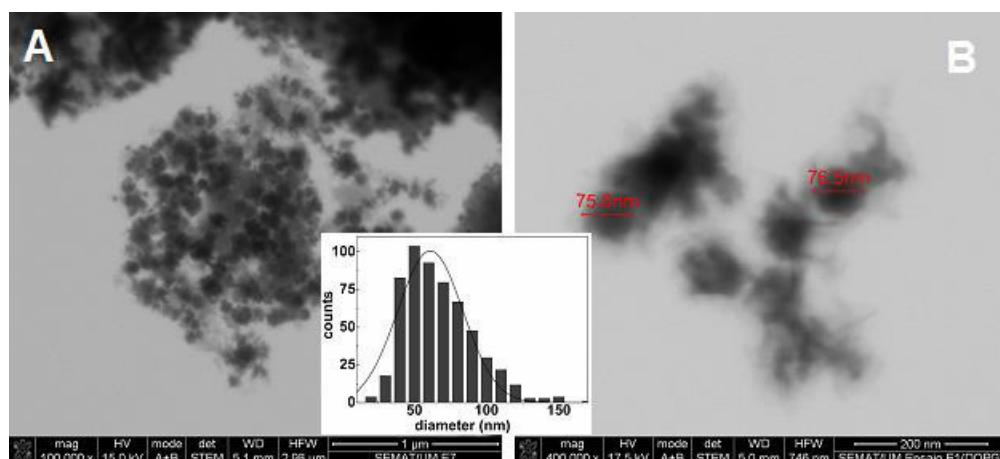


Fig. 9. SEM images of dry magnetoliposomes of nickel nanoparticles covered by a DOPG lipid bilayer. Inset: Particles size histogram of image A and fitting to a Gaussian distribution.

SEM results revealed that the DOPG DMLs are approximately monodisperse (Fig. 9B), with size around 76 nm. The fit to a Gaussian distribution of the particles size histogram obtained from SEM images (Fig. 9A) allowed determining a diameter of 65 ± 28 nm. DLS measurements revealed one population with a hydrodynamic diameter of 98 ± 16 nm, pointing again to some dimerization in aqueous media.

These results are promising for future application of DMLs as drug transport/delivery systems, specially the DOPG-based system, as its size is below 100 nm with a narrow size distribution.

4.3 Interaction of magnetoliposomes with giant unilamellar vesicles (GUVs)

Non-specific interactions of the aqueous magnetoliposomes (AMLs) with giant unilamellar vesicles (GUVs), models of cell membranes, were also evaluated by FRET. For that purpose, the labeled lipid NBD- C_6 -HPC was included in Egg-PC AMLs, acting as energy donor, while the hydrophobic probe Nile Red, also incorporated in AMLs, acts as acceptor.

Nile Red is a well-known solvatochromic probe, which in polar media exhibits a red shift in the emission maximum, together with fluorescence quenching. Owing to its capability to establish H-bonds with protic solvents, Nile Red fluorescence in water is very weak and red shifted ($\lambda_{\max} \sim 660$ nm) [61]. Nile Red has been used as a lipid probe, due to its hydrophobic nature [62-65].

The significant overlap between NBD- C_6 -HPC emission band and Nile Red absorption spectrum (Fig. 10 – inset) indicates that FRET process between these two fluorescent molecules is expected to be efficient, if the donor-acceptor distance is below 100 Å [39]. In fact, when both fluorophores are incorporated in magnetoliposomes at appropriate surface densities, efficient energy transfer is observed, exciting only the donor (NBD) (Fig. 10).

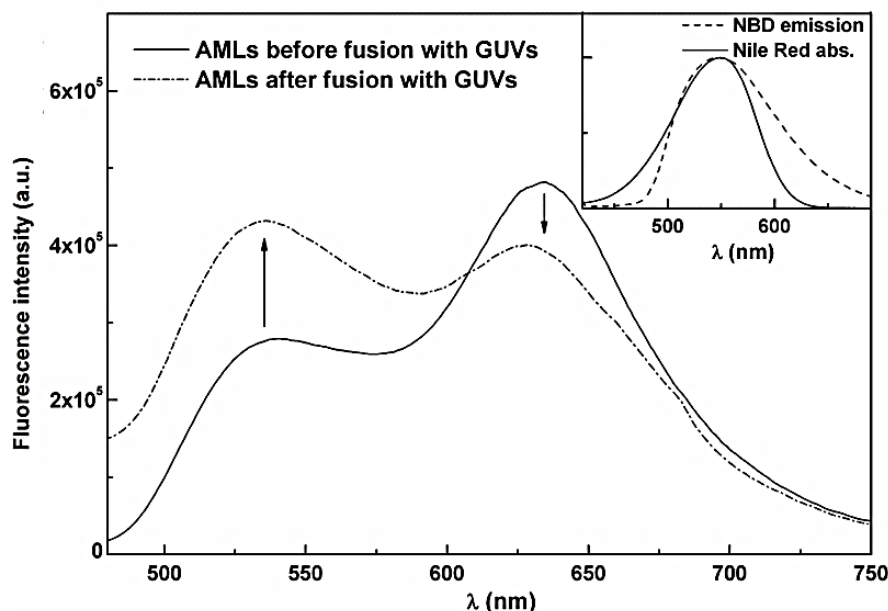


Fig. 10. Fluorescence spectra ($\lambda_{\text{exc}} = 400$ nm) of AMLs of Egg-PC and Ni/silica core/shell NPs containing both NBD- C_6 -HPC (10^{-6} M) and Nile Red (2×10^{-6} M), before and after interaction with GUVs. Inset: Spectral overlap (spectra are normalized) between the fluorescence emission of the donor (NBD- C_6 -HPC) and the absorption of the acceptor (Nile Red).

Two fluorescence bands are observed, the first ($\lambda_{\max} = 535$ nm) corresponding to NBD-C₆-HPC emission and the second one to Nile Red, with maximum at 630 nm. This second band arises from the energy transfer of excited NBD molecules to Nile Red. When the magnetoliposomes interact with GUVs, if fusion occurs, a larger membrane is formed [66]. This leads to an increase in the donor-acceptor distance and a corresponding decrease in the energy transfer efficiency from the NBD moieties, as is experimentally observed. These experimental results are consistent with membrane fusion between the AMLs and GUVs. This process of membrane fusion is illustrated in Fig. 11. Thus, a proof-of-concept is presented in this work, allowing to conclude that both aqueous and dry magnetoliposomes may be used as drug transport and delivery systems, as they can be guided with a magnetic field and can release the encapsulated drugs by fusion with the cell membrane.

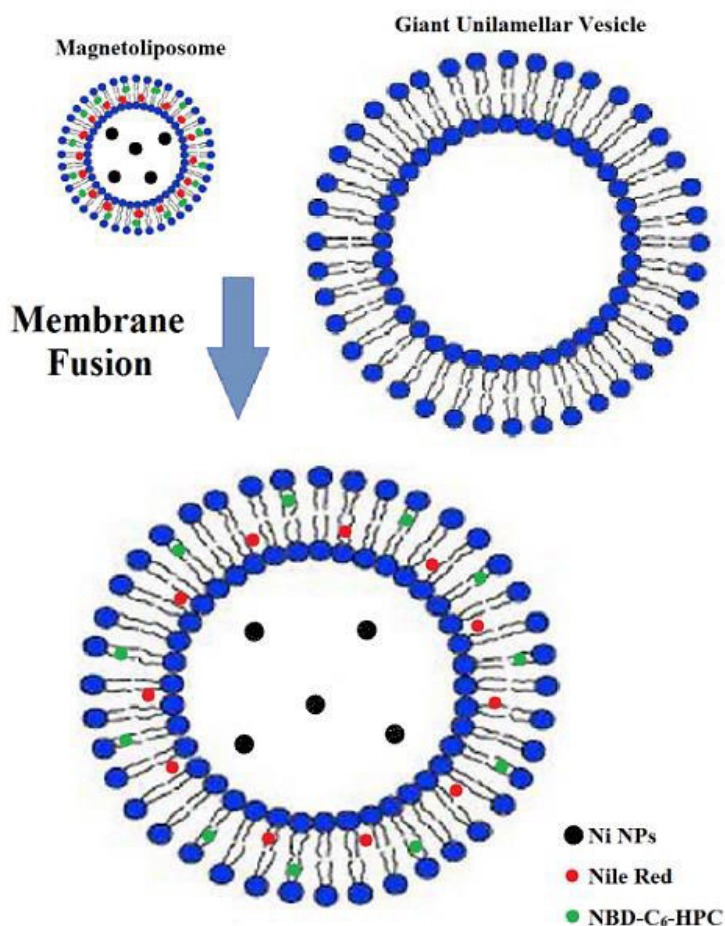


Fig. 11. Schematic illustration of the fusion between the GUVs and magnetoliposomes labeled with both NBD-C₆-HPC and Nile Red.

5. Conclusions

In this work, magnetic nickel nanoparticles were successfully synthesized using microheterogeneous templating media.

SQUID measurements of Ni NPs synthesized in CTAB aqueous solution allowed to determine a coercive field of 80 Oe.

Nickel nanoparticles were successfully encapsulated into liposomes, forming aqueous (AMLs) or dry magnetoliposomes (DMLs). DMLs with AOT surfactant or DOPG double chain present low polydispersity and mean diameter lower than 100 nm, essential for *in vivo* applications. FRET measurements point to membrane fusion between the magnetoliposomes and models of cell membranes (GUVs).

These results may be important for future drug delivery applications of antitumor drugs using magnetoliposomes for encapsulation and transport of antitumor drugs and taking advantage of the possibilities of hyperthermia.

6. Acknowledgements

This work was supported by FEDER through the COMPETE/QREN/EU Program and by the Portuguese Foundation for Science and Technology (FCT) in the framework of the Strategic Project of CFUM [PEst-C/FIS/UI0607/2013 (F-COMP-01-0124-FEDER-022711)] and through the research project PTDC/QUI/81238/2006 (FCOMP-01-0124-FEDER-007467).

FCT, POPH-QREN and FSE are acknowledged for the PhD grant of A. R. O. Rodrigues (SFRH/BD/90949/2012) and for financial support to MAP-Fis PhD Programme.

7. References

- [1] B. P. Timko, K. Whitehead, W. Gao, D. S. Kohane, O. Farokhzad, D. Anderson, R. Langer, *Annu. Rev. Mater. Res.* **41** (2011) 1-20.
- [2] S. Mornet, S. Vasseur, F. Grasset, E. Duguet, *J. Mater. Chem.* **14** (2004) 2161-2175.
- [3] M. Mezei, V. Gulasekharan, *J. Pharm. Pharmacol.* **34** (1982) 473-474.
- [4] R. L. Juliano, *Trends Pharmacol. Sci.* **2** (1981) 39-42.
- [5] G. Poste, C. Cucana, A. Raz, P. Bugelski, R. Kirsh, I.J. Fidler, *Cancer Res.* **24** (1982) 1412-1422.
- [6] T. L. Andresen, S. S. Jensen, K. Jorgensen, *Prog. Lipid Res.* **44** (2005) 68-97.
- [7] N. A. Ochekepe, P. O. Olorunfemi, N. C. Ngwuluka, *Trop. J. Pharm. Res.* **8** (2009) 265-274.
- [8] A. S. Lubbe, C. Bergemann, J. Brock, D. G. McClure, *J. Magn. Magn. Mater.* **194** (1999) 149-155.
- [9] S. Dandamudi, R. B. Campbell, *Biomaterials* **28** (2007) 4673-4683.
- [10] H.-J. Weinmann, W. Ebert, B. Misselwitz, H. S.-Willich, *Eur. J. Radiol.* **46** (2003) 33-44.
- [11] N. Nuytten, M. Hakimhashemi, T. Ysenbaert, L. Defour, J. Trekker, S. J. Soenen, P. Van der Meeren, M. Cuyper, *Colloids Surf. B. Biointerfaces* **80** (2010) 227-231.
- [12] U. I. Tromsdorf, N. C. Bigall, M. G. Kaul, O. T. Bruns, M. S. Nikolic, B. Mollwitz, R. A. Sperling, R. Reimer, H. Hohenberg, W. J. Parak, S. Forster, U. Beisiegel, G. Adam, H. Weller, *Nano Lett.* **7** (2007) 2422-2427.
- [13] E. Amstad, J. Kohlbrecher, E. Müller, T. Schweizer, M. Textor, E. Reimhult, *Nano Lett.* **11** (2011) 1664-1670.
- [14] G. Gregoriadis, *Trends Biotechnol.* **13** (1995) 527-537.
- [15] S. Dandamudi, R. B. Campbell, *Biochim. Biophys. Acta* **1768** (2007) 427-438.
- [16] D. L. Huber, *Small* **1** (2005) 482-501.
- [17] K. M. Krishnan, *IEEE Trans. Magn.* **46** (2010) 2523-2559.
- [18] P. Tartaj, M. P. Morales, S. V.-Verdaguer, T. G.-Carreno, C. J. Serna, *J. Phys. D: Appl. Phys.* **36** (2003) 182-197.

- [19] M. Faraji, Y. Yamini, M. Rezaee, *J. Iran Chem. Soc.* **7** (2010) 1-37.
- [20] C. M. Niemeyer, *Angew. Chem. Int. Ed.* **40** (2001) 4128-4158.
- [21] I. M. Hafez, S. Ansell, P. R. Cullis, *Biophys. J.* **79** (2000) 1438-1446.
- [22] J. B. Sun, J. H. Duan, S. L. Dai, J. Ren, L. Guo, W. Jiang, Y. Li, *Biotechnol. Bioeng.* **101** (2008) 1313-1320.
- [23] Y. Malam, M. Loizidou, A. M. Seifalian, *Trends Pharmacol. Sci.* **30** (2009) 592-599.
- [24] N. Sounderya, Y. Zhang, *Recent Patents Biomed. Eng.* **1** (2008) 34-42.
- [25] C. Sun, J.S.H. Lee, M. Zhang, *Adv. Drug Deliv. Rev.* **60** (2008) 1252-1265.
- [26] D. M. Huang, T. H. Chung, Y. Hung, F. Lu, S.-H. Wu, C. Y. Mou, M. Yao, Y. C. Chen, *Toxicol. Appl. Pharmacol.* **231** (2008) 208-215.
- [27] T. Kim, E. Momin, J. Choi, T. Kim, E. Momin, J. Choi, K. Yuan, H. Zaidi, J. Kim, M. Park, N. Lee, M. T. McMahon, A. Quinones-Hinojosa, J. W. M. Bulte, T. Hyeon, A. A. Gilad, *J. Am. Chem. Soc.* **133** (2011) 2955-2961.
- [28] A. Akbarzadeh, M. Samiei, S. Davaran, *Nanoscale Res. Lett.* **7** (2012) 144-176.
- [29] R. Kotitz, W. Weitschies, L. Trahms, W. Brewer, W. Semmler, *J. Magn. Magn. Mater.* **194** (1999) 62-68.
- [30] T. T. Y. Tan, S. Liu, Y. Zhang, M. Y. Han, S. T. Selvan in *Comprehensive Nanoscience and Technology*, D. Andrews, G. Scholes and G. Wiederrecht, Eds., Academic Press, 2010.
- [31] D.-H. Chen, C.-H. Hsieh, *J. Mater. Chem.* **12** (2002) 2412-2415.
- [32] S. Jain, V. Mishra, P. Singh, P. K. Dubey, D. K. Saraf, S.P. Vyas, *Int. J. Pharm.* **261** (2003) 43-55.
- [33] C. J. Meledandri, T. Ninjbadgar, D. F. Brougham, *J. Mater. Chem.* **21** (2011) 214-222.
- [34] S. Santra, R. Tapeç, N. Theodoropoulou, J. Dobson, A. Hebard, W. Tan, *Langmuir* **17** (2001) 2900-2906.
- [35] S. Batzri, E. D. Korn, *Biochim. Biophys. Acta* **298** (1973) 1015-1019.
- [36] J. M. H. Kremer, M. W. J. vd Esker, C. Pathmamanoharan, P. H. Wiersema, *Biochemistry* **16** (1977) 3932-3935.

- [37] Y. Tamba, H. Terashima, M. Yamazaki, *Chem. Phys. Lipids* **164** (2011) 351-358.
- [38] T. Tanaka, Y. Tamba, S. Md. Masum, Y. Yamashita, M. Yamazaki, *Biochim. Biophys. Acta* **1564** (2002) 173-182.
- [39] B. Valeur, *Molecular Fluorescence – Principles and Applications*, Wiley-VCH, Weinheim, 2002.
- [40] J. N. Demas, G. A. Crosby, *J. Phys. Chem.* **75** (1971) 991-1024.
- [41] S. Fery-Forgues, D. Lavabre, *J. Chem. Educ.* **76** (1999) 1260-1264.
- [42] I. Johnson, M. T. Z. Spence, *Molecular Probes Handbook: A Guide to Fluorescent Probes and Labeling Technologies*, 11th Edition, Invitrogen, 2011.
- [43] B. Chu, *Laser Light Scattering – Basic Principles and Practice*, 2nd Edition, Academic Press, New York, 1991.
- [44] C. S. Johnson Jr., D. A. Gabriel, *Laser Light Scattering*, Dover, New York, 1994.
- [45] P. J. Patty, B. J. Frisken, *Appl. Opt.* **45** (2006) 2209-2216.
- [46] C. F. Bohren, D. R. Huffman, *Absorption and Scattering of Light by Small Particles*, Wiley-VCH, New York, 2007.
- [47] S. Park, Y. K. Lee, M. Jung, K. H. Kim, N. Chung, E. K. Ahn, Y. Lim, K. H. Lee, *Inhal. Toxicol.* **19** (2007) 59-65.
- [48] M. Ahamed, *Toxicol. in Vitro* **25** (2011) 930-936.
- [49] P. N. Prasad, *Nanophotonics*, Wiley-Interscience, New Jersey, 2004.
- [50] Y. Kobayashi, M. A. Correa-Duarte, L. M. Liz-Marzán, *Langmuir* **17** (2001) 6375-6379.
- [51] S. Chakrabarty, K. Chatterjee, *ISRN Nanotechnol.* 2011 (2011) Article ID 719027.
- [52] A. L. Aden, M. Kerker, *J. Appl. Phys.* **22** (1951) 1242-1246.
- [53] A. Quirantes Sierra, A. V. Delgado, *J. Phys. D: Appl. Phys.* **30** (1997) 2123-2131
- [54] E. D. Palik, *Handbook of Optical Constants of Solids*, Elsevier Science & Tech., 1985.
- [55] I. H. Malitson, *J. Opt. Soc. Am.* **55** (1965) 1205-1208.
- [56] M. Ardhammar, P. Lincoln, B. Nordén, *PNAS* **99** (2002) 15313-15317.

- [57] M. Benelmekki, A. Montras, A.J. Martins, P.J.G. Coutinho, Ll. M. Martinez, *J. Magn. Magn. Mater.* **323** (2011) 1945-1949.
- [58] J. P. Chen, C. M. Sorensen, K. J. Klabunde, G. C. Hadjipanayis, E. Devlin, A. Kostikas, *Phys. Rev. B* **54** (1996) 9288-9296.
- [59] H. Curtis, N. Barnes, *Biology*, 5th Edition, Worth Publishers, New York, 1989.
- [60] E. M. S. Castanheira, M. S. D. Carvalho, A. R. O. Rodrigues, R. C. Calhelha, M.-J. R. P. Queiroz, *Nanoscale Res. Lett.* **6** (2011) article 379.
- [61] G. Hungerford, E. M. S. Castanheira, M. E. C. D. Real Oliveira, M. G. Miguel, H. D. Burrows, *J. Phys. Chem. B* **106** (2002) 4061-4069.
- [62] P. Greenspan, S.D. Fowler, *J. Lipid Res.* **26** (1985) 781-789.
- [63] I. G. Krishnamoorthy, *J. Phys. Chem. B* **105** (2001) 1484-1488.
- [64] P. J. G. Coutinho, E. M. S. Castanheira, M. C. Rei, M. E. C. D. Real Oliveira, *J. Phys. Chem. B* **106** (2002) 12841-12486.
- [65] E. Feitosa, F. R. Alves, A. Niemiec, M. E. C. D. Real Oliveira, E. M. S. Castanheira, A. L. F. Baptista, *Langmuir* **22** (2006) 3579-3585.
- [66] D. K. Struck, D. Hoekstra, R. E. Pagano, *Biochemistry* **20** (1981) 4093-4099.

**Magnetic liposomes based on nickel ferrite nanoparticles for
biomedical applications**

Ana Rita O. Rodrigues, I. T. Gomes, Bernardo G. Almeida, J. P. Araújo, Elisabete M. S.
Castanheira, Paulo J. G. Coutinho

Physical Chemistry Chemical Physics **17** (2015) 18011-18021

INDEX

1. Abstract
2. Introduction
3. Experimental
4. Results and discussion
5. Conclusions
6. Acknowledgments
7. References
8. Supplementary information

1. Abstract

Nickel ferrite nanoparticles with superparamagnetic behavior at room temperature were synthesized by a coprecipitation method. These magnetic nanoparticles were either covered with a lipid bilayer, forming dry magnetic liposomes (DMLs), or entrapped in liposomes, originating aqueous magnetoliposomes (AMLs). A new and promising method for the synthesis of DMLs is described. The presence of the lipid bilayer in DMLs was confirmed by FRET (Förster Resonance Energy Transfer) measurements between the fluorescent-labeled lipids NBD-C₁₂-HPC (NBD acting as donor) included in the second lipid layer and rhodamine B-DOPE (acceptor) in the first lipid layer. An average donor-acceptor distance of 3 nm was estimated. Assays of the non-specific interactions of magnetoliposomes with biological membranes (modeled using giant unilamellar vesicles, GUVs) were performed. Membrane fusion between both aqueous and dry magnetoliposomes and GUVs was confirmed by FRET, which is an important result regarding applications of these systems both as hyperthermia agents and antitumor drug nanocarriers.

2. Introduction

Guided transport of biologically active substances to target specific sites in human body has been a focus of research in therapeutics in the past years. Most of the active molecules used in therapy are toxic and cause systemic side effects.^{1,2} In chemotherapy, for example, the dosage used of active molecules is often selected by how much a patient can physically withstand rather than by how much is needed to treatment. Typically, in conventional chemotherapy, less than 0.1% of the drugs are taken up by tumor cells and the remaining 99.9% attack healthy tissues, making the efficiency of the treatment being compromised from the outset.³⁻⁵ The ability to guide transported drugs and focus the active molecules to specific sites in the human body can overcome systemic toxicity problems, allow a lower drug dosage and a more efficient treatment not only in cancer, but also in other diseases.

Magnetic nanoparticles (MNPs) offer major advantages due to their unique size and physicochemical and magnetic properties, making them suitable to be guided and localized to therapeutic sites of interest by external magnetic field gradients and used in cancer treatment by hyperthermia.^{6,7} In biomedical applications, iron oxide and ferrite

nanoparticles have been widely used because of their outstanding properties, such as superparamagnetic behaviour, high saturation magnetization and excellent chemical stability.^{8,9} The preparation methods will determine their final shape, size distribution, surface chemistry and magnetic properties.^{10,11} However, magnetic nanoparticles have the tendency to agglomerate and form sediments which could be a safety concern.¹² Many coating systems, such as liposomes,¹³ polymers¹⁴ and hydrogels¹⁵ have been studied to overcome this problem. Liposomes have been proposed as an ideal encapsulation system, as they can be made of natural nontoxic molecules and can encapsulate both lipophilic and hydrophilic compounds in their lipid bilayer and aqueous core, respectively. Encapsulating magnetic nanoparticles in liposomes will preserve the magnetic properties and improve pharmacokinetics.¹⁶

Nickel is considered a metal of biological interest, as it presents magnetic properties at room temperature. However, its toxicity and high reactivity make pure nickel nanoparticles not suitable for biomedical applications. The coating of nickel nanoparticles with a silica shell¹⁷ or the use of nickel ferrite nanoparticles have been proposed, the latter being generally less cytotoxic for HeLa cells than cobalt or zinc ferrites.^{18,19}

In this work, nickel ferrite nanoparticles (NPs) were synthesized and characterized. These NPs were either entrapped in liposomes, originating aqueous magnetoliposomes (AMLs), or covered with a lipid bilayer, forming dry magnetoliposomes (DMLs), the last ones prepared by a new promising route. The interaction between the prepared magnetoliposomes and models of cell membranes (giant unilamellar vesicles, GUVs) was also evaluated using FRET (Förster Resonance Energy Transfer), keeping in mind future applications of drug delivery using this type of magnetic systems.

3. Experimental

All the solutions were prepared using spectroscopic grade solvents and ultrapure water (Milli-Q grade).

3.1 Preparation of nickel ferrite nanoparticles (NPs)

NiFe₂O₄ NPs were obtained by a co-precipitation method in 5 mL aqueous solution, by reacting 1 mL of NiCl₂ (1 M) and 2 mL of FeCl₃.6H₂O (1 M) with 1.818 mL

of sodium hydroxide (18.94 M). After 40 minutes at 80°C, under magnetic stirring, NiFe₂O₄ NPs were formed.

Citric acid (Merck) was added in some assays in a molar ratio 1:1, as it prevents nanoparticles aggregation and can preserve monodispersity.⁹ Some of the particles, after several cycles of centrifugation and aqueous redispersion, were subjected to calcination using different temperatures and calcination times.

3.2 Preparation of magnetoliposomes

Aqueous magnetoliposomes (AMLs) are formed by the encapsulation of the synthesized magnetic NPs in liposomes. Egg yolk phosphatidylcholine (Egg-PC), from Sigma-Aldrich, was used for lipid vesicle formation. A 10 mM Egg-PC solution in ethanol was injected, under vigorous vortexing, to an aqueous solution of NPs (ethanolic injection method).²⁰ After encapsulation, the ferrofluid was washed with water and purified by ultracentrifugation to remove all the non-encapsulated NPs.

A new route for the synthesis of dry magnetoliposomes (DMLs) was developed. First, 15 µL of the NiFe₂O₄ NPs aqueous dispersion obtained in 3.1 was diluted with 3 mL of water and centrifuged. Then, the deposited particles were dispersed in 70 µL water in an ultrasonicator, for one minute at 189 W, and 3 mL of chloroform were added. After vigorous agitation, 300 µL of a 20 mM methanolic solution of 1,2-dioleoyl-*sn*-glycero-3-phospho-(1'-*rac*-glycerol) (sodium salt) (DOPG, from Sigma-Aldrich) were added under vortexing, to form the first lipid layer of the DMLs. The particles were washed twice by centrifugation with a mixed solution of methanol/acetone 1:1 (v/v), in order to remove all the lipid that was not attached to the NPs. The second lipid layer was then formed by the injection of 300 µL of DOPG (20 mM), under vortexing, in a 3 mL aqueous dispersion of the particles with the first layer. This second step is analogous to the build-up of the second lipid layer in the already reported DMLs synthesis method.²¹ The resulting DMLs were then washed and purified with pure water by centrifugation in order to preserve their structure.

For comparison with this new method, dry magnetoliposomes were also synthesized by the method previously described.²¹

3.3 Preparation of Giant Unilamellar Vesicles (GUVs)

Soybean lecithin (*L*-α-Phosphatidylcholine), from Sigma-Aldrich, was used for GUVs preparation, using a procedure previously described.^{22,23} 100 µL of soybean

lecithin (1 mM) were dried under an argon stream to produce a thin and homogeneous lipid film. 40 μL of water were added to the film and it was incubated at 45°C for 30 minutes. Next, 3 mL of 0.1 M glucose solution were added and the resulting mixture was again incubated at 37°C for 2 hours. Finally, after incubation, the GUVs suspension was centrifuged at 14000 g for 30 minutes at 20°C, to remove multilamellar vesicles and lipid aggregates.

3.4 Spectroscopic measurements

3.4.1 General methods

Absorption spectra were recorded in a Shimadzu UV-3101PC UV-vis-NIR spectrophotometer. Fluorescence measurements were performed using a Fluorolog 3 spectrofluorimeter, equipped with double monochromators in both excitation and emission and a temperature controlled cuvette holder. Fluorescence spectra were corrected for the instrumental response of the system.

3.4.2 FRET measurements

The interaction of aqueous magnetoliposomes with models of biological membranes (GUVs) was evaluated by Förster Resonance Energy Transfer (FRET). Magnetoliposomes were labeled with both NBD-C₁₂-HPC (1-palmitoyl-2-{12-[(7-nitro-2-1,3-benzoxadiazol-4-yl)amino]hexa- noyl}-*sn*-glycero-3-phosphocholine, from Avanti Polar Lipids, structure in Fig. 1), acting as energy donor, and the hydrophobic probe Nile Red (from Fluka, structure also shown in Fig. 1) as energy acceptor. FRET efficiency, Φ_{RET} , defined as the proportion of donor molecules that have transferred their excess energy to acceptor molecules, can be obtained by taking the ratio of the donor integrated fluorescence intensities in the presence of acceptor (F_{DA}) and in the absence of acceptor (F_{D}) (eqn (1)),²⁴

$$\Phi_{\text{RET}} = 1 - \frac{F_{\text{DA}}}{F_{\text{D}}} \quad (1)$$

The distance between donor and acceptor molecules can be determined through the FRET efficiency (eqn (2)),

$$r_{\text{AD}} = R_0 \cdot \left[\frac{1 - \Phi_{\text{RET}}}{\Phi_{\text{RET}}} \right]^{1/6} \quad (2)$$

where R_0 is the Förster radius (critical distance), that can be obtained by the spectral overlap, $J(\lambda)$, between the donor emission and the acceptor absorption, according to eqn (3) and (4) (with R_0 in Å, λ in nm, $\varepsilon_A(\lambda)$ in $M^{-1} \text{ cm}^{-1}$),²⁴

$$R_0 = 0.2108 [k^2 \Phi_D^0 n^{-4} J(\lambda)]^{1/6} \quad (3)$$

$$J(\lambda) = \int_0^\infty I_D(\lambda) \varepsilon_A(\lambda) \lambda^4 d\lambda \quad (4)$$

where $k^2 = 2/3$ is the orientational factor assuming random orientation of the dyes, Φ_D^0 is the fluorescence quantum yield of the donor in the absence of energy transfer, n is the refraction index of the medium, $I_D(\lambda)$ is the fluorescence spectrum of the donor normalized so that $\int_0^\infty I_D(\lambda) d\lambda = 1$, and $\varepsilon_A(\lambda)$ is the molar absorption coefficient of the acceptor.

FRET assays were also employed to confirm the formation of the lipid bilayer in the dry magnetoliposomes (DMLs). The rhodamine B labeled lipid *N*-(lissamine Rhodamine B sulfonyl)-1,2-dioleoyl-*sn*-3-phosphatidylethanolamine (Rh-DOPE) (ammonium salt) (from Avanti Polar Lipids, structure in Fig. 1) was included in the first lipid layer (acting as energy acceptor), while the nitrobenzoxazole labeled lipid NBD-C₁₂-HPC was included in the second lipid layer (energy donor).

The fluorescence quantum yield, Φ_s , of the energy donor (the dye NBD) in magnetoliposomes was determined by the standard method (eqn (5)),^{25,26}

$$\Phi_s = \left[\frac{(A_r F_s n_s^2)}{(A_s F_r n_r^2)} \right] \Phi_r \quad (5)$$

where A is the absorbance at the excitation wavelength, F the integrated emission area and n is the refraction index of the solvents. Subscripts refer to the reference (r) or sample (s) compound. The absorbance value at excitation wavelength was always less than 0.1, in order to avoid inner filter effects. The NBD-C₁₂-HPC fluorescent labeled lipid incorporated in lipid membranes was used as reference, $\Phi_r = 0.32$ at 25°C, as reported by Invitrogen.²⁷

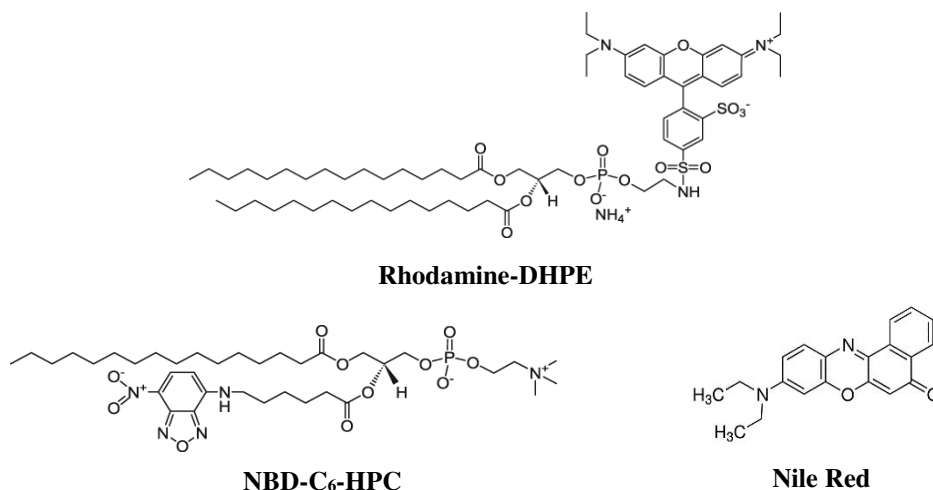


Fig. 1 Structures of the fluorescent labeled lipids and the dye Nile Red.

3.5 Structural characterization

3.5.1 Transmission electron microscopy (TEM)

HR-TEM images of nickel ferrite nanoparticles were recorded using a Transmission Electron Microscope JEOL JEM 2010F operating at 200 kV coupled to an Electron Dispersive Spectroscopic analyzer (EDS) at C.A.C.T.I (Centro de Apoyo Científico e Tecnológico á Investigación), Vigo, Spain. The processing of TEM images was performed using ImageJ software. It consisted in enhancing local contrast followed by automatic local thresholding and particle analysis. The area of each particle allowed an estimation of the particle diameter. The resulting histograms were fitted to Gaussian distributions.

Diffraction pattern indexing was made using the relationship between the R ratio and the Miller indices, hkl . For a cubic crystal, the following holds

$$\frac{R_m}{R_n} = \frac{(h_m^2 + k_m^2 + l_m^2)^{1/2}}{(h_n^2 + k_n^2 + l_n^2)^{1/2}} \quad (6)$$

3.5.2 Scanning electron microscopy (SEM)

Scanning electron microscopy (SEM) images of dry magnetoliposomes were recorded using a Scanning Electron Microscope FEI - Nova 200 NanoSEM. For the negative staining procedure, a 2% aqueous solution of ammonium molybdate tetrahydrate (from Sigma-Aldrich) was prepared. Then, 20 μ L of sample and 20 μ L of staining solution were mixed and a drop of this mixture was placed onto the Formvar grid, held by

tweezers. After 20 seconds, almost all the solution was removed with filter paper and left dry.

3.5.3 X-Ray Diffraction (XRD) and DLS measurements

X-Ray Diffraction (XRD) analyses were performed using a conventional Philips PW 1710 diffractometer, operating with Cu K α radiation, in a Bragg-Brentano configuration.

The mean diameter and size distribution of the magnetic liposomes were measured using a Dynamic Light Scattering (DLS) equipment (NANO ZS Malvern Zetasizer) at 25°C, using a He-Ne laser of 633 nm and a detector angle of 173°. Five independent measurements were performed for each sample. The data analysis was performed using the method previously described.¹⁷

3.6 Magnetic measurements

3.6.1 General methods

Magnetic measurements were performed at room temperature in a Superconducting Quantum Interference Device (SQUID) magnetometer (Quantum Design MPMS5XL), using applied magnetic fields up to 5.5 T.

3.6.1.1 Temperature dependence of the magnetization and magnetic hysteresis cycles

The temperature dependence of the magnetization was measured in the temperature range from 5 K to 380 K. The curves were obtained by initially cooling the sample under an applied magnetic field of $H = 100$ Oe (field cooled, FC) and then measuring its magnetization with increasing temperature (applied field of $H = 50$ Oe). Subsequently, after reaching 380 K, the sample was re-cooled, this time with no applied magnetic field (zero-field-cooled, ZFC) and the magnetization measurements were again performed with increasing temperature, under the same magnetic field of $H = 50$ Oe. From the behavior of the FC and ZFC curves, the blocking temperature (T_B) of the superparamagnetic nanoparticles can be obtained.²⁸ The magnetization hysteresis loop measurements were made by fixing the temperature and measuring the magnetization at a series of different applied magnetic fields. This type of study gives information about the maximum magnetization and the degree at which the sample remains magnetized

when the applied field is removed, and how easily the sample magnetization can be reversed, the so-called coercive field.

4. Results and Discussion

4.1 Nanoparticles characterization

4.1.1 UV-Visible Absorption Spectra

Fig. 2 shows the UV-Visible absorption spectra of the synthesized nickel ferrite NPs. For small metal particles (size below 20 nm), the absorption process dominates and a single band around 355 nm is usually observed, while, when size increases, light scattering becomes dominant. The importance of light absorption over scattering depends, not only on NPs size, but also on their shape, composition and environment.²⁹ The absorption band observed around 355 nm, before and after calcination, confirmed the metal oxide nature of the NPs (Fig. 2). After calcination, a higher dispersion was observed, that is consistent with a size increase upon calcination.³⁰

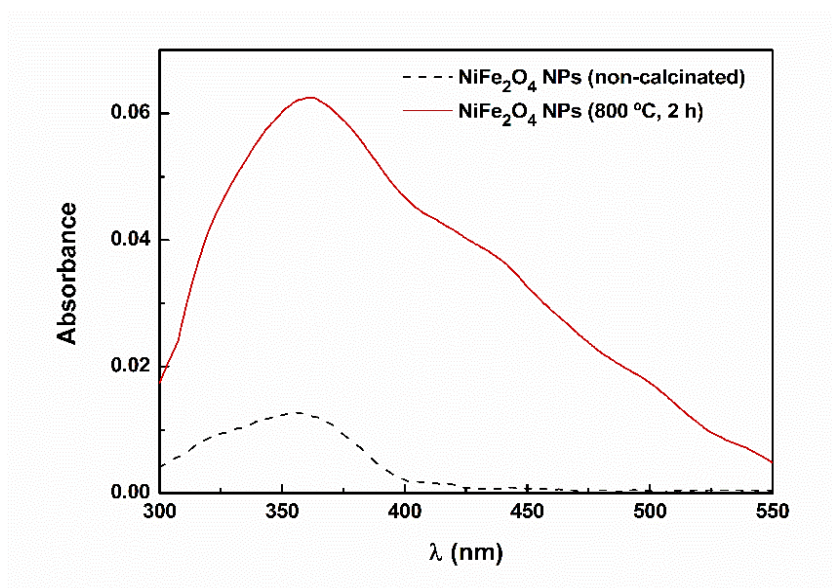


Fig. 2 UV-Visible absorption spectra of NiFe_2O_4 particles synthesized by the coprecipitation method, before and after calcination at 800°C for 2 hours.

4.1.2 XRD analysis

The synthesis of the nickel ferrite NPs was confirmed by XRD analysis (Fig. 3). NiFe_2O_4 XRD pattern shows that nanoparticle calcination is required to obtain a crystalline phase of nickel ferrite spinel. All the characteristic peaks for a pure crystalline phase of nickel ferrite spinel, marked by their indices, are shown in Fig. 3. Additional

peaks are observed, indicating the presence of other crystalline phases. One possible phase is the orthorhombic sodium ferric dioxide (β -NaFeO₂, group Pn2₁a, CIF 1008191)³¹ and the corresponding peaks are identified in Fig. 3 with a ▼ symbol. This phase can be obtained either through a high temperature solid reaction³¹ or by solvo thermal method,³² and its presence is possible because a high concentration of sodium hydroxide was used in the experimental procedure for NiFe₂O₄ synthesis. In order to obtain a good fit of the diffractogram through Rietveld analysis using FullProf software,³³ it was necessary to include yet another phase, which was nickel oxide (NiO, space group Fm3m, CIF 1010381). This phase has diffraction peaks that overlap the NiFe₂O₄ spinel phase (space group Fd-3m) and are indicated in Fig. 3 with a ▽ symbol.

A good fit was obtained, as it can be observed in the residuals in Fig. 3. The reduced χ^2 obtained was 1.75 and the Bragg reliability factors, R_F , were 1.99, 4.77 and 2.5 for NiFe₂O₄, β -NaFeO₂ and NiO, respectively. This result was obtained by optimization of the isotropic thermal factor (B_{iso}) of each atom. Some negative values were obtained, that can be explained by surface roughness effects³⁴ (full details of the Rietveld optimization procedure are included in Supplementary Information).

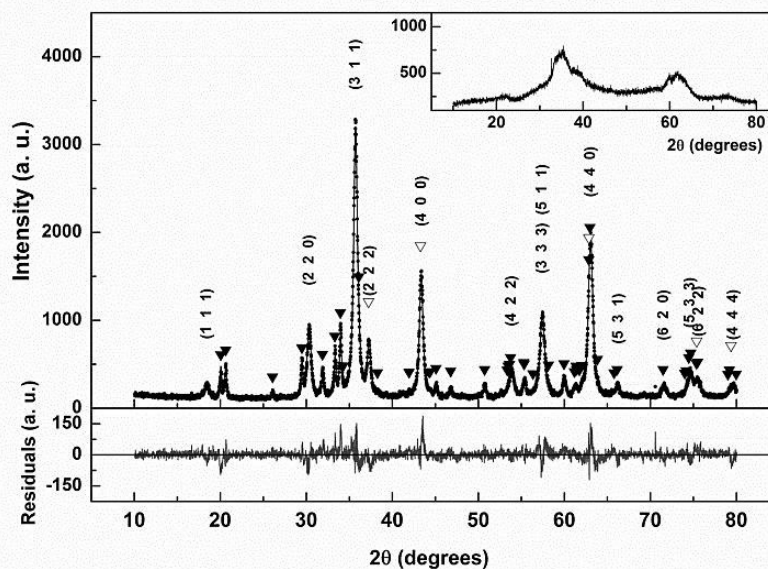


Fig. 3 XRD pattern of the NiFe₂O₄ NPs, before and after calcination at 800°C. (▼) β -FeNaO₂ phase; (▽) NiO phase. Inset: XRD pattern before calcination.

Fixing those parameters to zero, resulted in a slightly worse optimization with χ^2 of 2.43 and R_F factors of 3.75, 7.03 and 3.62 for the included phases in the same order.

The obtained fractional contribution of each phase and the estimated size are indicated in Table 1.

Table 1 Selected Rietveld analysis parameters.

Phase	B_{iso} factors	Scale Factor	ATZ	Volume (\AA^3)	Fractional Contribution (%)	Size (nm)
NiFe ₂ O ₄	Optimized	1.72×10^{-7}	1080076.5	579.048	67.2	13.2
	Fixed	1.99×10^{-7}		578.819	69.8	13.4
NaFeO ₂	Optimized	3.17×10^{-4}	443.34	216.802	19.1	37.5
	Fixed	3.25×10^{-4}		216.693	17.5	37.9
NiO	Optimized	4.38×10^{-7}	688429.69	72.945	13.7	19.0
	Fixed	5.51×10^{-7}		72.912	12.7	17.5

The results in Fig. 3 and Table 1 correspond to an inverted spinel structure ($\text{Fe}^{\text{Td}}\text{Ni}^{\text{Oh}}\text{Fe}^{\text{Oh}}\text{O}_4$, Oh and Td representing, respectively, octahedral and tetrahedral sites). Defining the cation ordering in the spinel structure with a ferrite of type $\text{Ni}^{\text{Td}}_{(1-i)}\text{Fe}^{\text{Td}}_i\text{Ni}^{\text{Oh}}_i\text{Fe}^{\text{Oh}}_{(2-i)}$, the Rietveld optimization resulted in a $i = 0.76$ with χ^2 of 1.74 and R_F factors of 1.85, 4.80 and 2.52 for the included phases in the same order. Although the fitting of the XRD pattern did not improved much, the R_F of the NiFe₂O₄ improved significantly. In bulk form, nickel ferrite is a totally inverted spinel, $i = 1$.³⁵ At the nanoscale, values of $i = 0.9$ were reported for 3–4 nm nanoparticles,³⁶ but the bulk value was retained for particles of 40 nm size.³⁷

4.1.3 TEM images and elemental analysis

TEM images (Fig. 4) revealed that the synthesized NPs have diameters on the order of tens of nanometers, with a size distribution of 11 ± 5 nm, obtained from the histogram (Fig. 4B) of the image in Fig. 4A. This result is roughly in accordance with the values estimated by the Langevin function (see below) and with the estimated value from XRD measurements.

EDAX elemental analysis confirmed the presence of Ni, Fe and O elements in an atomic proportion near the calculated values for NiFe₂O₄ (Fig. 5, Table 2). Besides X-ray emission from Cu and C that originates from the TEM grid, additional peaks due to Na and Si are also observed (Fig. 5).

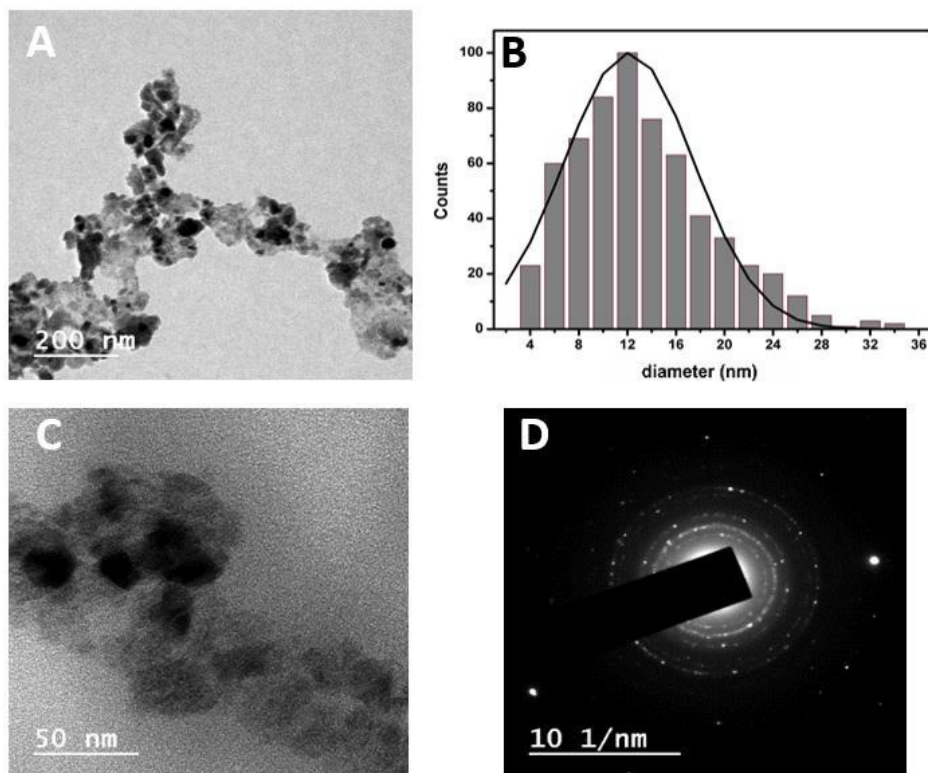


Fig. 4 TEM images (A and C) of the synthesized NiFe₂O₄ NPs, calcinated at 800°C, at different amplifications. **B**: Particles size histogram of image A and fitting to a Gaussian distribution. **D**: Corresponding electron diffraction pattern.

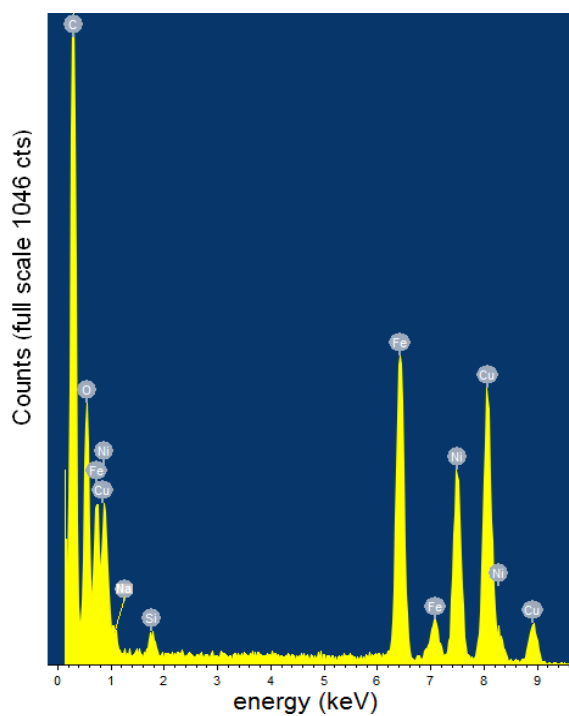


Fig. 5 EDAX elemental analysis of area corresponding to Fig. 4C.

Table 2 EDAX atomic percentages considering only Ni, Fe and O contributions and comparison with the values predicted for NiFe₂O₄ NPs.

Element	EDAX atomic (%)	Calculated atomic (%)
Ni	15.6	14.3
Fe	24.1	28.6
O	60.3	57.1

The former confirms the presence of NaFeO₂ and the latter probably originates from SiO₂, which results from the etching of the glass of test tubes in which the nanoparticles synthesis was conducted, at conditions of high pH and temperature. As no SiO₂ phase was detected by XRD, either the SiO₂ phase is amorphous or its overall amount is too low to be detected by XRD.

The selected area recorded electron diffraction pattern (Fig. 4D) indicates the good crystalline nature of the material. An interlattice plane distance of 0.29 nm, which corresponds to (2 2 0) plane, was calculated. Nickel ferrite nanoparticles have inverse spinel structure with a face centered cubic crystal structure. The identified planes (2 2 0), (3 1 1), (4 0 0), (3 3 3) + (5 1 1), and (4 4 0), from inside to outside, are in accordance with a face-centered cubic lattice of the spinel ferrite structure.³⁸

TEM images on other sample regions allowed the detection of other type of particles, with a larger size (~200 nm) (Fig. S1 in Supplementary Information). The EDAX analysis in that region is compatible with the presence of NiO particles (Fig. S2 in Supplementary Information). Interestingly, no sodium was detected and the quantity of Si is much less than in the EDAX analysis from Fig. 4C.

4.1.4 Magnetic properties

Nickel ferrite NPs are soft ferromagnetic particles and their magnetic behavior depends on the synthesis method and particle size.^{39,40} Fig. 6 shows the hysteresis loop of NiFe₂O₄ NPs after calcination at room temperature. A small hysteresis is observed, with a coercive field of 12 Oe. The presence of superparamagnetic behavior can be related to the magnetic squareness value of the hysteresis cycle, which is the ratio between the residual magnetizations (M_r) and the saturated magnetization (M_s). Magnetic squareness values indicative of superparamagnetism are of the order or below 0.1, meaning the loss of more than 90% of the magnetism on removal of the applied magnetic field.^{19,41} Here, the obtained magnetic squareness value for the nanoparticles is 7.2×10^{-5} which indicates that the synthesized NiFe₂O₄ nanoparticles present a superparamagnetic behavior at room

temperature. Additionally, the magnetization of NiFe₂O₄ NPs does not saturate up to the maximum field that was applied, as shown on Fig. 6, reaching 23.54 emu/g at an applied field of 5 T. This value is somewhat below the saturation value for bulk Ni ferrite (50 emu/g at 20°C)⁴² and this behavior can be attributed to the presence of the β-NaFeO₂ and NiO residual phases observed on the XRD results. β-NaFeO₂ is a weak ferromagnetic material at room temperature, with a magnetic moment per unit cell of $5 \times 10^{-4} \mu_B$,³¹ while NiO is antiferromagnetic.⁴² Thus, their presence on the samples then gives rise to a somewhat lower overall magnetization, as compared to a fully NiFe₂O₄ one.

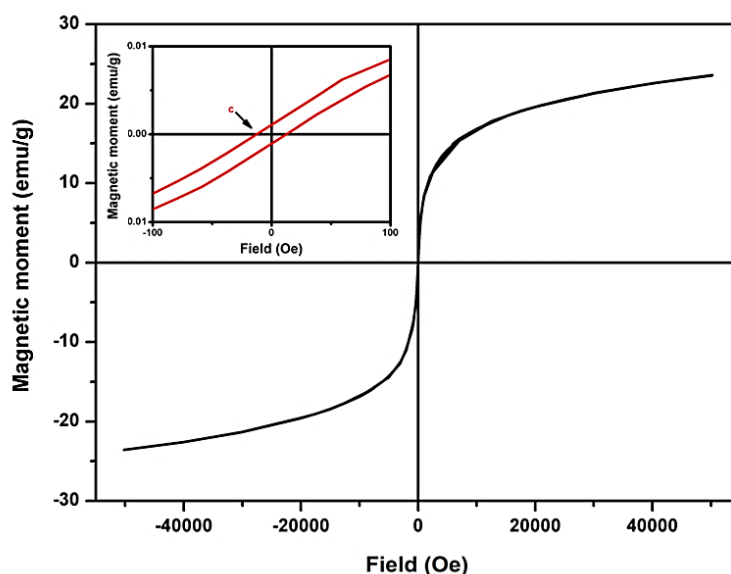


Fig. 6 Magnetic moment per gram of NiFe₂O₄ NPs (synthesized in the presence of citric acid, calcinated at 800°C) versus applied magnetic field. Inset: Hysteresis loop at room temperature.

For a superparamagnet, the temperature dependence of the zero-field-cooling and field-cooling magnetization curves present a different behavior. Starting from the low temperatures on the ZFC curve, as the temperature increases the blocked magnetic moments align with the applied measuring magnetic field, leading to an initial increase of the sample magnetization. However, as soon as thermal fluctuations are able to allow the moments to overcome the magnetic anisotropy energy barrier, the thermal randomization of the intraparticles magnetic moments produces a subsequent decrease of the magnetization curve, with increasing temperature. In this way, the zero-field-cooling curve peak corresponds to sample blocking temperature²⁸ and here a blocking temperature of $T_B = 214$ K, below room temperature, was obtained for NiFe₂O₄. On the other hand, on the FC curve, the magnetic moments were initially forced to be aligned

with the magnetic field imposed during cooling. This then gives a significant overall magnetization at low temperatures, as seen on the FC curve of Fig. 7, that monotonically decreases with increasing temperature. Below T_B , the magnetic nanoparticles show ferromagnetic behavior, as thermal fluctuations are not enough to randomize the intraparticles magnetic moments. Above the blocking temperature, NPs show superparamagnetic properties and the ZFC and FC curves are expected to show the same magnetization decreasing trend with increasing temperature. The observed difference between the ZFC and FC above T_B , up to ~ 250 K, is related with the size dispersion of the nanoparticles.

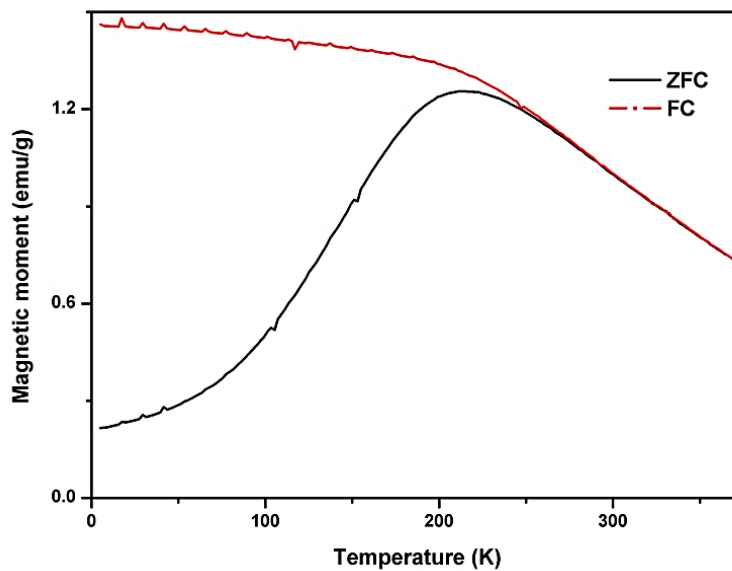


Fig. 7 ZFC and FC magnetization curves of NiFe_2O_4 NPs synthesized in the presence of citric acid calcinated at 800°C .

For an ensemble of superparamagnetic particles above the blocking temperature, the magnetization can be described by the Langevin function⁴²

$$M(H, T) = N\mu L\left(\frac{\mu H}{k_B T}\right) = N\mu\left(\coth\left(\frac{\mu H}{k_B T}\right) - \frac{k_B T}{\mu H}\right) \quad (7)$$

where μ is the particle magnetic moment, k_B is the Boltzmann constant, T is the absolute temperature, N is the number of particles per volume and H is the applied magnetic field.

The magnetization hysteresis cycles were fitted with eqn (7), in order to determine μ . Considering a magnetic moment of $\mu_{\text{NiFe}_2\text{O}_4} = 2.3 \mu_B$ per NiFe_2O_4 ⁴², the number of formula units per particle can be obtained by dividing the fitted particle magnetic moment by $\mu_{\text{NiFe}_2\text{O}_4}$. Then, the particle radius can be obtained by assuming spherical particles with

density of 5.368 g/cm^3 .⁴³ Table 3 summarizes the results obtained for the fitting of eqn (7) to the hysteresis loops before and after calcination. The determined diameter is of the order of 7 nm after calcination. The high values for R^2 (Table 3) indicate that the experimental data closely follow a Langevin function, as expected for superparamagnetic NPs. Higher saturation magnetization values were obtained for the larger particles. After calcination at high temperatures, it was observed that the NiFe_2O_4 crystallite size increases and their corresponding surface area decreases.⁴⁴

Table 3 Magnetization saturation (M_s), mass (m) and size (d) of the synthesized NPs.

	R^2	M_s (emu/g)	m (g)	V (cm ³)	d (nm)
Before calcination	0.99886	17.57	1.94×10^{-19}	3.61×10^{-20}	4.12
After calcination at 800 °C	0.95936	25.00	7.69×10^{-19}	1.43×10^{-19}	6.50

4.2 Characterization of magnetoliposomes and interaction with model membranes

4.2.1 DLS and SEM measurements

As described in the Experimental Section, two types of magnetoliposomes were synthesized, aqueous magnetoliposomes (AMLs) and dry magnetoliposomes (DMLs). Dynamic Light Scattering (DLS) measurements revealed that aqueous magnetoliposomes of egg lecithin (Egg-PC) with entrapped nickel ferrite nanoparticles have diameters of 92 ± 18 nm. These values are in accordance with previous results reported for egg lecithin-based liposomes without NPs,^{17,45} showing that the small nickel ferrite nanoparticles have a very small influence on the size of aqueous magnetoliposomes.

DMLs containing nickel ferrite NPs covered by the phospholipid DOPG were prepared by the method previously reported²¹ and by the new method proposed here. The hydrodynamic diameter obtained for the DMLs prepared by the previous method was 94 ± 3 nm, similar (but less polydisperse) to the one reported for DMLs containing nickel nanoparticles.¹⁷

DMLs containing calcinated NiFe_2O_4 nanoparticles and prepared by the new method display higher hydrodynamic diameters of 178 ± 15 nm, also with a narrow size distribution. SEM images of these DMLs show sizes below 100 nm and an approximately spherical shape (Fig. 8A). The application of negative staining allows the visualization of the lipid layer (Fig. 8B) around the nanoparticles cluster. Some aggregation in aqueous media can justify the larger size of DMLs determined by DLS, also inferred from Figure

8B. Therefore, the new method for the synthesis of dry magnetoliposomes seems promising for DMLs based on calcinated magnetic nanoparticles.

Compared with other systems where magnetic nanoparticles are covered with molecules including functional groups like carboxylic acids, amines or phosphates that can be coupled to lipid molecules, the DMLs directly inherit the characteristics of low toxicity and improved pharmacokinetics of liposomes.

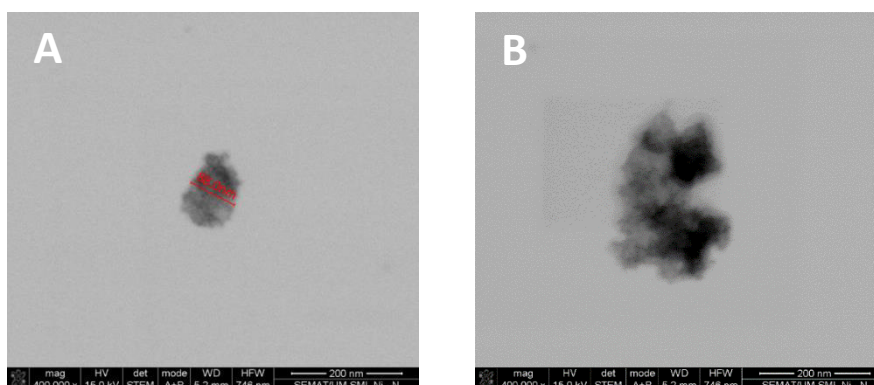


Fig. 8 A, B. SEM images of the synthesized DMLs based on NiFe_2O_4 NPs. In image **B**, a negative staining was applied.

4.2.2 AMLs interaction with model membranes

The non-specific interactions of the aqueous magnetoliposomes (AMLs) containing nickel ferrite nanoparticles with giant unilamellar vesicles (GUVs), models of cell membranes, were evaluated by FRET. For that purpose, the labeled lipid NBD- C_{12} -HPC (acting as energy donor) and the lipid probe Nile Red⁴⁶⁻⁵⁰ (acting as energy acceptor) were both included in AMLs. The significant overlap between the NBD- C_{12} -HPC emission band and the Nile Red absorption spectrum (Fig. 9A - inset) indicates that FRET process between these two fluorescent molecules is expected to be efficient, if the donor-acceptor distance is below 100 Å.²⁴ The fluorescence spectra of the AMLs containing NiFe_2O_4 nanoparticles were measured before and after interaction with GUVs. Before interaction with GUVs, two distinct emission bands are observed, the first ($\lambda_{\text{max}} = 550$ nm) corresponding to NBD- C_{12} -HPC emission and the second one at 630 nm, corresponding to Nile Red emission,⁴⁶⁻⁵⁰ that arises from the energy transfer of excited NBD molecules to Nile Red. After GUVs interaction, if fusion occurs, a larger membrane is formed,⁵¹ which leads to an increase in the donor-acceptor distance and a corresponding decrease in the energy transfer efficiency from the NBD moieties (scheme in Fig. 9B). The results in Fig. 9A (after interaction) are consistent with membrane fusion

between the AMLs and GUVs, as it is possible to observe an increase in the NBD (donor) emission band and the decrease of the Nile Red (acceptor) fluorescence band after interaction with GUVs.

Therefore, the aqueous magnetoliposomes based on nickel ferrite NPs can be used as magnetic nanocarriers for both hydrophilic (in the inner aqueous volume) and hydrophobic (in the lipid bilayer) drugs, with the capability of drug release in cells upon membrane fusion.

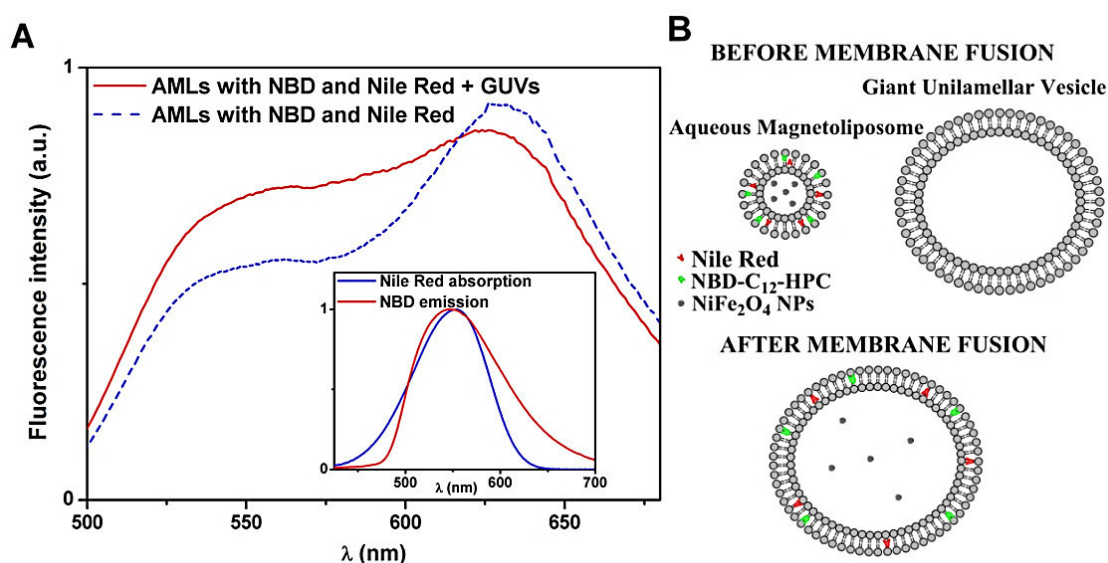


Fig. 9 A. Fluorescence spectra ($\lambda_{exc} = 400$ nm) of AMLs of egg lecithin and NiFe₂O₄ NPs containing both NBD-C₁₂-HPC and Nile Red, before and after interaction with GUVs. Inset: Spectral overlap (spectra are normalized) between the fluorescence emission of the donor (NBD-C₁₂-HPC) and the absorption of the acceptor (Nile Red). **B.** Schematic representation of membrane fusion between AMLs and GUVs.

4.2.3 DMLs formation and interaction with model membranes

Dry magnetoliposomes (DMLs) are expected to have better magnetic response when compared with AMLs. In fact, it has been shown that AMLs present poor magnetic properties similar to those of the aqueous ferrofluid,⁵² while DMLs keep almost the same magnetic properties as the neat nanoparticles.⁵³

The new method for the synthesis of DMLs described here is a promising route to obtain liposomes with improved magnetic properties. Almost every magnetic nanoparticle synthesis methods reported in literature require calcination.^{30,39,54-58} Comparing with literature, our route stands out because coating of the magnetic NPs cluster with the lipid bilayer occurs only after NPs synthesis. This way, the calcination

process that may improve the magnetic properties, can be used without risk of “burning” the lipid layer.

In this procedure, NPs clusters were covered by a double layer of the anionic phospholipid DOPG. The formation of the lipid bilayer was confirmed by FRET. For that purpose, the NDB labeled lipid NBD- C_{12} -HPC, was included in the second lipid layer of the DMLs, acting as energy donor, while the labeled lipid Rhodamine B-DOPE, included in the first lipid layer, acts as energy acceptor.

Fluorescence spectra of DMLs containing only the energy donor (NBD- C_{12} -HPC) or only the acceptor (Rhodamine B-DOPE) and DMLs containing both labeled lipids were measured (Fig. 10), exciting only the donor NBD ($\lambda_{exc} = 465$ nm). As expected, characteristic NBD emission is detected for DMLs labeled only with NBD- C_{12} -HPC, while negligible fluorescence is observed for the DMLs containing only Rhodamine B-DOPE (as Rhodamine B is not directly excited at this wavelength). The fluorescence spectrum of the DMLs containing both donor and acceptor labeled lipids shows a decrease in the NBD emission band, contrasting with a strong increase in the Rhodamine-DOPE emission band that results from the energy transfer of the excited NBD to Rhodamine.

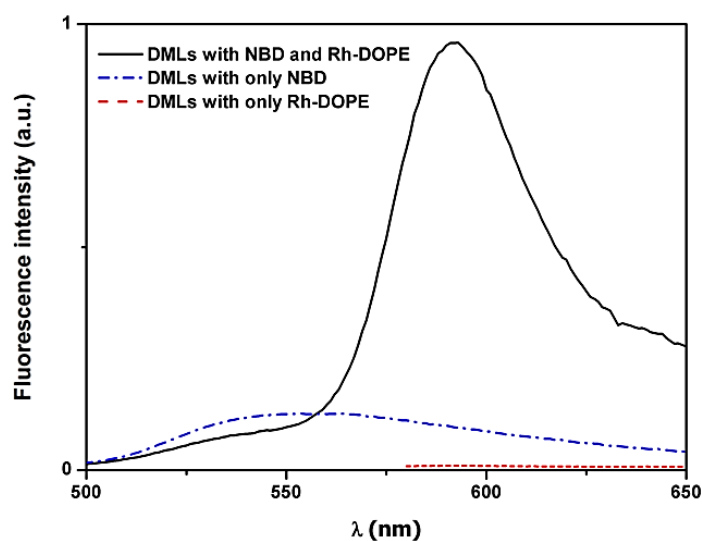


Fig. 10 Fluorescence spectra ($\lambda_{exc} = 470$ nm, no Rhodamine excitation) of DMLs covered with DOPG labeled with only NBD- C_{12} -HPC; DMLs labeled with only Rhodamine B-DOPE and DMLs labeled with both NBD- C_{12} -HPC and Rhodamine B-DOPE.

From eqn (1) to (4), a FRET efficiency of 23% was calculated, with a corresponding donor-acceptor distance (r_{AD}) of 3.11 nm. Cell membrane has a typical thickness of 7 to 9 nm.⁵⁹ Therefore, the r_{AD} value obtained clearly indicates that the labeled lipids Rhodamine-DOPE and NBD- C_{12} -HPC are placed in the first and second

lipid layer, respectively, in the structures formed. This confirms the structure of lipid bilayer around NPs clusters and, therefore, the synthesis of DMLs by the new method.

The non-specific interaction of the synthesized NiFe_2O_4 DMLs with models of cell membranes (GUVs) was also evaluated by FRET, using a similar procedure to the one used for AMLs. Therefore, the fluorescence spectra of DMLs containing both the labeled lipid NBD- C_{12} -HPC (energy donor) and the labeled lipid Rhodamine B-DOPE (energy acceptor) were measured before and after interaction with GUVs (Fig. 11).

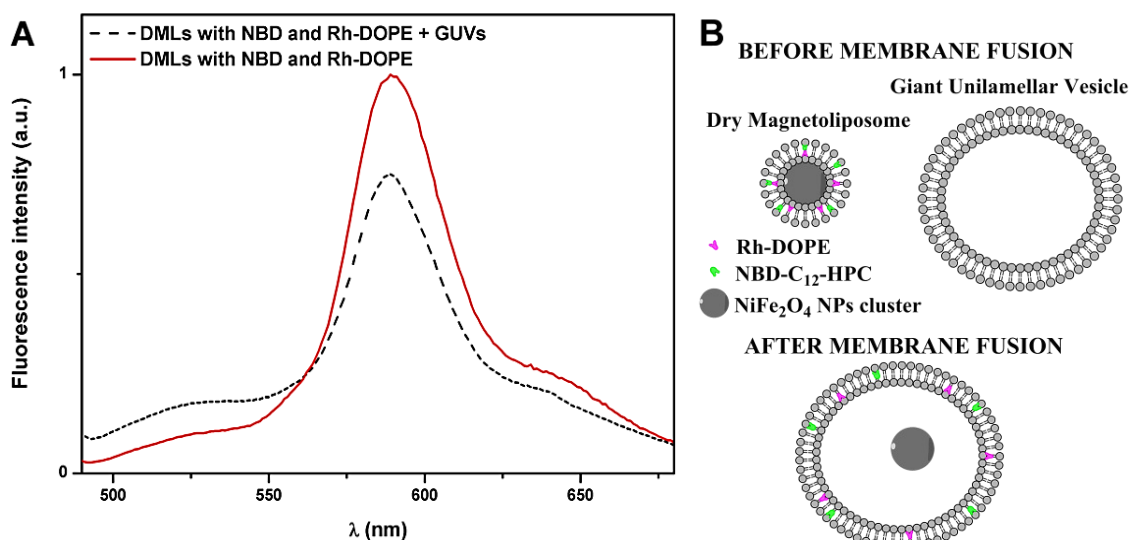


Fig. 11 **A.** Fluorescence spectra ($\lambda_{\text{exc}} = 470$ nm) of DMLs labeled with NBD- C_{12} -HPC and Rhodamine B-DOPE, before and after interaction with GUVs. **B:** Illustration of the fusion between the GUVs and DMLs labeled with both NBD- C_{12} -HPC and Rhodamine B-DOPE.

As expected, before membrane fusion, two emission bands were observed, the first one corresponding to the NBD emission and the second to the Rhodamine-DOPE emission, resulting from the energy transfer of the excited NBD. After membrane fusion, a larger membrane should be formed, with a corresponding increase in the donor-acceptor distance, and so an energy transfer decrease is expected (Fig. 11B). The fluorescence spectrum of the DMLs after membrane fusion reveals an increase in the donor emission and a decrease in the acceptor band as predictable (Fig. 11A), confirming membrane fusion between the two systems. Therefore, the dry magnetoliposomes are also promising systems as nanocarriers for hydrophobic drugs, as they can be guided by a magnetic field to the therapeutic site and release the drug upon fusion with cell membranes. It is expected that DMLs present better magnetic properties than AMLs, due to the lack of aqueous

dilution of NPs. To our knowledge, it is the first time that fusion between dry magnetoliposomes (DMLs) and models of cell membranes is reported.

5. Conclusions

In this work, small nickel ferrite nanoparticles, with a size distribution of 11 ± 5 nm, were synthesized by coprecipitation method followed by calcination at 800°C. These particles present superparamagnetic behavior at room temperature.

Both aqueous and dry magnetoliposomes were prepared using the calcinated Ni ferrite nanoparticles, using a new method for DMLs synthesis. Both AMLs and DMLs exhibit an appropriate size to biomedical applications, namely as anticancer drug nanocarriers with a simultaneous capability of hyperthermia.

FRET measurements confirmed membrane fusion between both the aqueous and dry magnetoliposomes and models of cell membranes (GUVs). To our knowledge, it is the first time that fusion between dry magnetoliposomes and models of cell membranes is reported.

6. Acknowledgements

This work was supported by FEDER through the COMPETE/QREN/EU Program and by the Portuguese Foundation for Science and Technology (FCT) in the framework of the Strategic Project of CFUM [PEst-C/FIS/UI0607/2013 (F-COMP-01-0124-FEDER-022711)].

FCT, POPH-QREN and FSE are acknowledged for the PhD grant of A. R. O. Rodrigues (SFRH/BD/90949/2012) and for financial support to MAP-Fis PhD Programme.

7. References

1. A. A. Kuznetsov, A. R. Harutyunyan and E. K. Dobrinsky, *Scientific and Clinical Applications of Magnetic Carriers*, Plenum Press, New York, 1997.
2. A. A. Kuznetsov, V. I. Filippov, O. A. Kuznetsov, V. G. Gerlivanov, E. K. Dobrinsky and S. I. Malashin, New ferro-carbon adsorbents for magnetically guided transport of anti-cancer drugs, *J. Magn. Magn. Mater.*, 1999, **194**, 22-30.
3. R. Reszka, P. Beck, I. Fichtner, M. Hentschel, J. Richter and J. Kreuter, Body distribution of free liposomal and nanoparticle associated mitoxantrone in B16-Melanoma-bearing mice, *J. Pharmacol. Exp. Ther.*, 1997, **280**, 232-237.
4. A. A. M. van der Veldt, N. H. Hendrikse, E. F. Smit, M. P. J. Mooijer, A. Y. Rijnders, W. R. Gerritsen, J. J. M. van der Hoeven, A. D. Windhorst, A. A. Lammertsma and M. Lubberink, Biodistribution and radiation dosimetry of ¹¹C-labelled docetaxel in cancer patients, *Eur. J. Nucl. Med. Mol. Imaging*, 2010, **37**, 1950-1958.
5. M. Perry, *The chemotherapy source book*, 2nd ed. Baltimore: Williams & Wilkins, 1996.
6. A. S. Lubbe, C. Bergemann, J. Brock and D. G. McClure, Physiological aspects in magnetic drug-targeting, *J. Magn. Magn. Mater.*, 1999, **194**, 149-155.
7. S. Dandamudi and R. B. Campbell, The drug loading, cytotoxicity and tumor vascular targeting characteristics of magnetite in magnetic drug targeting, *Biomaterials*, 2007, **28**, 4673-4683.
8. H. Markides, M. Rotherham and A. J. El Haj, Biocompatibility and Toxicity of Magnetic Nanoparticles in Regenerative Medicine, *J. Nanomater.*, 2012, 1-11.
9. C. Pereira, A. M. Pereira, C. Fernandes, M. Rocha, R. Mendes, M. P. and C. Freire, Superparamagnetic MFe₂O₄ (M = Fe, Co, Mn) Nanoparticles: Tuning the Particle Size and Magnetic Properties through a Novel One-Step Coprecipitation Route, *Chem. Mater.* 2012, **24**, 1496-1504.
10. S. Dandamudi and R. B. Campbell, Development and characterization of magnetic cationic liposomes for targeting tumor microvasculature, *Biochim. Biophys. Acta*, 2007, **1768**, 427-438.
11. A. Akbarzadeh, M. Samiei and S. Davaran, Magnetic nanoparticles: preparation, physical properties, and applications in biomedicine, *Nanoscale Res. Lett.*, 2012, **7**, 144-157.

12. S. F. Medeiros, A. M. Santos, H. Fessi and A. Elaissari, Stimuli-responsive magnetic particles for biomedical applications, *Int. J. Pharm.*, 2011, **403**, 139-161.
13. P. Pradhan, J. Giri, F. Rieken, C. Koch, O. Mykhaylyk, M. Doblinger, R. Banerjee, D. Bahadur and C. Plank, Targeted temperature sensitive magnetic liposomes for thermo-chemotherapy, *J. Control. Release*, 2010, **142**, 108-121.
14. F. Li, J. Sun, H. Zhu, X. Wen, C. Lin and D. Shi, Preparation and characterization novel polymer-coated magnetic nanoparticles as carriers for doxorubicin, *Colloids Surf. B: Biointerfaces*, 2011, **88**, 58-62.
15. T. Mitsumata, A. Honda, H. Kanazawa and M. Kawai, Magnetically tunable elasticity for magnetic hydrogels consisting of carrageenan and carbonyl iron particles, *J. Phys. Chem. B*, 2012, **116**, 12341-12348.
16. J. J. W. Bulte, M. de Cuyper, D. Despres and J. A. Frank, Short vs. long-circulating magnetoliposomes as bone marrow-seeking MR contrast agents, *J. Magn. Reson. Imaging*, 1999, **9**, 329-335.
17. A. R. O. Rodrigues, I. T. Gomes, B. G. Almeida, J. P. Araújo, E. M. S. Castanheira and P. J. G. Coutinho, Magnetoliposomes based on nickel/silica core/shell nanoparticles: synthesis and characterization, *Mat. Chem. Phys.*, 2014, **148**, 978-987.
18. A. Tomitaka, A. Hirukawa, T. Yamada, S. Morishita and Y. Takemura, Biocompatibility of various ferrite nanoparticles evaluated by *in vitro* cytotoxicity assays using HeLa cells, *J. Magn. Magn. Mat.*, 2009, **321**, 1482-1484.
19. L. Khanna and N. K. Verma, Synthesis, characterization and *in vitro* cytotoxicity study of calcium ferrite nanoparticles, *Mater. Sci. Semicond. Process.*, 2013, **16**, 1842-1848.
20. J. M. H. Kremer, M. W. J. v. d. Esker, C. Pathmamanoharan and P. H. Wiersema, Vesicles of variable diameter prepared by a modified injection method, *Biochemistry*, 1977, **16**, 3932-3935.
21. C. J. Meledandri, T. Ninjbadgar and D. F. Brougham, Size-controlled magnetoliposomes with tunable magnetic resonance relaxation enhancements, *J. Mater. Chem.*, 2011, **21**, 214-222.
22. Y. Tamba, H. Terashima and M. Yamazaki, A membrane filtering method for the purification of giant unilamellar vesicles, *Chem. Phys. Lipids*, 2011, **164**, 351-358.

23. T. Tanaka, Y. Tamba, S. M. Masum, Y. Yamashita and M. Yamazaki, La³⁺ and Gd³⁺ induce shape change of giant unilamellar vesicles of phosphatidylcholine, *Biochim. Biophys. Acta*, 2002, **1564**, 173-182.
24. B. Valeur, *Molecular Fluorescence – Principles and Applications*, Wiley-VCH, Weinheim, 2002.
25. J. N. Demas and G. A. Crosby, The measurement of photoluminescence quantum yields. – Review, *J. Phys. Chem.*, 1971, **75**, 991-1024.
26. S. Fery-Forgues and D. Lavabre, Are fluorescence quantum yields so tricky to measure? A demonstration using familiar stationery products, *J. Chem. Educ.*, 1999, **76**, 1260-1264.
27. I. Johnson and M. T. Z. Spence, *Molecular Probes Handbook: A Guide to Fluorescent Probes and Labeling Technologies*, 11th Ed., Invitrogen, 2011.
28. A. S. Edelstein and R. C. Cammarata, *Nanomaterials: Synthesis, Properties and Applications*, Taylor & Francis Group, New York, 1996.
29. T. K. Sau and A. L. Rogach, *Complex-shaped Metal Nanoparticles: Bottom-Up Syntheses and Applications*, Wiley-VCH, Weinheim, 2012.
30. J. Jiang and Y-M. Yang, Facile synthesis of nanocrystalline spinel NiFe₂O₄ via novel soft chemistry route, *Mater. Lett.*, 2007, **61**, 4276-4279.
31. M. Viret, D. Rubi, D. Colson, D. Lebeugle, A. Forget, P. Bonville, G. Dhahenne, R. Saint-Martin, G. André and F. Ott, β-NaFeO₂: a new room temperature multiferroic material, *Mater. Res. Bull.*, 2012, **47**, 2294-2298.
32. D. Mishra, R. Arora, S. Lahiri, S. S. Amritphale and N. Chandra, A novel process for making alkaline iron oxide nanoparticles by a solvo thermal approach, *J. Struc. Chem.*, 2014, **55**, 525-529.
33. J. Rodriguez-Carvajal, *FULLPROF: A Program for Rietveld Refinement and Pattern Matching Analysis*, Abstracts of the Satellite Meeting on Powder Diffraction of the XV Congress of the IUCr, p. 127, Toulouse, 1990.
34. W. Pitschke, H. Hermann and N. Mattern, The influence of surface roughness on diffracted X-ray intensities in Bragg–Brentano geometry and its effect on the structure determination by means of Rietveld analysis, *Powder Diffr.* 1993, **8**, 74-83.

35. J. M. Hastings and L. M. Corliss, Neutron Diffraction Studies of Zinc Ferrite and Nickel Ferrite, *Rev. Mod. Phys.*, 1953, **25**, 114.
36. S. Chkoundali, S. Ammar, N. Jouini, F. Fiévet, P. Molinié, M. Danot, F. Villain and J.-M. Grenèche, Nickel ferrite nanoparticles: elaboration in polyol medium via hydrolysis, and magnetic properties, *J. Phys.-Condens. Mat.*, 2004, **16**, 4357-4372.
37. M. H. Nilsen, C. Nordhei, A. L. Ramstad, D. G. Nicholson, M. Poliakoff and A. Cabañas, XAS (XANES and EXAFS) investigations of nanoparticulate ferrites synthesized continuously in near critical and supercritical water, *J. Phys. Chem. C*, 2007, **111**, 6252-6262.
38. M. Ritu, A simple and effective method of the synthesis of single phase nanosized NiFe₂O₄ particles, *Int. J. Scientific & Engineering Res.* Vol. 4 (8), August 2013.
39. M. George, A. M. John, S. S. Nair, P. A. Joy and M. R. Anantharaman, Finite size effects on the structural and magnetic properties of sol-gel synthesized NiFe₂O₄ powders, *J. Magn. Magn. Mater.*, 2006, **302**, 190-195.
40. M. Kooti and A. N. Sedeh, Synthesis and characterization of NiFe₂O₄ magnetic nanoparticles by combustion method, *J. Mater. Sci. Technol.*, 2013, **29**, 34-38.
41. D. L. Schulz, R. A. Sailer and A. N. Caruso, Superparamagnetic Transition Metal Iron Oxygen Nanoparticles, *US Patent No. 0194733* (2009).
42. B. D. Cullity and C. D. Graham, *Introduction to Magnetic Materials*, John Wiley & Sons Inc., Hoboken, New Jersey, 2009; ISBN: 9780471477419.
43. *Nanopowder, Nanotube and Nanopowder Dispersion Products Index*, US Research Nanomaterials, Inc., Houston, Texas, USA.
44. Z. Shi, J. Zhang, D. Gao, Z. Zhu, Z. Yang, Z. Zhang and D. Xue, Magnetic resonance of the NiFe₂O₄ nanoparticles in the Gigahertz range, *Nanoscale Res. Lett.*, 2013, **8**, article 404.
45. M.-J. R. P. Queiroz, S. Dias, D. Peixoto, A. R. O. Rodrigues, A. D. S. Oliveira, P. J. G. Coutinho, L. A. Vale-Silva, E. Pinto and E. M. S. Castanheira, New potential antitumoral di(hetero)arylether derivatives in the thieno[3,2-*b*]pyridine series: Synthesis and fluorescence studies in solution and in nanoliposomes, *J. Photochem. Photobiol. A: Chem.*, 2012, **238**, 71-80.
46. G. Hungerford, E. M. S. Castanheira, M. E. C. D. Real Oliveira, M. G. Miguel and H. D. Burrows, Monitoring ternary systems of C₁₂E₅/water/tetradecane via the fluorescence of solvatochromic probes, *J. Phys. Chem. B*, 2002, **106**, 4061-4069.

47. P. Greenspan and S. D. Fowler, Spectrofluorometric studies of the lipid probe, Nile Red, *J. Lipid Res.*, 1985, **26**, 781-789.
48. I. and G. Krishnamoorthy, Probing the link between proton transport and water content in lipid membranes, *J. Phys. Chem. B*, 2001, **105**, 1484-1488.
49. P. J. G. Coutinho, E. M. S. Castanheira, M. C. Rei and M.E.C.D. Real Oliveira, Nile Red and DCM Fluorescence Anisotropy Studies in C₁₂E₇/DPPC Mixed Systems, *J. Phys. Chem. B*, 2002, **106**, 12841-12486.
50. E. Feitosa, F. R. Alves, A. Niemiec, M. E. C. D. R. Oliveira, E. M. S. Castanheira and A. L. F. Baptista, Cationic liposomes in mixed didodecyldimethylammonium bromide and dioctadecyldimethylammonium bromide aqueous dispersions studied by differential scanning calorimetry, Nile Red fluorescence, and turbidity, *Langmuir*, 2006, **22**, 3579-3585.
51. D. K. Struck, D. Hoekstra and R. E. Pagano, Use of resonance energy transfer to monitor membrane fusion, *Biochemistry*, 1981, **20**, 4093-4099.
52. S. García-Jimeno, E. Escribano, J. Queralt, J. Estelrich, Magnetoliposomes prepared by reverse-phase followed by sequential extrusion: Characterization and possibilities in the treatment of inflammation, *Int. J. Pharmaceut.*, 2011, **405**, 181-187.
53. S. Zhang, H. Niu, Y. Zhang, J. Liu, Y. Shia, X. Zhang, Y. Cai, Biocompatible phosphatidylcholine bilayer coated on magnetic nanoparticles and their application in the extraction of several polycyclic aromatic hydrocarbons from environmental water and milk samples, *J. Chromatogr. A*, 2012, **1238**, 38-45.
54. M. Mozaffari, J. Amighian and E. Darsheshdar, Magnetic and structural studies of nickel-substituted cobalt ferrite nanoparticles, synthesized by the sol-gel method, *J. Magn. Magn. Mater.*, 2014, **305**, 19-22.
55. S. A. S. Ebrahimi and J. Azadmanjiri, Evaluation of NiFe₂O₄ ferrite nanocrystalline powder synthesized by a sol-gel auto-combustion method, *J. Non-Crystal. Solids*, 2007, **353**, 802-804.
56. D-H. Chen and X-R. He, Synthesis of nickel ferrite nanoparticles by sol-gel method, *Mater. Res. Bull.*, 2001, **36**, 1369-1377.
57. M. Aliahmad and M. Noori, Synthesis and characterization of nickel ferrite nanoparticles by chemical method, *Indian J. Phys.*, 2013, **87**, 431-434.

58. M. G. Naseri, M. H. M. Ara, E. B. Saion and A. H. Shaari, Superparamagnetic magnesium ferrite nanoparticles fabricated by a simple, thermal-treatment method, *J. Magn. Magn. Mater.*, 2014, **350**, 141-147.

59. H. Curtis and N. Barnes, *Biology*, 5th Edition, Worth Publishers, New York, 1989.

8. Supplementary Information

8.1 TEM images

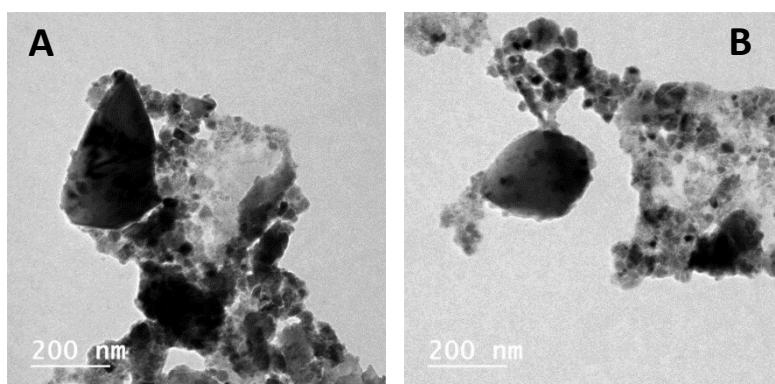


Fig. S1 TEM images of the synthesized NiFe_2O_4 NPs, containing NiO-rich particles (the larger ones).

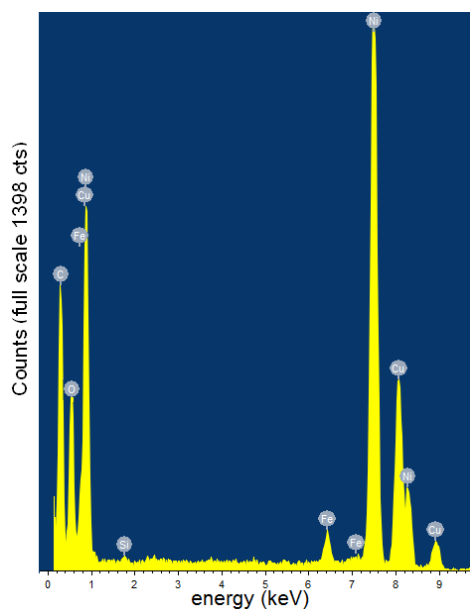


Fig. S2 EDAX elemental analysis of area corresponding to Figure S1A.

Table S1 EDAX atomic percentages considering only Ni, Fe and O contributions and comparison with the values predicted for NiO NPs.

Element	EDAX Atomic (%)	Calculated atomic (%)
Ni	54.2	50.0
Fe	2.5	0
O	43.3	50.0

8.2 Details of Rietveld XRD analysis using FullProf Software

Bragg-Brentano (X-rays) geometry

March-Dollase model for preferred orientation with

$G_1 = 0$ and $G_2 = 1$ which corresponds to **no preferred orientation** ($P_h = 1$)

Background defined by a 6 coefficient polynomial centered at $2\Theta = 40^\circ$

Profile function used was T-C-H Pseudo-Voigt function convoluted with asymmetry due to axial divergence, as formulated by van Laar and Yelon.^{S1}

Instrumental Resolution Function obtained with a XRD pattern of a reference sample

U-inst	V-inst	W-inst	X-inst	Y-inst	Z-inst
-0.02522	0.00705	0.02608	0.00000	0.00000	0.00000

where U, V, W, X, Y and Z define the variation of Gaussian and Lorentzian widths of the peaks profile with diffraction angle.^{S2,S3}

Zero point fixed to -0.0608 (obtained from the XRD pattern of a reference sample)

Displacement peak-shift parameter: $SyCos = 0.0122 \pm 0.0006$ (Fit 1)

0.0113 ± 0.0007 (Fit 2)

0.0118 ± 0.0006 (Fit 3)

$$\Delta(2\theta) = - SyCos \times Cos(\theta)$$

Transparency peak-shift parameter: $SySin = 0.020 \pm 0.003$ (Fit 1)

0.012 ± 0.003 (Fit 2)

0.023 ± 0.003 (Fit 3)

$$\Delta(2\theta) = SySin \times Sin(2\theta)$$

Phase 1: NiFe₂O₄

Number of Space group: 227

Hermann-Mauguin Symbol: F d -3 m

Hall Symbol: -F 4vw 2vw 3

Atom coordinates, occupation and isothermal factors (Bs)

Atom	x/a	y/b	z/b	Occ	B
Fe_T	0.125	0.125	0.125	1	-1.272 ± 0.007
	0.125	0.125	0.125	1	0
	0.125	0.125	0.125	0.76 ± 0.03	-1.282 ± 0.007
Fe_Oh	0.5	0.5	0.5	1	-1.150 ± 0.007
	0.5	0.5	0.5	1	0
	0.5	0.5	0.5	1.24 ± 0.03	-1.132 ± 0.007
Ni_Oh	0.5	0.5	0.5	1	-1.150 ± 0.007
	0.5	0.5	0.5	1	0
	0.5	0.5	0.5	0.76 ± 0.03	-1.132 ± 0.007
O	0.2515 ± 0.00003	0.2515 ± 0.00003	0.2515 ± 0.00003	4	-1.861 ± 0.015
	0.2512 ± 0.00003	0.2512 ± 0.00003	0.2512 ± 0.00003	4	0
	0.2517 ± 0.00003	0.2517 ± 0.00003	0.2517 ± 0.00003	4	-1.88 ± 0.015
Ni_T	0.125	0.125	0.125	0	-1.272 ± 0.007
	0.125	0.125	0.125	0	0
	0.125	0.125	0.125	0.24±0.03	-1.282 ± 0.007

Profile parameters

Overall scale factor: 0.0000001722 ± 0.0000000001 (Fit 1)
0.00000019887 ± 0.00000000009 (Fit 2)
0.00000001723 ± 0.00000000001 (Fit 3)

Cell parameters:

a = 8.3350 ± 0.0001 (Fit 1)
8.3339 ± 0.0001 (Fit 2)
8.3352 ± 0.0001 (Fit 3)

b = 8.3350 ± 0.0001 (Fit 1)
8.3339 ± 0.0001 (Fit 2)
8.3352 ± 0.0001 (Fit 3)

c = 8.3350 ± 0.0001 (Fit 1)
8.3339 ± 0.0001 (Fit 2)
8.3352 ± 0.0001 (Fit 3)

Preferred orientation: G₁ = 1
G₂ = 0

X (strain enlargement) and Y (size enlargement) parameters:

$$X = 0$$

$$Y = 0.4263 \pm 0.0003 \quad (\text{Fit 1})$$

$$0.4195 \pm 0.0003 \quad (\text{Fit 2})$$

$$0.4258 \pm 0.0003 \quad (\text{Fit 3})$$

Phase 2: FeNaO₂

Number of Space group: 33

Hermann-Mauguin Symbol: P n a 21

Hall Symbol: P 2c -2n

COD ID: 1008191

Atom coordinates, occupation and isothermal factors (Bs)

Atom	x/a	y/b	z/b	Occ	B
Fe	0.062	0.13	0	1	0.33 ± 0.03
	0.062	0.13	0	1	0
	0.062	0.13	0	1	0.37 ± 0.03
Na	0.416	0.151	0.489	1	-2.40 ± 0.03
	0.416	0.151	0.489	1	0
	0.416	0.151	0.489	1	-2.41 ± 0.03
O1	0.043	0.084	0.339	1	2.15 ± 0.08
	0.043	0.084	0.339	1	0
	0.043	0.084	0.339	1	2.26 ± 0.08
O2	0.38	0.153	0.927	1	-2.60 ± 0.05
	0.38	0.153	0.927	1	0
	0.38	0.153	0.927	1	-2.52 ± 0.05

Profile parameters

$$\text{Overall scale factor: } 0.0003173 \pm 0.0000005 \quad (\text{Fit 1})$$

$$0.0003247 \pm 0.0000004 \quad (\text{Fit 2})$$

$$0.0003172 \pm 0.0000005 \quad (\text{Fit 3})$$

Cell parameters:

$$a = 5.61077 \pm 0.00008 \quad (\text{Fit 1})$$

$$5.60964 \pm 0.00009 \quad (\text{Fit 2})$$

$$5.61087 \pm 0.00008 \quad (\text{Fit 3})$$

$$b = 7.1917 \pm 0.0001 \quad (\text{Fit 1})$$

$$7.1909 \pm 0.0001 \quad (\text{Fit 2})$$

$$7.1919 \pm 0.0001 \quad (\text{Fit 3})$$

$$c = 5.37289 \pm 0.00008 \quad (\text{Fit 1})$$

$$5.37188 \pm 0.00009 \quad (\text{Fit 2})$$

$$5.37294 \pm 0.00008 \quad (\text{Fit 3})$$

Preferred orientation: $G_1 = 1$
 $G_2 = 0$

X (strain enlargement) and Y (size enlargement) parameters:

$$X = 0$$

$$Y = 0.1500 \pm 0.0003 \quad (\text{Fit 1})$$

$$0.1483 \pm 0.0004 \quad (\text{Fit 2})$$

$$0.1497 \pm 0.0003 \quad (\text{Fit 3})$$

Phase 3: NiO

Number of Space group: 225
Hermann-Mauguin Symbol: F m -3 m
Hall Symbol: -F 4 2 3
COD ID: 1010381

Atom coordinates, occupation and isothermal factors (Bs)

Atom	x/a	y/b	z/b	Occ	B
Ni	0	0	0	1	0.55 ± 0.02
	0	0	0	1	0
	0	0	0	1	0.61 ± 0.02
O	0.5	0.5	0.5	1	-1.66 ± 0.05
	0.5	0.5	0.5	1	0
	0.5	0.5	0.5	1	-1.68 ± 0.05

Profile parameters

Overall scale factor: $0.00000044 \pm 0.00000001 \quad (\text{Fit 1})$
 $0.000000450 \pm 0.000000007 \quad (\text{Fit 2})$
 $0.00000044 \pm 0.00000001 \quad (\text{Fit 3})$

Cell parameters:

$$a = 4.1783 \pm 0.0006 \quad (\text{Fit 1})$$

$$4.1777 \pm 0.0007 \quad (\text{Fit 2})$$

$$4.1784 \pm 0.0006 \quad (\text{Fit 3})$$

$b = 4.1783 \pm 0.0006$ (Fit 1)
 4.1777 ± 0.0007 (Fit 2)
 4.1784 ± 0.0006 (Fit 3)

$c = 4.1783 \pm 0.0006$ (Fit 1)
 4.1777 ± 0.0007 (Fit 2)
 4.1784 ± 0.0006 (Fit 3)

Preferred orientation: $G_1 = 1$
 $G_2 = 0$

X (strain enlargement) and Y (size enlargement) parameters:
 $X = 0$

$Y = 0.296 \pm 0.008$ (Fit 1)
 0.321 ± 0.009 (Fit 2)
 0.296 ± 0.008 (Fit 3)

8.3 Figures of merit

Fit 1

==> RELIABILITY FACTORS WITH ALL NON-EXCLUDED POINTS FOR PATTERN:
1

=> Cycle: 27 => MaxCycle:250
 => N-P+C: 3471
 => R-factors (not corrected for background) for Pattern: 1
 => Rp: 6.17 Rwp: 8.05 Rexp: 6.19 Chi2: 1.69 L.S.
 refinement
 => Conventional Rietveld R-factors for Pattern: 1
 => Rp: 11.7 Rwp: 13.0 Rexp: 10.00 Chi2: 1.69
 => Deviance: 0.589E+04 Dev* : 1.694
 => DW-Stat.: 1.2601 DW-exp: 1.9117
 => N-sigma of the GoF: 28.699

==> RELIABILITY FACTORS FOR POINTS WITH BRAGG CONTRIBUTIONS FOR
PATTERN: 1

=> N-P+C: 3248
 => R-factors (not corrected for background) for Pattern: 1
 => Rp: 6.16 Rwp: 8.05 Rexp: 6.10 Chi2: 1.75 L.S.
 refinement
 => Conventional Rietveld R-factors for Pattern: 1
 => Rp: 11.3 Rwp: 12.8 Rexp: 9.68 Chi2: 1.75
 => Deviance: 0.569E+04 Dev* : 1.750
 => DW-Stat.: 1.3033 DW-exp: 1.9093
 => N-sigma of the GoF: 30.026

=> Global user-weighted Chi2 (Bragg contrib.): 1.80

BRAGG R-Factors and weight fractions for Pattern # 1

=> Phase: 1 Nickel iron oxide 14174 Trevorite
=> Bragg R-factor: 1.99 Vol: 579.048(0.014) Fract(%) :
67.23(0.27)
=> Rf-factor= 1.85 ATZ: 1080076.500 Brindley:
1.0000

=> Phase: 2 IronIII sodium oxide - -beta
=> Bragg R-factor: 9.20 Vol: 216.802(0.006) Fract(%) :
19.03(0.08)
=> Rf-factor= 4.77 ATZ: 443.342 Brindley:
1.0000

=> Phase: 3 Nickel oxide
=> Bragg R-factor: 4.44 Vol: 72.945(0.019) Fract(%) :
13.74(0.40)
=> Rf-factor= 2.50 ATZ: 688429.688 Brindley:
1.0000

Fit 2

==> RELIABILITY FACTORS WITH ALL NON-EXCLUDED POINTS FOR PATTERN:
1

=> Cycle: 15 => MaxCycle:250
=> N-P+C: 3480
=> R-factors (not corrected for background) for Pattern: 1
=> Rp: 7.51 Rwp: 9.47 Rexp: 6.20 Chi2: 2.33 L.S.
refinement
=> Conventional Rietveld R-factors for Pattern: 1
=> Rp: 14.4 Rwp: 15.4 Rexp: 10.05 Chi2: 2.33
=> Deviance: 0.814E+04 Dev* : 2.337
=> DW-Stat.: 0.9106 DW-exp: 1.9065
=> N-sigma of the GoF: 55.568

==> RELIABILITY FACTORS FOR POINTS WITH BRAGG CONTRIBUTIONS FOR
PATTERN: 1

=> N-P+C: 3255
=> R-factors (not corrected for background) for Pattern: 1
=> Rp: 7.55 Rwp: 9.52 Rexp: 6.10 Chi2: 2.43 L.S.
refinement
=> Conventional Rietveld R-factors for Pattern: 1
=> Rp: 14.0 Rwp: 15.2 Rexp: 9.73 Chi2: 2.43
=> Deviance: 0.794E+04 Dev* : 2.436
=> DW-Stat.: 0.9332 DW-exp: 1.9037
=> N-sigma of the GoF: 57.806

=> Global user-weighted Chi2 (Bragg contrib.): 2.49

BRAGG R-Factors and weight fractions for Pattern # 1

```

-----
=> Phase: 1      Nickel iron oxide 14174 Trevorite
=> Bragg R-factor: 6.35      Vol: 578.819( 0.017) Fract(%):
69.77( 0.15)
=> Rf-factor= 3.75      ATZ: 1080076.500 Brindley:
1.0000

=> Phase: 2      IronIII sodium oxide - -beta
=> Bragg R-factor: 11.7     Vol: 216.693( 0.006) Fract(%):
17.51( 0.04)
=> Rf-factor= 7.03     ATZ: 443.342 Brindley:
1.0000

=> Phase: 3      Nickel oxide
=> Bragg R-factor: 8.43     Vol: 72.912( 0.021) Fract(%):
12.72( 0.21)
=> Rf-factor= 3.62     ATZ: 688429.688 Brindley:
1.0000

```

Fit 3

```

==> RELIABILITY FACTORS WITH ALL NON-EXCLUDED POINTS FOR PATTERN:
1

```

```

=> Cycle: 70 => MaxCycle:250
=> N-P+C: 3470
=> R-factors (not corrected for background) for Pattern: 1
=> Rp: 6.16 Rwp: 8.04 Rexp: 6.19 Chi2: 1.69 L.S.
refinement
=> Conventional Rietveld R-factors for Pattern: 1
=> Rp: 11.7 Rwp: 13.0 Rexp: 10.01 Chi2: 1.69
=> Deviance: 0.588E+04 Dev* : 1.693
=> DW-Stat.: 1.2627 DW-exp: 1.9123
=> N-sigma of the GoF: 28.545

```

```

==> RELIABILITY FACTORS FOR POINTS WITH BRAGG CONTRIBUTIONS FOR
PATTERN: 1

```

```

=> N-P+C: 3247
=> R-factors (not corrected for background) for Pattern: 1
=> Rp: 6.15 Rwp: 8.04 Rexp: 6.09 Chi2: 1.74 L.S.
refinement
=> Conventional Rietveld R-factors for Pattern: 1
=> Rp: 11.3 Rwp: 12.8 Rexp: 9.68 Chi2: 1.74
=> Deviance: 0.568E+04 Dev* : 1.749
=> DW-Stat.: 1.3060 DW-exp: 1.9099
=> N-sigma of the GoF: 29.868

=> Global user-weighted Chi2 (Bragg contrib.): 1.80

```

BRAGG R-Factors and weight fractions for Pattern # 1

```

=> Phase: 1      Nickel iron oxide 14174 Trevorite
=> Bragg R-factor:  2.03      Vol:  579.089( 0.015)  Fract(%):
67.18( 0.29)
=> Rf-factor=  1.85      ATZ:      1080076.500  Brindley:
1.0000

=> Phase: 2      IronIII sodium oxide - -beta
=> Bragg R-factor:  9.22      Vol:  216.814( 0.006)  Fract(%):
19.00( 0.09)
=> Rf-factor=  4.80      ATZ:      443.342  Brindley:
1.0000

=> Phase: 3      Nickel oxide
=> Bragg R-factor:  4.50      Vol:   72.954( 0.020)  Fract(%):
13.82( 0.43)
=> Rf-factor=  2.52      ATZ:      688429.688  Brindley:
1.0000

```

Microstructural analysis was performed by Fullprof software using the broadening of the XRD peaks with an implementation previously described [S2,S3].

8.4 References

S1. B. van Laar, W. B. Yelon, The peak in neutron powder diffraction, *J. Appl. Cryst.*, 1984, **17**, 47-54.

S2. J. Rodríguez-Carvajal, T. Roisnel, Line Broadening analysis Using FullProf: Determination of Microstructural Properties, *Materials Science Forum*, 2004, **443-444**, 123-126.

S3. J. Rodríguez-Carvajal, *Study of Micro-Structural Effects by Powder Diffraction Using the Program FULLPROF*, IV Congreso de la Sociedad Mexicana de Cristalografía, Morelia, Michoacan, México, Libro de Resúmenes, 2003, 66-75.
http://sdpd.univ-lemans.fr/DU-SDPD/pdf/Microstructural_effects.pdf

2.3

Magnetoliposomes based on manganese ferrite nanoparticles as nanocarriers for antitumor drugs

Ana Rita O. Rodrigues, José M. F. Ramos, I. T. Gomes, Bernardo G. Almeida, J. P. Araújo, Maria João R. P. Queiroz, Paulo J. G. Coutinho, Elisabete M. S. Castanheira

RSC Advances **6** (2016) 17302-17313

INDEX

1. Abstract
2. Introduction
3. Experimental
4. Results and discussion
5. Conclusions
6. Acknowledgments
7. References
8. Supplementary information

1. Abstract

Manganese ferrite nanoparticles with a size distribution of 26 ± 7 nm (from TEM measurements) were synthesized by the coprecipitation method. The obtained nanoparticles exhibit a superparamagnetic behaviour at room temperature with a magnetic squareness of 0.016 and a coercivity field of 6.3 Oe. These nanoparticles were either entrapped in liposomes (aqueous magnetoliposomes, AMLs) or covered with a lipid bilayer, forming solid magnetoliposomes (SMLs). Both types of magnetoliposomes, exhibiting sizes below or around 150 nm, were found to be suitable for biomedical applications. Membrane fusion between magnetoliposomes (both AMLs and SMLs) and GUVs (giant unilamellar vesicles), the latter used as models of cell membranes, was confirmed by Förster Resonance Energy Transfer (FRET) assays, using a NBD labeled lipid as the energy donor and Nile Red or Rhodamine B-DOPE as the energy acceptor. A potential antitumor thienopyridine derivative was successfully incorporated into both aqueous and solid magnetoliposomes, pointing to a promising application of these systems in oncological therapy, simultaneously as hyperthermia agents and nanocarriers for antitumor drugs.

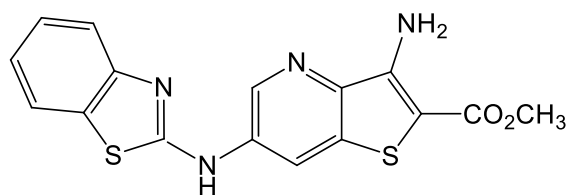
2. Introduction

Since their discovery, liposomes have been described as an ideal nanoencapsulation system that protect and transport loaded compounds to the sites of interest.¹⁻³ In fact, liposomes can overcome many of the problems associated with other systems used in therapy, such as those involving solubility, pharmacokinetics, *in vivo* stability and toxicity.^{4,5} However, this system still presents some issues for *in vivo* application, namely its recognition and capture by the immune system⁶ and also the location in therapeutic sites for drug release.⁷ In order to overcome these problems, magneto-sensitive liposomes have been proposed.⁸ The magnetic components allow concentration of the liposomes in the desired area of the patient's organs by magnetic forces, often augmented by magnetic agglomeration.⁹⁻¹¹ This way, a new therapy emerges, involving the guided transport of biologically active substances, most of them toxic and with systemic side effects. The ability to guide transported drugs and focus the active molecules to specific sites in the human body can overcome systemic toxicity problems, allowing a lower drug dosage and a more efficient treatment, not only in cancer but also in other diseases.

Magneto-sensitive liposomes result from the encapsulation of magnetic nanoparticles into liposomes. The so-called magnetoliposomes (MLs) combine the amazing physical properties of these two types of particles and preserve the magnetic properties of the magnetic nanoparticles.¹² This ideal system can be exploited in a great array of biomedical applications. In therapy, the most promising applications of magnetoliposomes are magnetic guided drug delivery and hyperthermia.^{13,14} Otherwise, in diagnosis, magnetic nanoparticles have been used as contrast agents in MRI (magnetic resonance imaging).¹⁵

Magnetic nanoparticles (NPs) of transition metal ferrites (MFe_2O_4 , $M = Mn, Co, Ni$, etc.), having a spinel structure, are of strong interest for biomedical applications. These nanoparticles are remarkable soft-magnetic materials with superparamagnetic behavior and have great properties, such as good chemical stability and mechanical hardness.^{16,17} In particular, manganese ferrite NPs have received an increased attention. Their magnetic susceptibility is higher than for other ferrite nanoparticles,¹⁸ suggesting that they may be used in magnetic drug targeting and as an ultrasensitive negative contrast agent in MRI.^{19,20} Also, manganese ferrite NPs showed good biocompatibility and slight toxicity against HeLa cells.²¹

The preparation method of magnetic NPs determines their final shape, size distribution, surface chemistry and magnetic properties.^{22,23} In this work, manganese ferrite nanoparticles were synthesized by the coprecipitation method. These NPs were either entrapped in liposomes, originating aqueous magnetoliposomes (AMLs), or covered with a lipid bilayer, forming solid magnetoliposomes (SMLs). A potent antitumor heteroaryl-aminothieno[3,2-*b*]pyridine derivative (Figure 1), previously synthesized,²⁴ was incorporated into both types of magnetoliposomes, keeping in mind future biomedical applications. In fact, magnetoliposomes are promising for dual cancer therapy, both by hyperthermia and anticancer drug delivery, besides the ability to attain magnetic guidance to the therapeutic site of interest.



Compound 1

Fig. 1 Structure of the methyl 3-amino-6-(benzo[*d*]thiazol-2-ylamino)thieno[3,2-*b*]pyridine-2-carboxylate (**1**).

3. Experimental

All the solutions were prepared using spectroscopic grade solvents and ultrapure water (Milli-Q grade).

3.1 Manganese ferrite nanoparticles preparation

Manganese ferrite nanoparticles (NPs) were synthesized by the coprecipitation method, in 5 mL aqueous solution. First, an aqueous solution containing 612 μL of 50% NaOH solution was heated to 90°C. Then, a mixture containing 500 μL of 0.5 M $\text{MnSO}_4 \cdot \text{H}_2\text{O}$ aqueous solution and 500 μL of 1 M $\text{FeCl}_3 \cdot 6\text{H}_2\text{O}$ aqueous solution was added drop by drop to the previously warmed NaOH solution under magnetic stirring. Manganese nanoparticles were formed after two hours at 90°C.

3.2 Preparation of magnetoliposomes

Aqueous magnetoliposomes (AMLs) resulted from the entrapment of the synthesized magnetic NPs in liposomes. Egg yolk phosphatidylcholine (Egg-PC), from Sigma-Aldrich, was used for lipid vesicle formation. A 10 mM Egg-PC solution in ethanol was injected, under vigorous vortexing, to an aqueous solution of magnetic nanoparticles (ethanolic injection method).²⁵ Then, the ferrofluid was washed with water and purified by ultracentrifugation to remove all the non-encapsulated NPs.

Solid magnetoliposomes (SMLs) were prepared by the method previously developed by us.²⁶ First, 10 μL of the synthesized MnFe_2O_4 NPs were dispersed in 3 mL of water and centrifuged. Then, the deposited particles were dispersed in 10 μL water in an ultrasonicator for one minute at 189 W, and 3 mL of chloroform were added to the aqueous dispersion of NPs. After vigorous agitation, 165 μL of a 20 mM solution of 1,2-dioleoyl-*sn*-glycero-3-phospho-(1'-*rac*-glycerol) (sodium salt) (DOPG, from Sigma-Aldrich) were added under vortexing, to form the first lipid layer of the SMLs. The particles were washed twice by magnetic decantation with pure water, in order to remove the lipid that was not attached to the NPs. The second lipid layer was then formed by the injection of 165 μL of DOPG (20 mM), under vortexing, in a 3 mL aqueous dispersion of the particles with the first lipid layer. The resulting SMLs were then washed and purified with pure water by centrifugation.

Compound **1** was incorporated into aqueous magnetoliposomes by the co-injection method, as already described for liposomes.²⁷ In solid magnetoliposomes,

compound **1** was incorporated by injection of an ethanolic solution together with the formation of the second lipid layer.

3.3 Preparation of Giant Unilamellar Vesicles (GUVs)

Soybean lecithin (*L*- α -Phosphatidylcholine), from Sigma-Aldrich, was used for GUVs preparation, using a procedure previously described.^{28,29} 100 μ L of soybean lecithin solution (1 mM) were dried under an argon stream to produce a thin and homogeneous lipid film. 40 μ L of water were added to the film and it was incubated at 45°C for 30 minutes. Then, 3 mL of 0.1 M glucose aqueous solution were added and the resulting mixture was again incubated at 37°C for 2 hours. Finally, after incubation, the GUVs suspension was centrifuged at 14000 g for 30 minutes at 20°C, to remove multilamellar vesicles and lipid aggregates.

3.4 Spectroscopic measurements

3.4.1 General methods

Absorption spectra were recorded in a Shimadzu UV-3101PC UV-Vis-NIR spectrophotometer. Fluorescence measurements were performed using a Fluorolog 3 spectrofluorimeter, equipped with double monochromators in both excitation and emission and a temperature controlled cuvette holder. Fluorescence spectra were corrected for the instrumental response of the system.

3.4.2 FRET measurements

Assays of non-specific interaction between magnetoliposomes and models of biological membranes (GUVs) were performed by Förster Resonance Energy Transfer (FRET). The NBD labeled lipids NBD-PE (*N*-(7-nitrobenz-2-oxa-1,3-diazol-4-yl)-1,2-dihexadecanoyl-*sn*-glycero-3-phosphoethanolamine, ammonium salt) or NBD-C₁₂-HPC (1-palmitoyl-2-{12-[(7-nitro-2-1,3-benzoxadiazol-4-yl)amino]hexanoyl}-*sn*-glycero-3-phosphocholine), from Avanti Polar Lipids, were used as the energy donors, while the hydrophobic dye Nile Red (from Fluka) or the labeled lipid Rhodamine B-DOPE (*N*-(lissamine Rhodamine B sulfonyl)-1,2-dioleoyl-*sn*-3-phosphatidylethanolamine (ammonium salt)), from Avanti Polar Lipids, were used as the energy acceptors.

FRET efficiency, Φ_{RET} , defined as the proportion of donor molecules that have transferred their excess energy to acceptor molecules, can be obtained by taking the ratio

of the donor integrated fluorescence intensities in the presence of acceptor (F_{DA}) and in the absence of acceptor (F_D) (eqn. 1),³⁰

$$\Phi_{RET} = 1 - \frac{F_{DA}}{F_D} \quad (1)$$

The distance between donor and acceptor molecules can be determined through the FRET efficiency (eqn. 2),

$$r_{AD} = R_0 \cdot \left[\frac{1 - \Phi_{RET}}{\Phi_{RET}} \right]^{1/6} \quad (2)$$

where R_0 is the Förster radius (critical distance), that can be obtained by the spectral overlap, $J(\lambda)$, between the donor emission and the acceptor absorption, according to equations (3) and (4) (with R_0 in Å, λ in nm, $\varepsilon_A(\lambda)$ in $M^{-1} \text{ cm}^{-1}$),³⁰

$$R_0 = 0.2108 [k^2 \Phi_D^0 n^{-4} J(\lambda)]^{1/6} \quad (3)$$

$$J(\lambda) = \int_0^\infty I_D(\lambda) \varepsilon_A(\lambda) \lambda^4 d\lambda \quad (4)$$

where $k^2 = 2/3$ is the orientational factor assuming random orientation of the dyes, Φ_D^0 is the fluorescence quantum yield of the donor in the absence of energy transfer, n is the refraction index of the medium, $I_D(\lambda)$ is the fluorescence spectrum of the donor normalized so that $\int_0^\infty I_D(\lambda) d\lambda = 1$, and $\varepsilon_A(\lambda)$ is the molar absorption coefficient of the acceptor.

The fluorescence quantum yield, Φ_s , of the energy donor (the dye NBD) in magnetoliposomes was determined by the standard method (equation (5)),^{31,32}

$$\Phi_s = \left[\frac{(A_r F_s n_s^2)}{(A_s F_r n_r^2)} \right] \Phi_r \quad (5)$$

where A is the absorbance at the excitation wavelength, F the integrated emission area and n is the refraction index of the solvents. Subscripts refer to the reference (r) or sample (s) compound. The absorbance value at excitation wavelength was always less than 0.1, in order to avoid inner filter effects. The NBD-C₁₂-HPC fluorescent labeled lipid incorporated in lipid membranes was used as reference, $\Phi_r = 0.32$ at 25°C, as reported by Invitrogen.³³

3.4.3 Fluorescence anisotropy measurements.

The steady-state fluorescence anisotropy, r , is calculated by

$$r = \frac{I_{VV} - GI_{VH}}{I_{VV} + 2GI_{VH}} \quad (6)$$

where I_{VV} and I_{VH} are the intensities of the emission spectra obtained with vertical and horizontal polarization, respectively (for vertically polarized excitation light), and $G = I_{HV}/I_{HH}$ is the instrument correction factor, where I_{HV} and I_{HH} are the emission intensities obtained with vertical and horizontal polarization (for horizontally polarized excitation light).

3.5 Structural characterization

3.5.1 Transmission Electron Microscopy (TEM)

HR-TEM images of manganese ferrite nanoparticles and solid magnetoliposomes were recorded using a Transmission Electron Microscope JEOL JEM 2010F operating at 200 kV coupled to an Electron Dispersive Spectroscopic analyzer (EDS) at C.A.C.T.I (Centro de Apoio Científico e Tecnológico à Investigação), Vigo, Spain. A drop of the sample was placed onto a TEM copper grid with Formvar/Carbon (ref. S162-4 from Agar Scientific), held by tweezers and left to dry. The processing of TEM images was performed using ImageJ software. It consisted in enhancing local contrast followed by manual selection of particles. The area of each particle allowed an estimation of its size. The resulting histograms were fitted to Gaussian distributions.

3.5.2 X-Ray Diffraction (XRD) and DLS measurements

X-Ray Diffraction (XRD) analyses were performed using a conventional Philips PW 1710 diffractometer, operating with Cu K_{α} radiation, in a Bragg-Brentano configuration.

The mean diameter and size distribution of the magnetic liposomes were measured using a Dynamic Light Scattering (DLS) equipment (NANO ZS Malvern Zetasizer) at 25°C, using a He-Ne laser of 633 nm and a detector angle of 173°. Five independent measurements were performed for each sample. The data analysis was performed using the methodology previously described.³⁴

3.6 Magnetic measurements

3.6.1 General methods

Magnetic measurements were performed at room temperature in a Superconducting Quantum Interference Device (SQUID) magnetometer (Quantum Design MPMS5XL), using applied magnetic fields up to 5.5 T.

3.6.2 Temperature dependence of the magnetization and magnetic hysteresis cycles

The temperature dependence of the magnetization was measured in the temperature range from 5 K to 380 K. The curves were obtained by initially cooling the sample under an applied magnetic field of $H = 100$ Oe (field cooled, FC) and then measuring its magnetization with increasing temperature (applied field of $H = 50$ Oe). Subsequently, after reaching 380 K, the sample was re-cooled, this time with no applied magnetic field (zero-field-cooled, ZFC) and the magnetization measurements were again performed with increasing temperature, under the same magnetic field of $H = 50$ Oe. From the behavior of the FC and ZFC curves, the blocking temperature (T_B) of the superparamagnetic nanoparticles can be obtained.³⁵ The magnetization hysteresis loop measurements were made by fixing the temperature and measuring the magnetization at a series of different applied magnetic fields. This type of study gives information about the maximum magnetization and the degree at which the sample remains magnetized when the applied field is removed, and how easily the sample magnetization can be reversed, the so-called coercive field.

4. Results and discussion

4.1 Nanoparticles characterization

4.1.1 XRD analysis

XRD measurements confirm the synthesis of the manganese ferrite NPs (Figure 2). No calcination was required to obtain a crystalline phase (Figure 2C). However, the absence of thermal treatment results in a significant amorphous background in the XRD pattern. This background disappears upon thermal treatment at 800°C, but originates the presence of a hematite phase (Figure 2D). The synthesis conditions are especially important, as changing the reaction time from 2 hours to 6 hours made the sample amorphous (Figure 2A). This state remained upon calcination at 500°C and 600°C.

Treatment at 700°C or 800°C allowed the crystallization of the manganese ferrite phase, but with a much higher percentage of hematite (Figure 2B).

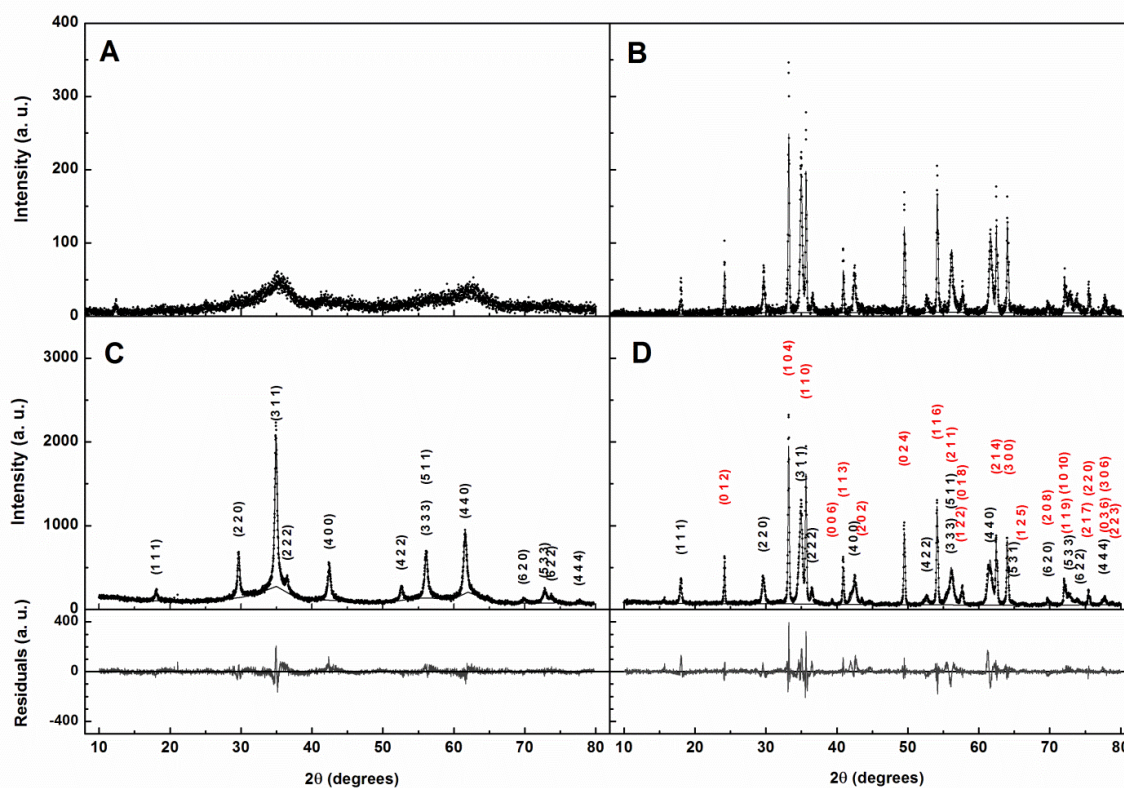


Fig. 2 XRD pattern of the MnFe_2O_4 NPs. Left: Without thermal treatment. Right: Calcinated at 800°C. **A** and **B**: Synthesis time of 6 hours. **C** and **D**: Synthesis time of 2 hours and results of Rietveld analysis (MnFe_2O_4 : space group $\text{Fd-}3\text{m:}2$ (227); CIF 1528316; Fe_2O_3 : space group $\text{R-}3$ 2/c (167); CIF 9000139).

All the characteristic peaks for a pure crystalline phase of manganese ferrite spinel,³⁶ marked by their indices, are shown in Figure 2. Rietveld analysis using a background defined by linear interpolation between a set of points at constant scattering angles but with fitted intensities resulted in good fits, allowing an estimation of sample composition and particle size. Table 1 summarizes the main results of the Rietveld analysis of the obtained samples, with and without thermal treatment at 800°C.

Calcination treatment at a higher temperature of 900°C results in huge variations in the XRD spectrum which was then dominated by the presence of Mn_2O_3 and hematite phases, with only traces of manganese ferrite. The size estimation shown in Table 1 is a lower limit, as the XRD peak broadening was considered to arise only from size effects. Inclusion of strain does not improve significantly the fit of the experimental data and originates higher size estimates. For example, in case of the data in Figure 2C (2 h

synthesis time without thermal treatment), a maximum strain value of 0.022% corresponds to a size of 25.1 nm and the χ^2 and R_F values decrease to 1.67 and 4.53, respectively. From these XRD results, the sample obtained with 2 hours reaction time and without thermal treatment was selected for further characterization and for the preparation of magnetoliposomes.

Table 1. Selected Rietveld analysis parameters.

Reaction time	Calcination temperature	Phase	Fraction (%)	Overall temperature B factor	Size (nm)	R_F	χ^2
2 h	none	MnFe ₂ O ₄	100	-0.18	16.5	4.74	1.69
		Fe ₂ O ₃	---	---	---	---	
2 h	800°C	MnFe ₂ O ₄	55	2.88	13.1	5.98	3.09
		Fe ₂ O ₃	45	1.84	140	4.24	
6 h	700°C	MnFe ₂ O ₄	46	1.61	14	14.6	1.54
		Fe ₂ O ₃	54	0.95	252	5.36	
6 h	800°C	MnFe ₂ O ₄	53	0.59	25	15.3	1.60
		Fe ₂ O ₃	47	-0.25	345	7.69	

4.1.2 UV-Visible Absorption Spectra

Figure 3 displays the UV-Visible absorption spectrum of the synthesized manganese ferrite NPs. The optical band gap can be estimated using a Tauc plot,³⁷ which corresponds to the following equation:

$$(\alpha h\nu)^{1/n} \propto (h\nu - E_g) \quad (7)$$

where α is the absorption coefficient that is proportional to the absorbance value and E_g is the optical band gap. The value of n depends on the nature of the transition, being 1/2 for an indirect band gap and 2 for a direct one.

A linear relation was only obtained for $n = 1/2$ which means that MnFe₂O₄ behaves as an indirect semiconductor. This was already reported by Rafique *et al.*³⁸ with a band gap of 0.98 eV. From Figure 3, a similar value of 1.08 eV was calculated.

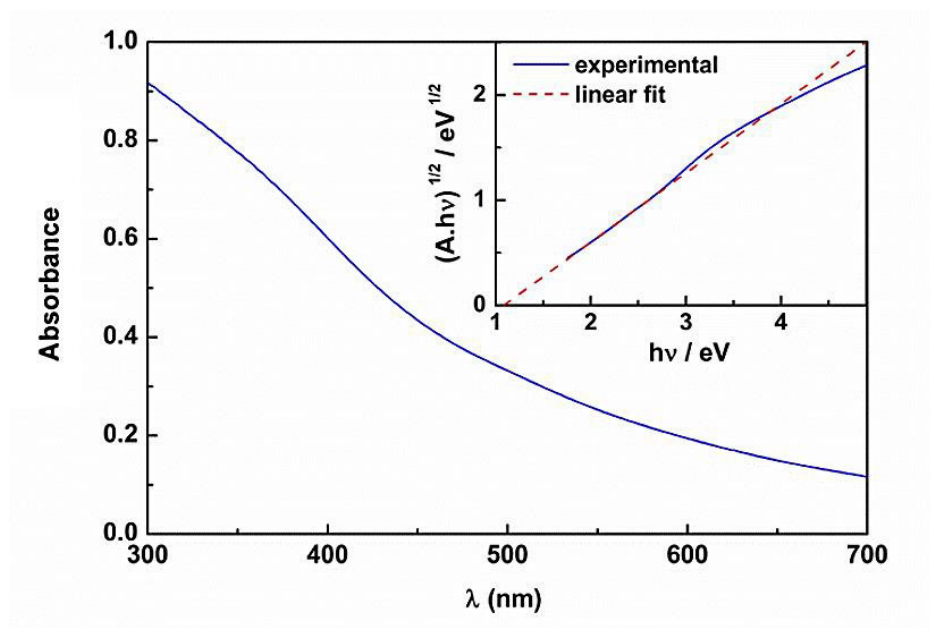


Fig. 3 UV-Visible absorption spectra of MnFe_2O_4 nanoparticles synthesized by the coprecipitation method. Inset: Tauc plot.

4.1.3 TEM images and elemental analysis

TEM images revealed that the synthesized MnFe_2O_4 NPs are generally of small size, with a few larger particles. Particle sizes on the order of tens of nanometers (Figure 4), with a size distribution of 26 ± 7 nm, were obtained from the histogram (C) of image A. From image 4B, it was possible to obtain an interlattice plane distance of 0.49 nm, which corresponds to the (1 1 1) diffraction plane. EDAX elemental analysis confirmed the presence of uniform distribution of Mn, Fe and O elements for this type of ferrite nanoparticles (Figure 4D and Table 2). The high copper content (Figure 4D) is due to the use of copper grids.

Table 2. Atomic percentages of individual elements in MnFe_2O_4 nanoparticles.

Element	EDAX atomic (%)	Calculated atomic (%)
Mn	13.8	14.3
Fe	23.6	28.6
O	62.6	57.1

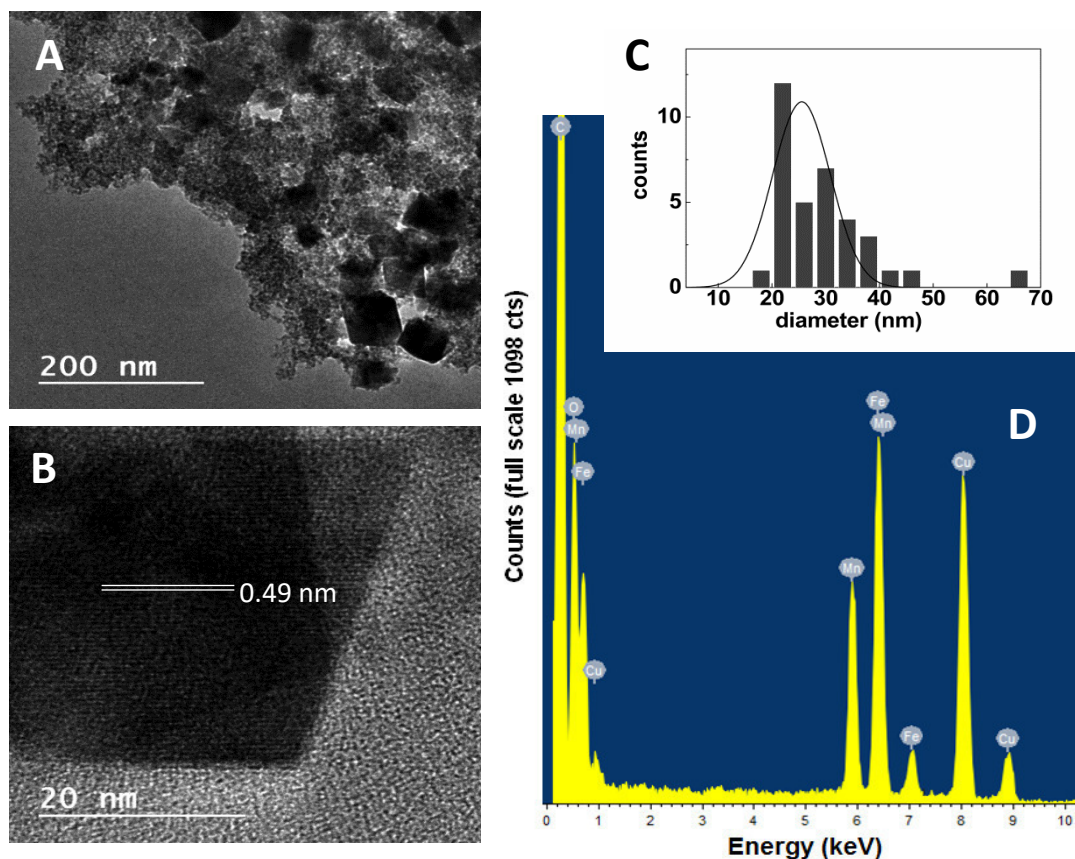


Fig. 4 A, B: TEM images of the synthesized MnFe_2O_4 NPs at different amplifications. **C:** Particles size histogram of image A and fitting to a Gaussian distribution. **D:** EDAX elemental analysis of area corresponding to image A.

4.1.4 Magnetic properties

Manganese ferrite nanoparticles are soft ferromagnetic particles and their magnetic behavior depends on the synthesis method and particle size.^{22,23} Figure 5 shows the hysteresis loop of MnFe_2O_4 NPs at room temperature. A very small hysteresis is observed, with a coercive field of 6.3 Oe. The presence of superparamagnetic behavior can be related to the magnetic squareness value of the hysteresis cycle, which is the ratio between the residual magnetizations (M_r) and the saturation magnetization (M_s). Magnetic squareness values indicative of superparamagnetism are of the order or below 0.1, meaning the loss of more than 90% of the magnetization removal of the applied magnetic field.^{39,40} Here, the obtained magnetic squareness value of the nanoparticles is 0.016, which indicates that the synthesized MnFe_2O_4 NPs present a superparamagnetic behavior at room temperature. Additionally, the magnetization of MnFe_2O_4 NPs does not saturate up to the maximum field that was applied, as shown on figure 5, reaching 36 emu/g at an applied field of 5 T.

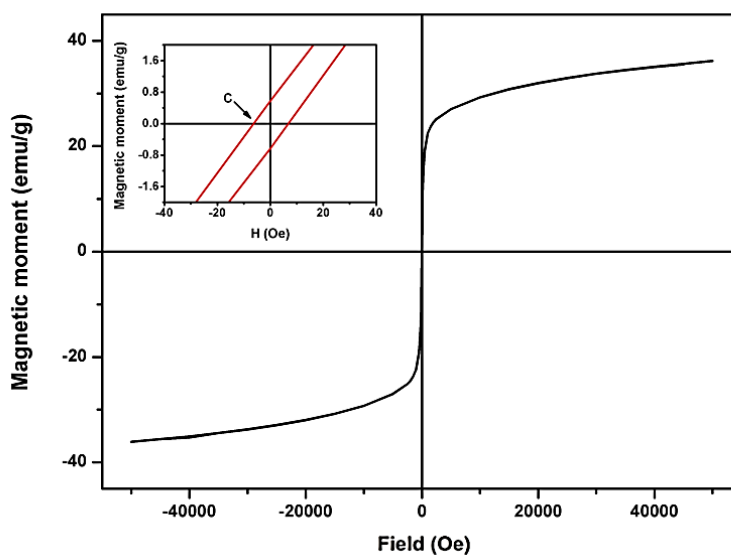


Fig. 5 Magnetization hysteresis loop of MnFe_2O_4 NPs measured at room temperature. Inset: Enlargement of the loop, in the low field region.

For a superparamagnet, the temperature dependence of the zero-field-cooling and field-cooling magnetization curves presents a different behavior. Starting from the low temperatures on the ZFC curve, as temperature increases the blocked magnetic moments align with the applied measuring magnetic field, leading to an initial increase of the sample magnetization. However, as soon as thermal fluctuations are able to allow the moments to overcome the magnetic anisotropy energy barrier, the thermal randomization of the intra-particles magnetic moments produces a subsequent decrease of the magnetization curve, with increasing temperature. In this way, the zero-field-cooling curve peak corresponds to the sample blocking temperature⁴¹ and here a blocking temperature of $T_B \sim 316$ K, was obtained for MnFe_2O_4 nanoparticles.

On the other hand, on the FC curve, the magnetic moments were initially forced to be aligned with the magnetic field imposed during cooling. This then gives a significant overall magnetization at low temperatures, as seen on the FC curve of Figure 6, which monotonically decreases with increasing temperature. Below T_B , the magnetic nanoparticles show ferromagnetic behavior, as thermal fluctuations are not enough to randomize the intra-particles magnetic moments. Above the blocking temperature, NPs show superparamagnetic properties and the ZFC and FC curves are expected to show the same magnetization decreasing trend with increasing temperature. The observed

difference between the ZFC and FC above T_B is related with the size dispersion of the nanoparticles.

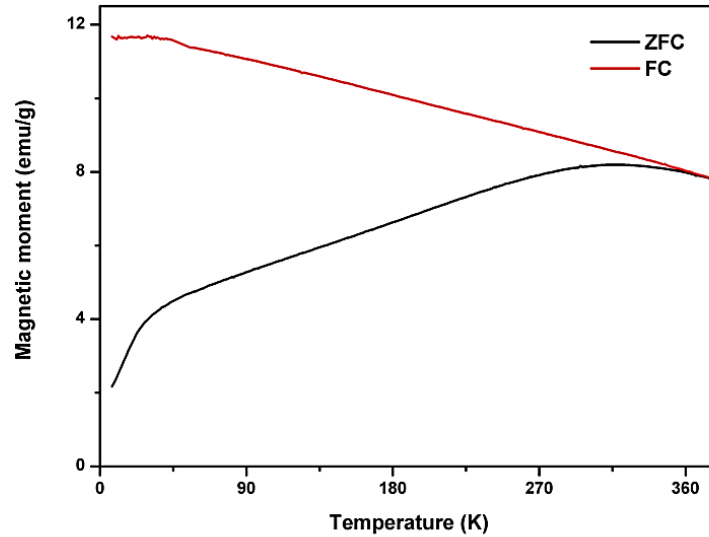


Fig. 6 ZFC and FC magnetization curves of manganese ferrite nanoparticles.

For an ensemble of superparamagnetic particles above the blocking temperature, the magnetization can be described by the Langevin function⁴¹

$$M(H, T) = N\mu L\left(\frac{\mu H}{k_B T}\right) = N\mu \left(\coth\left(\frac{\mu H}{k_B T}\right) - \frac{k_B T}{\mu H} \right) \quad (7)$$

where μ is the particle magnetic moment, k_B is the Boltzmann constant, T is the absolute temperature, N is the number of particles per volume and H is the applied magnetic field.

The magnetization hysteresis cycles were fitted to equation (7), in order to determine the particle magnetic moment, μ . Considering a magnetic moment of $\mu_{\text{MnFe}_2\text{O}_4} = 4.6\mu_B$ per MnFe_2O_4 ,⁴¹ the number of formula units per particle can be obtained by dividing the fitted particle magnetic moment by $\mu_{\text{MnFe}_2\text{O}_4}$. The particle radius can be estimated by assuming spherical particles, with a density value of 4.87 g/cm^3 .⁴² Table 3 shows the results obtained for the fitting of equation (7) to the hysteresis loops. The value determined for diameter is of the order of 14 nm. The high value of R^2 (Table 3) indicates that the experimental data closely follow a Langevin function, as expected for superparamagnetic nanoparticles. The obtained nanoparticle diameter is consistent with the corresponding values obtained from the XRD results, indicating a well ordered manganese ferrite phase without significant surface oxidation or secondary residual phases. Here, the higher magnetization and lower coercivity as compared, e.g., to nickel

ferrite nanoparticles,²⁶ makes the prepared manganese ferrite nanoparticles promising candidates for biomedical applications.

Table 3. Magnetization saturation (M_s), mass (m) and size (d) of the synthesized manganese ferrite nanoparticles.

Sample	R^2	M_s (emu/g)	m (g)	V (cm ³)	d (nm)
MnFe ₂ O ₄	0.9879	31.8	6.98×10^{-18}	1.43×10^{-18}	13.97

4.2 Characterization of magnetoliposomes

4.2.1 DLS and TEM measurements

Two types of magnetoliposomes were synthesized, aqueous magnetoliposomes (AMLs) and solid magnetoliposomes (SMLs). Dynamic Light Scattering (DLS) measurements revealed that aqueous magnetoliposomes of egg phosphatidylcholine (Egg-PC) with entrapped manganese ferrite nanoparticles have diameters of 82 ± 13 nm (size distribution in Figure S1 of Supplementary Information). These values are in accordance with previous results reported for egg lecithin-based liposomes without nanoparticles^{34,43} showing that, as previously observed for nickel ferrite NPs,²⁶ the manganese ferrite nanoparticles have a very small influence on the size of aqueous magnetoliposomes. Neat Egg-PC aqueous magnetoliposomes containing lauric acid coated MnFe₂O₄ nanoparticles were previously prepared by Pradhan and coworkers,⁴⁴ using two different techniques, thin film hydration and double emulsion, resulting in magnetoliposomes of *ca.* 300 nm diameter. This size is significantly larger than the one obtained here using the ethanolic injection method. Pradhan *et al.*⁴⁴ also reported that PEGylated Egg-PC:Cholesterol 2:1 AMLs prepared by thin film hydration (with diameter around 188 nm) are the most promising systems (amongst a series of different Egg-PC:Chol compositions) for hyperthermia treatment of cancer.

Solid magnetoliposomes (SMLs) were obtained by coverage of a cluster of manganese ferrite NPs by the phospholipid DOPG, using the method previously developed for Ni ferrite NPs.²⁶ This method already proved to originate SML structures, with a lipid bilayer surrounding a cluster of magnetic nanoparticles.²⁶

TEM images revealed that the synthesized SMLs have diameters slightly above 100 nm (Figure 7) therefore being suitable for biomedical applications. Dynamic Light Scattering measurements allowed determining a hydrodynamic diameter of 152 ± 24 nm,

roughly in accordance with TEM data (DLS size distribution is shown in Figure S2 of Supplementary Information).

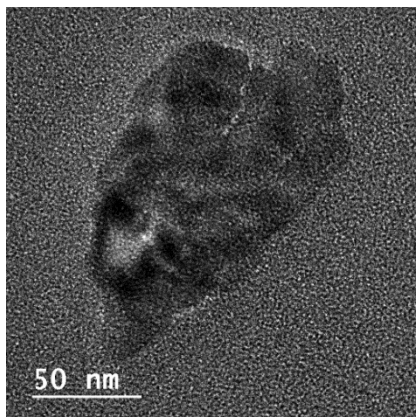


Fig. 7 TEM image of the solid magnetoliposomes (SMLs) containing MnFe_2O_4 NPs.

4.3 AMLs interaction with model membranes

The non-specific interaction of aqueous magnetoliposomes (AMLs) with models of cell membranes (giant unilamellar vesicles, GUVs) was evaluated by Förster Resonance Energy Transfer (FRET). For that purpose, the labeled lipid NBD- C_{12} -HPC and the hydrophobic dye Nile Red were both incorporated in the lipid bilayer of the aqueous magnetoliposomes, the NBD moiety acting as the energy donor and the hydrophobic dye Nile Red as the energy acceptor.⁴⁵⁻⁴⁹ If the donor-acceptor distance is below 100 Å,³⁰ improved FRET efficiency is expected, as the spectral overlap between the donor fluorescence band and the acceptor absorption is high (Figure 8A - inset).

When the aqueous magnetoliposomes interact with model membranes (GUVs), if fusion occurs, a larger membrane is originated and an increase in the donor-acceptor distance is expected, with a corresponding decrease in the energy transfer efficiency. Fluorescence spectra of Egg-PC AMLs, before and after interaction with GUVs, were measured exciting only the donor (NBD). Before interaction with GUVs, two emission bands are clearly observed. The first ($\lambda_{\text{max}} = 550$ nm) corresponds to NBD- C_{12} -HPC emission and the second ($\lambda_{\text{max}} = 630$ nm) to Nile Red emission, that results from the energy transfer of excited NBD molecules to Nile Red. After interaction with GUVs, an increase in the NBD (donor) emission band and a decrease of the Nile Red (acceptor) fluorescence band is observed.

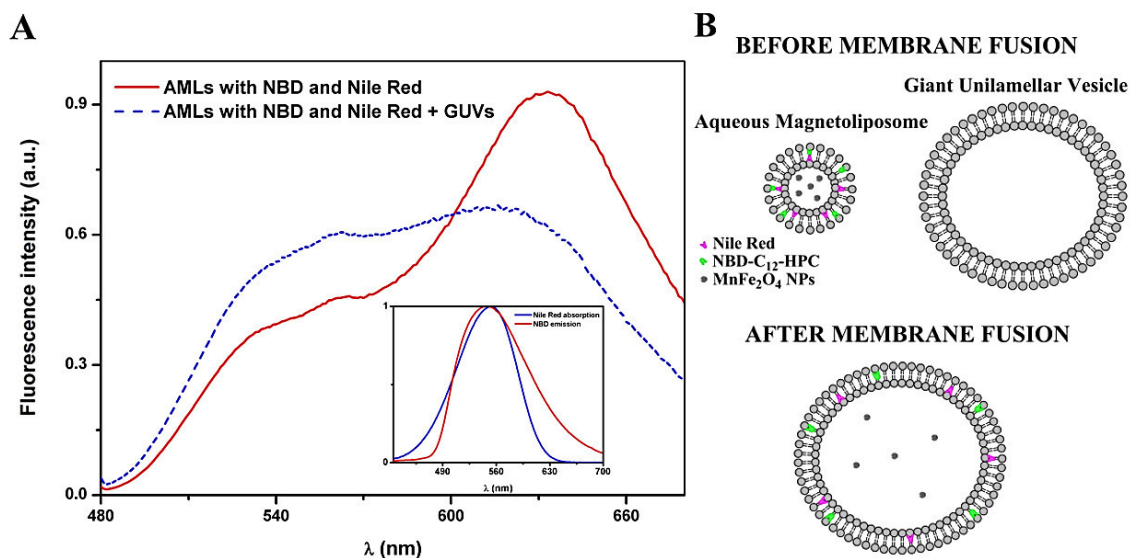


Fig. 8 A. Fluorescence spectra ($\lambda_{exc} = 400$ nm) of AMLs of egg lecithin and $MnFe_2O_4$ NPs containing both NBD- C_{12} -HPC and Nile Red, before and after interaction with GUVs. Inset: Spectral overlap (spectra are normalized) between the fluorescence emission of the donor (NBD- C_{12} -HPC) and the absorption of the acceptor (Nile Red). **B.** Schematic representation of membrane fusion between AMLs and GUVs.

These results are similar to the ones previously observed for AMLs based on $NiFe_2O_4$ nanoparticles²⁶ and confirm membrane fusion between the two systems, AMLs and GUVs (scheme in Figure 8B). Therefore, AMLs based on manganese ferrite nanoparticles are promising as magnetic nanocarriers for both hydrophilic and hydrophobic drugs, as they can be guided with a magnetic field and can release the encapsulated drugs by fusion with the cell membranes.

4.4 SMLs formation and interaction with model membranes

Solid magnetoliposomes (SMLs) are expected to present a better magnetic response when compared with AMLs, because SMLs keep almost the same magnetic properties as the neat nanoparticles.⁵⁰ Besides, it was shown that AMLs display poor magnetic characteristics, similar to those of the aqueous ferrofluid.⁵¹

The method previously developed for the synthesis of SMLs of calcinated nickel ferrite nanoparticles²⁶ was also used here with manganese ferrite NPs. The formation of a DOPG bilayer around $MnFe_2O_4$ NPs was investigated by FRET assays. For that purpose, the NBD labeled lipid NBD- C_6 -HPC was included in the second lipid layer of the SMLs (NBD acting as the energy donor), while the labeled lipid Rhodamine B-DOPE (energy acceptor) was included in the first lipid layer. The emission of SMLs containing

both donor and acceptor labeled lipids was measured exciting only the donor NBD, and was compared with the emission of SMLs labeled with only the energy donor (Figure 9). Comparing the fluorescence spectra of the two systems, a decrease in the NBD emission band and the presence of a pronounced Rhodamine B emission is observed in SMLs containing both fluorophores, evidencing the energy transfer from the excited NBD to Rhodamine.

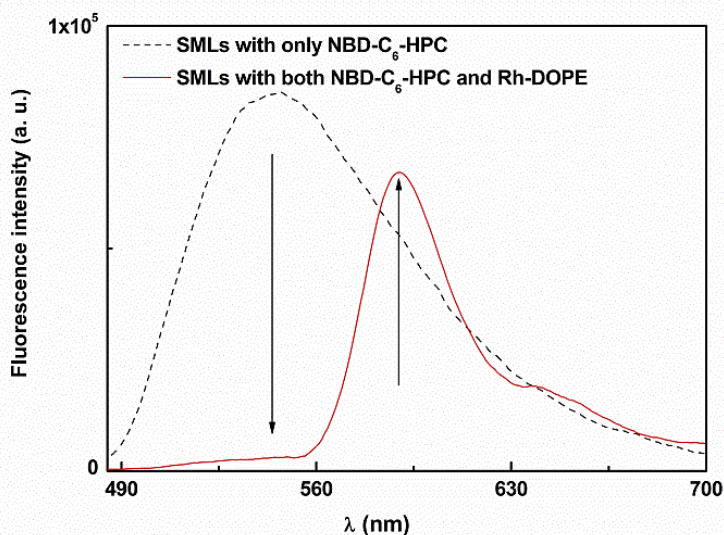


Fig. 9 Fluorescence spectra ($\lambda_{exc} = 470$ nm, no rhodamine excitation) of SMLs covered with DOPG labeled with only NBD-C₆-HPC and SMLs labeled with both NBD-C₆-HPC and rhodamine B-DOPE.

A FRET efficiency of 86% was calculated from eqn. (1) to (4), with a corresponding donor-acceptor distance (r_{AD}) of 3.9 nm. Typically, a cell membrane presents a thickness of 7 to 9 nm.⁵² Therefore, it can be concluded that the labeled lipids Rh-DOPE and NBD-C₆-HPC are located in the first and second lipid layer, respectively, around the nanoparticle clusters, confirming the synthesis of the solid magnetoliposomes.

For the study of SMLs interaction with model membranes (GUVs), the same labeled lipids were both included in the SMLs membrane. However, upon interaction with GUVs, FRET measurements did not allow observing the decrease of energy transfer by the increase in NBD (donor) emission band and the decrease of Rhodamine (acceptor) fluorescence band after interaction. Differently, a significant increase in both donor (NBD) and acceptor (Rhodamine) emission bands was detected (data not shown). One possible explanation for the rise in both emission bands upon interaction with GUVs is a quenching effect of both donor and acceptor emissions by the cluster of MnFe₂O₄ nanoparticles in SMLs. Upon fusion with model membranes (GUVs), the distance

between the NPs cluster and the fluorescent moieties in the SMLs membrane would increase, leading to an unquenching effect. To confirm this hypothesis, the SMLs membrane was labeled only with Rhodamine B-DOPE, and the emission spectrum was measured before and after interaction with GUVs (Figure 10). After interaction, an increase in the fluorescence emission was observed (Figure 10A), confirming the unquenching effect caused by the increase of the distance between NPs and the rhodamine moiety.

These results indicate that the SMLs can also fuse with cell membranes and are promising as nanocarrier systems for hydrophobic drugs, which can be released upon fusion with cell membranes.

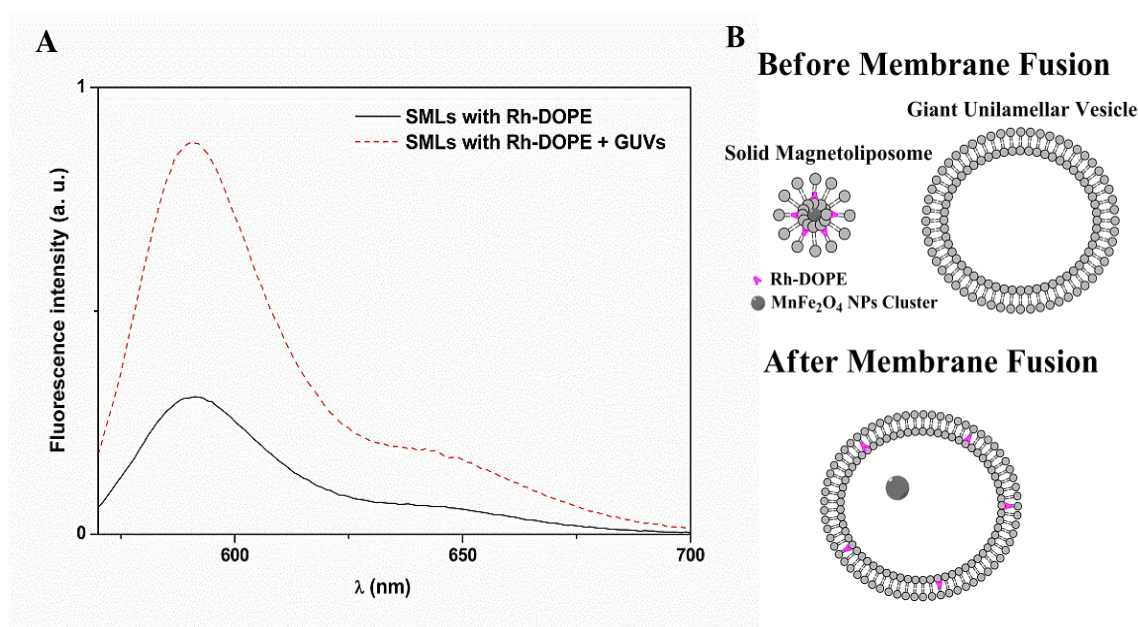


Fig. 10 **A.** Fluorescence spectra ($\lambda_{\text{exc}} = 560$ nm) of SMLs based on MnFe₂O₄ NPs covered with DOPG labeled with Rhodamine B-DOPE before and after interaction with GUVs. **B.** Schematic representation of the fusion between the GUVs and labeled SMLs.

4.5 Incorporation of a potential antitumor drug

The thienopyridine derivative **1** (Figure 1) presents very low growth inhibitory concentration values (GI_{50}), between 3.5 and 6.9 μM , when tested *in vitro* against several human tumor cell lines, namely MCF-7 (breast adenocarcinoma), A375-C5 (melanoma) and NCI-H460 (non-small cell lung cancer) and was the most active of a series of analogues.²⁴ Moreover, this compound has shown a very low affinity for the multidrug resistance protein MDR1,²⁷ being promising as an anticancer agent in oncological therapy, as MDR1 promotes drug resistance in cells.

Compound **1** was incorporated in both AMLs and SMLs of Mn ferrite NPs. Figure 11 shows the emission spectra of **1** in AMLs, SMLs and liposomes (without magnetic nanoparticles and with the same concentration of compound). It is possible to observe a quenching effect of the compound emission by the magnetic nanoparticles, proving the incorporation of the thienopyridine derivative in these magnetic nanocarriers. As expected, the fluorescence quenching is much more pronounced for solid magnetoliposomes, where the magnetic nanoparticles are closer to the antitumor compound, which is located mainly in the lipid membrane.²⁷

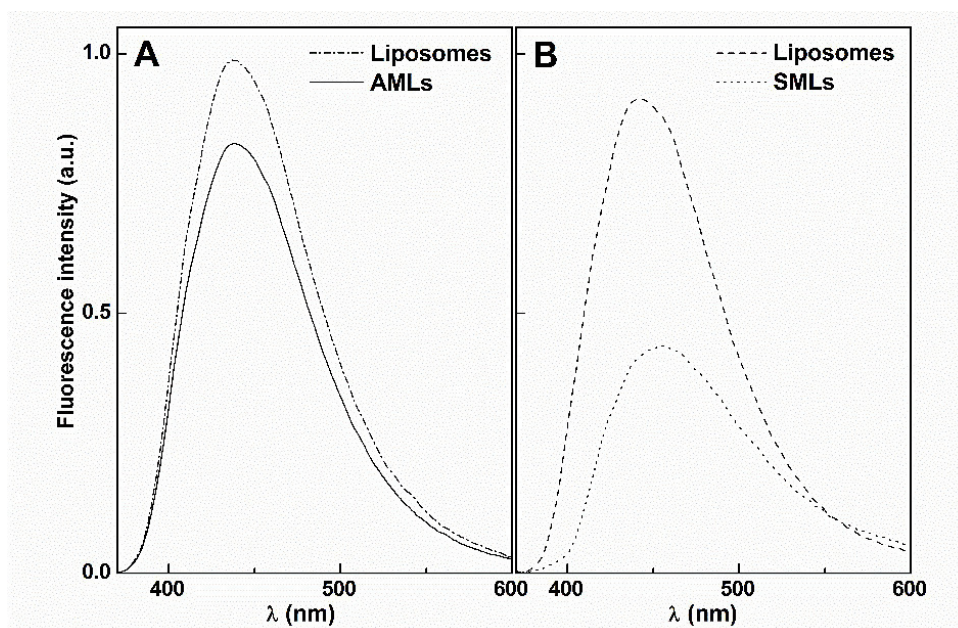


Fig. 11 Fluorescence spectra ($\lambda_{exc} = 360$ nm) of compound **1** (3×10^{-6} M) in liposomes and magnetoliposomes of Mn ferrite nanoparticles. **A.** Liposomes and AMLs of the phospholipid Egg-PC; **B.** Liposomes and SMLs of the phospholipid DOPG.

Fluorescence anisotropy measurements (Table 4) confirm that this compound is fully incorporated in both types of magnetoliposomes, located mainly in the lipid bilayer, as anisotropy values are similar to those previously determined in liposomes of the same lipids.²⁷

Interaction with model membranes (GUVs) was also investigated for both types of magnetoliposomes with incorporated compound **1**. In the case of AMLs, a FRET assay was performed, where the magnetoliposomes containing the antitumor drug **1** were labeled with NBD-PE, compound **1** acting as the energy donor and the NBD moiety as the energy acceptor. It was possible to confirm membrane fusion between AMLs and GUVs, proved by the diminution of FRET process from the drug to NBD (Figure 12A).

Table 4 - Steady-state fluorescence anisotropy (r) values for antitumor compound **1** in liposomes (without NPs), aqueous magnetoliposomes (AMLs) and solid magnetoliposomes (SMLs).

	Lipid formulation	Temperature (°C)	r	
Liposomes	Egg-PC (100%) [27]	25	0.176	
	Egg-PC:Ch (7:3) [27]	25	0.137	
	DPPC (100%) [27]	25	0.256	
		55	0.130	
	DOPG (100%)	25	0.181	
		55	0.143	
AMLs	Egg-PC (100%)	25	0.171	
	Egg-PC:Ch (7:3)	25	0.152	
	DPPC (100%)	25	0.201	
		55	0.136	
	SMLs	DOPG (100%)	25	0.189
			55	0.127

Otherwise, for SMLs, taking into account the fluorescence quenching caused by the presence of Mn ferrite NPs, compound **1** was incorporated in solid magnetoliposomes and the emission spectrum of compound **1** was measured before and after interaction with GUVs (Figure 12B). The unquenching effect observed after interaction with GUVs proves the membrane fusion between SMLs and the model membranes.

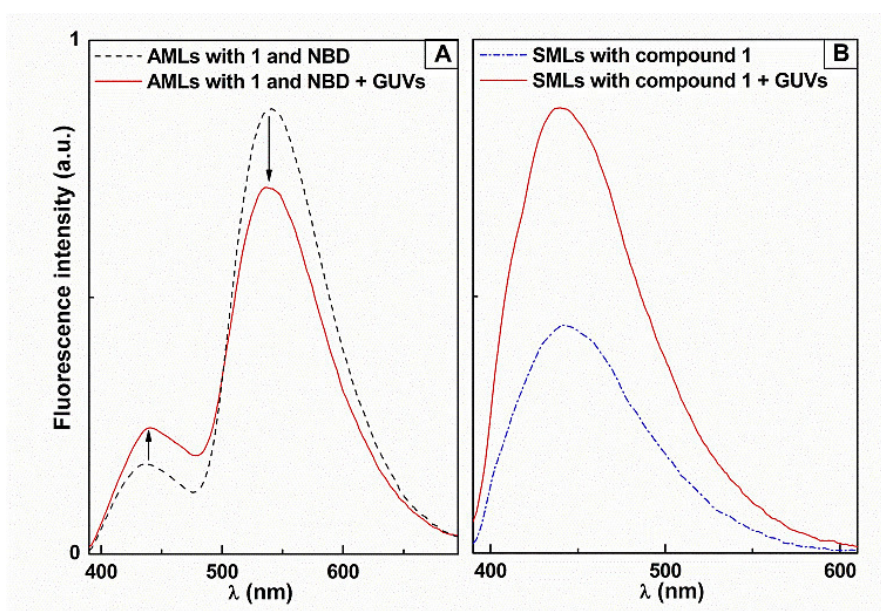


Fig. 12 A. Fluorescence spectra ($\lambda_{\text{exc}} = 360$ nm) of AMLs of Egg-PC and MnFe_2O_4 NPs containing both NBD-PE (4×10^{-6} M) and compound **1** (4×10^{-6} M), before and after interaction with GUVs. **B.** Fluorescence spectra ($\lambda_{\text{exc}} = 360$ nm) of compound **1** (4×10^{-6} M) in SMLs of DOPG and MnFe_2O_4 NPs before and after interaction with GUVs.

Therefore, the magnetoliposomes here prepared are promising as carriers for this antitumor compound. These results show that both aqueous and solid drug-loaded magnetoliposomes are promising as therapeutic agents, as they can be guided with a magnetic field to the therapeutic site and can release the loaded drug by fusion with the cell membrane.

5. Conclusions

In this work, small manganese ferrite nanoparticles were synthesized by coprecipitation method. Superparamagnetic properties were obtained for the MnFe_2O_4 NPs, with maximum magnetization of 36 emu/g at 5 T applied field and coercivity of 6.3 Oe.

The manganese ferrite nanoparticles were successfully encapsulated into liposomes (forming aqueous magnetoliposomes, AMLs) or covered by a lipid bilayer (solid magnetoliposomes, SMLs). FRET measurements pointed to membrane fusion between the magnetoliposomes (AMLs and SMLs) and models of cell membranes.

A potent antitumor thienopyridine derivative was successfully incorporated in both AMLs and SMLs. To our knowledge, it is the first time that solid magnetoliposomes based on manganese ferrite nanoparticles were prepared and evaluated as anticancer drug carriers.

These results are promising for future drug delivery applications of anticancer drugs using magnetoliposomes of MnFe_2O_4 nanoparticles simultaneously as drug nanocarriers and hyperthermia agents.

6. Acknowledgements

This work was supported by FEDER through the COMPETE/QREN/EU Program and by the Portuguese Foundation for Science and Technology (FCT) in the framework of the Strategic Projects of CFUM [PEst-C/FIS/UI0607/2013 (F-COMP-01-0124-FEDER-022711)] and CQ/UM [PEst-C/QUI/UI0686/2013 (FCOMP-01-0124-FEDER-022716)].

FCT, POPH-QREN and FSE are acknowledged for the PhD grant of A. R. O. Rodrigues (SFRH/BD/90949/2012) and for financial support to MAP-Fis PhD Programme.

7. References

1. M. Mezei and V. Gulasekharan, Liposomes – a selective drug delivery system for the topical route of administration, *Life Sci.*, 1980, **26**, 1473-1477.
2. R. L. Juliano, Liposomes as a drug delivery system. *Trends Pharm. Sci.*, 1981, **2**, 39-41.
3. G. Poste, C. Cucana, A. Raz, P. Bugelski, R. Kirsj and I. J. Fidler, Analysis of the fate of systemically administered liposomes and implication for their use in drug delivery, *Cancer Res.*, 1982, **42**, 1412-1422.
4. T. L. Andresen, S. S. Jensen and K. Jorgensen, Advanced strategies in liposomal cancer therapy: Problems and prospects of active and tumor specific drug release, *Prog. Lipid Res.*, 2005, **44**, 68-97.
5. N. A. Ocheke, P. O. Olorunfemi and N. C. Ngwuluka, Nanotechnology and Drug Delivery, Part 1: Background and Applications, *Trop. J. Pharm. Res.*, 2009, **8**, 265-274.
6. Y. Seow and M. J. Wood, Biological Gene Delivery Vehicles: Beyond Viral Vectors, *Mol. Ther.*, 2009, **17**, 767-777.
7. T. M. Allen and P. R. Cullis, Liposomal drug delivery systems: From concept to clinical applications, *Adv. Drug Delivery Rev.*, 2013, **65**, 36-48.
8. M. M. Elmi and M. N. Sarbolouki, A simple method for preparation of immunomagnetic liposomes, *Int. J. Pharm.*, 2001, **215**, 45-50.
9. A. A. Kuznetsov, V. I. Filippov, O. A. Kuznetsov, V. G. Gerlivanov, E. K. Dobrinsky and S. I. Malashin, New ferro-carbon adsorbents for magnetically guided transport of anti-cancer drugs, *J. Magn. Magn. Mater.*, 1999, **194**, 22-30.
10. O. A. Kuznetsov, N. A. Brusentsov, A. A. Kuznetsov, N. Y. Yurchenko, N. E. Osipov and F. S. Bayburtskiy, Correlation of the coagulation rates and toxicity of biocompatible ferromagnetic microparticles, *J. Magn. Magn. Mater.*, 1999, **194**, 83-89.
11. A. A. Kuznetsov, V. I. Filippov, R. N. Alyautdin, N. L. Torshina and O. A. Kuznetsov, Application of magnetic liposomes for magnetically guided transport of muscle relaxants and anti-cancer photodynamic drugs, *J. Magn. Magn. Mater.*, 2001, **225**, 95-100.

12. K. Nahar, S. Absar, B. Patel and F. Ahsan, Starch-coated magnetic liposomes as an inhalable carrier for accumulation of fasudil in the pulmonary vasculature, *Int. J. Pharm.*, 2014, **464**, 185-195.
13. G. Béalle, R. Di Corato, J. Kolosnjaj-Tabi, V. Dupuis, O. Clément, F. Gazeau, C. Wilhelm and C. Ménager, Ultra Magnetic Liposomes for MR Imaging, Targeting, and Hyperthermia, *Langmuir*, 2012, **28**, 11834-11842.
14. A. Hervault and N. T. K. Thanh, Magnetic nanoparticle-based therapeutic agents for thermo-chemotherapy treatment of cancer, *Nanoscale*, 2014, **6**, 11553-11573.
15. H-J. Weinmann, W. Ebert, B. Misselwitz and H. Schmitt-Willich, Tissue-specific MR contrast agents. *Eur. J. Radiol.*, 2003, **46**, 33-44.
16. C. Pereira, A. M. Pereira, C. Fernandes, M. Rocha, R. Mendes, M. P. F.-Garcia, A. Guedes, P. B. Tavares, J.-M. Grenèche, J. P. Araújo and C. Freire, Superparamagnetic MFe₂O₄ (M = Fe, Co, Mn) Nanoparticles: Tuning the Particle Size and Magnetic Properties through a Novel One-Step Coprecipitation Route, *Chem. Mater.*, 2012, **24**, 1496-1504.
17. D. Carta, M. F. Casula, P. Floris, A. Falqui, G. Mountjoy, A. Boni, C. Sangregorio and A. Corrias, Synthesis and microstructure of manganese ferrite colloidal nanocrystals, *Phys. Chem. Chem. Phys.* 2010, **12**, 5074-5083.
18. L. I. Cabrera, A. Somoza, J. F. Marco, C. J. Serna and M. P. Morales, Synthesis and surface modification of uniform MFe₂O₄ (M = Fe, Mn, and Co) nanoparticles with tunable sizes and functionalities, *J. Nanoparticle Res.*, 2012, **14**, 1-14.
19. H. Yang, C. Zhang, X. Shi, H. Hu, X. Du, Y. Fang, Y. Ma, H. Wu and S. Yang, Water-soluble superparamagnetic manganese ferrite nanoparticles for magnetic resonance imaging, *Biomaterials*, 2010, **31**, 3667-3673.
20. J. Lu, S. Ma, J. Sun, C. Xia, C. Liu, Z. Wang, X. Zhao, F. Gao, Q. Gong, B. Song, X. Shuai, H. Ai and Z. Gu, Manganese ferrite nanoparticle micellar nanocomposites as MRI contrast agents for liver imaging, *Biomaterials*, 2009, **30**, 2919-2928.
21. A. Tomitaka, A. Hirukawa, T. Yamada, S. Morishita and Y. Takemura, Biocompatibility of various ferrite nanoparticles evaluated by in vitro cytotoxicity assays using HeLa cells, *J. Magn. Magn. Mater.*, 2009, **321**, 1482-1484.
22. S. Dandamudi and R. B. Campbell, Development and characterization of magnetic cationic liposomes for targeting tumor microvasculature, *Biochim. Biophys. Acta*, 2007, **1768**, 427-438.

23. A. Akbarzadeh, M. Samiei and S. Davaran, Magnetic nanoparticles: preparation, physical properties, and applications in biomedicine, *Nanoscale Res. Lett.*, 2012, **7**, 144-157.
24. M.-J. R. P. Queiroz, R. C. Calhelha, L. Vale-Silva, E. Pinto and M. S.-J. Nascimento, Novel [6-(hetero)arylamino]thieno[3,2-*b*]pyridines: synthesis and antitumoral activities, *Eur. J. Med. Chem.*, 2010, **45**, 5732-5738.
25. J. M. H. Kremer, M. W. J. v. d. Esker, C. Pathmamanoharan and P. H. Wiersema, Vesicles of variable diameter prepared by a modified injection method, *Biochemistry*, 1977, **16**, 3932-3935.
26. A. R. O. Rodrigues, I. T. Gomes, B. G. Almeida, J. P. Araújo, E. M. S. Castanheira and P. J. G. Coutinho, Magnetoliposomes based on nickel ferrite nanoparticles for biomedical applications, *Phys. Chem. Chem. Phys.*, 2015, **17**, 18011-18021.
27. C.N.C. Costa, A.C.L. Hortelão, J.M.F. Ramos, A.D.S. Oliveira, R.C. Calhelha, M.-J.R.P. Queiroz, P.J.G. Coutinho and E.M.S. Castanheira, A new antitumoral Heteroarylaminothieno[3,2-*b*]pyridine derivative: its incorporation into liposomes and interaction with proteins monitored by fluorescence, *Photochem. Photobiol. Sci.*, 2014, **13**, 1730-1740.
28. Y. Tamba, H. Terashima and M. Yamazaki, A membrane filtering method for the purification of giant unilamellar vesicles, *Chem. Phys. Lipids*, 2011, **164**, 351-358.
29. T. Tanaka, Y. Tamba, S. M. Masum, Y. Yamashita and M. Yamazaki, La³⁺ and Gd³⁺ induce shape change of giant unilamellar vesicles of phosphatidylcholine, *Biochim. Biophys. Acta*, 2002, **1564**, 173-182.
30. B. Valeur, *Molecular Fluorescence – Principles and Applications*, Wiley-VCH, Weinheim, 2002.
31. J. N. Demas and G. A. Crosby, The measurement of photoluminescence quantum yields. – Review, *J. Phys. Chem.*, 1971, **75**, 991-1024.
32. S. Fery-Forgues and D. Lavabre, Are fluorescence quantum yields so tricky to measure? A demonstration using familiar stationary products, *J. Chem. Educ.*, 1999, **76**, 1260-1264.
33. I. Johnson and M. T. Z. Spence, *Molecular Probes Handbook: A Guide to Fluorescent Probes and Labeling Technologies*, 11th Ed., Invitrogen, 2011.

34. A. R. O. Rodrigues, I. T. Gomes, B. G. Almeida, J. P. Araújo, E. M. S. Castanheira and P. J. G. Coutinho, Magnetoliposomes based on nickel/silica core/shell nanoparticles: synthesis and characterization, *Mat. Chem. Phys.*, 2014, **148**, 978-987.
35. A. S. Edelstein and R. C. Cammaratra, *Nanomaterials: Synthesis, Properties and Applications*, Taylor & Francis Group, New York, 1996.
36. C. Dong, G. Wang, D. Guo, C. Jiang and D. Xue, Investigation of the thermal stability of Mn ferrite particles synthesized by a modified co-precipitation method, *Sci. China Phys. Mech. Astron.*, 2013, **56**, 568-572.
37. O. Stenzel, *The Physics of Thin Film Optical Spectra – An Introduction*, Springer, Berlin, 2005.
38. M. Y. Rafique, P. Li-Qing, Q. Javed, M. Z. Iqbal, Q. Hong-Mei, M. H. Farooq, G. Zhen-Gang and M. Tanveer, Growth of monodisperse nanospheres of MnFe_2O_4 with enhanced magnetic and optical properties, *Chinese Phys. B*, 2013, **22**, article 107101.
39. D. L. Schulz, R. A. Sailer and A. N. Caruso, Superparamagnetic Transition Metal Iron Oxygen Nanoparticles, *US Patent No. 0194733* (2009).
40. L. Khanna and N. K. Verma, Synthesis, characterization and in vitro cytotoxicity study of calcium ferrite nanoparticles, *Mater. Sci. Semicond. Process.*, 2013, **16**, 1842-1848.
41. B. D. Cullity and C. D. Graham, *Introduction to Magnetic Materials*, John Wiley & Sons Inc., Hoboken, New Jersey (USA), 2009.
42. D. R. Lide, Ed., *CRC Handbook of Chemistry and Physics*, 89th Ed., CRC Press/Taylor and Francis, Boca Raton, FL, USA, 2009,
43. M.-J. R. P. Queiroz, S. Dias, D. Peixoto, A. R. O. Rodrigues, A. D. S. Oliveira, P. J. G. Coutinho, L. A. Vale-Silva, E. Pinto and E. M. S. Castanheira, New potential antitumoral di(hetero)-arylether derivatives in the thieno[3,2-*b*]pyridine series: Synthesis and fluorescence studies in solution and in nanoliposomes, *J. Photochem. Photobiol. A: Chem.*, 2012, **238**, 71-80.
44. P. Pradhan, J. Giri, R. Banerjee, J. Bellare and D. Bahadur, Preparation and characterization of manganese ferrite-based magnetic liposomes for hyperthermia treatment of cancer, *J. Magn. Magn. Mater.*, 2007, **311**, 208-215.

45. G. Hungerford, E. M. S. Castanheira, M. E. C. D. Real Oliveira, M. G. Miguel and H. D. Burrows, Monitoring ternary systems of C₁₂E₅/water/tetradecane via the fluorescence of solvatochromic probes, *J. Phys. Chem. B*, 2002, **106**, 4061-4069.
46. P. Greenspan and S. D. Fowler, Spectrofluorometric studies of the lipid probe, Nile Red, *J. Lipid Res.*, 1985, **26**, 781-789.
47. I. and G. Krishnamoorthy, Probing the link between proton transport and water content in lipid membranes, *J. Phys. Chem. B*, 2001, **105**, 1484-1488.
48. P. J. G. Coutinho, E. M. S. Castanheira, M. C. Rei and M. E. C. D. Real Oliveira, Nile Red and DCM Fluorescence Anisotropy Studies in C₁₂E₇/DPPC Mixed Systems, *J. Phys. Chem. B*, 2002, **106**, 12841-12846.
49. E. Feitosa, F. R. Alves, A. Niemiec, M. E. C. D. R. Oliveira, E. M. S. Castanheira and A.L.F. Baptista, Cationic liposomes in mixed didodecyl-dimethylammonium bromide and dioctadecyldimethylammonium bromide aqueous dispersions studied by differential scanning calorimetry, Nile Red fluorescence, and turbidity, *Langmuir*, 2006, **22**, 3579-3585.
50. S. Zhang, H. Niu, Y. Zhang, J. Liu, Y. Shia, X. Zhang and Y. Cai, Biocompatible phosphatidylcholine bilayer coated on magnetic nanoparticles and their application in the extraction of several polycyclic aromatic hydrocarbons from environmental water and milk samples, *J. Chromatogr. A*, 2012, **1238**, 38-45.
51. S. García-Jimeno, E. Escribano, J. Queralt and J. Estelrich, Magnetoliposomes prepared by reverse-phase followed by sequential extrusion: Characterization and possibilities in the treatment of inflammation, *Int. J. Pharmaceut.*, 2011, **405**, 181-187.
52. H. Curtis and N. Barnes, *Biology*, 5th Edition, Worth Publishers, New York, 1989.

8. Supplementary Information

8.1 Size distributions obtained by Dynamic Light Scattering (DLS)

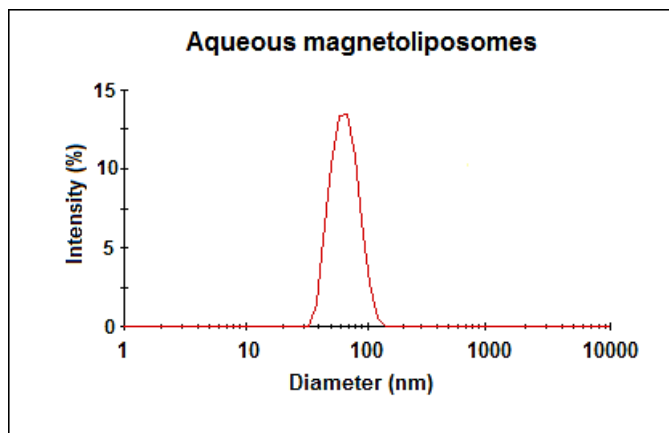


Fig. S1 Size distribution of Egg-PC aqueous magnetoliposomes (AMLs) containing MnFe_2O_4 nanoparticles.

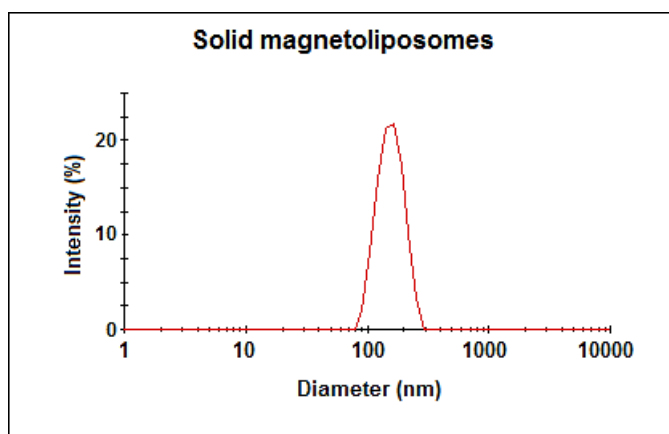


Fig. S2 Size distribution of DOPG solid magnetoliposomes (SMLs) containing MnFe_2O_4 nanoparticles.

**Magnetic liposomes as nanocarriers for promising antitumor
thieno[3,2-*b*]pyridin-7-arylamines: photophysical and
biological studies**

Ana Rita O. Rodrigues, B. G. Almeida, Juliana M. Rodrigues, Maria João R. P. Queiroz,
R. C. Calhelha, Isabel C. F. R. Ferreira, A. Pires, A. M. Pereira, J. P. Araújo, Paulo J. G.
Coutinho, Elisabete M. S. Castanheira

RSC Advances **7** (2017) 15352-15361

INDEX

1. Abstract
2. Introduction
3. Experimental
4. Results and discussion
5. Conclusions
6. Acknowledgments
7. References
8. Supplementary information

1. Abstract

Magnetoliposomes containing superparamagnetic manganese ferrite nanoparticles were tested as nanocarriers for two new promising antitumor drugs, a *N*-(3-methoxyphenyl)thieno[3,2-*b*]pyridin-7-amine (**1**) and a *N*-(2-methoxyphenyl)thieno[3,2-*b*]pyridin-7-amine (**2**). The fluorescence emission of both compounds was studied in different polar and non-polar media, evidencing a strong intramolecular charge transfer character of the excited state of both compounds. These *in vitro* potent antitumor thienopyridine derivatives were successfully incorporated in both aqueous and solid magnetoliposomes, with encapsulation efficiencies higher than 75%. The magnetic properties of magnetoliposomes containing manganese ferrite nanoparticles were measured for the first time, proving a superparamagnetic behaviour. Growth inhibition assays on several human tumor cell lines showed very low GI₅₀ values for drug-loaded aqueous magnetoliposomes, comparing in most cell lines with the ones previously obtained using the neat compounds. These results are important for future drug delivery applications using magnetoliposomes in oncology, through a dual therapeutic approach (simultaneous chemotherapy and magnetic hyperthermia).

2. Introduction

The high potential of magnetic nanoparticles for biomedical applications has been widely recognized due to their unique size and physicochemical properties. Nanoparticles with superparamagnetic behavior are preferred in biomedicine, as they exhibit a strong magnetization only when an external magnetic field is applied.^{1,2}

Liposomes entrapping magnetic nanoparticles (magnetoliposomes) are of large importance in drug delivery, as they can be guided and localized to the therapeutic site of interest by external magnetic field gradients and used in cancer treatment by hyperthermia.^{3,4} Magnetoliposomes have been proposed as T2 contrast agents (negative contrast enhancement) in MRI,⁵ while in therapy they have been used as a chemotherapy alternative through magnetic-controlled drug delivery and thermotherapy.⁶⁻⁸ Considering the wide applications of magnetoliposomes, much attention has been paid to the synthesis of different kinds of magnetic nanoparticles⁹⁻¹¹ and liposomes.¹²⁻¹⁵

Magnetoliposomes are specially promising as nanocarriers for potential antitumor drugs. Thienopyridine derivatives have been reported as possessing antiangiogenic,¹⁶⁻²¹

antitumor,²¹⁻²⁹ or both activities.³⁰ Among the potential antitumor di(hetero)arylamines in the thieno[3,2-*b*]pyridine series, prepared earlier by some of us, the ones with an *o*-methoxy or *m*-methoxy groups relative to the NH (compounds **1** and **2**, Fig. 1) presented the lowest growth inhibitory concentration (GI₅₀) values in several human tumor cell lines, between 0.09 and 0.31 μM for compound **1** and between 1.40 and 5.91 μM for compound **2**.²⁹ Compound **1** revealed to be more active than the well-known anticancer agent ellipticine against the cell lines MCF-7 (breast adenocarcinoma), NCI-H460 (non-small cell lung carcinoma), HepG2 (hepatocellular carcinoma), HCT15 (colon adenocarcinoma), and HeLa (cervical carcinoma), while compound **2** showed the lowest GI₅₀ against HeLa cells. However, these compounds also presented low GI₅₀ values in non-tumor PLP2 cells (1.94 μM for compound **1** and 6.56 μM for compound **2**).²⁹

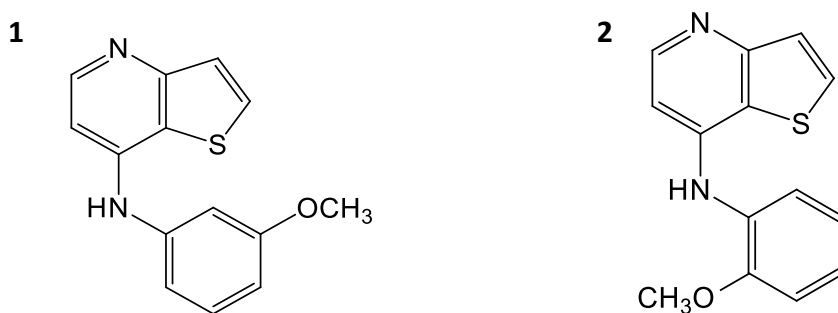


Fig. 1 Structure of compound **1**, *N*-(3-methoxyphenyl)- thieno[3,2-*b*]pyridin-7-amine), and compound **2**, *N*-(2-methoxy-phenyl)thieno[3,2-*b*]pyridin-7-amine).

Considering future applications of these new compounds as antitumor drugs, they were incorporated in magnetoliposomes, either aqueous or solid, containing manganese ferrite nanoparticles, suitable for biomedical applications.³¹

Magnetoliposomes may constitute ideal nanocarrier systems for encapsulation and transport of these drugs, as they can be guided and localized in tumor cells by a magnetic field gradient, and act simultaneously as chemotherapy/hyperthermia agents in a synergistic approach, reducing drug dosage due to the dual therapeutic effect.

3. Experimental

All the solutions were prepared using spectroscopic grade solvents and ultrapure water (Milli-Q grade).

3.1 Preparation of magnetoliposomes

Manganese ferrite nanoparticles (NPs) were synthesized by the coprecipitation method, as previously described.³¹ For magnetoliposomes preparation, the lipids egg yolk phosphatidylcholine (Egg-PC), dipalmitoylphosphatidylcholine (DPPC) and cholesterol (Ch), from Sigma-Aldrich, were used. For aqueous magnetoliposomes preparation, a 10 mM lipid solution in ethanol was injected, under vigorous vortexing, to an aqueous solution of magnetic nanoparticles, above the melting transition temperature of the lipids (ethanolic injection method).³² After encapsulation, the ferrofluid was washed with water and purified by ultracentrifugation to remove all the non-encapsulated NPs.

Solid magnetoliposomes (SMLs) were prepared by a method previously developed.³³ First, 10 μ L of the synthesized MnFe_2O_4 NPs were dispersed in 3 mL of water and centrifuged. Then, the deposited particles were dispersed in 10 μ L water in an ultrasonicator, for one minute at 189 W, and 3 mL of chloroform were added to the aqueous dispersion of NPs. After vigorous agitation, 165 μ L of a 20 mM solution of dipalmitoylphosphatidylcholine (DPPC) were added under vortexing, to form the first lipid layer of the SMLs. The particles were washed twice by magnetic decantation with pure water, in order to remove the lipid that was not attached to the NPs. The second lipid layer was then formed by the injection of 165 μ L of DPPC (20 mM), under vortexing, in a 3 mL aqueous dispersion of the particles with the first layer. The resulting SMLs were then washed and purified with ultrapure water by centrifugation.

Compounds **1** and **2** were incorporated into aqueous magnetoliposomes by the co-injection method, as already described.³⁴ In solid magnetoliposomes, the diarylamines **1** and **2** were incorporated by injection of an ethanolic solution together with the formation of the second lipid layer.

3.2 Spectroscopic measurements

3.2.1 General methods

Absorption spectra were recorded in a Shimadzu UV-3101PC UV-Vis-NIR spectrophotometer. Fluorescence measurements were performed using a Fluorolog 3 spectrofluorimeter, equipped with double monochromators in both excitation and emission and a temperature controlled cuvette holder. Fluorescence spectra were corrected for the instrumental response of the system.

The fluorescence quantum yields, Φ_s , were determined by the standard method (eqn (1)),^{35,36}

$$\Phi_s = \left[\frac{(A_r F_s n_s^2)}{(A_s F_r n_r^2)} \right] \Phi_r \quad (1)$$

where A is the absorbance at the excitation wavelength, F the integrated emission area and n is the refraction index of the solvents. Subscripts refer to the reference (r) or sample (s) compound. The absorbance value at excitation wavelength was always less than 0.1, in order to avoid inner filter effects.

3.2.2 Fluorescence anisotropy measurements

The steady-state fluorescence anisotropy, r , is calculated by

$$r = \frac{I_{VV} - GI_{VH}}{I_{VV} + 2GI_{VH}} \quad (2)$$

where I_{VV} and I_{VH} are the intensities of the emission spectra obtained with vertical and horizontal polarization, respectively (for vertically polarized excitation light), and $G = I_{HV}/I_{HH}$ is the instrument correction factor, where I_{HV} and I_{HH} are the emission intensities obtained with vertical and horizontal polarization (for horizontally polarized excitation light).

3.2.3 FRET measurements

The formation of a DPPC bilayer around manganese ferrite nanoparticles was investigated by Förster Resonance Energy Transfer (FRET), using the labeled lipids NBD-C₆-HPC (1-palmitoyl-2-{6-[(7-nitro-2-1,3-benzoxadiazol-4-yl)amino]hexanoyl}-sn-glycero-3-phosphocholine) and Rhodamine B-DOPE (*N*-(lissamine Rhodamine B sulfonyl)-1,2-dioleoyl-sn-3-phosphatidyl-ethanolamine (ammonium salt)), both from Avanti Polar Lipids (Fig. 2).

FRET efficiency, Φ_{RET} , defined as the proportion of donor molecules that have transferred their excess energy to acceptor molecules, can be obtained by taking the ratio of the donor integrated fluorescence intensities in the presence of acceptor (F_{DA}) and in the absence of acceptor (F_D) (eqn (3)),³⁷

$$\Phi_{RET} = 1 - \frac{F_{DA}}{F_D} \quad (3)$$

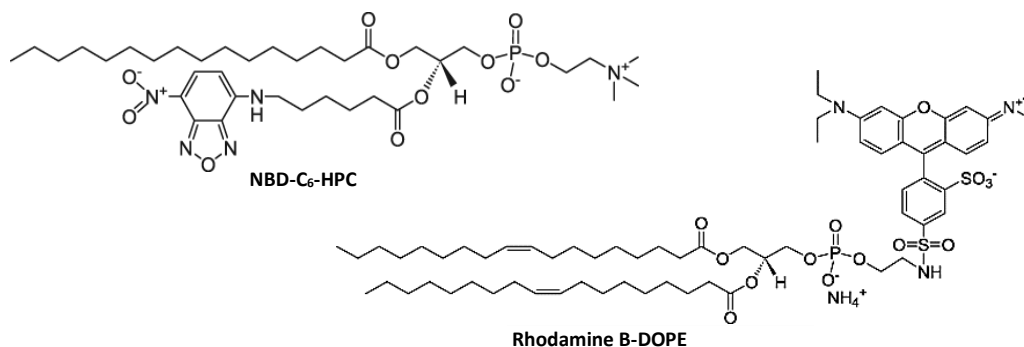


Fig. 2 Structure of the labeled lipids NBD-C₆-HPC and Rhodamine B-DOPE.

The distance between donor and acceptor molecules can be determined through the FRET efficiency (eqn. (4)),

$$r_{AD} = R_0 \cdot \left[\frac{1 - \Phi_{RET}}{\Phi_{RET}} \right]^{1/6} \quad (4)$$

where R_0 is the Förster radius (critical distance), that can be obtained by the spectral overlap, $J(\lambda)$, between the donor emission and the acceptor absorption, according to eqn (5) and (6) (with R_0 in Å, λ in nm, $\epsilon_A(\lambda)$ in $M^{-1} cm^{-1}$),³⁷

$$R_0 = 0.2108 [k^2 \Phi_D^0 n^{-4} J(\lambda)]^{1/6} \quad (5)$$

$$J(\lambda) = \int_0^\infty I_D(\lambda) \epsilon_A(\lambda) \lambda^4 d\lambda \quad (6)$$

where $k^2 = 2/3$ is the orientational factor assuming random orientation of the dyes, Φ_D^0 is the fluorescence quantum yield of the donor in the absence of energy transfer, n is the refraction index of the medium, $I_D(\lambda)$ is the fluorescence spectrum of the donor normalized so that $\int_0^\infty I_D(\lambda) d\lambda = 1$, and $\epsilon_A(\lambda)$ is the molar absorption coefficient of the acceptor.

For determination of fluorescence quantum yield of NBD-C₆-HPC (energy donor) in magnetoliposomes, this fluorescent labeled lipid incorporated in lipid membranes was used as reference, $\Phi_r = 0.32$ at 25°C, as reported by Invitrogen.³⁸

3.2.4 *Compound Encapsulation Efficiency*

The encapsulation efficiency, *EE* (%), of antitumor compounds was determined through fluorescence emission measurements. After preparation, drug-loaded magnetoliposomes (MLs) were subjected to centrifugation at 11000 rpm for 60 minutes. The supernatant was pipetted out and its fluorescence was measured, allowing to determine the compound concentration using a calibration curve previously obtained. Three independent measurements were performed for each system and standard deviations (SD) were calculated. The encapsulation efficiency of compounds **1** and **2** was determined using the following equation:

$$EE(\%) = \frac{(total\ amount - amount\ of\ non\ encapsulated\ compound)}{total\ amount} \times 100 \quad (7)$$

3.2.5 *Scanning electron microscopy (SEM)*

Scanning electron microscopy (SEM) images of solid magnetoliposomes were recorded using a Scanning Electron Microscope FEI - Nova 200 NanoSEM. For the negative staining procedure, a 2% aqueous solution of ammonium molybdate tetrahydrate was prepared. Then, 20 μ L of sample and 20 μ L of staining solution were mixed and a drop of this mixture was placed onto a Formvar grid, held by tweezers. After 20 seconds, almost all the solution was removed with filter paper and left dry.

3.2.6 *Magnetic properties of magnetoliposomes*

Magnetic measurements were performed at room temperature in a Superconducting Quantum Interference Device (SQUID) magnetometer (Quantum Design MPMS5XL), using applied magnetic fields up to 5.5 T.

The magnetization hysteresis loop measurements were performed by fixing the temperature and measuring the magnetization at a series of different applied magnetic fields. This type of study gives information about the saturation magnetization, the degree at which the sample remains magnetized when the applied field is removed, and how easily the sample magnetization can be reversed, the so-called coercive field. The magnetization was corrected for the diamagnetic contribution from the lipids and water and normalized by the mass of the samples, which was determined after drying them.

3.2.7 Growth inhibitory activity of drug-loaded AMLs on human tumor cell lines and on porcine liver primary cells

Two types of aqueous magnetoliposomes with different compositions (100% Egg-PC and 95:5 Egg-PC:DSPE-PEG2000-Folate, from Avanti Polar Lipids) were loaded with compound **1** or compound **2**, with different compound concentrations (0.03 μM to 7.5 μM). *In vitro* cytotoxicity evaluation was assessed for four human tumor cell lines, namely MCF-7 (breast adenocarcinoma), NCI-H460 (non-small cell lung cancer), HeLa (cervical carcinoma) and T3M4 (pancreatic cancer). The cell line PLP2 (non-tumor cells) was used to evaluate the toxicity to healthy tissues. The cell lines were obtained from Leibniz Institute DSMZ – German Collection of Microorganisms and Cell Cultures.

The cells were routinely maintained as adherent cell cultures in RPMI-1640 medium containing 10% heat-inactivated FBS, at 37°C, in a humidified air incubator containing 5% CO₂. Each cell line was plated at an appropriate density (1.0×10^4 cells per well) in 96-well plates and allowed to attach for 24 h. The cells were then treated for 48 h with the different solutions. Following this incubation period, the adherent cells were fixed by adding cold 10% TCA (100 μL) and incubated for 60 min at 4°C. Plates were then washed with deionized water and dried. A sulforhodamine B (SRB) solution (0.1% in 1% acetic acid, 100 μL) was then added to each plate-well and incubated for 30 min at room temperature. Unbound SRB was removed by washing with 1% acetic acid. The plates were air-dried and the bound SRB was solubilized with 10 mM Tris-HCl buffer (200 μL , pH = 7.4). The absorbance was then measured at 540 nm in a microplate reader [39,40]. The results were expressed in GI₅₀ values (concentration that inhibited 50% of net cell growth).

4. Results and discussion

4.1 Photophysical properties in homogeneous solution

The promising antitumor properties of the di(hetero)arylamines **1** and **2** (Fig. 1)²⁹ inspired us to study the photophysical behaviour of these compounds in homogeneous solution, as they exhibit intrinsic fluorescence. Thus, the absorption and fluorescence properties of the thieno[3,2-*b*]pyridine derivatives **1** and **2** were studied in several solvents of different polarity. The maximum absorption (λ_{abs}) and emission wavelengths (λ_{em}), molar absorption coefficients and fluorescence quantum yields are shown in Table

1. The normalized fluorescence spectra are displayed in Fig. 3 and 4 (examples of absorption spectra are also shown).

The thieno[3,2-*b*]pyridines **1** and **2** present moderate to high absorption coefficient values ($\epsilon \geq 7 \times 10^3 \text{ M}^{-1} \text{ cm}^{-1}$) in all solvents, having also very reasonable fluorescence quantum yields (Table 1), a similar behaviour to that observed in other thienopyridine derivatives previously studied.^{26,34,42,43}

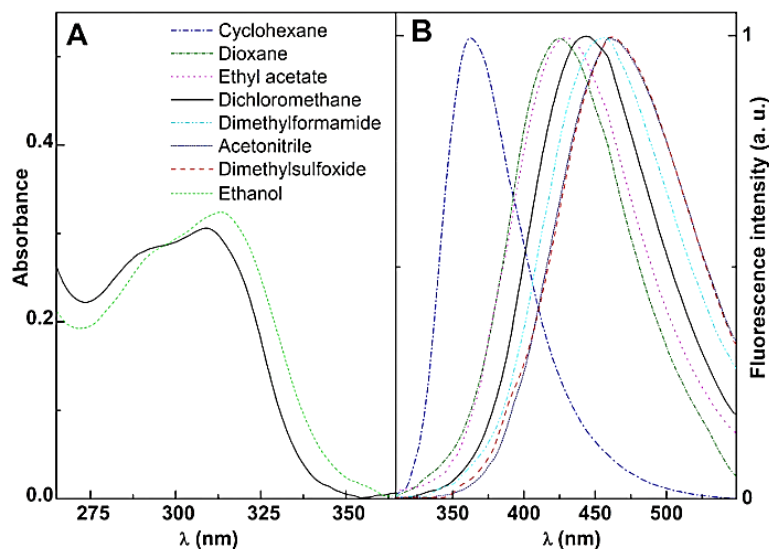


Fig. 3 (A) Absorption spectra of 2×10^{-5} M solutions of compound **1** in dichloromethane and ethanol, as examples. (B) Normalized fluorescence spectra ($\lambda_{\text{exc}} = 310$ nm) of 3×10^{-6} M solutions of compound **1** in several solvents.

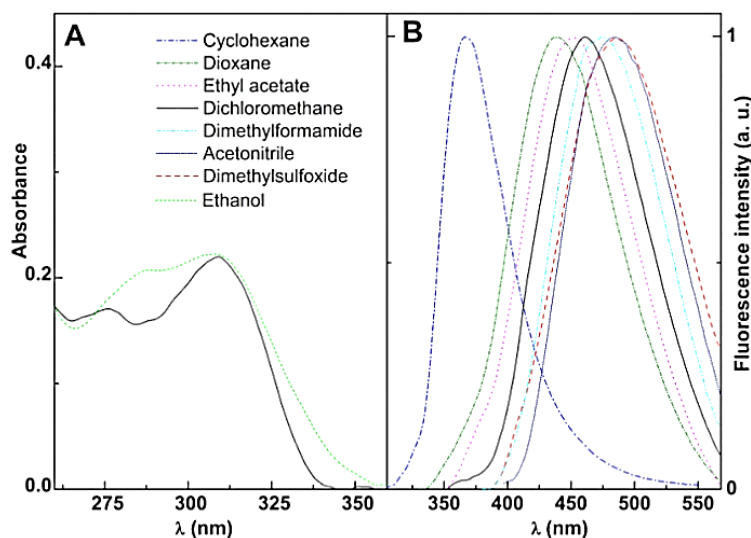


Fig. 4 (A) Absorption spectra of 2×10^{-5} M solutions of compound **2** in dichloromethane and ethanol, as examples. (B) Normalized fluorescence spectra ($\lambda_{\text{exc}} = 310$ nm) of 3×10^{-6} M solutions of compound **2** in several solvents.

Table 1 Maximum absorption (λ_{abs}) and emission (λ_{em}) wavelengths, molar absorption coefficients (ϵ) and fluorescence quantum yields (Φ_{F}) for the thieno[3,2-*b*]pyridine derivatives **1** and **2** in several solvents.

Solvent	λ_{abs} (nm) ($\epsilon / 10^4 \text{ M}^{-1} \text{ cm}^{-1}$)		λ_{em} (nm)		Φ_{F} ^a	
	1	2	1	2	1	2
Cyclohexane	292 (1.29); 312 <i>sh</i>	283 <i>sh</i> ; 314 (0.77)	363	366	0.37	0.42
Dioxane	300 (1.67)	282 <i>sh</i> ; 312 (1.17)	428	436	0.35	0.30
Ethyl acetate ^b	293 <i>sh</i> ; 302 (1.01)	284 (1.30); 315 (1.18)	431	450	0.60	0.59
Dichloromethane	293 <i>sh</i> ; 310 (1.54)	283 <i>sh</i> ; 312 (1.15)	444	461	0.53	0.39
<i>N,N</i> -Dimethylformamide	312 (2.09)	313 (0.78)	457	476	0.43	0.40
Acetonitrile	294 <i>sh</i> ; 312 (2.03)	283 <i>sh</i> ; 318 (1.01)	459	485	0.30	0.18
Dimethylsulfoxide ^b	311 (1.96)	313 (1.39)	461	486	0.48	0.36
Ethanol	313 (1.77)	287 <i>sh</i> ; 313 (1.06)	---	---	---	---

^a Relative to anthracene in ethanol ($\Phi_{\text{r}} = 0.27$ [41]). Error about 10%.

^b Solvents *cut-off*: Ethyl acetate: 265 nm; dimethylsulfoxide: 270 nm; *N,N*-dimethylformamide: 275 nm. *sh*: shoulder

Additional common features with other thienopyridines are the negligible fluorescence in protic media (due to hydrogen bonding with this type of solvents), the red shifts in emission and band enlargement with increasing solvent polarity,^{26,34,42,43} usually attributed to an intramolecular charge transfer (ICT) character of the excited state.³⁷ The effect is more pronounced for compound **2**, exhibiting larger bathochromic shifts in polar solvents (a red shift of 120 nm between cyclohexane and dimethylsulfoxide, Table 1).

The significant sensitivity of the emission of diarylamines **1** and **2** to their environment can be useful to understand their behaviour in magnetoliposomes of different compositions.

4.2 Magnetoliposomes formulations

Both aqueous (AMLs) and solid (SMLs) magnetoliposomes containing manganese ferrite nanoparticles were prepared. The influence of lipid membrane fluidity in AMLs was investigated using egg-phosphatidylcholine (Egg-PC), a fluid phosphatidylcholine mixture at room temperature,⁴⁴ dipalmitoylphosphatidylcholine (DPPC), with a melting transition temperature of 41 °C,⁴⁵ and Egg-PC/Cholesterol 7:3, the latter mixture usually being used as model of biological membranes.^{46,47} Neat Egg-PC and Egg-PC:Cholesterol aqueous magnetoliposomes containing lauric acid coated MnFe₂O₄ nanoparticles were also previously prepared by Pradhan and coworkers,⁴⁸ the

Egg-PC:Cholesterol 2:1 being the most promising formulation for hyperthermia treatment of cancer.

Here, DPPC was used for the first time in the preparation of solid magnetoliposomes containing manganese ferrite NPs. The interest of this phospholipid is its melting transition temperature slightly above the physiological temperature, thus being promising for the release of drugs enhanced by the phase transition in combined chemotherapy/hyperthermia strategies. In fact, several studies have demonstrated that the thermal enhancement of the cytotoxic activity of many anticancer agents is maximized at mild hyperthermia temperatures (40.5 – 43°C).⁴⁹

The formation of the double DPPC bilayer around a cluster of magnetic nanoparticles was investigated by FRET assays. Thus, the NBD labeled lipid NBD-C₆-HPC was included in the second lipid layer of SMLs (NBD acting as the energy donor), while the labeled lipid Rhodamine B-DOPE (energy acceptor) was incorporated in the first lipid layer. The emission of SMLs containing both donor and acceptor labeled lipids was measured exciting only NBD, and was compared with the emission of SMLs labeled with only the energy donor (Fig. 5). Comparing the fluorescence spectra of the two systems, a decrease in the NBD emission band and the presence of a pronounced Rhodamine emission is observed in SMLs containing both fluorophores, evidencing the energy transfer from the excited NBD to Rhodamine B.

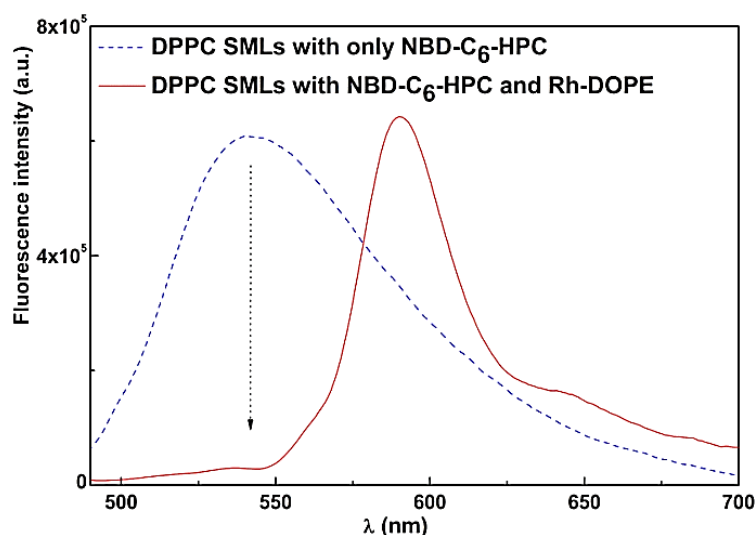


Fig. 5 Fluorescence spectra ($\lambda_{exc} = 470$ nm, no rhodamine excitation) of SMLs with DPPC bilayer labeled with only NBD-C₆-HPC and SMLs labeled with both NBD-C₆-HPC and rhodamine B-DOPE.

A FRET efficiency of 85% was calculated from equations (3) to (6), with a corresponding donor-acceptor distance (r_{AD}) of 5.3 nm. Considering that a cell membrane presents a thickness of 7 to 9 nm,⁵⁰ it can be concluded that the labeled lipids Rhodamine-DOPE and NBD-C₆-HPC are located in the first and second lipid layer, respectively, around the nanoparticle clusters, confirming the synthesis of the solid magnetoliposomes.

Analogous results were obtained for SMLs of DPPC:Cholesterol 2:1. These results are also similar to the ones already reported for SMLs of the phospholipid DOPG containing manganese ferrite nanoparticles,³¹ indicating that the method previously developed by us for the preparation of DOPG solid magnetoliposomes³³ can also be employed for different lipids. Size distributions of 124 ± 23 nm (by number) and of 141 ± 38 nm (by intensity) were obtained through Dynamic Light Scattering measurements for SMLs of phospholipid DPPC (Fig. S1 in Supporting Information), showing an appropriate size for biomedical applications. SEM images of these SMLs also evidence structures with diameters lower than 150 nm (Fig. S2 in Supporting Information), in accordance with DLS data.

4.3 Magnetic properties of magnetoliposomes

Previously synthesized manganese ferrite nanoparticles have shown to be superparamagnetic at room temperature.³¹ Here, the magnetic hysteresis cycles of aqueous magnetoliposomes and solid magnetoliposomes were measured at 316 K and are displayed in Fig. 6. The hysteresis loop of neat MnFe₂O₄ NPs is also shown, for comparison.

In terms of hysteresis, both nanosystems present a similar behaviour to the one of neat NPs, with small coercive fields of 4.22 Oe and 8.43 Oe for SMLs and AMLs, respectively (Fig. 6). Table 2 summarizes the magnetic data obtained from the loops. The presence of superparamagnetic behaviour can be evidenced by determining the magnetic squareness value, which is the ratio between the remnant magnetization, M_r , and the saturation magnetization, M_s . Magnetic squareness values indicative of superparamagnetism are of the order or below 0.1, meaning the loss of more than 90% of the magnetization upon removal of the applied magnetic field.^{51,52} The magnetic squareness values for AMLs and SMLs clearly indicate the presence of a superparamagnetic behaviour (Table 2).

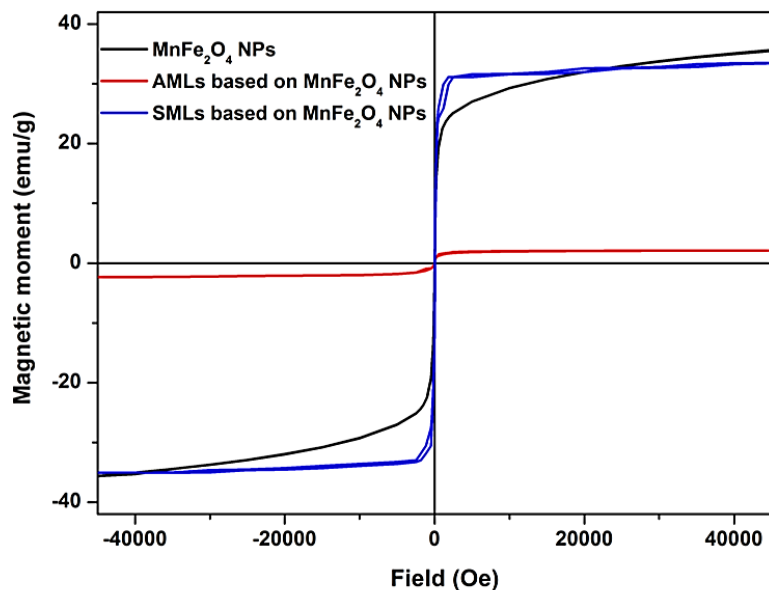


Fig. 6 Magnetization hysteresis cycles, measured at 316 K, of neat MnFe_2O_4 nanoparticles, DPPC SMLs and Egg-PC AMLs containing MnFe_2O_4 NPs.

Table 2 Coercive field (H_c), saturation magnetization (M_s), remnant magnetization (M_r) and ratio M_r/M_s for manganese ferrite NPs and magnetoliposomes.

System	H_c (Oe)	M_s (emu/g)	M_r (emu/g)	M_r/M_s
MnFe_2O_4 NPs ²⁹	6.30	36.00	0.58	0.016
SMLs (DPPC)	4.22	34.16	0.90	0.03
AMLs (Egg-PC)	8.43	1.17	0.08	0.07

As previously reported for magnetoliposomes based on iron oxide nanoparticles,^{53,54} the saturation magnetization of the manganese ferrite nanoparticles decreases after encapsulation into liposomes, this decrease being much more pronounced in the case of AMLs. For SMLs, the saturation magnetization is close to the one of neat MnFe_2O_4 nanoparticles, while for AMLs a strong decrease is observed (Table 2). This is due to the lower molar ratio between magnetic NPs and lipids for AMLs, when compared to SMLs and bare NPs samples, which contributes to an overall lower saturation magnetization of the combined lipid + nanoparticles system. On the other hand, on AMLs and SMLs, a more clear saturation of the hysteresis loops is observed as compared to the bare NPs (Fig. 6). This indicates an increased degree of clustering of the nanoparticles encapsulated in liposomes, which enhances the interparticle magnetic interaction and favors the alignment of their magnetic moments, as is more clearly observed at higher applied magnetic fields.

4.4 Fluorescence studies in (magneto)liposomes

The thieno-pyridine derivatives **1** and **2** were encapsulated in magnetoliposomes, both aqueous (AMLs) and solid (SMLs). For comparison, studies in liposomes (without magnetic nanoparticles) of the same lipid compositions were also performed.

Examples of fluorescence emission spectra of compounds **1** and **2** in magnetoliposomes are shown in Fig. 7 (maximum emission wavelengths are presented in Table 3). Emission in liposomes (without magnetic nanoparticles and with the same concentration of compound) is also shown for comparison. A quenching effect of compounds emission by the magnetic nanoparticles is observed, proving the incorporation of these potential drugs in the magnetic nanocarriers. As expected, the fluorescence quenching is significantly more pronounced in solid magnetoliposomes, where the magnetic nanoparticles are closer to the antitumor compounds. This behaviour is similar to the previously observed with another antitumor thienopyridine derivative in AMLs and SMLs containing MnFe_2O_4 NPs.³¹

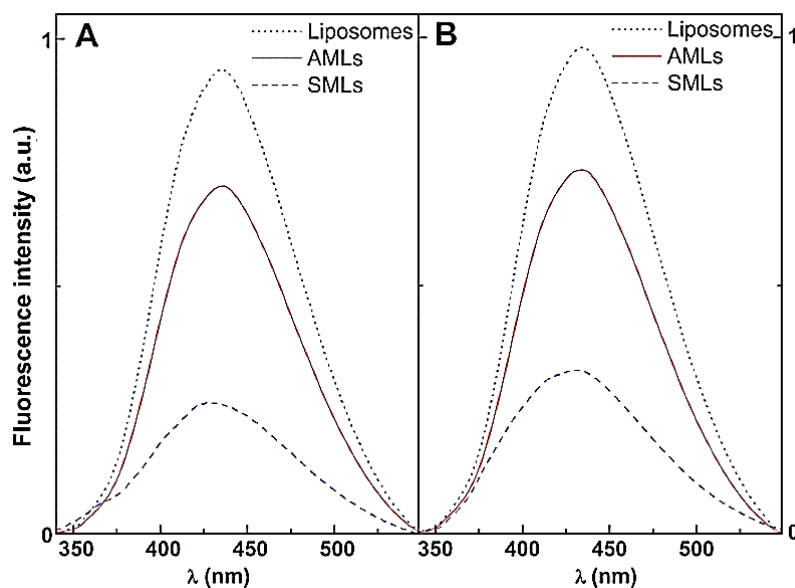


Fig. 7 Normalized fluorescence spectra of compounds **1** and **2** (3×10^{-6} M) in liposomes and magnetoliposomes (Egg-PC AMLs and DPPC SMLs), at room temperature ($\lambda_{\text{exc}} = 310$ nm). (A) Compound **1**; (B) Compound **2**.

Relevant information about the location of these antitumor compounds in (magneto)liposomes can be obtained through fluorescence anisotropy (r) measurements, as the r value increases with the rotational correlational time of the fluorescent molecule (and, thus, with the viscosity of the environment, eqn (8)),³⁷

$$\frac{1}{r} = \frac{1}{r_0} \left(1 + \frac{\tau}{\tau_c} \right) \quad (8)$$

where r_0 is the fundamental anisotropy, τ is the excited-state lifetime and τ_c is the rotational correlation time.

The fluorescence (steady-state) anisotropies of these diarylamines in the several systems are displayed in Table 3. For comparison, the fluorescence anisotropy values in the highly viscous solvent glycerol ($\eta = 993.4$ cP at 25°C)⁵⁵ at room temperature were also measured (Table 3). Upon temperature increase, the excited-state lifetime of these molecules is predicted to decrease, due to the increment of the non-radiative deactivation pathways (mainly the rate constant for internal conversion $S_1 \rightarrow S_0$). According to equation (8), an increase of the fluorescence anisotropy is expected from a diminution of the excited-state lifetime. The anisotropy values for **1** and **2** in DPPC-based systems decrease significantly at 55°C (Table 3) and this behaviour can be attributed to a decrease in the rotational correlation time of the fluorophore. This originates from the decrease of membrane microviscosity upon changing from the gel to the liquid-crystalline phase of DPPC above 41°C (melting transition temperature).

Table 3 Steady-state fluorescence anisotropy (r) values and maximum emission wavelengths (λ_{em}) for diarylamines **1** and **2** in several liposome and magnetoliposome formulations, at 25°C and 55°C.

	Lipid formulation	T (°C)	λ_{em} (nm)		r	
			1	2	1	2
Liposomes (without NPs)	Egg-PC (100%)	25	432	433	0.195	0.222
	Egg-PC:Ch (7:3)	25	433	434	0.212	0.202
	DPPC (100%)	25	432	433	0.200	0.222
		55	430	431	0.141	0.101
AMLs	Egg-PC (100%)	25	432	433	0.191	0.230
	Egg-PC:Ch (7:3)	25	433	435	0.220	0.201
	DPPC (100%)	25	432	433	0.202	0.287
		55	432	432	0.153	0.140
SMLs	DPPC (100%)	25	430	427	0.159	0.135
		55	428	424	0.101	0.051
Glycerol	----	25	---	---	0.304	0.321

The differences in anisotropy values between the compounds incorporated in lipid systems and in glycerol at room temperature can also be attributed to the distinct environment viscosities, as lipid membranes, exhibiting viscosity values around 100-200 cP,^{56,57} are much less viscous than glycerol. These results indicate that both compounds are mainly located in the lipid bilayers.

The effect of cholesterol (Ch) in Egg-PC membranes, as reported by fluorescence anisotropy values, is different for compounds **1** and **2** (a slight increase in fluidity reported by compound **2** and a diminution for compound **1**). However, this effect is small and may be related with slightly different locations of these compounds in membranes. From the values of maximum emission wavelengths in AMLs and SMLs, an environment with polarity similar to dioxane or ethyl acetate is anticipated (Tables 1 and 3).

It was reported that membrane viscosity decreases from the outside to inside the membrane^{58,59} and this may justify, besides possible differences in compound excited-state lifetimes, the lower anisotropies for both compounds in solid magnetoliposomes, when compared to AMLs. Maximum emission wavelength values point to less polar environments felt by compounds in SMLs (Table 3), corroborating that these potential drugs are deeply located in SMLs membranes.

The encapsulation efficiencies of both compounds in AMLs and SMLs are presented in Table 4. Values of encapsulation efficiency are larger than 75%, the lowest *EE%* being observed for compound **2** in aqueous magnetoliposomes.

Table 4 Encapsulation efficiencies (*EE%*) of compounds **1** and **2** in magnetoliposomes.

System	<i>EE% ± SD</i>	
	Compound 1	Compound 2
AMLs (Egg-PC)	89.0 ± 4.5	75.9 ± 6.8
SMLs (DPPC)	88.1 ± 4.9	82.1 ± 6.1

These high encapsulation efficiencies point to a promising use of these nanocarriers in magnetically-guided transport of compounds **1** and **2**, and as agents for simultaneous chemotherapy and hyperthermia agents in oncological therapy. These potentialities will allow reducing the blood circulating time of the drugs and lowering side effects, which is especially important as both compounds are hydrophobic and present some cytotoxicity for normal PLP2 cells, with low GI_{50} values of $1.94 \pm 0.16 \mu\text{M}$ for compound **1** and $6.56 \pm 0.2 \mu\text{M}$ for compound **2**.²⁹

4.5 Growth inhibitory activity of drug-loaded AMLs on human tumor cell lines and on porcine liver primary cells

The tumor cell growth inhibitory activity of AMLs containing compounds **1** and **2** was evaluated in four human tumor cell lines, specifically MCF-7 (breast

adenocarcinoma), HeLa (cervical carcinoma), T3M4 (pancreatic cancer) and NCI-H460 (non-small cell lung cancer). Moreover, the toxicity of the drug-loaded AMLs towards non-tumor cells was studied using porcine liver primary cells (PLP2). This allowed the determination of the GI₅₀ values (μM), corresponding to the compound concentration which inhibited 50% of cell growth (Table 5). Besides the neat Egg-PC AMLs, the influence of 5% PEG-folate in AMLs formulation was also investigated, as folate receptors are generally overexpressed in tumor cells.

Table 5 Growth inhibitory activity of drug-loaded aqueous magnetoliposomes on various human tumor cell lines and non-tumor porcine liver primary cells (PLP2).

Cell line	GI ₅₀ values ^a (μM) for compound 1			GI ₅₀ values ^a (μM) for compound 2		
	Only compound 1 ²⁹	Egg-PC AMLs with compound 1	Egg-PC/PEG-Fol (95:5) AMLs with compound 1	Only compound 2 ²⁹	Egg-PC AMLs with compound 2	Egg-PC/PEG-Fol (95:5) AMLs with compound 2
HeLa	0.09 ± 0.00	0.15 ± 0.02	0.09 ± 0.01	1.40 ± 0.06	1.32 ± 0.15	1.44 ± 0.07
MCF7	0.25 ± 0.03	0.45 ± 0.01	0.44 ± 0.0003	5.88 ± 0.86	5.67 ± 0.62	5.56 ± 0.11
T3M4	----	0.26 ± 0.02	0.30 ± 0.002	----	1.56 ± 0.05	1.68 ± 0.07
NCI-H460	0.2 ± 0.03	0.37 ± 0.03	0.35 ± 0.07	5.40 ± 0.89	1.66 ± 0.22	1.79 ± 0.12
PLP2	1.94 ± 0.16	1.46 ± 0.03	1.37 ± 0.14	6.56 ± 0.2	3.48 ± 0.25	3.46 ± 0.13

^a GI₅₀ values correspond to the concentration which inhibited 50% of cell growth. Results are from three independent experiments (performed in triplicate), and are expressed as mean ± standard deviation (SD).

Both aqueous and solid magnetoliposomes (without compounds) evidenced no inhibitory activity on the same cell lines, including the non-tumor PLP2, when tested in the same conditions used with the drug-loaded systems. From the results obtained (Table 5), it can be concluded that the drug-loaded AMLs are efficient in inhibiting tumor cells, presenting GI₅₀ values similar to the ones determined previously using only the compounds,²⁹ except for compound 2 in these formulations, that presents very much low GI₅₀ values for the NCI-H460 lung cancer cell line. The presence of folate has only a significant effect for compound 1 in HeLa tumor cell line. For compound 2, the presence of folate in magnetoliposomes does not influence noticeably the results (Table 5). Nevertheless, the GI₅₀ values clearly show that aqueous magnetoliposomes are able to release the encapsulated compounds 1 and 2 and to inhibit the growth of tumor cells. It is also noteworthy the very low GI₅₀ values obtained with compounds 1 and 2 using the pancreatic tumor cell line T3M4, where the single compounds had not been previously tested.

In general, the results in PLP2 cells (Table 5) show that the encapsulated compounds are not toxic for the GI_{50} values in all tumor cell lines, apart from the compound **2**-loaded systems in MCF-7 cells, that present GI_{50} values higher than for PLP2.

The low GI_{50} values obtained for non-tumor PLP2 cells reinforce the importance of using a magnetic field gradient to guide and target these nanosystems for tumors *in vivo*, taking also advantage of hyperthermia capability.

Unfortunately, for the drug-loaded DPPC solid magnetoliposomes (SMLs), no satisfactory results were obtained, with very high GI_{50} values (above 7.5 μ M) in all tumor cell lines (Table S1 in Supplementary Information). This is possibly due to the fact that the phospholipid DPPC is in the rigid gel phase at room temperature, thus preventing the release of the compounds. The addition of 5% DSPE-PEG-Folate did not improve the results (Table S1). Other lipid formulations for SMLs will be tested in the near future, as well as assays at mild hyperthermia temperatures will be carried out. Also, confocal microscopy measurements will be performed to assess internalization of magnetoliposomes in cells.

5. Conclusions

In this work, the fluorescence emission of two new promising antitumor compounds, a *N*-(3-methoxyphenyl)thieno[3,2-*b*]pyridin-7-amine **1** and a *N*-(2-methoxyphenyl)thieno[3,2-*b*]pyridin-7-amine **2**, was studied in different environments. These *in vitro* potent antitumor thienopyridin-7-arylamine derivatives were successfully incorporated in both aqueous and solid magnetoliposomes based on superparamagnetic manganese ferrite nanoparticles, with high encapsulation efficiencies. The intrinsic fluorescence of the potential antitumor drugs was used as a tool to obtain information about compounds location in magnetoliposomes.

The magnetic properties of the manganese ferrite-based magnetoliposomes were measured for the first time, evidencing a superparamagnetic behaviour.

Growth inhibitory concentrations on tumor cell lines obtained with aqueous magnetoliposomes with encapsulated compounds **1** and **2** point to promising future drug delivery applications of these anticancer compounds *in vivo*, using magnetoliposomes simultaneously as drug nanocarriers and hyperthermia agents, to increase the efficacy of anticancer therapies.

6. Acknowledgements

This work was supported by the Portuguese Foundation for Science and Technology (FCT) in the framework of the Strategic Funding of CF-UM-UP (UID/FIS/04650/2013), CQUM (UID/QUI/00686/2013 and 2016) and CIMO (UID/AGR/00690/2013), the latter also supported by FEDER - Program PT2020.

FCT, POPH-QREN and FSE are acknowledged for the PhD grant of A. R. O. Rodrigues (SFRH/BD/90949/2012), the post-doc grant of R. C. Calhela (SFRH/BPD/68344/2010) and for financial support to MAP-Fis PhD Programme.

7. References

1. S. Mornet, S. Vasseur, F. Grasset and E. Duguet, Magnetic nanoparticle design for medical diagnosis and therapy, *J. Mater. Chem.*, 2004, **14**, 2161-2175
2. S. Dandamudi and R. B. Campbell, Development and characterization of magnetic cationic liposomes for targeting tumor microvasculature, *Biochim. Biophys. Acta*, 2007, **1768**, 427-438.
3. A. S. Lübbe, C. Bergemann, J. Brock and D. G. McClure, Physiological aspects in magnetic drug targeting, *J. Magn. Magn. Mater.*, 1999, **194**, 149-155.
4. S. Dandamudi and R. B. Campbell, The drug loading, cytotoxicity and tumor vascular targeting characteristics of magnetite in magnetic drug targeting, *Biomaterials*, 2007, **28** 4673-4683.
5. H.-J. Weinmann, W. Ebert, B. Misselwitz and H. S.-Willich, Tissue-specific MR contrast agents, *Eur. J. Radiol.*, 2003, **46**, 33-44.
6. N. Nuytten, M. Hakimhashemi, T. Ysenbaert, L. Defour, J. Trekker, S. J. Soenen, P. Van der Meeren and M. Cuyper, PEGylated lipids impede the lateral diffusion of adsorbed proteins at the surface of (magneto)liposomes, *Colloids Surf. B: Biointerfaces*, 2010, **80**, 227-231.
7. U. I. Tromsdorf, N. C. Bigall, M. G. Kaul, O. T. Bruns, M. S. Nikolic, B. Mollwitz, R. A. Sperling, R. Reimer, H. Hohenberg, W. J. Parak, S. Forster, U. Beisiegel, G. Adam and H. Weller, Size and surface effects on the MRI relaxivity of manganese ferrite nanoparticle contrast agents, *Nano Lett.*, 2007, **7**, 2422-2427.
8. E. Amstad, J. Kohlbrecher, E. Müller, T. Schweizer, M. Textor and E. Reimhult, Triggered release from liposomes through magnetic actuation of iron oxide nanoparticle containing membranes, *Nano Lett.*, 2011, **11**, 1664-1670.
9. P. Tartaj, M. P. Morales, S. Veintemillas-Verdaguer, T. Gonzalez-Carreno and C. J. Serna, The preparation of magnetic nanoparticles for applications in biomedicine, *J. Phys. D: Appl. Phys.*, 2003, **36**, 182-197.
10. M. Faraji, Y. Yamini and M. Rezaee, Magnetic nanoparticles: Synthesis, stabilization, functionalization, characterization, and applications, *J. Iran. Chem. Soc.*, 2010, **7**, 1-37.
11. C. M. Niemeyer, Nanoparticles, proteins, and nucleic acids: Biotechnology meets materials science, *Angew. Chem. Int. Ed. Engl.* 2001, **40**, 4128-4158.

12. G. Gregoriadis, Engineering liposomes for drug delivery, *Trends Biotechnol.*, 1995, **13**, 527-537.
13. I. M. Hafez, S. Ansell and P. R. Cullis, Tunable pH-sensitive liposomes composed of mixtures of cationic and anionic lipids, *Biophys. J.*, 2000, **79**, 1438-1446.
14. J. B. Sun, J. H. Duan, S. L. Dai, J. Ren, L. Guo, W. Jiang and Y. Li, Preparation and anti-tumor efficiency evaluation of doxorubicin-loaded bacterial magnetosomes: Magnetic nanoparticles as drug carriers isolated from *Magnetospirillum gryphiswaldense*, *Biotechnol. Bioeng.*, 2008, **101**, 1313-1320.
15. Y. Malam, M. Loizidou and A. M. Seifalian, Liposomes and nanoparticles: nanosized vehicles for drug delivery in cancer, *Trends Pharmacol. Sci.*, 2009, **30**, 592-599.
16. M. J. Munchhof, J. S. Beebe, J. M. Casavant, B. A. Cooper, J. L. Doty, R. C. Higdon, S. M. Hillerman, C. I. Soderstrom, E. A. Knauth, M. A. Marx, A. M. K. Rossi, S. B. Sobolov and J. Sun, Design and SAR of thienopyrimidine and thienopyridine inhibitors of VEGFR-2 kinase activity, *Bioorg. Med. Chem. Lett.*, 2004, **14**, 21-24.
17. H. R. Heyman, R. R. Frey, P. F. Bousquet, G. A. Cunha, M. D. Moskey, A. A. Ahmed, N. B. Soni, P. A. Marcotte, L. J. Pease, K. B. Glaser, M. Yates, J. J. Bouska, D. H. Albert, C. L. Black-Schaefer, P. J. Dandliker, K. D. Stewart, P. Rafferty, S. K. Davidsen, M. R. Michaelides, M. L. Curtin, Thienopyridine urea inhibitors of KDR kinase, *Bioorg. Med. Chem. Lett.*, 2007, **17**, 1246-1249.
18. S. Claridge, F. Raepfel, M.-C. Granger, N. Bernstein, O. Saavedra, L. Zhan, D. Llewellyn, A. Wahhab, R. Deziel, J. Rahil, N. Beaulieu, H. Nguyen, I. Dupont, A. Barsalou, C. Beaulieu, I. Chute, S. Gravel, M.-F. Robert, S. Lefebvre, M. Dubay, R. Pascal, J. Gillespie, Z. Jin, J. Wang, J. M. Besterman, A. R. MacLeod and A. Vaisburg, Discovery of a novel and potent series of thieno[3,2-*b*]pyridine-based inhibitors of *c*-Met and VEGFR-2 tyrosine kinases, *Bioorg. Med. Chem. Lett.*, 2008, **18**, 2793-2798.
19. O. Saavedra, S. Claridge, L. Zhan, F. Raepfel, M.-C. Granger, S. Raepfel, M. Mannion, F. Gaudette, N. Zhou, L. Isakovic, N. Bernstein, R. Déziel, H. Nguyen, N. Beaulieu, C. Beaulieu, I. Dupont, J. Wang, R. Macleod, J. M. Besterman and A. Vaisburg, N³-Arylmalonamides: a new series of thieno[3,2-*b*]pyridine based inhibitors of *c*-Met and VEGFR2 tyrosine kinases, *Bioorg. Med. Chem. Lett.*, 2009, **19**, 6836-6839.

20. S. Raeppl, S. Claridge, O. Saavedra, F. Gaudette, L. Zhan, M. Mannion, N. Zhou, F. Raeppl, M.-C. Granger, L. Isakovic, R. Déziel, H. Nguyen, N. Beaulieu, C. Beaulieu, I. Dupont, M.-F. Robert, S. Lefebvre, M. Dubay, J. Rahil, J. Wang, H. Ste-Croix, A. R. Macleod, J. Besterman and A. Vaisburg, *N*-(3-Fluoro-4-(2-arylthieno[3,2-*b*]pyridin-7-yloxy)phenyl)-2-oxo-3-phenyl-imidazolidine-1-carboxamides: a novel series of dual *c*-Met/VEGFR2 receptor tyrosine kinase inhibitors, *Bioorg. Med. Chem. Lett.*, 2009, **19**, 1323-1328.
21. V. A. Machado, D. Peixoto, R. Costa, H. J. C. Froufe, R. C. Calhelha, R. M. V. Abreu, I. C. F. R. Ferreira, R. Soares and M.-J. R. P. Queiroz, Synthesis, antiangiogenesis evaluation and molecular docking studies of 1-aryl-3-[(thieno[3,2-*b*]pyridin-7-ylthio)phenyl]ureas: Discovery of a new substitution pattern for type II VEGFR-2 Tyr kinase inhibitors, *Bioorg. Med. Chem.*, 2015, **23**, 6497-6509.
22. I. Hayakawa, R. Shioya, T. Agatsuma, H. Furukawa and Y. Sugano, Thienopyridine and benzofuran derivatives as potent anti-tumor agents possessing different structure-activity relationships, *Bioorg. Med. Chem. Lett.*, 2004, **14**, 3411-3414.
23. M.-J. R. P. Queiroz, R. C. Calhelha, L. A. Vale-Silva, E. Pinto, M. S.-J. Nascimento, Novel 6-[(hetero)arylamino]thieno[3,2-*b*]pyridines: synthesis and antitumoral activities, *Eur. J. Med. Chem.*, 2010, **45**, 5732-5738.
24. M.-J. R. P. Queiroz, R. C. Calhelha, L. A. Vale-Silva, E. Pinto, R. T. Lima, M. H. Vasconcelos, Efficient synthesis of new 6-(hetero)arylthieno[3,2-*b*]pyridines by Suzuki-Miyaura coupling. Antitumoral evaluation and SARs, *Eur. J. Med. Chem.*, 2010, **45**, 5628-5634.
25. M.-J. R. P. Queiroz, R. C. Calhelha, L. A. Vale-Silva, E. Pinto, G. M. Almeida and M. H. Vasconcelos, Synthesis and evaluation of tumor cell growth inhibition of novel methyl 3-amino-6-[(hetero)arylethynyl]thieno[3,2-*b*]pyridine-2-carboxylates. Structure-activity relationships and effects on the cell cycle and apoptosis, *Eur. J. Med. Chem.*, 2011, **46**, 236-240.
26. M.-J. R. P. Queiroz, S. Dias, D. Peixoto, A. R. O. Rodrigues, A. D. S. Oliveira, P. J. G. Coutinho, L. A. Vale-Silva, E. Pinto and E. M. S. Castanheira, New potential antitumoral di(hetero)-arylether derivatives in the thieno[3,2-*b*]pyridine series: synthesis and fluorescence studies in solution and in nanoliposomes, *J. Photochem. Photobiol. A: Chem.*, 2012, **238**, 71-80.
27. R. M. V. Abreu, I. C. F. R. Ferreira, R. C. Calhelha, R. T. Lima, M. H. Vasconcelos, F. Adegas, R. Chaves and M.-J. R. P. Queiroz, Anti-hepatocellular carcinoma activity using HepG2 cells and hepatotoxicity of 6-substituted methyl 3-

aminothieno[3,2-*b*]pyridine-2-carboxylate derivatives: in vitro evaluation, cell cycle analysis and QSAR studies, *Eur. J. Med. Chem.*, 2011, **46**, 5800-5806.

28. R. C. Calhelha, I. C. F. R. Ferreira, D. Peixoto, R. M. V. Abreu, L. A. Vale-Silva, E. Pinto, R. T. Lima, M. I. Alvelos, M. H. Vasconcelos, M.-J. R. P. Queiroz, Aminodi(hetero)aryl- amines in the thieno[3,2-*b*]pyridine series: synthesis, effects in human tumor cells growth, cell cycle analysis, apoptosis and evaluation of toxicity using non-tumor cells, *Molecules*, 2012, **17**, 3834-3843.

29. M.-J. R. P. Queiroz, D. Peixoto, R. C. Calhelha, P. Soares, T. Santos, R. T. Lima, J. F. Campos, R. M. V. Abreu, I. C. F. R. Ferreira and M. H. Vasconcelos, New di(hetero)arylethers and di(hetero)arylamines in the thieno[3,2-*b*]pyridine series: Synthesis, growth inhibitory activity on human tumor cell lines and non-tumor cells, effects on cell cycle and on programmed cell death, *Eur. J. Med. Chem.*, 2013, **69**, 855-862.

30. V. A. Machado, D. Peixoto, M.-J. R. P. Queiroz and R. Soares, Antiangiogenic 1-aryl-3-[3-(thieno[3,2-*b*]pyridin-7-ylthio)phenyl]ureas inhibit MCF-7 and MDA-MB-231 human breast cancer cell lines through PI3K/Akt and MAPK/Erk pathways, *J. Cell. Biochem.*, 2016, **117**, 2791-2799.

31. A. R. O. Rodrigues, J. M. F. Ramos, I. T. Gomes, B. G. Almeida, J. P. Araújo, M.-J. R. P. Queiroz, Paulo J. G. Coutinho and Elisabete M. S. Castanheira, Magnetoliposomes based on manganese ferrite nanoparticles as nanocarriers for antitumor drugs, *RSC Advances*, 2016, **6**, 17302-17313.

32. J. M. H. Kremer, M. W. J. v. d. Esker, C. Pathmamanoharan and P. H. Wiersema, Vesicles of variable diameter prepared by a modified injection method, *Biochemistry*, 1977, **16**, 3932-3935.

33. A. R. O. Rodrigues, I. T. Gomes, B. G. Almeida, J. P. Araújo, E. M. S. Castanheira and P. J. G. Coutinho, Magnetoliposomes based on nickel ferrite nanoparticles for biomedical applications, *Phys. Chem. Chem. Phys.*, 2015, **17**, 18011-18021.

34. C.N.C. Costa, A.C.L. Hortelão, J.M.F. Ramos, A.D.S. Oliveira, R.C. Calhelha, M.-J.R.P. Queiroz, P.J.G. Coutinho and E.M.S. Castanheira, A new antitumoral Heteroarylaminothieno[3,2-*b*]pyridine derivative: its incorporation into liposomes and interaction with proteins monitored by fluorescence, *Photochem. Photobiol. Sci.*, 2014, **13**, 1730-1740.

35. J. N. Demas and G. A. Crosby, The measurement of photoluminescence quantum yields. – Review, *J. Phys. Chem.*, 1971, **75**, 991-1024.

36. S. Fery-Forgues and D. Lavabre, Are fluorescence quantum yields so tricky to measure? A demonstration using familiar stationery products, *J. Chem. Educ.*, 1999, **76**, 1260-1264.
37. B. Valeur, *Molecular Fluorescence – Principles and Applications*, Wiley-VCH, Weinheim, 2002.
38. I. Johnson and M. T. Z. Spence, *Molecular Probes Handbook: A Guide to Fluorescent Probes and Labeling Technologies*, 11th Ed., Invitrogen, 2011.
39. M. I. Dias, L. Barros, M. Dueñas, E. Pereira, A. M. Carvalho, R. C. Alves, M. B. P. P. Oliveira, C. Santos-Buelga and I. C. F. R. Ferreira, Chemical composition of wild and commercial *Achillea millefolium L.* and bioactivity of the methanolic extract, infusion and decoction, *Food Chem.*, 2013, **141**, 4152-4160.
40. V. Vichai and K. Kirtikara, Sulforhodamine B colorimetric assay for cytotoxicity screening, *Nat. Protoc.* 2006, **1**, 1112-1116.
41. W. Dawson and M. Windsor, Fluorescence yields of aromatic compounds, *J. Phys. Chem.*, 1968, **72**, 3251-3260.
42. M.-J. R. P. Queiroz, D. Peixoto, A. R. O. Rodrigues, P. Mendes, C. N. C. Costa, P. J. G. Coutinho and E. M. S. Castanheira, New 1,3-diarylureas linked by C-C Suzuki coupling to the methyl 3-aminothieno[3,2-*b*]pyridine-2-carboxylate moiety: synthesis and fluorescence studies in solution and in lipid membranes, *J. Photochem. Photobiol. A: Chem.*, 2013, **255**, 27-35.
43. M. S. D. Carvalho, A. C. L. Hortelão, R. C. Calhela, A. S. Abreu, P. J. G. Coutinho, M.-J. R. P. Queiroz and E. M. S. Castanheira, Fluorescence studies on potential antitumor 6-(hetero)arylthieno[3,2-*b*]pyridine derivatives in solution and in nanoliposomes, *J. Photochem. Photobiol. A: Chem.*, 2013, **264**, 56-66.
44. D. Papahadjopoulos and N. Miller, Phospholipid model membranes. I. Structural characteristics of hydrated liquid crystals, *Biochim. Biophys. Acta*, 1967, **135**, 624-638.
45. B. Lentz, Membrane ‘fluidity’ as detected by diphenylhexatriene probes, *Chem. Phys. Lipids*, 1989, **50**, 171-190.
46. C. Toniolo, M. Crisma, F. Formaggio, C. Peggion, V. Monaco, C. Goulard, S. Rebuffat and B. Bodo, Effect of *N*^α-Acyl Chain Length on the Membrane-Modifying Properties of Synthetic Analogs of the Lipopeptaibol Trichogin GA IV, *J. Am. Chem. Soc.*, 1996, **118**, 4952-4958.

47. M. Lucaciu, S. Rebuffat, C. Goulard, H. Duclohier, G. Molle and B. Bodo, Interaction of the 14-residue peptaibols, harzianins HC, with lipid bilayers: permeability modifications and conductance properties, *Biochim. Biophys. Acta*, 1997, **1323**, 85-96.
48. P. Pradhan, J. Giri, R. Banerjee, J. Bellare and D. Bahadur, Preparation and characterization of manganese ferrite-based magnetic liposomes for hyperthermia treatment of cancer, *J. Magn. Magn. Mater.*, 2007, **311**, 208-215.
49. A. Hervault and N. T. K. Thanh, Magnetic nanoparticle-based therapeutic agents for thermo-chemotherapy treatment of cancer, *Nanoscale*, 2014, **6**, 11553-11573.
50. H. Curtis and N. Barnes, *Biology*, 5th Edition, Worth Publishers, New York, 1989.
51. D. L. Schulz, R. A. Sailer and A. N. Caruso, Superparamagnetic Transition Metal Iron Oxygen Nanoparticles, *US Patent* No. 0194733, 2009.
52. L. Khanna and N. K. Verma, Synthesis, characterization and in vitro cytotoxicity study of calcium ferrite nanoparticles, *Mater. Sci. Semicond. Process.*, 2013, **16**, 1842-1848.
53. S. Zhang, H. Niu, Y. Zhang, J. Liu, Y. Shia, X. Zhang and Y. Cai, Biocompatible phosphatidylcholine bilayer coated on magnetic nanoparticles and their application in the extraction of several polycyclic aromatic hydrocarbons from environmental water and milk samples, *J. Chromatogr. A*, 2012, **1238**, 38-45.
54. S. García-Jimeno, E. Escribano, J. Queralt and J. Estelrich, Magnetoliposomes prepared by reverse-phase followed by sequential extrusion: Characterization and possibilities in the treatment of inflammation, *Int. J. Pharmaceut.*, 2011, **405**, 181-187.
55. D. R. Lide, Ed., *CRC Handbook of Chemistry and Physics*, 89th Ed., CRC Press/Taylor and Francis, Boca Raton, FL, USA, 2009.
56. J. N. Israelachvili, S. Marcelja and R. G. Horn, Physical principles of membrane organization, *Q. Rev. Biophys.*, 1980, **13**, 121-200.
57. D. B. Kell and C. M. Harris, On the dielectrically observable consequences of the diffusional motions of lipids and proteins in membranes. 1. Theory and overview, *Eur. Biophys. J.*, 1985, **12**, 181-197.

58. L. Tilley, K. R. Thulborn and W. H. Sawyer, An assessment of the fluidity gradient of the lipid bilayer as determined by a set of *n*-(9-anthroyloxy)fatty acids (*n* = 2, 6, 9, 12, 16), *J. Biol. Chem.*, 1979, **254**, 2592-2594.
59. M. A. Bahri, B. J. Heyne, P. Hans, A. E. Seret, A. A. Mouithys-Mickalad and M. D. Hoebeke, Quantification of lipid bilayer effective microviscosity and fluidity effect induced by propofol, *Biophys. Chem.*, 2005, **114**, 53-61.

8. Supplementary information

8.1 Size distribution of SMLs of the lipid DPPC by Dynamic Light Scattering (DLS)

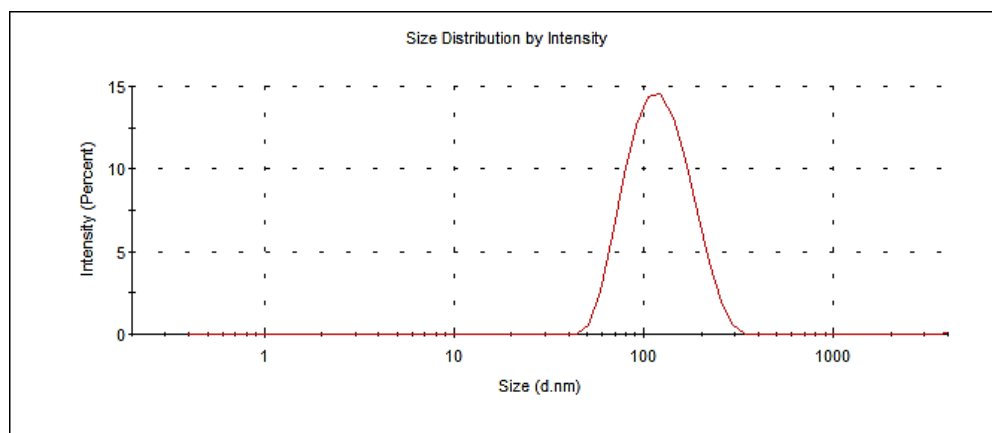


Fig. S1 Size distribution (by intensity) obtained from DLS for solid magnetoliposomes of DPPC containing manganese ferrite nanoparticles, at 25°C.

8.2 SEM image of SMLs of the lipid DPPC

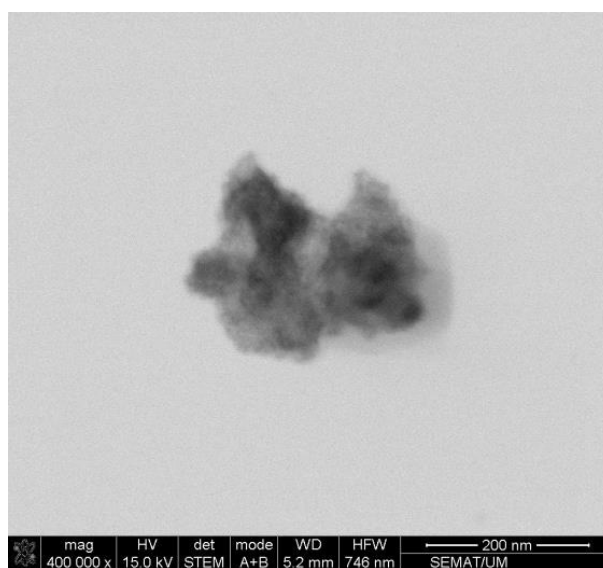


Fig. S2 SEM image (with application of a negative staining) for solid magnetoliposomes of the lipid DPPC containing manganese ferrite nanoparticles, showing an aggregate of two magnetoliposomes.

8.3 Growth inhibitory activity of drug-loaded solid magnetoliposomes

Table S1 Growth inhibitory activity of drug-loaded solid magnetoliposomes on various human tumor cell lines and non-tumor porcine liver primary cells (PLP2).

Cell line	GI ₅₀ values ^{a,b} (μM) for compound 1		GI ₅₀ values ^{a,b} (μM) for compound 2	
	DPPC SMLs with compound 1	DPPC/PEG-Fol (95:5) SMLs with compound 1	DPPC SMLs with compound 2	DPPC/PEG-Fol (95:5) SMLs with compound 2
HeLa	> 7.5	> 7.5	> 7.5	> 7.5
MCF7	> 7.5	> 7.5	> 7.5	> 7.5
T3M4	> 7.5	> 7.5	> 7.5	> 7.5
NCI-H460	> 7.5	> 7.5	> 7.5	> 7.5
PLP2	> 7.5	> 7.5	> 7.5	> 7.5

^a GI₅₀ values correspond to the concentration which inhibited 50% of cell growth. Results are from three independent experiments (performed in triplicate).

^b Maximum compound concentration tested: 7.5 μM.

**Solid and aqueous magnetoliposomes as nanocarriers for a
new potential drug active against breast cancer**

Ana Rita O. Rodrigues, Pedro M. F. Fernandes, Pedro M. Silva, V. A. Machado,
Bernardo G. Almeida, J. P. Araújo, Maria-João R. P. Queiroz, Elisabete M. S.
Castanheira, Paulo J. G. Coutinho

Colloids and Surfaces B: Biointerfaces **158** (2017) 460-468

INDEX

1. Abstract
2. Introduction
3. Experimental
4. Results and discussion
5. Conclusions
6. Acknowledgments
7. References
8. Supplementary information

1. Abstract

Iron oxide nanoparticles, with diameters around 12 nm, were synthesized by coprecipitation method. The magnetic properties indicate a superparamagnetic behavior with a coercive field of 9.7 Oe and a blocking temperature of 118 K. Both aqueous and solid magnetoliposomes containing magnetite nanoparticles have sizes below 150 nm, suitable for biomedical applications. Interaction between both types of magnetoliposomes and models of biological membranes was proven. A new antitumor compound, a diarylurea derivative of thienopyridine, active against breast cancer, was incorporated in both aqueous and solid magnetoliposomes, being mainly located in the lipid membrane. A promising application of these magnetoliposomes in oncology is anticipated, allowing a combined therapeutic approach, using both chemotherapy and magnetic hyperthermia.

2. Introduction

The potential of magnetic nanoparticles for biomedical applications has been recognized, as they offer major advantages due to their unique size and physicochemical properties [1]. Nanoparticles with superparamagnetic behavior are preferred for these purposes, as they exhibit a strong magnetization only when an external magnetic field is applied [2-4]. Liposomes entrapping magnetic nanoparticles (magnetoliposomes) can be guided and localized in the therapeutic site by external magnetic field gradients and used in cancer therapy by hyperthermia [5-8]. Moreover, liposomes revealed advantageous in overcoming issues of solubility, pharmacokinetics, toxicity and *in vivo* stability and toxicity of other delivery systems [9-11]. Magnetoliposomes have been used as a chemotherapy alternative through magnetically-controlled drug delivery and thermotherapy [12-15]. Iron oxide nanoparticles (Fe_3O_4 , $\gamma\text{-Fe}_2\text{O}_3$) have been widely used due to their proven biocompatibility and low toxicity [16-20]. Magnetoliposomes containing magnetite nanoparticles have been used in MRI [21], environmental applications [22], thermo/chemotherapy [23] and treatment of other diseases [24]. These nanosystems take advantage of the very large saturation magnetization reported for magnetite nanoparticles [16,17,22], higher than the one observed for nickel ferrite [25] and manganese ferrite nanoparticles [26].

Thienopyridines including their diarylurea derivatives have shown different biological activities, namely as antitumoral agents [27] and receptor tyrosine kinase inhibitors [28]. Recently, a strong VEGFR-2 inhibition activity, with very low IC_{50} values (on the order of 10 nM) was reported for a series of new arylurea derivatives of thienopyridines [29]. Also, a potent antiproliferative activity on two human breast cancer cell lines of distinct types, a hormone-dependent MCF-7 and hormone independent MDA-MB-231 cell lines was described for this type of compounds [30].

In this work, both aqueous and dry magnetoliposomes based on magnetite nanoparticles were prepared by soft templating methods and characterized. The interaction between the prepared magnetoliposomes and models of cell membranes (giant unilamellar vesicles, GUVs) was evaluated using FRET (Förster Resonance Energy Transfer).

A new diarylurea derivative of thienopyridine **1** (Figure 1), with potent activity against breast cancer cell lines [30], was incorporated in both types of magnetoliposomes. Compound **1** exhibits a strong antitumor activity in MCF-7 and MDA-MB-231 breast tumor cell lines (IC_{50} of 1.2 μ M and 5.0 μ M, respectively [30]), the latter being the most aggressive and difficult to treat. Specifically, the therapy against the highly metastatic MDA-MB-231 cancer cells could strongly benefit from the synergistic effect of chemotherapy and magnetic hyperthermia. Therefore, these studies are of main importance for the development of combined thermo/chemotherapy for breast cancer.

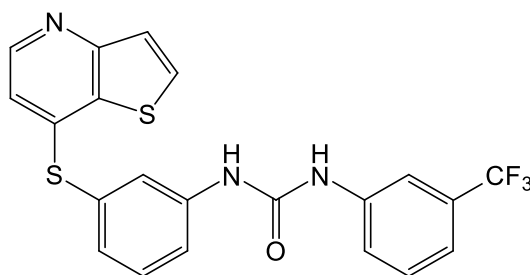


Figure 1. Structure of the diarylurea derivative of thienopyridine.

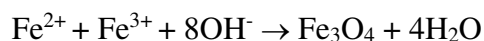
3. Experimental

All the solutions were prepared using spectroscopic grade solvents and ultrapure water (Milli-Q grade).

3.1 Magnetite nanoparticles preparation

3.1.1 Coprecipitation method

Magnetite nanoparticles (NPs) were prepared by a coprecipitation method in aqueous solution, using fresh Fe^{2+} and Fe^{3+} solutions in a 1:2 stoichiometry [31]. A 0.15 M iron (II) sulfate solution ($\text{FeSO}_4 \cdot 7\text{H}_2\text{O}$) and a 0.3 M iron (III) sulfate solution ($\text{Fe}_2(\text{SO}_4)_3 \cdot 9\text{H}_2\text{O}$) were used. 27 μL of each solution were added to 2 mL of water and 200 μL of sodium hydroxide (2.3 M) and the mixture was kept at 80°C for 2 hours, in absence of oxygen. The magnetite nanoparticles formed through the reaction:



After the synthesis, the precipitated nanoparticles were washed several times with ultrapure water, recovered by magnetic decantation and redispersed in the initial volume of water.

3.1.2 Reverse coprecipitation method

In the reverse coprecipitation method, only one iron solution is used [32,33]. 121 μL of NaOH solution (50%, 18.9 M) were added to 10 mL of ultrapure water to adjust pH to ~ 13 . A fresh 0.2 M solution of iron (II) sulfate was prepared. 5 mL of the latter solution were added, drop by drop, to the NaOH solution, under magnetic stirring. On an alternative procedure, the 5 mL of Fe^{2+} solution were added, also drop by drop, in five portions of 1 mL each, each addition separated by 10 minutes. In both cases, the total concentration of iron was 66 mM. The reaction was kept for one hour at room temperature.

The precipitated nanoparticles were then washed several times with ultrapure water and recovered by magnetic decantation.

3.2 Preparation of magnetoliposomes

3.2.1 Aqueous magnetoliposomes

Aqueous magnetoliposomes (AMLs) are formed when the magnetic nanoparticles are encapsulated in liposomes. Egg yolk phosphatidylcholine (Egg-PC), from Sigma-Aldrich, was used for lipid vesicle formation. A 10 mM Egg-PC solution in ethanol was injected, under vigorous vortexing, to an aqueous solution of nanoparticles (ethanolic injection method [34,35]). After encapsulation, the ferrofluid was washed with

water and purified by magnetic decantation and centrifugation to remove all the non-encapsulated NPs.

3.2.2 *Solid magnetoliposomes*

DPPC (1,2-Dipalmitoyl-*sn*-glycero-3-phosphocholine) and DOPG (1,2-Dioleoyl-*sn*-glycero-3-phospho-*rac*-(1-glycerol) sodium salt) from Avanti Polar Lipids, was used to produce a double lipid layer around the magnetite nanoparticles, following the procedure previously developed by us for nickel ferrite nanoparticles [25]. First, 760 μL of the synthesized magnetite NPs (in 2.1.1) were centrifuged. Then, the deposited particles were redispersed in 10 μL water in an ultrasonicator for one minute at 189 W, and 3 mL of chloroform were added to the aqueous dispersion of NPs. After vigorous agitation, 165 μL of a 20 mM solution of DPPC (or DOPG) were added under vortexing, to form the first lipid layer of solid magnetoliposomes (SMLs). The particles sedimented using a small magnet and the supernatant was discarded. The particles were then washed twice by magnetic decantation with pure water, in order to remove the lipid that was not attached to the NPs. The second lipid layer was then formed by the injection of 165 μL of lipid (20 mM), under vortexing, in a 3 mL aqueous dispersion of the particles with the first lipid layer. The resulting SMLs were then washed twice, purified with pure water by centrifugation and redispersed in 3 mL.

Compound **1** was incorporated into aqueous magnetoliposomes by the co-injection method, as already described [26]. In solid magnetoliposomes, compound **1** was incorporated by injection of an ethanolic solution together with the formation of the second lipid layer [26].

3.3 Preparation of Giant Unilamellar Vesicles (GUVs)

Soybean lecithin (*L*- α -Phosphatidylcholine), from Sigma-Aldrich, was used for GUVs preparation, using a procedure previously described [36,37]. A film of soybean lecithin was obtained by evaporation under an ultrapure nitrogen stream of a 1 mM lipid solution. This film was incubated with 20 μL of water at 45°C for 45 minutes. Then, 3 mL of 0.1 M glucose solution was added, and the resulting mixture was again incubated at 37°C.

3.4 Spectroscopic measurements

3.4.1 General methods

Absorption spectra were recorded in a Shimadzu UV-3101PC UV-vis-NIR spectrophotometer. Fluorescence measurements were performed using a Fluorolog 3 spectrofluorimeter, equipped with double monochromators in both excitation and emission and a temperature controlled cuvette holder. Fluorescence spectra were corrected for the instrumental response of the system.

3.4.2 FRET measurements

The interaction of magnetoliposomes with models of biological membranes (GUVs) was evaluated by Förster Resonance Energy Transfer (FRET). FRET efficiency, Φ_{RET} , defined as the proportion of donor molecules that have transferred their excess energy to acceptor molecules, was calculated through donor emission quenching, by taking the ratio of the donor integrated fluorescence intensities in the presence of acceptor and in the absence of acceptor [38]. The distance between donor and acceptor molecules was determined through the FRET efficiency (equation 1),

$$r_{\text{AD}} = R_0 \cdot \left[\frac{1 - \Phi_{\text{RET}}}{\Phi_{\text{RET}}} \right]^{1/6} \quad (1)$$

where R_0 is the Förster radius (critical distance), that can be obtained by the spectral overlap, $J(\lambda)$, between the donor emission and the acceptor absorption, according to equations (2) and (3) (with R_0 in Å, λ in nm, $\varepsilon_A(\lambda)$ in $\text{M}^{-1} \text{cm}^{-1}$), [38]

$$R_0 = 0.2108 [k^2 \Phi_D^0 n^{-4} J(\lambda)]^{1/6} \quad (2)$$

$$J(\lambda) = \int_0^\infty I_D(\lambda) \varepsilon_A(\lambda) \lambda^4 d\lambda \quad (3)$$

where $k^2 = 2/3$ is the orientational factor assuming random orientation of the dyes, Φ_D^0 is the fluorescence quantum yield of the donor in the absence of energy transfer, n is the refraction index of the medium, $I_D(\lambda)$ is the fluorescence spectrum of the donor normalized so that $\int_0^\infty I_D(\lambda) d\lambda = 1$, and $\varepsilon_A(\lambda)$ is the molar absorption coefficient of the acceptor.

FRET assays were employed to confirm the formation of the second lipid bilayer in the solid magnetoliposomes (SMLs). For that purpose, the rhodamine B labeled lipid Rhodamine-DHPE (1,2-dipalmitoyl-*sn*-glycero-3-phosphoethanolamine-*N*-(lissamine

rhodamine B sulfonyl) (ammonium salt) (from Avanti Polar Lipids, structure in Figure S1 of the Supplementary Material) was included the first lipid layer, while the nitrobenzoxazole labeled lipid NBD-C₆-HPC (1-palmitoyl-2-{6-[(7-nitro-2-1,3-benzoxadiazol-4-yl)amino]hexanoyl}-*sn*-glycero-3-phosphocholine) (from Avanti Polar Lipids, structure also in Figure S1) was included in the second lipid layer.

For the study of the interaction of magnetoliposomes with GUVs, the former were labeled with both NBD-C₆-HPC and the hydrophobic probe Nile Red (from Fluka, structure in Figure S1).

The fluorescence quantum yield, Φ_s , of the energy donor (in both cases, the dye NBD) in magnetoliposomes was determined by the standard method (equation 4) [39,40],

$$\Phi_s = \left[\frac{(A_r F_s n_s^2)}{(A_s F_r n_r^2)} \right] \Phi_r \quad (4)$$

where A is the absorbance at the excitation wavelength, F the integrated emission area and n the refraction index of the solvents used. Subscripts refer to the reference (r) or sample (s). The absorbance at the excitation wavelength was always lower than 0.1 to avoid the inner filter effects. The NBD-C₆-HPC molecule intercalated in lipid membranes was used as reference, $\Phi_r = 0.32$ at 25°C, as reported by Invitrogen [41].

3.4.3 Fluorescence anisotropy measurements

The steady-state fluorescence anisotropy, r , is calculated by

$$r = \frac{I_{VV} - GI_{VH}}{I_{VV} + 2GI_{VH}} \quad (5)$$

where I_{VV} and I_{VH} are the intensities of the emission spectra obtained with vertical and horizontal polarization, respectively (for vertically polarized excitation light), and $G = I_{HV}/I_{HH}$ is the instrument correction factor, where I_{HV} and I_{HH} are the emission intensities obtained with vertical and horizontal polarization (for horizontally polarized excitation light).

3.5 Structural characterization

Scanning electron microscopy (SEM) images of magnetite nanoparticles and solid magnetoliposomes were recorded using a Scanning Electron Microscope *FEI - Nova 200 NanoSEM*. In the case of SMLs, a negative staining was employed. For that, a 2% aqueous solution of ammonium molybdate tetrahydrate was prepared. Then, 20 μ L of

sample and 20 μL of staining solution were mixed and a drop of this mixture was placed onto a Formvar grid, held by tweezers. After 20 seconds, almost all the solution was removed with filter paper and left dry.

The processing of SEM images was performed using ImageJ software. It consisted in enhancing local contrast followed by automatic local thresholding and particle analysis. The area of each particle allowed an estimation of its size. The resulting histograms were fitted to Gaussian distributions.

Liposomes mean diameter and size distribution (polydispersity index) were measured using a Dynamic Light Scattering (DLS) equipment (NANO ZS Malvern Zetasizer) at 25°C, using a He-Ne laser of $\lambda = 632.8$ nm and a detector angle of 173°. Five independent measurements were performed for each sample.

X-Ray Diffraction (XRD) analyses were performed using a conventional Philips PW 1710 diffractometer, operating with Cu K_{α} radiation, in a Bragg-Brentano configuration.

3.6 Magnetic measurements

Magnetic measurements were performed at room temperature in a Superconducting Quantum Interference Device (SQUID) magnetometer (Quantum Design MPMS5XL), using applied magnetic fields up to 5.5 T.

The temperature dependence of the magnetization was measured in the temperature range from 5 K to 380 K. The curves were obtained by initially cooling the sample under an applied magnetic field of $H = 100$ Oe (field cooled, FC) and then measuring its magnetization with increasing temperature (applied field of $H = 50$ Oe). Subsequently, after reaching 380 K, the sample was re-cooled, this time with no applied magnetic field (zero-field-cooled, ZFC) and the magnetization measurements were again performed with increasing temperature, under the same magnetic field of $H = 50$ Oe. From the behavior of the FC and ZFC curves, the blocking temperature (T_B) of the superparamagnetic nanoparticles can be obtained [42]. The magnetization hysteresis loop measurements were made by fixing the temperature and measuring the magnetization at a series of different applied magnetic fields. This type of study gives information about the maximum magnetization and the degree at which the sample remains magnetized when the applied field is removed, and how easily the sample magnetization can be reversed, the so-called coercive field.

3.7 Nanoparticles encapsulation efficiency in AMLs

The nanoparticles encapsulation efficiency in aqueous magnetoliposomes (AMLs) was estimated from the spectrophotometric determination of iron (III) content, through the formation of a phenylfluorone complex sensitized with Triton X-100 [43]. To obtain iron (III) from the magnetoliposomes, the latter were digested by heating at 500° C overnight, to remove all the biological components. Then, 1 mL of concentrated nitric acid (from Sigma-Aldrich) was added and the sample was heated to 80° C for 2 hours. The temperature was then raised to 150° C for 48 h, and the pH was increased until 5.5 by successive cycles of addition and evaporation of ultrapure water (Milli-Q grade). Finally, 1 mL of water was added to the digested sample and, after ultrasonication for one hour, the iron (III) content of magnetoliposomes was released.

For the spectrophotometric measurements, the standard addition method was employed. 100 µL of the digested sample and 2×10^{-5} M, 3×10^{-5} M, 4×10^{-5} M, 5×10^{-5} M or 6×10^{-5} M of iron (III) stock solution were added to 1.6×10^{-4} M phenylfluorone and 4×10^{-3} M Triton X-100 solutions. The pH was then adjusted to 9 using 0.05 M borax buffer [43]. A calibration curve for the determination of iron (III) concentration was previously obtained. Three independent measurements were performed and standard deviations (SD) were calculated. The encapsulation efficiency, $EE(\%)$, of iron oxide nanoparticles (NPs) in AMLs was determined by equation:

$$EE(\%) = \frac{(\text{total amount of NPs} - \text{amount of non-encapsulated NPs})}{\text{total amount of NPs}} \times 100 \quad (6)$$

4. Results and discussion

4.1 Characterization of magnetite nanoparticles

4.1.1 Scanning electron microscopy (SEM)

SEM images of the nanoparticles prepared by coprecipitation in aqueous solution (preparation method described in 3.1.1) revealed generally spherical nanoparticles uniform in size, with a size distribution of 11.6 ± 1.6 nm (Figure 2).

Magnetite nanoparticles obtained by reverse coprecipitation method in aqueous solution (protocol 3.1.2.) exhibit larger sizes and a higher polydispersity (Figure 3), with some “fibrous” structures in the case of adding iron (II) in five times, with 10 minutes intervals (Figure 3B). For nanoparticles prepared adding all Fe^{2+} at once, a size

distribution of 21.7 ± 3.8 nm was obtained, while a diameter of 20.9 ± 2.7 nm was determined for the nanoparticles obtained with addition of Fe^{2+} in five portions.

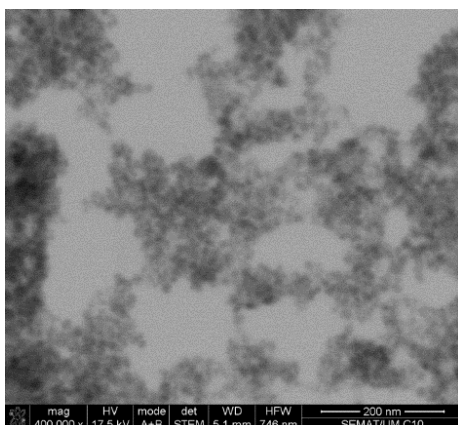


Figure 2. SEM image of magnetite nanoparticles prepared by coprecipitation method in aqueous solution. Inset: Particles size histogram and fitting to a Gaussian distribution.

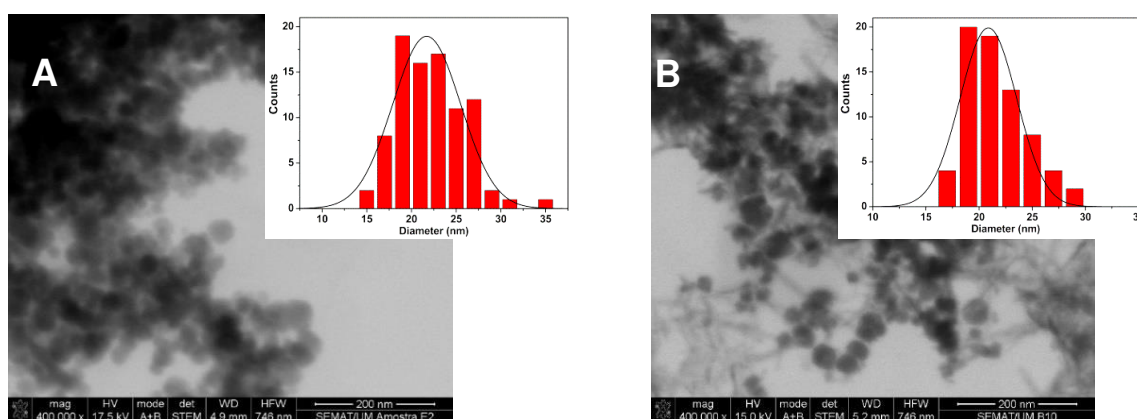


Figure 3. SEM images of magnetite nanoparticles prepared by reverse coprecipitation method in aqueous solution. **A:** Addition of all Fe^{2+} at once; **B:** Addition of Fe^{2+} in five portions, with 10 minutes intervals. Insets: Particles size histograms and fitting to Gaussian distributions.

According to these results, magnetite nanoparticles prepared by coprecipitation method in aqueous solution (Figure 2, corresponding to protocol 3.1.1) were chosen for further characterization and for the preparation of aqueous and solid magnetoliposomes, considering their small size, low polydispersity and low degree of aggregation.

4.1.2 XRD measurements

The synthesis of magnetite NPs consisting of a pure crystalline phase was confirmed by XRD analysis (Figure 4), since all their characteristic peaks (CIF 9000926), marked by their indices, are observed. The absence of high temperature thermal treatment

results in a significant amorphous background in the XRD pattern. Rietveld analysis using FullProf software [44] was performed by modeling the background as a linear interpolation between a set of points at constant scattering angles, but with fitted intensities. A good fit was possible by using preferred orientation correction at (1 1 0) plane, as it can be observed in the residuals (Figure 4B).

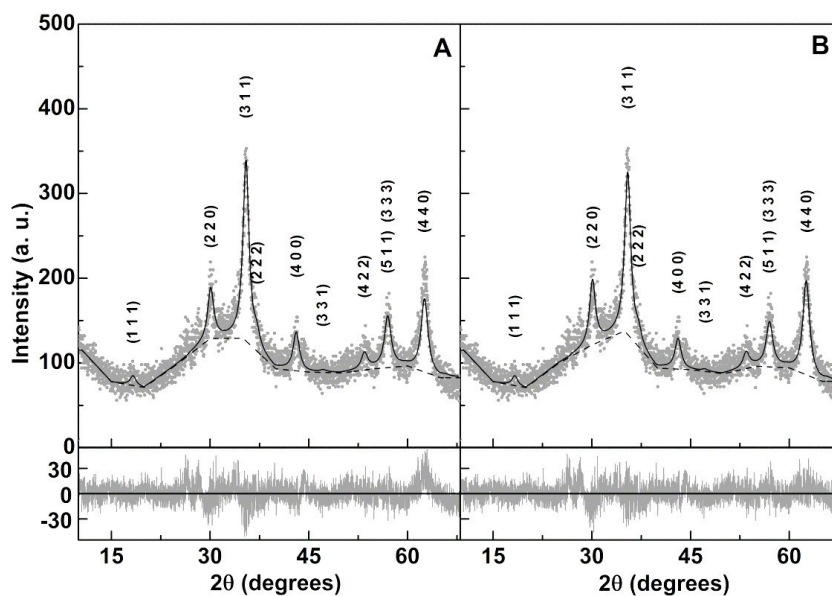


Figure 4. Rietveld analysis of XRD patterns of the sample, with (A) and without (B) preferred orientation correction at (1 1 0) plane.

This correction is based on the March function [45], equation 7,

$$\left(r^2 \cos^2 \alpha + \frac{\sin^2 \alpha}{r}\right)^{-3/2} \quad (7)$$

where, for a platy habit, α is the acute angle between the scattering vector and the normal to the crystallites. The obtained fitted value indicates a degree of preferred orientation of $(1 - r) = 0.41$. Preferred orientation of crystallites within a powder sample was also reported for the case of Cd doped ZnO [46] and Mn doped ZnO [47]. The obtained reduced χ^2 was 1.20, with an R_F value of 7.49%, and the estimated size of the Fe_3O_4 crystallites based on the Scherrer formula was 5.6 nm. The value of R_F improves to 5.67% if the overall isothermal factor, B_{over} , is optimized, but an unreasonable value of -2.95 is obtained. A summary of the results of Rietveld analysis is shown in Table S1 of the Supplementary Material.

4.1.3 Magnetic Properties

The magnetic properties of the nanoparticles synthesized by coprecipitation method (Figure 2) were characterized by measuring their corresponding magnetic hysteresis loop, which shows the relationship between the induced magnetic moment and the applied magnetic field (H). Figure 5 shows the hysteresis cycle measured on the prepared magnetite nanoparticles. A magnetic squareness value (ratio between the residual magnetization, M_r , and the saturation magnetization, M_s) of 0.023 was obtained, indicating that the synthesized nanoparticles are superparamagnetic at room temperature [42,48]. Typical magnetic properties were observed, with a very slight hysteresis, a saturation magnetization of 62 emu/g (Figure 5A) and a coercive field of 9.7 Oe (Figure 5B). Reported values for saturation magnetization of Fe_3O_4 nanoparticles typically vary from 50 to 80 emu/g, depending on their size [46-56].

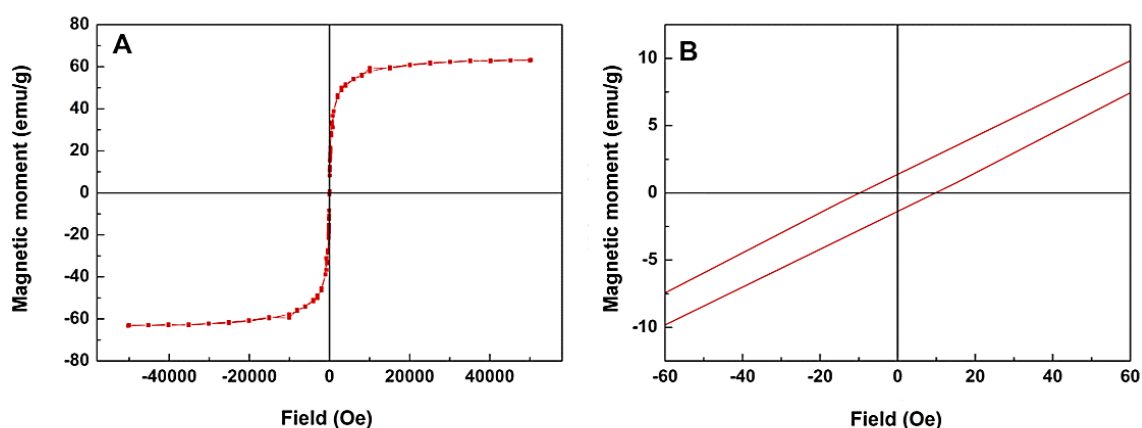


Figure 5. **A:** Magnetization hysteresis cycle of magnetite nanoparticles at $T = 300$ K. **B:** Enlargement of the hysteresis loop of Figure 5A, in the low field region.

Previous reports found negligible coercivity values for magnetite NPs of 8 nm size, while for nanoparticles of 12 nm a coercivity of 18 Oe was observed [49-50]. It was also shown that Fe_3O_4 nanoparticles with 16 nm and a coercive field of 27 Oe were able to produce heat with high efficiency in hyperthermia applications [49]. The low coercive field and the very reasonable saturation magnetization of the synthesized Fe_3O_4 nanoparticles point to a promising utility for hyperthermia applications. In fact, the inductive heating capability of magnetic nanoparticles, under AC magnetic field, is directly proportional to the area of the hysteresis cycle [55] and thus decreases as the coercive field is reduced, but increases as the saturation magnetization gets higher. A low

coercive field in superparamagnetic particles is important to avoid extensive permanent agglomeration. Its negative effect on inductive heating capability can however be compensated by the occurrence of small clusters of magnetic nanoparticles, that originate an additional and significant heating capacity, enough to reach therapeutic temperatures [57].

The superparamagnetic particles are characterized by distinct behaviors of the temperature dependence of zero-field-cooling and field-cooling magnetization curves. Starting from the low temperatures on the ZFC curve, as the temperature increases the blocked magnetic moments align with the applied measuring magnetic field, leading to an initial increase of the sample magnetization. However, as soon as thermal fluctuations are able to allow the moments to overcome the magnetic anisotropy energy barrier, the thermal randomization of the intraparticles magnetic moments produces a subsequent decrease of the magnetization curve, with increasing temperature. The zero-field-cooling curve peak corresponds to the blocking temperature, T_B [42], and here a value of $T_B = 118$ K was obtained for Fe_3O_4 NPs (Figure S2 in Supplementary Material). On the FC curve, the magnetic moments were initially forced to be aligned with the magnetic field imposed during cooling. This then gives a significant overall magnetization at low temperatures, as seen on the FC curve (Figure S2), which monotonically decreases with increasing temperature. Above the blocking temperature, NPs present superparamagnetic behavior and the ZFC and FC curves show the same temperature dependence of the magnetization, which can be approached by Curie law. At lower temperature, the ZFC and FC curves separate each other indicating that some nanoparticles are thermally blocked and are not able to completely align with the applied field. Here, the nanoparticles show ferromagnetic behavior, as thermal fluctuations are not enough to randomize the intraparticles magnetic moments.

For an ensemble of superparamagnetic particles above the blocking temperature, the magnetization can be described by the Langevin function [42]

$$M(H, T) = N\mu L\left(\frac{\mu H}{k_B T}\right) = N\mu\left(\coth\left(\frac{\mu H}{k_B T}\right) - \frac{k_B T}{\mu H}\right) \quad (8)$$

where μ is the particle magnetic moment, k_B is the Boltzmann constant, T is the absolute temperature, N is the number of particles per volume and H is the applied magnetic field. The magnetization hysteresis cycle was fitted to equation (8), assuming a spherical shape and using the density of Fe_3O_4 NPs, 5.18 g/cm^3 [56]. Diameters around 5.4 nm were

estimated, the high R^2 value ($R^2 = 0.9934$) indicating a good fit to the experimental data. This particle diameter is in excellent agreement with the one obtained from XRD analysis (section 4.1.2., Table S1).

4.2 Characterization of magnetoliposomes and interaction with model membranes

Two types of magnetoliposomes were prepared, aqueous magnetoliposomes (AMLs) and solid magnetoliposomes (SMLs) and the interaction with GUVs (giant unilamellar vesicles), used as models of cell membranes, was investigated.

4.2.1 Aqueous magnetoliposomes

Aqueous magnetoliposomes were obtained by ethanolic injection of the lipids in the aqueous ferrofluid. This method is very advantageous for hydrophobic drugs (with very limited solubility in water, as is the case of compound **1**), which can be loaded in (magneto)liposomes by coinjection. The NPs encapsulation efficiency in these liposomes was calculated from the spectrophotometric determination of iron (III), following the procedure described in [43]. The encapsulation efficiency, obtained from three independent assays, was $EE(\%) \pm SD(\%) = 46.(9) \pm 15$. This result compares well with the ones reported for the extrusion method by Sabaté *et al.* ($EE = 19\%$ in the worst case) [58] and Ferreira *et al.* ($EE = 66\%$ in their best formulation) [59] and proves the suitability of the ethanolic injection method when hydrophobic drugs are considered to be loaded in AMLs. It is also probable that the encapsulation efficiency is dependent on the initial amount of ferrofluid used, as reported [58,59].

The size distribution of aqueous magnetoliposomes (AMLs) of egg phosphatidylcholine containing magnetite nanoparticles was measured by DLS. A hydrodynamic diameter of 112 ± 19 nm was determined (Figure S3 in Supplementary Material). This size is slightly larger than those obtained for AMLs of the same lipid containing nickel ferrite [25] or manganese ferrite [26] nanoparticles.

The possibility of membrane fusion between aqueous magnetoliposomes (AMLs) and giant unilamellar vesicles (GUVs), used as models of cell membranes, was evaluated by FRET. The labeled lipid NBD- C_6 -HPC and the lipid probe Nile Red were both included in AMLs, NBD acting as the energy donor and Nile Red as the energy acceptor [60]. The solvatochromic and hydrophobic dye Nile Red [61-65] exhibits a red shift in emission maximum in polar solvents. Moreover, owing to its capability to establish

H-bonds with protic solvents, Nile Red fluorescence in water is very weak, exhibiting a maximum wavelength around 660 nm [65].

When both fluorophores are incorporated in magnetoliposomes, an efficient energy transfer process is observed, exciting only the donor NBD (Figure S4 in Supplementary Material). Two fluorescence bands are observed, the first ($\lambda_{\text{max}} = 535 \text{ nm}$) corresponding to NBD emission and the second to Nile Red fluorescence ($\lambda_{\text{max}} = 630 \text{ nm}$), arising from the energy transfer of excited NBD molecules to Nile Red. If the magnetoliposomes interact with GUVs, a larger membrane will be formed by fusion. Consequently, an increase in the donor-acceptor distance will occur with a corresponding decrease in the energy transfer efficiency from NBD to Nile Red. This is observed in Figure S4, through the increase in donor emission and the decrease of acceptor fluorescence, proving membrane fusion between both systems. The assay was performed for AMLs of Egg-PC (Figure S4-A), which is in the liquid-crystalline phase at room temperature and AMLs of DPPC (Figure S4-B), which is in the gel phase at 25°C. Aqueous magnetoliposomes of DPPC/cholesterol were also recently obtained by Ferreira *et al.* [59]. Our results in Figure S4 confirm that fusion with GUVs occurs for both AMLs of Egg-PC and DPPC. This result is similar to those previously observed with aqueous magnetoliposomes of Egg-PC containing different types of magnetic nanoparticles [25,26,60].

4.2.2 *Solid magnetoliposomes*

SMLs were synthesized by the procedure previously developed by us using nickel ferrite and manganese ferrite nanoparticles [25,26]. SMLs containing iron oxide nanoparticles and with lipid bilayers of unsaturated lipids were previously obtained by Meledandri *et al.* [21], using the lipids DOPG and DOPC (18:1 PC), and by Zhang *et al.* [22], using soybean phosphatidylcholine. In this work, clusters of magnetic nanoparticles were covered with the phospholipid dipalmitoyl phosphatidylcholine (DPPC or 16:0 PC), which possesses two saturated hydrocarbon chains and a melting transition temperature of 41°C [66]. For comparison, SMLs containing a lipid bilayer of the unsaturated lipid dioleoyl phosphatidylglycerol (DOPG or 18:1 PG) were also prepared.

The formation of a DPPC bilayer around the nanoparticles was confirmed by FRET between NBD (donor) and Rhodamine (acceptor), using a methodology reported in previous works [25,26]. Briefly, the labeled lipid Rhodamine-DHPE was included in the first (inner) lipid layer and the labeled lipid NBD-C₆-HPC was included in the second

(outer) lipid layer. A Φ_D^0 value of 0.11 for NBD-C₆-HPC in magnetite SMLs was determined. An energy transfer efficiency of 75% was obtained, corresponding to a donor-acceptor distance of 3.43 nm (equations 1-3). This result evidences the formation of the double lipid layer in DPPC SMLs, considering the usual thickness of a biological membrane (7 to 9 nm [67]).

Dynamic Light Scattering measurements revealed that the DOPG and DPPC SMLs are approximately monodisperse (Figures S5 and S6 in Supplementary Material). Hydrodynamic diameters of 136 ± 32 nm and of 127 ± 28 nm were obtained, respectively, for DOPG and DPPC SMLs, revealing that these nanosystems are suitable for drug delivery applications, due to their size below 150 nm and low polydispersity. The structure of solid magnetoliposomes does not present an inner water pool and, therefore, solid magnetoliposomes can be observed by SEM microscopy. SEM image (Figure 6) of DPPC SMLs containing Fe₃O₄ nanoparticles shows spherical structures with *ca.* 123 nm diameter, in accordance with DLS results. These SMLs are structurally similar to the ones first reported by De Cuyper and Joniau [68], but the preparation method is much simpler and expedite, as there is neither the need for an initial step of coating of the magnetic nanoparticles with lauric acid, nor the dialysis procedure, that can take up to two days.

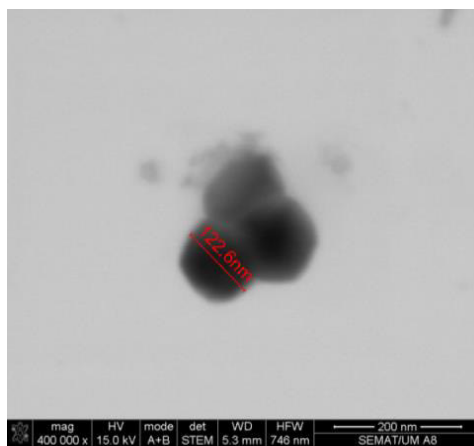


Figure 6. SEM image of solid magnetoliposomes of the lipid DPPC containing magnetite nanoparticles.

4.3 Incorporation of the antitumor compound 1 in magnetoliposomes

The thienopyridine derivative **1** (Figure 1) presents very low growth inhibitory concentration values in MCF-7 breast adenocarcinoma cell line and in the aggressive MDA-MB-231 breast tumor cell line [30]. For this reason, compound **1** was incorporated in both AMLs and SMLs containing magnetite nanoparticles and the incorporation was monitored by fluorescence emission, taking advantage of the intrinsic fluorescence of this

potential drug. Figure 7 shows the emission spectra of **1** in AMLs, SMLs and liposomes (without magnetic nanoparticles and with the same concentration of compound). It is possible to observe a quenching effect of the fluorescence emission by the magnetic nanoparticles, much more pronounced in SMLs, indicating the incorporation of the thienopyridine derivative in both AMLs and SMLs, as previously observed for another thienopyridine derivative in magnetoliposomes containing manganese ferrite NPs [26].

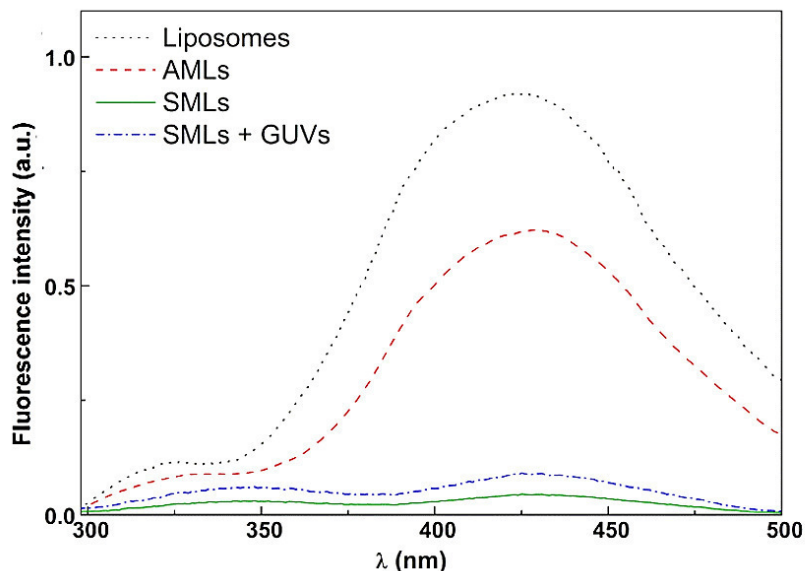


Figure 7. Fluorescence spectra ($\lambda_{\text{exc}} = 290 \text{ nm}$) of compound **1** ($3 \times 10^{-6} \text{ M}$) in liposomes and magnetoliposomes (AMLs and SMLs) of DPPC containing magnetite nanoparticles, and in SMLs after interaction with GUVs.

Fluorescence anisotropy (steady-state) values for compound **1** are presented on Table 1. For comparison, the anisotropy of the compound was measured in the highly viscous solvent glycerol ($\eta = 0.9934 \text{ Pa}\cdot\text{s}$ at room temperature [69]), with much larger viscosity than the one usually reported for lipid membranes (between 0.1 and 0.2 Pa.s [70,71]). The measured steady-state anisotropies clearly indicate that this antitumor compound is mainly located in the lipid membrane of liposomes. These values are significantly lower than the one measured in glycerol, mainly due to the distinct viscosities of both types of media (despite possible differences in excited-state lifetimes).

Comparing the anisotropy values at 25°C and 55°C in DPPC-based systems, it must be noted that an increase of the steady-state anisotropy is predicted from a diminution of the excited-state lifetime, according to Perrin equation [38]. Upon a rise of temperature, the excited-state lifetime is expected to decrease, due to the increment of the non-radiative deactivation pathways, mainly the rate constant for internal conversion

$S_1 \rightarrow S_0$. As the anisotropy values decrease strongly at higher temperature (Table 1), this behavior can be attributed to a decrease of the rotational correlation time of the fluorescent compound. This is a result of the diminution of membrane microviscosity upon changing from the gel to the liquid-crystalline phase of the lipid DPPC ($T_m = 41^\circ\text{C}$ [66]). The lipid DOPG is highly fluid at room temperature [72], justifying very low anisotropy values of the compound in liposomes and magnetoliposomes of this lipid. Egg lecithin is a natural mixture of phosphatidylcholines (mainly 16:0 PC, 18:0 PC and 18:1 PC [73]), this composition justifying lower anisotropy values than those of DPPC at room temperature, due to the presence of the unsaturated lipid 18:1 PC.

Table 1. Steady-state fluorescence anisotropy (r) values for antitumor compound **1** in liposomes, aqueous magnetoliposomes (AMLs) and solid magnetoliposomes (SMLs).

	Lipid	Temperature	r
Liposomes	Egg-PC	25°C	0.182
	DPPC	25°C	0.251
		55°C	0.157
	DOPG	25°C	0.061
AMLs	Egg-PC	25°C	0.185
	DPPC	25°C	0.258
		55°C	0.147
	DOPG	25°C	0.056
SMLs	DPPC	25°C	0.169
		55°C	0.112
	DOPG	25°C	0.043
Glycerol	---	25°C	0.308

Comparing liposomes and magnetoliposomes, it can be observed that anisotropy values for this antitumor compound in AMLs and SMLs are, in general, similar to those determined in liposomes of the same lipids. In DPPC SMLs, the anisotropy values are lower than in DPPC liposomes or AMLs. This result points to a deeper location of the compound in SMLs membrane, as it was reported that microviscosity decreases from the interface to the interior of the membrane [74,75]. This justifies the strong quenching of compound fluorescence in SMLs. Together, these results confirm that this potential antitumor drug is fully incorporated in both types of magnetoliposomes, located mainly in the lipid bilayer and experiencing changes in fluidity between the rigid gel phase (25°C) and the liquid-crystalline phase (55°C) in the case of DPPC.

Interaction of SMLs entrapping compound **1** with model membranes was also investigated. Comparing compound emission before and after interaction with GUVs (Figure 7), an unquenching effect is detected upon interaction, confirming membrane fusion of SMLs with GUVs. Therefore, the magnetoliposomes here prepared are promising as carriers for this antitumor compound active against breast cancer. Based on the experimental results, we anticipate that both aqueous and solid drug-loaded magnetoliposomes have potential as therapeutic agents in future applications of chemo/thermotherapy of cancer.

5. Conclusions

In this work, magnetite nanoparticles with size around 12 nm were synthesized by coprecipitation method. Fe₃O₄ NPs exhibit superparamagnetic properties, with maximum magnetization of 62 emu/g at 5 T applied field, a coercivity of 9.7 Oe and a blocking temperature of 118 K. Both aqueous and solid magnetoliposomes containing magnetite nanoparticles, with sizes below 150 nm and low polydispersity, were prepared and their interaction with model membranes by fusion was demonstrated.

A new antitumor compound active against breast cancer was successfully incorporated in both AMLs and SMLs, which is a promising result for the application of these nanocarriers in dual oncological therapy for breast cancer, using both hyperthermia and chemotherapy.

6. Acknowledgements

This work was supported by the Portuguese Foundation for Science and Technology (FCT) in the framework of the Strategic Funding of CF-UM-UP (UID/FIS/04650/2013) and of CQUM (UID/QUI/00686/2016).

FCT, POPH-QREN and FSE are acknowledged for the PhD grants of A. R. O. Rodrigues (SFRH/BD/90949/2012) and V. A. Machado (SFRH/BD/77373/2011) and for financial support to MAP-Fis Joint Doctoral Programme.

7. References

- [1] S. Mornet, S. Vasseur, F. Grasset, E. Duguet, Magnetic nanoparticle design for medical diagnosis and therapy, *J. Mater. Chem.* 14 (2004) 2161-2175.
- [2] A. S. Lubbe, C. Bergemann, J. Brock, D. G. McClure, Physiological aspects in magnetic drug-targeting, *J. Magn. Magn. Mater.* 194 (1999) 149-155.
- [3] D. Frascione, C. Diwoky, G. Almer, P. Opriessnig, C. Vonach, K. Gradauer, G. Leitinger, H. Mangge, R. Stollberger, R. Prassl, Ultrasmall superparamagnetic iron oxide (USPIO)-based liposomes as magnetic resonance imaging probes, *Int. J. Nanomedicine* 7 (2012) 2349-2359.
- [4] S. Dandamudi, R. B. Campbell, The drug loading, cytotoxicity and tumor vascular targeting characteristics of magnetite in magnetic drug targeting, *Biomaterials* 28 (2007) 4673-4683.
- [5] S. Dandamudi, R. B. Campbell, Development and characterization of magnetic cationic liposomes for targeting tumor microvasculature, *Biochim. Biophys. Acta* 1768 (2007) 427-438.
- [6] S. Takemori, K. Tazawa, H. Nagae, I. Yamashita, H. Kato, T. Kasagi, M. Maeda, T. Honda, M. Fujimaki, A study of DDS in hyperthermia: inductive heating with use of dextran magnetite (DM), *Drug Deliv. Syst.* 6 (1991) 465-470.
- [7] A. Jordan, P. Wust, H. Föhling, W. John, A. Hinz, R. Felix, Inductive heating of ferrimagnetic particles and magnetic fluids: physical evaluation of their potential for hyperthermia, *Int. J. Hyperthermia* 9 (1993) 51-68.
- [8] A. Hervault, N. T. K. Thanh, Magnetic nanoparticle-based therapeutic agents for thermo-chemotherapy treatment of cancer, *Nanoscale* 6 (2014) 11553-11573.
- [9] G. Poste, C. Cucana, A. Raz, P. Bugelski, R. Kirsh, I. J. Fidler, Analysis of the fate of systemically administered liposomes and implications for their use in drug delivery, *Cancer Res.* 24 (1982) 1412-1422.
- [10] G. Gregoriadis, Engineering liposomes for drug delivery: progress and problems, *Trends Biotechnol.* 13 (1995) 527-537.
- [11] T. L. Andresen, S. S. Jensen, K. Jørgensen, Advanced strategies in liposomal cancer therapy: problems and prospects of active and tumor specific drug release, *Prog. Lipid Res.* 44 (2005) 68-97.

- [12] H.-J. Weinmann, W. Ebert, B. Misselwitz, H. Schmitt-Willich, Tissue-specific MR contrast agents, *Eur. J. Radiol.* 46 (2003) 33-44.
- [13] N. Nuytten, M. Hakimhashemi, T. Ysenbaert, L. Defour, J. Trekker, S. J. Soenen, P. Van der Meeren, M. Cuyper, PEGylated lipids impede the lateral diffusion of adsorbed proteins at the surface of (magneto)liposomes, *Colloids Surf. B: Biointerfaces* 80 (2010) 227-231.
- [14] U. I. Tromsdorf, N. C. Bigall, M. G. Kaul, O. T. Bruns, M. S. Nikolic, B. Mollwitz, R. A. Sperling, R. Reimer, H. Hohenberg, W. J. Parak, S. Forster, U. Beisiegel, G. Adam, H. Weller, Size and surface effects on the MRI relaxivity of manganese ferrite nanoparticle contrast agents, *Nano Lett.* 7 (2007) 2422-2427.
- [15] E. Amstad, J. Kohlbrecher, E. Müller, T. Schweizer, M. Textor, E. Reimhult, Triggered release from liposomes through magnetic actuation of iron oxide nanoparticle containing membranes, *Nano Lett.* 11 (2011) 1664-1670.
- [16] R. Hiergeist, W. Andrä, N. Buske, R. Hergt, I. Hilger, U. Richter, W. Kaiser, Application of magnetite ferrofluids for hyperthermia, *J. Magn. Magn. Mater.* 201 (1999) 420-422.
- [17] P. Tartaj, M. P. Morales, S. Veintemillas-Verdaguer, T. González-Carreño, J. C. Serna, The preparation of magnetic nanoparticles for applications in biomedicine, *J. Phys. D Appl. Phys.* 36 (2003) R182-R197.
- [18] J. Ramos, J. Forcada, Surfactant-free miniemulsion polymerization as a simple synthetic route to a successful encapsulation of magnetite nanoparticles, *Langmuir* 27 (2011) 7222-7230.
- [19] C. Gonçalves, Y. Lalatonne, L. Melro, G. Badino, M. F. M. Ferreira, L. David, C.F.G.C. Geraldes, L. Motte, J. A. Martins, F. M. Gama, New dextrin nanomagnetogels as contrast agents for magnetic resonance imaging, *J. Mater. Chem. B* 1 (2013) 5853-5864.
- [20] US National Institutes of Health, University of Edinburgh, "Cell tracking using superparamagnetic particles of iron oxide (SPIO) and magnetic resonance imaging (MRI) - a pilot study", Clinical trial, University of Edinburgh, UK, 2009.
- [21] C. J. Meledandri, T. Ninjbadgar, D. F. Brougham, Size-controlled magnetoliposomes with tunable magnetic resonance relaxation enhancements, *J. Mater. Chem.* 21 (2011) 214-222.
- [22] S. Zhang, H. Niu, Y. Zhang, J. Liu, Y. Shia, X. Zhang, Y. Cai, Biocompatible phosphatidylcholine bilayer coated on magnetic nanoparticles and their application in the

extraction of several polycyclic aromatic hydrocarbons from environmental water and milk samples, *J. Chromatogr. A* 1238 (2012) 38-45.

[23] A. Hardiansyah, L.-Y. Huang, M.-C. Yang, T.-Y. Liu, S.-C. Tsai, C.-Y. Yang, C.-Y. Kuo, T.-Y. Chan, H.-M. Zou, W.-N. Lian, C.-H. Lin, Magnetic liposomes for colorectal cancer cells therapy by high-frequency magnetic field treatment, *Nanoscale Res. Lett.* 9 (2014) article 497.

[24] S. García-Jimeno, E. Escribano, J. Queralt, J. Estelrich, Magnetoliposomes prepared by reverse-phase followed by sequential extrusion: characterization and possibilities in the treatment of inflammation, *Int. J. Pharmaceut.* 405 (2011) 181-187.

[25] A. R. O. Rodrigues, I. T. Gomes, B. G. Almeida, J. P. Araújo, Elisabete M. S. Castanheira, Paulo J. G. Coutinho, Magnetic liposomes based on nickel ferrite nanoparticles for biomedical applications, *Phys. Chem. Chem. Phys.* 17 (2015) 18011-18021.

[26] A. R. O. Rodrigues, J. M. F. Ramos, I. T. Gomes, B. G. Almeida, J. P. Araújo, M.-J. R. P. Queiroz, Paulo J. G. Coutinho, Elisabete M. S. Castanheira, Magnetoliposomes based on manganese ferrite nanoparticles as nanocarriers for antitumor drugs, *RSC Advances* 6 (2016) 17302-17313.

[27] I. Hayakama, R. Shioya, T. Agatsuma, H. Furukawa, Y. Sugano, Thienopyridine and Benzofuran derivatives as potent anti-tumor agents possessing different structureactivity relationship, *Bioorg. Med. Chem.* 14 (2004) 3411-3414.

[28] H. R. Heyman, R. R. Frey, P. F. Bousquet, G. A. Cunha, M. D. Moskey, A. A. Ahmed, N. B. Soni, P. A. Marcotte, L. J. Pease, K. B. Glaser, M. Yates, J. J. Bouska, D. H. Albert, C. L. Black Schaefer, P. J. Dandliker, K. D. Stewart, P. Rafferty, S. K. Davidsen, M. R. Michaelides, M. L. Curtin, Thienopyridine urea inhibitors of KDR kinase, *Bioorg. Med. Chem. Lett.* 17 (2007) 1246-1249.

[29] V. A. Machado, D. Peixoto, R. Costa, H. J. C. Froufe, R. C. Calhelha, R. M. V. Abreu, I. C. F. R. Ferreira, R. Soares, M.-J. R. P. Queiroz, Synthesis, antiangiogenesis evaluation and molecular docking studies of 1-aryl-3-[(thieno[3,2-*b*]pyridin-7-ylthio)phenyl]ureas: Discovery of a new substitution pattern for type II VEGFR-2 Tyr kinase inhibitors, *Bioorg. Med. Chem.* 23 (2015) 6497-6509.

[30] V. A. Machado, D. Peixoto, M.-J. R. P. Queiroz, R. Soares, Antiangiogenic 1-aryl-3-[3-(thieno[3,2-*b*]pyridin-7-ylthio)phenyl]ureas inhibit MCF-7 and MDA-MB-231 human breast cancer cell lines through PI3K/Akt and MAPK/Erk pathways, *J. Cell. Biochem.* 117 (2016) 2791-2799.

- [31] I. Martínez-Mera, M. E. Espinosa-Pesqueira, R. Pérez-Hernández, J. Arenas-Alatorre, Synthesis of magnetite (Fe_3O_4) nanoparticles without surfactants at room temperature, *Materials Lett.* 61 (2007) 4447-4451.
- [32] N. Mahmed, O Heczko, O. Söderberg, S.-P. Hannula, Room temperature synthesis of magnetite ($\text{Fe}_{3-\delta}\text{O}_4$) nanoparticles by a simple reverse co-precipitation method, *IOP Conf. Series: Mater. Sci. Eng.* 18 (2011) Symposium 2A.
- [33] S. Santra, R. Tapeç, N. Theodoropoulou, J. Dobson, A. Hebard, W. Tan, Synthesis and Characterization of Silica-Coated Iron Oxide Nanoparticles in Microemulsion: The Effect of Nonionic Surfactants, *Langmuir* 17 (2001) 2900-2906.
- [34] S. Batzri, E. D. Korn, Single bilayer liposomes prepared without sonication, *Biochim. Biophys. Acta* 298 (1973) 1015-1019.
- [35] J. M. H. Kremer, M. W. J. vd Esker, C. Pathmamanoharan, P. H. Wiersema, Vesicles of variable diameter prepared by a modified injection method, *Biochemistry* 16 (1977) 3932-3935.
- [36] Y. Tamba, H. Terashima, M. Yamazaki, A membrane filtering method for the purification of giant unilamellar vesicles, *Chem. Phys. Lipids* 164 (2011) 351-358.
- [37] T. Tanaka, Y. Tamba, S. Md. Masum, Y. Yamashita, M. Yamazaki, La^{3+} and Gd^{3+} induce shape change of giant unilamellar vesicles of phosphatidylcholine, *Biochim. Biophys. Acta* 1564 (2002) 173-182.
- [38] B. Valeur, *Molecular Fluorescence – Principles and Applications*, Wiley-VCH, Weinheim, 2002.
- [39] J. N. Demas, G. A. Crosby, Measurement of photoluminescence quantum yields. Review, *J. Phys. Chem.* 75 (1971) 991-1024.
- [40] S. Fery-Forgues, D. Lavabre, Are fluorescence quantum yields so tricky to measure? A demonstration using familiar stationary products, *J. Chem. Educ.* 76 (1999) 1260-1264.
- [41] I. Johnson, M. T. Z. Spence, *Molecular Probes Handbook: A Guide to Fluorescent Probes and Labeling Technologies*, 11th Ed., Invitrogen, 2011.
- [42] A. S. Edelstein, R. C. Cammaratra, *Nanomaterials: Synthesis, Properties and Applications*, Taylor & Francis Group, New York, 1996.
- [43] M. Tarek, M. Zaki, A. Y. El-Sayed, Spectrophotometric determination of iron as phenylfluorone complex sensitized with Triton X-100, *Fresenius Z. Anal. Chem.* 334 (1989) 335-339.

- [44] J. Rodriguez-Carvajal, FULLPROF: A Program for Rietveld refinement and pattern matching analysis, *Abstracts of the Satellite Meeting on Powder Diffraction of the XV Congress of the IUCr*, p. 127, Toulouse, 1990.
- [45] W. A. Dollase, Correction of intensities for preferred orientation in powder diffractometry: Application of the March model, *J. Appl. Cryst.* 19 (1986) 267-272.
- [46] L.T. Jule, F. B. Dejene, A. G. Ali, K. T. Roro, A. Hegazy, N. K. Allam, E. El Shenawy, Wide visible emission and narrowing band gap in Cd-doped ZnO nanopowders synthesized via sol-gel route, *J. Alloys Compd.* 687 (2016) 920-926.
- [47] S. Yildirimcan, K. Ocakoglu, S. Erat, F. M. Emen, S. Repp, E. Erdem, The effect of growing time and Mn concentration on the defect structure of ZnO nanocrystals: X-ray diffraction, infrared and EPR spectroscopy, *RSC Adv.* 6 (2016) 39511-39521.
- [48] B. D. Cullity, C. D. Graham, *Introduction to Magnetic Materials*, John Wiley & Sons Inc., Hoboken, New Jersey, 2009; ISBN: 9780471477419.
- [49] Z. Li-Ying, D. Yong-Hua, Z. Ling, G. Hong-Chen, Magnetic behavior and heating effect of Fe₃O₄ ferrofluids composed of monodisperse nanoparticles, *Chin. Phys. Lett.* 24 (2010) 483-486.
- [50] W. Lu, Y. Shen, A. Xie, W. Zhang, Green synthesis and characterization of superparamagnetic Fe₃O₄ nanoparticles, *J. Magn. Magn. Mater.* 322 (2010) 1828-1833.
- [51] C. Hui, C. Shen, T. Yang, L. Bao, J. Tian, H. Ding, C. Li, H.-J. Gao, Large-scale Fe₃O₄ nanoparticles soluble in water synthesized by a facile method, *J. Phys. Chem. C* 112 (2008) 11336-11339.
- [52] S. Zhao, S. Asuha, One-pot synthesis of magnetite nanopowder and their magnetic properties, *Powder Technol.* 197 (2010) 295-297.
- [53] W. Pei, H. Kumada, T. Natusme, H. Saito, S. Ishio, Study on magnetite nanoparticles synthesized by chemical method, *J. Magn. Magn. Mater.* 310 (2007) 2375-2377.
- [54] K. Parekh, R. V. Upadhyay, V. K. Aswal, Monodispersed superparamagnetic Fe₃O₄ nanoparticles: synthesis and characterization, *J. Nanosci. Nanotechnol.*, 9 (2009) 2104-2110.
- [55] D.-L. Zhao, X.-W. Zeng, Q.-S. Xia, J.-T. Tang, Preparation and coercivity and saturation magnetization dependence of inductive heating property of Fe₃O₄ nanoparticles in an alternating current magnetic field for localized hyperthermia, *J. Alloys Compd.* 469 (2009) 215-218.

- [56] L. Blaney, Magnetite (Fe_3O_4): Properties, Synthesis, and Applications, *Lehigh Review*, 15 (2007) article 5.
- [57] J. Pearce, A. Giustini, R. Stigliano, P. J. Hoopes, Magnetic Heating of Nanoparticles: The Importance of Particle Clustering to Achieve Therapeutic Temperatures, *J. Nanotechnol. Eng. Med.* 4 (2013) article 011005.
- [58] R. Sabaté, R. Barnadas-Rodríguez, J. Callejas-Fernández, R. Hidalgo-Alvarez, J. Estelrich, Preparation and characterization of extruded magnetoliposomes, *Int. J. Pharm.* 347 (2008) 156-162.
- [59] R. V. Ferreira, T. M. M. Martins, A. M. Goes, J. D. Fabris, L. C. D. Cavalcante, L. E. F. Outon, R. Z. Domingues, Thermosensitive gemcitabine-magnetoliposomes for combined hyperthermia and chemotherapy, *Nanotechnology* 27 (2016) 085105.
- [60] A. R. O. Rodrigues, I. T. Gomes, B. G. Almeida, J. P. Araújo, E. M. S. Castanheira, P. J. G. Coutinho, Magnetoliposomes based on nickel/silica core/shell nanoparticles: synthesis and characterization, *Mat. Chem. Phys.* 148 (2014) 978-987.
- [61] D. K. Struck, D. Hoekstra, R. E. Pagano, Use of resonance energy transfer to monitor membrane fusion, *Biochemistry* 20 (1981) 4093-4099.
- [62] P. Greenspan, S.D. Fowler, Spectrofluorometric studies of the lipid probe, Nile red, *J. Lipid Res.* 26 (1985) 781-789.
- [63] I. and G. Krishnamoorthy, Probing the Link between Proton Transport and Water Content in Lipid Membranes, *J. Phys. Chem. B* 105 (2001) 1484-1488.
- [64] P. J. G. Coutinho, E. M. S. Castanheira, M. C. Rei, M. E. C. D. Real Oliveira, Nile Red and DCM Fluorescence Anisotropy Studies in $\text{C}_{12}\text{E}_7/\text{DPPC}$ Mixed Systems, *J. Phys. Chem. B* 106 (2002) 12841-12846.
- [65] G. Hungerford, E. M. S. Castanheira, M. E. C. D. Real Oliveira, M. G. Miguel, H. D. Burrows, *Monitoring Ternary Systems of $\text{C}_{12}\text{E}_5/\text{Water}/\text{Tetradecane}$ via the Fluorescence of Solvatochromic Probes*, *J. Phys. Chem. B* 106 (2002) 4061-4069.
- [66] B. R. Lentz, Membrane “fluidity” as detected by diphenylhexatriene probes, *Chem. Phys. Lipids* 50 (1989) 171-190.
- [67] H. Curtis, N. Barnes, *Biology*, 5th Edition, Worth Publishers, New York, 1989.
- [68] M. De Cuyper, M. Joniau, Magnetoliposomes. Formation and structural characterization. *Eur. Biophys. J.* 15 (1988) 311-319.

- [69] D. R. Lide, Ed., *CRC Handbook of Chemistry and Physics*, 89th Ed., CRC Press/Taylor and Francis, Boca Raton, FL, USA, 2009.
- [70] J. N. Israelachvili, S. Marcelja, R. G. Horn, Physical principles of membrane organization, *Q. Rev. Biophys.* 13 (1980) 121-200.
- [71] D. B. Kell, C. M. Harris, On the dielectrically observable consequences of the diffusional motions of lipids and proteins in membranes. 1. Theory and overview, *Eur. Biophys. J.* 12 (1985) 181-197.
- [72] R. Veldhuizen, K. Nag, S. Orgeig, F. Possmayer, The role of lipids in pulmonary surfactant, *Biochim. Biophys. Acta* 1408 (1998) 90-108.
- [73] D. Papahadjopoulos, N. Miller, Phospholipid model membranes. I. Structural characteristics of hydrated liquid crystals, *Biochim. Biophys. Acta* 135 (1967) 624-638.
- [74] L. Tilley, K. R. Thulborn, W. H. Sawyer, An assessment of the fluidity gradient of the lipid bilayer as determined by a set of *n*-(9-anthroyloxy)fatty acids (*n* = 2, 6, 9, 12, 16), *J. Biol. Chem.* 254 (1979) 2592-2594.
- [75] M. A. Bahri, B. J. Heyne, P. Hans, A. E. Seret, A. A. Mouithys-Mickalad, M. D. Hoebeke, Quantification of lipid bilayer effective microviscosity and fluidity effect induced by propofol, *Biophys. Chem.* 114 (2005) 53-61.

8. Supplementary information

8.1 Structure of the fluorescent probes

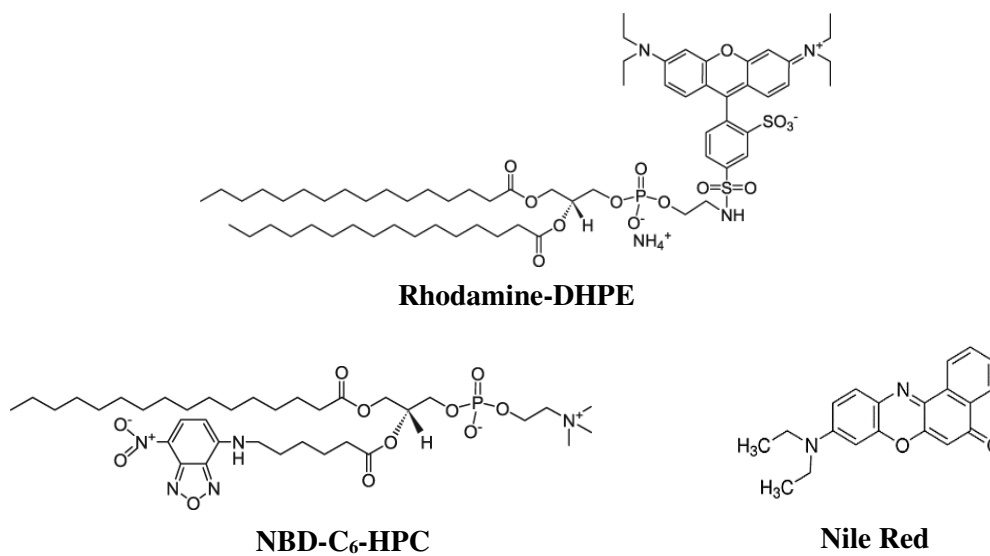


Figure S1. Structures of the fluorescent labeled lipids and the dye Nile Red.

8.2 Results of the Rietveld analysis

Table S1. Selected Rietveld analysis parameters.

Analysis	$O_{x,y,z}$ (*)	Preferred orientation	Overall temperature factor, B_{over}	Size (nm)	R_F	χ^2
A	0.24965	No ($r = 1$)	0	5.5	7.56	1.29
B	0.25074	Yes ($r = 0.59$)	0	5.6	7.49	1.20
C	0.24674	Yes ($r = 0.72$)	-2.95	5.4	5.67	1.14

(*) Value in CIF file nr. 9000926 is 0.25470

8.3 ZFC and FC curves for magnetite NPs obtained by SQUID

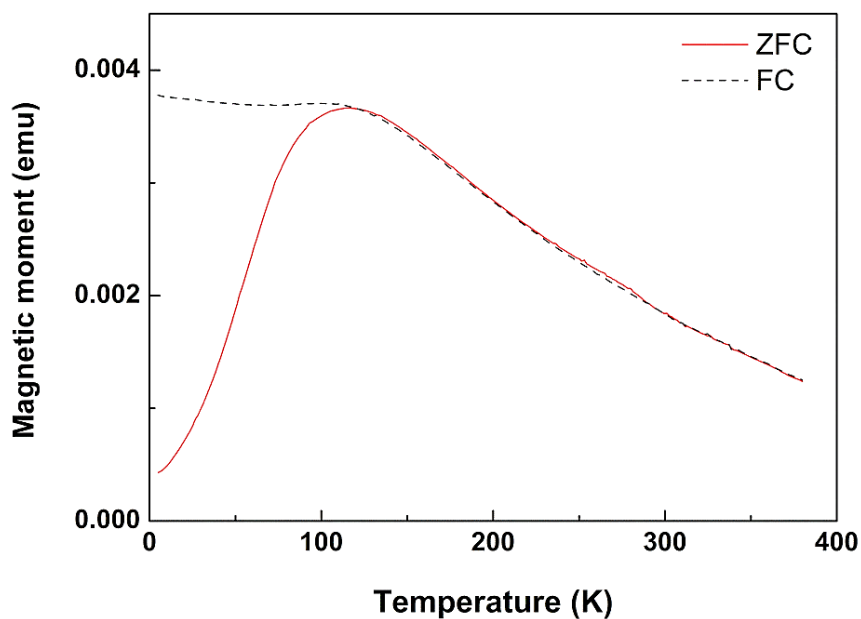


Figure S2. ZFC and FC magnetization curves of Fe₃O₄ nanoparticles.

8.4 Size distribution of aqueous magnetoliposomes obtained by Dynamic Light Scattering (DLS)

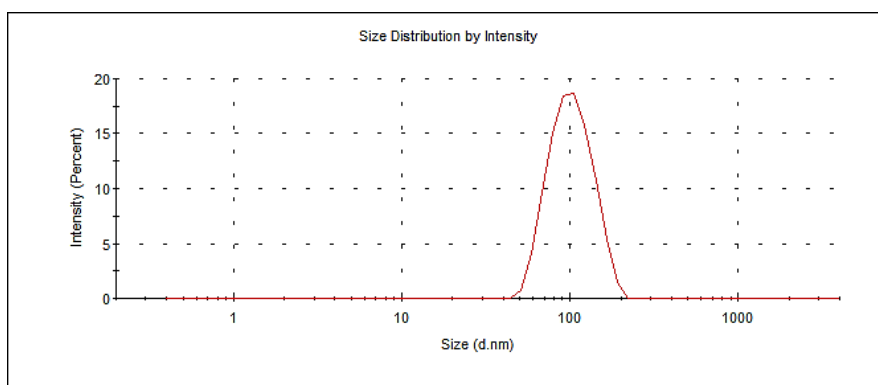


Figure S3. Size distribution obtained by DLS for aqueous magnetoliposomes of Egg phosphatidylcholine containing magnetite NPs (at 25°C).

8.5 Interaction with model membranes (GUVs) monitored by FRET

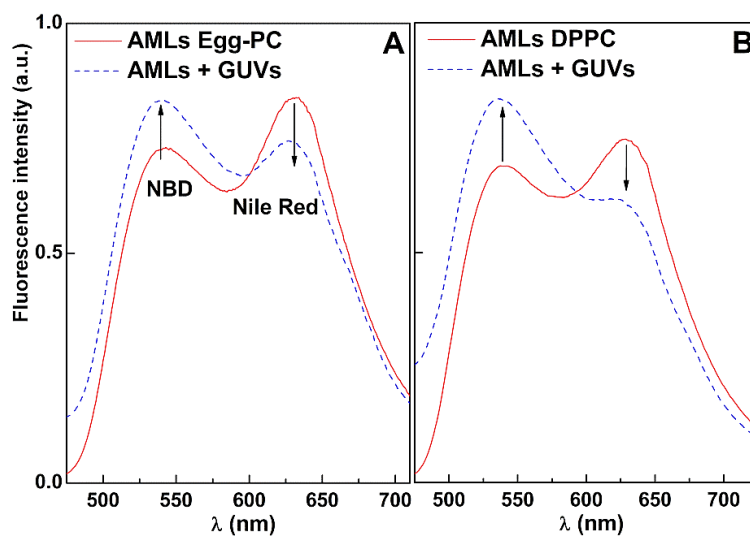


Figure S4. Fluorescence spectra ($\lambda_{\text{exc}} = 410 \text{ nm}$) of AMLs containing magnetite NPs, labelled with both NBD- $\text{C}_6\text{-HPC}$ ($2 \times 10^{-6} \text{ M}$) and Nile Red ($2 \times 10^{-6} \text{ M}$), before and after interaction with GUVs. **A:** AMLs of Egg-PC; **B:** AMLs of DPPC.

8.6 Size distribution of SMLs obtained by Dynamic Light Scattering (DLS)

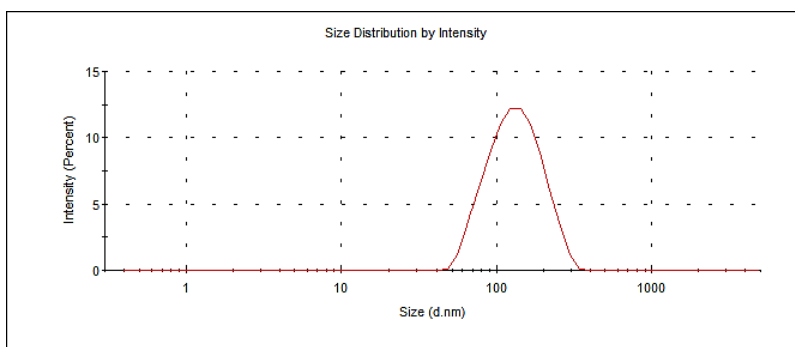


Figure S5. Size distribution obtained by DLS for solid magnetoliposomes of DOPG containing magnetite NPs (at 25°C).

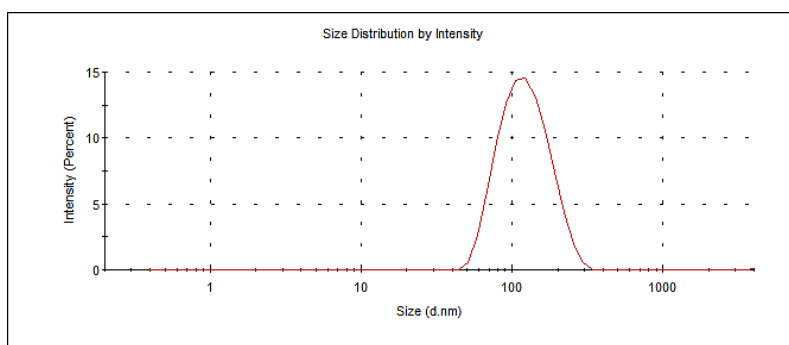


Figure S6. Size distribution obtained by DLS for solid magnetoliposomes of DPPC containing magnetite NPs (at 25°C).

Chapter 3

Overview of results

In this chapter, the results of research of the last four years are summarized, and a comparison of results obtained for the different systems is presented. Also, a few and unpublished data will be included here.

As it was described on chapter 2, in the last four years, magnetoliposomes based on several magnetic nanoparticles and with different structures were developed. Both solid and aqueous magnetoliposomes based on nickel nanoparticles, Ni/silica core/shell nanoparticles, and several ferrite (NiFe_2O_4 , MnFe_2O_4 and Fe_3O_4) nanoparticles were prepared. The main goal of this work was to design magnetoliposomes with promising properties for their application as nanocarriers for antitumor drugs. For this purpose, magnetic nanoparticles were synthesized by co-precipitation method and characterized in terms of their structure, composition and magnetic behavior. All the nanoparticles exhibited appropriate sizes with a narrow size distribution (Table 3.1), with a crystalline structure (Table 3.1), and superparamagnetic behavior at room temperature (Table 3.2), except nickel nanoparticles that showed a ferromagnetic behavior.

Table 3.1. Crystalline structure and size of the prepared nanoparticles, obtained by DLS, XRD, SEM, TEM and Langevin fit to $M(H)$.

	Calcina- tion	Crystalline Structure	Size (nm)				
			DLS	XRD	SEM	TEM	M(H)
Nickel (100%)	---	---	88 ± 7	---	66 ± 24	---	---
(1:5)	---	---	---	---	~ 110	---	---
(1:10)	---	---	157 ± 16	---	---	---	---
Ni/Silica	(1:30)	---	175 ± 24	---	---	---	---
(1:42)	---	---	---	---	~ 400	---	---
(1:60)	---	---	185 ± 21	---	---	---	---
NiFe₂O₄	800° C (2 hours)	inverse spinel	---	13.2	----	11 ± 5	6.5
MnFe₂O₄	---	spinel	---	16.5	---	26 ± 7	14
Fe₃O₄	---	inverse spinel	---	5.6	11.6 ± 1.6	---	5.4

The blocking temperature (T_B) distributions of MnFe_2O_4 nanoparticles were determined through the temperature derivative of the difference between the FC and ZFC magnetization curves (Figure 3.1, data not published). Here, the maxima correspond to the blocking temperature of the main size distribution (Table 3.2).¹ This method has shown to be more precise than the one that considers T_B as the maximum of the ZFC curve.² In accordance with TEM images (Figure 4A, article 2.3), where a few large particles were observed, two distributions were obtained. Blocking temperatures of 15.66

K and 133.52 K were obtained for smaller and larger particles distribution, respectively. Thus, the high value obtained for T_B measured directly through the maximum of the ZFC-FC (Table 3.2) can be explained by the presence of these two size distributions, where the large size distribution of the bigger nanoparticles contributes for a more pronounced shift of the ZFC peak, as their magnetic moments are unblocked at higher temperatures.

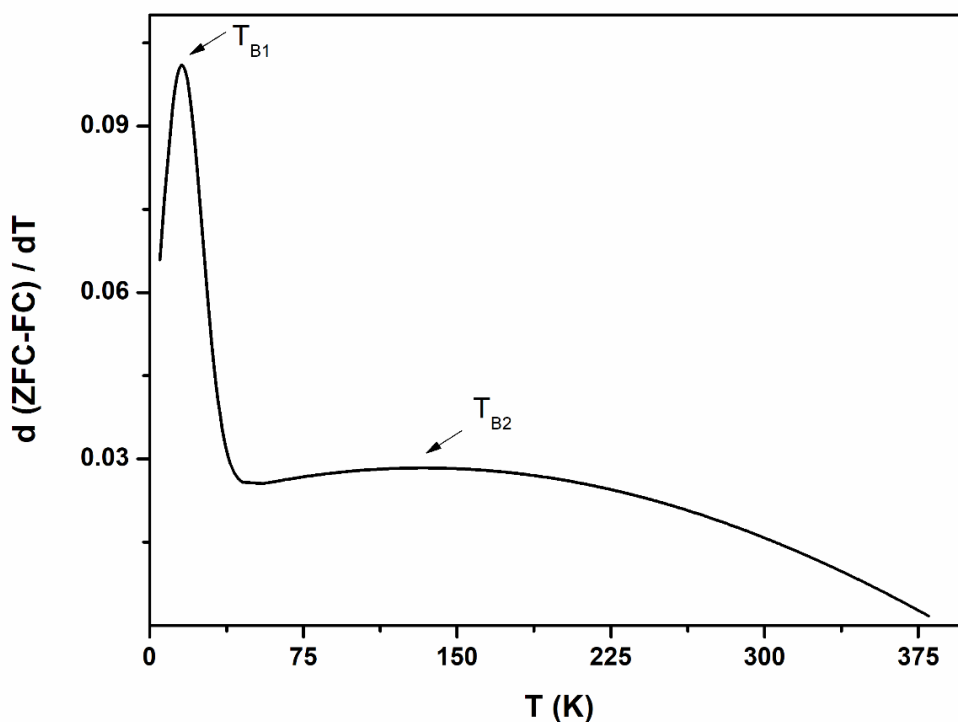


Figure 3.1. Blocking temperature distributions obtained from derivative $d(\text{ZFC-FC})/dT$.

Table 3.2. Blocking temperature (T_B), saturation magnetization (M_s), remnant magnetization (M_r), magnetic squareness value (M_r/M_s) and coercive field (H_c) of the synthesized NPs, at room temperature.

	T_B (K)		M_s (emu/g)	M_r (emu/g)	M_r/M_s	H_c (Oe)
	ZFC-FC	$\frac{d(\text{ZFC} - \text{FC})}{dT}$				
Nickel	---	---	51.20	18.00	0.35	80.00
NiFe ₂ O ₄	214	---	23.54	2.0×10^{-3}	7.2×10^{-5}	12.00
MnFe ₂ O ₄	~ 316	15.66 (T_{B1}) 133.52 (T_{B2})	36.00	0.58	0.016	6.30
Fe ₃ O ₄	---	---	62.00	1.43	0.023	9.70

The magnetic nanoparticles were then encapsulated in liposomes (AMLs) or covered by a lipid bilayer (SMLs). The structural and magnetic properties of magnetoliposomes were evaluated. In chapter 1, it was described that ideal nanoencapsulation systems must have sizes below 200 nm, in order to have an enhanced EPR effect.³ Thus, all the synthesized magnetoliposomes exhibited appropriate sizes for their application *in vivo* (Table 3.3).

Keeping in mind effective drug delivery applications, all systems show potential for further development towards this kind of application, as they have shown to fuse with models of cell membranes, thus being able to deliver encapsulated compounds. Moreover, the four different antitumor compounds studied were efficiently encapsulated in magnetoliposomes. Concerning encapsulation efficiency, experimental results (unpublished data) allowed to determine an encapsulation efficiency for compound **A** (corresponding to compound **1** of article 2.3.) of $(98.4 \pm 0.8)\%$, when encapsulated in AMLs based on NiFe₂O₄ NPs (this value was obtained using the procedure described in article 2.4, section 3.2.4). This result indicates that AMLs based on NiFe₂O₄ NPs are very promising nanocarriers for compound **A**, presenting a slightly higher encapsulation efficiency than those obtained for compounds **B** and **C** (corresponding to compounds **1** and **2** of article 2.4., respectively), when encapsulated in AMLs and SMLs based on MnFe₂O₄ NPs.

Regarding magnetic properties, as it was already mentioned, all the nanoparticles (except Ni nanoparticles) showed a superparamagnetic behavior at room temperature (Table 3.2), being suitable for combined cancer therapy, through simultaneous drug delivery and hyperthermia. The nanoparticles with the best magnetic properties were the Fe₃O₄ NPs, with a high saturation magnetization of 62 emu/g. However, the physical problem concerning magnetic properties is that their encapsulation compromises the saturation magnetization. Considering magnetic hyperthermia, it was observed that SMLs based on MnFe₂O₄ NPs are more promising than AMLs based on the same type of NPs, as with SMLs it is possible to keep almost the same magnetization as the one of net nanoparticles (tables 3.3 and 3.4). Despite the saturation magnetization of the SMLs based on manganese ferrite NPs is not so high as the one of Fe₃O₄ NPs (and probably of their SMLs), they are very promising for synergistic hyperthermia/chemotherapy, where the required values of M_s are not as high as the ones for hyperthermia therapy alone.⁴

Table 3.3. Hydrodynamic diameter of magnetoliposomes obtained by DLS and diameters of synthesized magnetoliposomes obtain by SEM and TEM. Liposomes (without magnetic nanoparticles) sizes are also shown for comparison.

	NPs	Lipids	Size (nm)		
			DLS	SEM	TEM
Liposomes	---	Egg-PC	92 ± 10	---	---
	---	DPPC	115 ± 12	---	---
AMLs	Ni	Egg-PC	103 ± 20	---	---
		DPPC	115 ± 12	---	---
	Ni/silica (1:20)	Egg-PC	135 ± 34	---	---
		DPPC	175 ± 23	---	---
		Egg-PC	92 ± 18	---	---
	MnFe ₂ O ₄	Egg-PC	82 ± 13	---	---
	Fe ₃ O ₄	Egg-PC	112 ± 19	---	---
SMLs	Ni	DOPG	98 ± 16	65 ± 28	---
		AOT	67 ± 26	115 ± 26	---
	NiFe ₂ O ₄ ^a	DOPG	94 ± 3	---	---
	NiFe ₂ O ₄ ^b	DOPG	178 ± 15	< 100	---
	MnFe ₂ O ₄	DOPG	152 ± 24	---	~ 100
		DPPC	124 ± 23	< 150	---
	Fe ₃ O ₄	DOPG	136 ± 32	---	---
		DPPC	127 ± 28	~ 123	---

^a SMLs obtained by ethanolic injection method

^b SMLs obtained by new method described in section 3.2, article 2.2.

Table 3.4. Saturation magnetization (M_s), remnant magnetization (M_r), magnetic squareness value (M_r/M_s) and coercive field (H_c) of aqueous and solid magnetoliposomes based on MnFe₂O₄, at room temperature.

	M_s (emu/g)	M_r (emu/g)	M_r/M_s	H_c (Oe)
SMLs	34.16	0.90	0.03	4.22
AMLs	1.17	0.08	0.07	8.43

A recent experiment performed in the framework of this thesis was a simple qualitative test of the motion of SMLs containing MnFe₂O₄ nanoparticles in water, under a magnetic field gradient. For that, an Agilent N5746A system was used as a DC power supply connected to a system of two large coils. First, the magnetoliposomes were

collected with a common small magnet on the right side of the Eppendorf and then a magnetic field of ~ 200 mT was turned on. After about 2.13 s, the magnetoliposomes moved approximately 0.4 cm (figure 3.2).

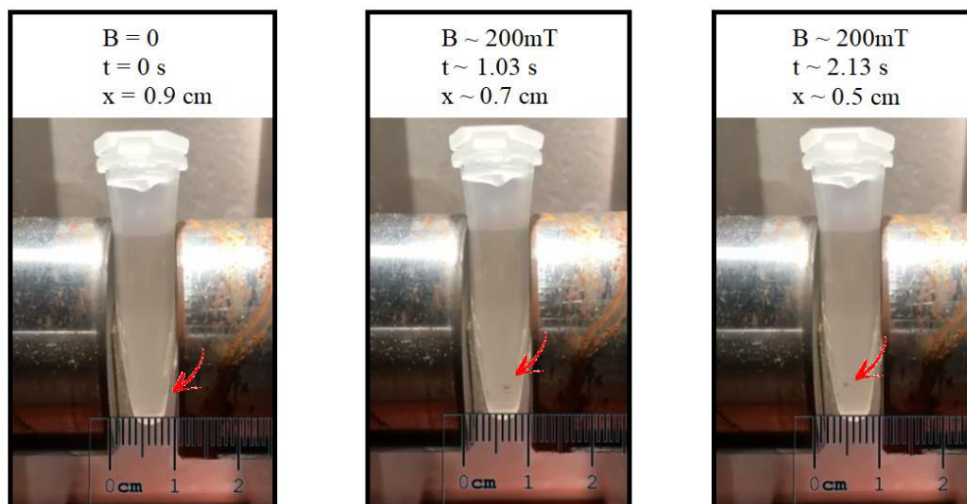


Figure 3.2. Images of an aqueous solution of SMLs based on MnFe_2O_4 NPs under a magnetic field gradient.

This simple experiment allowed concluding that SMLs based on MnFe_2O_4 nanoparticles are a promising nanoencapsulation system suitable for magnetically guided transport, as their position can be manipulated with a magnetic field gradient. Thus, using proper magnetic field engineering, these magnetoliposomes may be used to deliver anticancer drugs specifically to target tumor sites.

3.1 References

1. Pereira, C., Pereira, A. M., Fernandes, C., Rocha, M., Mendes, R., Garcia, M. P. F., Guedes, A., Tavares, P. B., Grenèche, J.-M., Araújo, J. P., Freire, C., *Chem. Mater.* **24** (2012) 1496-1504.
2. Tournus, F., Tamion, A., *J. Magn. Magn. Mater.* **2011** (323) 1118-1127.
3. Sawant, R. R., Torchilin, V. P., *AAPS J.* **14** (2012) 303-15.
4. Rao, W., Deng, Z.-S., Liu, J., *Crit. Rev. Biomed. Eng.* **38** (2010) 101–116.

Chapter 4

Conclusions and future perspectives

This thesis focused on developing magnetoliposomes as valuable nanosystems that combine the benefits of magnetic nanoparticles and liposomes. Due to their potentialities, special attention has been dedicated to synthesis methods that improve these nanosystems, while their potential has been deeply studied.

Initially, in this work, nickel/silica core/shell nanoparticles were synthesized, using microheterogeneous templating media for nickel core synthesis and TEOS hydrolysis for the silica shell. Although these nanoparticles presented a high saturation magnetization, around 50 emu/g, they did not exhibit a superparamagnetic behavior. Thus, in order to improve biocompatibility and attain the appropriate magnetic properties for biological applications, other types of magnetic nanoparticles were prepared. Therefore, small ferrite nanoparticles (NiFe_2O_4 , MnFe_2O_4 and Fe_3O_4) with superparamagnetic behavior at room temperature, were synthesized by coprecipitation method. All the types of synthesized nanoparticles were successfully encapsulated into liposomes (forming aqueous magnetoliposomes, AMLs) or covered by a lipid bilayer (creating solid magnetoliposomes, SMLs). Fe_3O_4 nanoparticles showed the highest saturation magnetization, 62 emu/g, and SMLs based on MnFe_2O_4 nanoparticles exhibited a magnetic behavior similar to net nanoparticles. Thus, SMLs based on Fe_3O_4 nanoparticles are very promising, as their saturation magnetization is expected to be as high as the one of the net nanoparticles. The magnetic properties of SMLs based on Fe_3O_4 nanoparticles will be evaluated in future work.

Four new promising antitumor drugs, thienopyridine derivatives, were efficiently incorporated in both AMLs and SMLs, with high encapsulation efficiencies. FRET measurements pointed to membrane fusion between both types of magnetoliposomes and models of cell membranes. Moreover, it was also demonstrated that AMLs based in MnFe_2O_4 nanoparticles are able to release two encapsulated antitumor compounds and to inhibit the growth of human tumor cell lines *in vitro*, while exhibiting non-toxicity for primary (non-tumor) cell lines. On the other hand, SMLs of the lipid DPPC showed no drug release in similar conditions, which could be related with the lipid composition, as DPPC is rigid at room temperature (in gel phase). Yet, this could be an advantageous outcome if compound release could be triggered by the application of an AC magnetic field. This will be focused on future work. In conclusion, the results obtained in this work point to be promising for future drug delivery applications of anticancer drugs using magnetoliposomes, simultaneously as drug nanocarriers and hyperthermia agents.

To our knowledge, it was the first time that magnetoliposomes (both AMLs and SMLs) based on NiFe_2O_4 nanoparticles and SMLs containing MnFe_2O_4 nanoparticles were synthesized. A new promising method for the synthesis of SMLs with improved magnetic properties was developed. Experimental evidence for membrane fusion between magnetoliposomes and models of cell membranes was obtained using FRET measurements in an innovative assay. Also, new promising potential anticancer drugs were preliminary tested in these nanosystems.

Despite the scientific work and the encouraging results obtained in the framework of this thesis, further research is still needed. As a follow-up of the work developed here, the following research is suggested:

- In the field of magnetic nanoparticles:
 - Exploring other types of ferrite nanoparticles, such as magnesium ferrite and calcium ferrite nanoparticles, considering magnetic properties, stability, and improved biocompatibility;
 - Exploring mixed ferrite/gold nanoparticles, either core/shell or nanoparticles decorated with gold, and evaluate their magnetic/plasmonic capabilities, aiming at developing multifunctional nanoparticles.
- In the field of magnetoliposomes:
 - To prepare magnetoliposomes with PEGylation;
 - To enhance cellular uptake via transferrin-mediated mechanism and/or improving functionalization with folate;
 - Testing pH-sensitive AMLs to improve drug release in tumor cells;
 - To evaluate the toxicity of magnetoliposomes in non-tumor cells;
 - To explore other lipid formulations for SMLs;
 - To improve AMLs magnetic properties;
 - To perform studies in tumor cell lines under the influence of an AC magnetic field;
 - To perform essays with well-established anticancer drugs already used in chemotherapy (doxorubicin, cisplatin, paclitaxel);
 - Determination of SAR using magnetic hyperthermia measurements;
 - *In vivo* studies.

Due to the complexity of magnetoliposomes, a multidisciplinary expertise, from organic and inorganic chemistry to bio- and magnetic-physics and pharmacology, is needed for a better understanding and effective application of these nanostructures. For the *in vivo* application of magnetoliposomes, the main difficulty is still the magnetic sources in clinical trials that need to be tailored, for a depth penetration treatment. Nevertheless, over the past decade, new concepts have been tested and progressive and promising work encourages the continuous investigation of magnetoliposomes applications in dual cancer therapy. The scientific community believes that the intensive work in this field should continue and much more encouraging results are yet to come.